New abundant 4CzIPN-derivatized Photosensitizers and Catalysts for
Photosynthetic Organic Reactions and Solar Fuels

by

Octavio Martinez Perez

A thesis submitted in partial fulfillment of the requirements for the degree of

Doctor of Philosophy

Department of Chemistry
University of Alberta

Abstract

The development of artificial photosynthetic systems is a promising strategy to meet future energy demands of our society and to reverse the impact of anthropogenic CO_2 in the environment. Energy conversion devices, such as photoelectrochemical cells are one key component in the transition to a society with an integrated renewable energy system. This dissertation describes a robust, high-yield route for the synthesis, characterization, and catalytic activity of photocatalysts for artificial photosynthesis as well as a solid-state synthesis method to prepare stable and efficient photocatalyst-semiconductor electrodes.

The research described here begins with the preparation of multiple Ru-polypyridyl complexes, well-known photosensitizers for photocatalytic water oxidation (OER) and carbon dioxide reduction reactions (CRR). To facilitate the integration of the photocatalytic systems to the electrical grid, the molecular assembly of these Ru-photosensitizers to OER or CRR catalysts with further immobilization onto semiconductor surfaces is a highly desirable achievement. Many factors influence the efficiency and durability of these systems. Among those factors, the anchoring moiety on the photocatalyst plays a crucial role. Anchorage groups, such as carboxylic or phosphonic ester groups commonly have been studied but these are not ideal in alkaline conditions. Here, Ru-polypyridyl photosensitizers are immobilized on semiconductor surfaces (ITO and TiO_2) via diazonium reduction, forming a C—O bond between the C5 on the 1,10-phenanthroline ligand and the O on the surface. The photosensitizer-semiconductor photoelectrodes are active and stable toward the photoelectrochemical oxidation of hydroquinone (H_2Q) and triethylamine (Et_3N) under neutral and basic conditions.

Sustainable chemical reactions for solar energy conversion and utilization require the implementation of earth-abundant, affordable, and versatile photosensitizers. The organic photosensitizer 1,2,3,5-tetrakis(carbazol-9-yl)-4,6-dicyanobenzene (4CzIPN) and its derivatives are well-known photocatalysts for visible-light-driven photoredox- and energy transfer-catalysis. Here, the derivatization of the dicyanobenzene moiety in 4CzIPN with an NHC group is described; 3CzIPN-

NHC. NHC ligands are well-known as strongly activating ligands in catalysis. 3CzIPN-NHC retains the bulk photophysical properties of the parent 4CzIPN photosensitizer. This synthesis opens a window for future tuning of the photosensitizer and incorporation into heterogeneous and homogenous photocatalysis. Upon surface functionalization of a TiO_2 with 3CzIPN-NHC, it described a new type of bonding to semiconductor surfaces. The NHC carbene center bonds to TiO_2, likely by forming hydrogen bonds to hydroxide/water groups on the surface of the semiconductor. Further, the 3CzIPN-NHC/TiO_2 surface is an active and stable photoelectrocatalyst, in the visible range (400–800 nm), towards the photoelectrooxidation of hydroquinone (H_2Q) and triethylamine (Et_3N) under neutral and alkaline conditions.

The last part of this dissertation describes the synthesis and photocatalytic activity of the Mn (I) [$Mn(CO)_3(bpy)$] catalyst coupled to an organic photosensitizer unit derived from 4CzIPN, the 3-CzIPN-imidazole. The photo and electrochemical conversion of CO_2 to carbon monoxide (CO) is, potentially, a useful step in the transformation of one of the most abundant greenhouse gases into fuels (CH_4, MeOH, etc.) and chemicals. The complex 3CzIPN-Imidazole-Mn is highly selective for the photoreduction of CO_2 to CO in CO_2-saturated acetonitrile (MeCN) solution under AM 1.5 G light. Achieving 60 TON_{CO}, the facile, robust, and low-cost preparation, in addition to strong absorption in the visible light range promotes this photocatalyst as a potent candidate for further family expansion, whether in the backbone of the catalyst or by changing the metal center with Fe or Co phthalocyanine and development into electro and photoelectrocatalysis.

Preface

Chapter 1 is the introductory section on solar energy storage, and carbon dioxide conversion and utilization.

Chapter 2 contains research on the synthesis of multiple Ru polypyridyl complexes. Part of this research was published as Wang, C.; Amiri, M.; Martinez Perez, O.; Endean, R. T.; Varley, S.; Rennie, B.; Rasu, L.; Bergens, S. H. "Modular Construction of Photoanodes with Covalently Bonded Ru- and Ir-Polypyridyl Visible Light Chromophores". *ACS Appl. Mater. Interfaces* **2018**, DOI:10.1021/acsami.8b06605. I was responsible for [Ru(bpy)(phen)(PhenO)](OTf)$_2$ preparation and characterization and data collection. The manuscript composition was carried out by Dr. Wang and Dr. Amiri. Dr. Bergens was the supervisor of the project. Additionally, most of the complexes prepared were published in another journal as Amiri, M.; Martinez Perez, O.; Endean, R. T.; Rasu, L.; Nepal, P: Xu, S.; Bergens, S. H. "Solid-phase Synthesis and Photoactivity of Ru-polypyridyl Visible Light Chromophores Bonded through Carbon to Semiconductor Surfaces". I was responsible for the synthesis and characterization of Ru polypyridyl complexes as well as the deposition on the various semiconductor surfaces, data collection and analysis.

Chapter 3 describes research that was published as Martinez-Perez, O.; Amiri, M.; Rasu, L.; Bergens, S. H. N-Heterocyclic Carbene Organic Dyes Derived from 2,4,5,6-Tetra(9H-Carbazol-9-Yl)Isophthalonitrile (4CzIPN) Bonded to TiO$_2$ Surfaces. *ECS J. Solid State Sci. Technol.* **2023**, *12* (10), 105006. https://doi.org/10.1149/2162-8777/acfff4. I was the first author and was responsible for the catalyst preparation and characterization, the data collection and analysis, and the manuscript composition. Dr. Mona Amiri assisted in the data collection and sample characterization (XPS, IPCE measurements). Dr. Rasu's exploratory findings assisted with the design of the precursors. Dr. Bergens was the supervisor of the research project.

Chapter 4 has been formatted and ready for submission to the ACS Catalysis journal as Visible-Light Driven CO$_2$ Reduction with a Manganese-Imidazole-3CzIPN Complex. Martinez-Perez, O.; Meldrum, A. and Bergens, S.H. I am the first author and

responsible for the catalyst preparation and characterization, photocatalytic activity, data collection and analysis, and manuscript composition. Dr. Meldrum was responsible for time-resolved photoluminescence decay measurements, data collection and analysis. Dr. Bergens was the supervisor of the research project.

Chapter 5 highlights and summarizes the most relevant discoveries of this dissertation and provides insights for future directions on this research.

Acknowledgements

I would like to express my sincerest gratitude and appreciation to all the people involved in the completion of this dissertation. Primarily, I would like to thank my supervisor Prof. Steve Bergens for all his attention, energy, and intellectual input toward the development of the projects contained in this work. His teachings, constant motivation, challenges, constructive feedback, and general positive attitude in the lab are immensely valuable to me. Also, I'm grateful to my supervisory committee members Prof. Arthur Mar, Prof. Mike Derrick Clive, Prof. Brad Easton, and Dr. Robert Jordan for all their comments and support for the completion of this dissertation and during my PhD career. Also, Dr. Al Meldrum was of great help for the completion of one of the projects. Special thanks to Dr. Anna D. Jordan for helping with the editing and revisions of this dissertation.

I am very thankful to the past and present members of the group, who were of great help to me at the beginning of the program and throughout the years. I would like to thank MSc. Prabin Nepal, Dr. Jinkun Liu, Dr. Loorthuraja Rasu, Dr. Riley Endean, Dr. Chao Wang, Dr. Shuai Xu, MSc. Elizabeth Murphy, Emily Majaesic, and Dr. Mona Amiri for all their support and friendship.

Additionally, I would like to express my gratitude to the people in the Department of Chemistry for all their invaluable support in multiple ways. Mark Miskolzie and Nupur Drabal from the Nuclear Magnetic Resonance Laboratory; Wayne Moffat, Jennifer Jones and staff of the Analytical and Instrumentation Laboratory; Jing Zheng and staff of the Mass Spectrometry Laboratory; Michael Barteski, Ryan Lewis, Andrew Yeung, Matthew Kingston and staff of chemical stores and receiving; Jason Dibbs of the glassblowing shop; Administrative Assistants Laura Pham, Connor Part, and Anita Weiler of Graduate Student Services; Undergraduate Lab coordinators: Dr. Norman Gee, and Dr. Jason Cooke. I would like to extend my gratitude to all the graduate professors in the Chemistry Department of the University of Alberta who taught me about the research conducted during my Ph.D.

I would like to also thank my friends who are and have remained close to me throughout the years: Victor, Daniel, Pacheco and Julio, life has been great with you

Table of Contents

List of Tables

List of Figures

List of Schemes

List of Abbreviations

® – registered trademark

AM 1.5 G – air mass 1.5 global

APSCs – all-polymer solar cells

BE – binding energy

BIH – 1,3-dimethyl-2-phenyl-2,3-dihydro-1H-benzo[d]imidazole

BHJ – bulk heterojunction

CB – conduction band

C_3N_4 – carbon nitride

CDCBs – carbazolyl dicyanobenzenes

CDOt – carbon nanodots

CCE – controlled current electrolysis

CE – counter electrode

CF – carbon fiber paper

CNT – carbon nanotube

CPE – controlled potential electrolysis

CRR – carbon dioxide reduction reaction

CV – cyclic voltammetry

Cz – carbazole

DCB – dicyanobenzene

DFT – density function theory

DSSC – dye-sensitized solar cell

DSPEC – dye-sensitized photoelectrochemical cell

EDS – energy-dispersive X-ray spectroscopy

FE – faradaic efficiency

FTIR – Fourier-transform infrared spectroscopy

FTO – fluorine-doped tin oxide

GC – glassy carbon

ICP–MS – inductively coupled plasma mass spectrometry

IPCE – incident photon-to-current conversion efficiency

ITO – indium tin oxide

LC – ligand centered

LCH – levelized cost of hydrogen

LLCT – ligand-to-ligand charge transfer

LUMO – lowest unoccupied molecular orbital

LSV – linear sweep voltammetry

ISC – intersystem crossing

ML – monolayer

MLCT – metal-to-ligand charge transfer

MWCNT – multi-wall carb nanotubes

NHC – N-Heterocyclic carbene

NHE – normal hydrogen electrode

NMR – nuclear magnetic resonance

ORR – oxygen reduction reaction

OLED – organic light-emitting diode

OSC – organic solar cells

PCE – power conversion efficiency

PEC – photoelectrochemical cell

PEM – proton exchange membrane (polymer electrolyte membrane)

PS – photosensitizer

PSC – perovskite solar cells

RDE – rotating disk electrode

RISC – reversed intersystem crossing

RHE – reversible hydrogen electrode

RRDE – rotating ring-disk electrode

SC – semiconductor

SCE – saturated calomel electrode

SEM – scanning electron microscopy

SET – single electron transfer

SOC – spin-orbital coupling

SOMO – singly occupied molecular orbital

STC – solar to chemical energy

STEC – solar to electrochemical energy

STES – solar to electrochemical storage

STP – solar to power

STT – solar to thermal energy

TEA – triethylamine

TEOA – triethanolamine

TEM – transmission electron microscopy

TOF – turnover frequency

TON – turnover number

UV–vis – ultraviolet–visible spectroscopy

VB – valence band

WE – working electrode

WOC – water oxidation catalyst

WOR – water oxidation reaction

XPS – X-ray photoelectron spectroscopy

XRD – X-ray diffraction

Chapter 1

Introduction

1.1 Solar Energy

Our society's energy requirements rely on the unsustainable and environmentally detrimental utilization of fossil fuels. Renewable sources, such as wind, hydro, thermal, and solar are an approach to mitigate the detrimental consequences of fossil fuel combustion and to fulfill the constantly increasing energy demand. However, as of 2021, renewable sources accounted for only 6.7% of the total energy consumed.[1] Solar energy offers a clean and practically limitless alternative. The amount of solar energy reaching the Earth's surface in one year is 3 x 10^{24} Joules (J), which exceeds society's annual energy consumption by nearly 10,000 times (3.1 x 10^{19} J).[1,2] In other words, harnessing only 0.01% of the total amount of solar energy reaching Earth's surface would meet our energy needs.

Solar energy is a vast renewable energy source that can be transformed into various forms, including heat, electricity, and fuels. Decades of research have been expended on transforming and storing solar energy, but most of these emerging technologies remain underdeveloped. One commercially available option is photovoltaics.[3] In 2022, the capacity of all photovoltaics installed worldwide exceeded 1 TW (~4–5% of the global electricity generated).[4] The cost of solar panels has declined dramatically, and their adoption has increased considerably. Still, technological challenges remain, such as developing affordable and scalable distribution and recycling, as well as storage technologies to ensure reliable and dispatchable energy.

1.2 Solar Energy Utilization Technologies

Solar utilization technologies are categorized by their function. They include solar cells for solar to power (STP), photocatalytic cells for solar to chemical energy (STC), photoelectrochemical cells for solar to electrochemical conversion aided by electrochemical potentials (STEC), photo-rechargeable batteries for solar to

electrochemical storage (STES), and solar thermal collectors for solar to thermal energy (STT).

1.2.1 Solar to Power: Solar Cells

Solar cells convert solar energy directly into electricity and presently offer the most potential for accessing renewable and clean energy. Solar cells' power conversion efficiency (PCE) quantifies the output of electrical energy relative to the input from solar photons. The highest PCE for a solar cell at the time of this writing is 47.1%, obtained with a multijunction system. There are also single junction GaAs solar cells and monocrystalline silicon cells whose PCE ranges from 28 to 45%.[5–7] The large-scale manufacture of these high-efficiency prototypes would be costly and energy-intensive, however, and the average PCE of most commercial solar cells is 20%.[6]

Dye-sensitized solar cells (DSSCs) mimic natural photosynthesis. In a typical DSSC, the absorber is a molecular chromophore (e.g., ruthenium or iridium-polypyridyl complexes, zinc porphyrin, or, more recently, organic dyes) coated on a porous nanostructured electrode (usually TiO_2). The chromophore absorbs light, injects electrons into the TiO_2 conduction band and accepts electrons from a redox couple (commonly I^-/I_3^- or Co-based redox couples at higher voltages) in a nonaqueous electrolyte. The highest efficiencies of this technology were obtained with Ru(II)-based chromophores with iodide-based redox couples, resulting in solar-to-electric power conversion efficiency (PCE) of 11.9% under full sun illumination (AM 1.5 G, 1,000 W m²).[8] Another type of DSSCs is based on light harvesting donor-π-bridge-acceptor (D-π-A) molecular dyes to capture light and produce electrons. The functionalization of the zinc-porphyrin core with the bulky bis(2′,4′-bis(hexyloxy)-[1,1′-biphenyl]-4-yl)amine donor and a 4-ethynylbenzoic acid yielded the green dye SM371, and incorporation of the proquinoidal benzothiadiazole (BTD) unit into this structure afforded the dye SM315 (Figure 1.1c). The photoexcited electrons are injected into the TiO_2 anode and transferred to Pt-ITO (indium tin oxide) cathodes. The redox agent ($[Co(bpy)_3]^{2+/3+}$) in an electrolyte is reduced at the surfaces of the cathodes. The PCE of these new-generation DSSCs has reached a record of 13% through the molecular engineering of push-pull porphyrin sensitizers and utilization of a $[Co(bpy)_3]^{2+/3+}$-based

redox electrolyte (Figure 1.1).[9] The photocatalytic performances demonstrate that the dyes SM371 and SM315 in this setting could achieve fill factors of up to 0.79 and 0.78 (Figure 1.1a), with power conversion efficiencies of 12% and 13%, respectively. The photocurrent spectrum (Figure 1.1b) demonstrates the panchromatic light response with strong absorption across the visible spectrum with IPCE values ~80% from 400-750 nm.
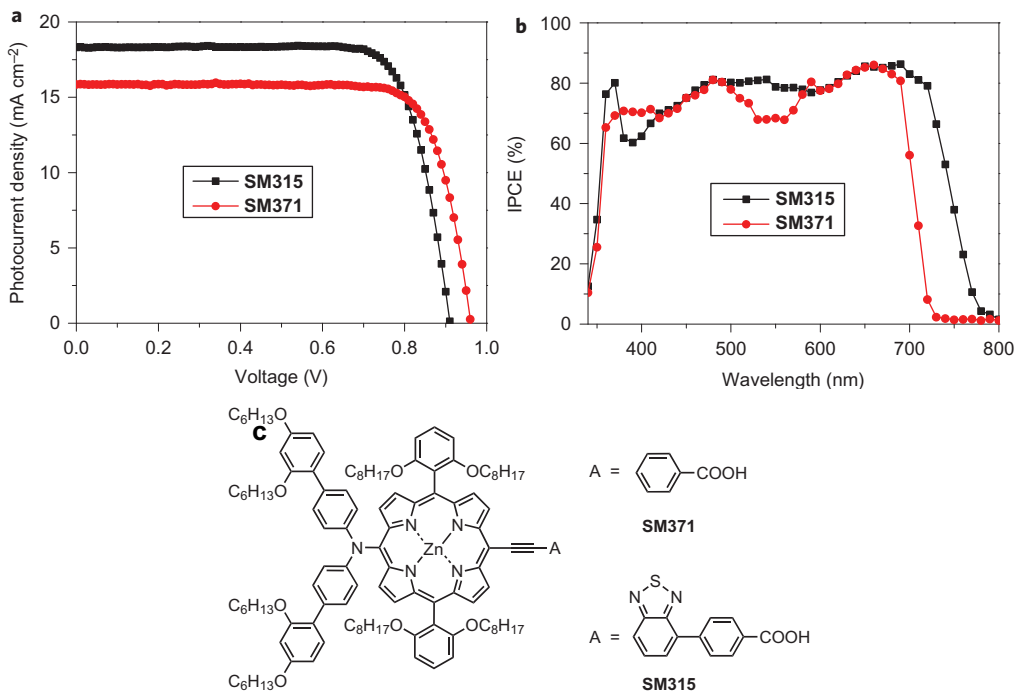
Figure 1.1. Photovoltaic performance of devices SM371 and SM315. (a) J-V curve under AM 1.5 G illumination (1000 W m^{-2}), (b) IPCE (%), (c) Structures of the dyes SM371 and SM315.

Si panels constituted around 95% of total solar panel production in 2021, and power conversion efficiencies ranged from approximately 16% to 21%.[10] The significant cost reductions in panels have resulted primarily from continuous and systematic decreases in manufacturing costs, including those associated with the polymer encapsulant, silver electrical contact screen-printing, and Si wafer production. Additionally, countries with scaling capabilities have facilitated the establishment of large panel-production facilities and have played a crucial role in driving down costs.[11] Si-based panels also require large amounts of energy to produce (requiring 1-4 years of operation to recuperate), methods must be developed for end-of-life recycling, and

the worldwide electricity grid must be reworked to incorporate the widespread adoption of solar panels.

Another emerging photovoltaic technology is perovskite solar cells. Halide perovskites offer several advantages over molecular chromophores, including absorption coefficients up to ten times higher than molecular dyes in DSSCs, superior charge carrier mobilities and lifetimes, good crystallinity, low cost, and ease of fabrication.[12] The efficiency of perovskite solar cells (PSCs) increased from 3.8% to 25.7% over the last decade, primarily due to the development of hole-transporting materials, prevention of perovskite degradation, and the construction of solid-state devices.[6] A major objective in current PSC research is to minimize electron-hole recombination by incorporating materials with energy levels aligned to enhance fast electron transfer. Similarly, implementing tandem PSC architectures also enables a broader absorption band, leading to higher PCEs.

Organic solar cells (OSCs) offer alternatives to their inorganic counterparts, with potential advantages, including cost-affordable, lightweight, easily processed devices with less environmental impact. Unlike solid-state solar cells, OSCs are compatible with flexible substrates, enabling the production of wearable devices. Recent advancements showcase a PCE of 16.5% in single-junction devices[13] and 17.3% in tandem devices.[14] The PCEs of OSCs likely will exceed 20% in the near future. Bulk heterojunction (BHJ) organic solar cells utilize small molecule electron donors and acceptors and offer advantages such as strong absorption, and the facile functionalization of the small molecules affords excellent optoelectronic and electrochemical properties and enhanced stability.[15,16] All-polymer solar cells (APSCs) utilize polymeric electron donors and acceptors. APSCs offer advantages such as tunable light harvesting, robust film morphology, compatibility for large-scale manufacturing, and long-term device stability; outstanding mechanical durability and stretchability also have been reported for APSCs.[17,18] The maximum PCE of APSCs is currently 10.3%. However, there has been a ten-fold increase in the number of research publications on APSCs, suggesting that there will be significant advances in this area in the near future.[19] The ultimate goal is to improve the PCE values by up to 15% (considered the market readiness metric).

1.2.2 Solar to Electrochemical Storage

Sunlight is intermittent, diffuse, and must be stored. Therefore, cost-effective electrochemical energy storage systems with photovoltaic cells are required for long-term, constant high energy output from solar power systems. Simply put, the solar energy from a photovoltaic module is stored in batteries to be provided as needed later. A representative example utilized high-efficiency crystalline silicon PV modules to charge iron phosphate lithium-ion batteries.[20] The solar energy to battery charge conversion efficiency reached 14.5%, including a photovoltaic efficiency of 15% and a reported battery charging efficiency of nearly 100%. This relatively high-efficiency system was achieved by directly charging the battery from the PV module.[20] In another representative example, the integration of a GaAs solar cell with an ultrafast rechargeable Zn micro-battery operated with a high (23.1%) energy storage efficiency. Further, after rapid charging for 5 s, the device continuously delivered power at 0.5 mA cm^{-2} for 110 s.[21]

Photo-responsive metal-O_2 batteries belong to the category of STES devices, characterized by an oxygen reduction reaction (ORR) during the discharging phase and an oxygen evolution reaction (OER) during the charging phase. Such devices present a new battery energy storage strategy, enabling on-demand energy output. Coupled with a Zn counter electrode in a Zn-air battery, visible-light enhanced oxygen redox reactions ORR/OER were catalyzed by $Ni_{12}P_5$ nanoparticles (NPs) on nitrogen-doped carbon nanotubes (NCNT) (Figure 1.2).[22] The $Ni_{12}P_5$@NCNT hybrid catalyst has unusually high catalytic activities for both ORR (onset potential at 0.90 V vs. RHE) and OER ($\eta = 360$ mV@10 mA cm^{-2}) under irradiation by visible light (300 W Xenon lamp equipped with an AM 1.5 G filter). The charge-discharge voltage gap of the photo-responsive Zn-air battery was quite low ($\sim$ 0.75 V @ 10 mA cm^{-2}, charge potential = 1.94 V, and discharge potential = 1.19 V), and it was stable to cycling over 500 cycles. The irradiation increased the efficiency from 61.3% to 64.2%.
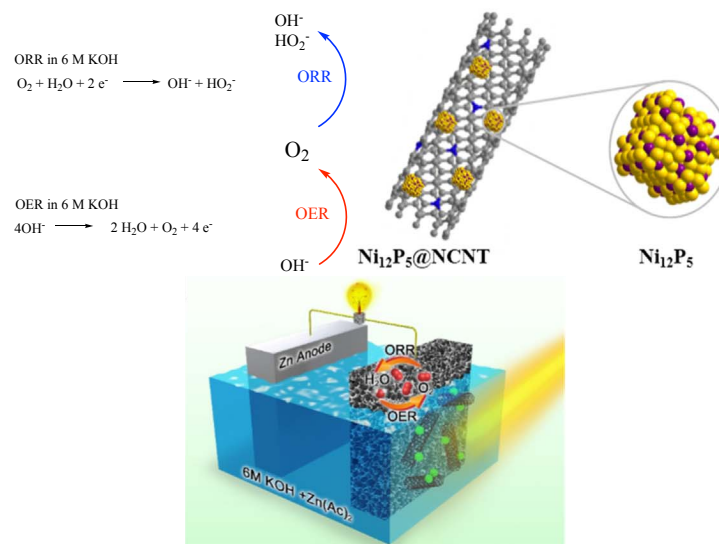
Figure 1.2. Schematic representation of a Zn-air battery under light illumination. Taken with permission from Ref.[22]

1.2.3 Solar to Thermal: Solar Collectors

For solar-to-thermal conversion, the efficient, cost-effective utilization of solar radiation by solar-to-thermal conversion relies on the advancement of artificial collectors. There are four primary types of solar collectors: parabolic trough collectors, linear Fresnel reflectors, power towers, and dish-engine systems (Figure 1.3).[23] Overall, these collectors produce local temperatures of 550 °C, 550 °C, >1000 °C, and 1200 °C, respectively.[24] These systems utilize either an oil or a molten salt as a heat-storage fluid to generate electricity. A common heat-storage fluid is a eutectic mixture consisting of 60% by weight sodium nitrate and 40% by weight potassium nitrate, commonly referred to as solar salt (Mpt = 220 °C). Then, the heat in the molten salt is exchanged to produce steam, which is used to drive a turbine and generate electricity. In 2018, solar thermal systems provided about 1.5 EJ (420 TWh) of electricity, 4.8% more than in 2017.[25]

Solar thermal installations typically are located in regions with abundant direct sunlight, such as desert areas in the southwestern United States, Australia, Morocco, or southern Spain. It should be noted that the overall cost of solar thermal systems has not experienced significant declines since the 1980s; on the contrary, relatively high maintenance costs are required to upkeep engine moving parts (in solar dish/engines),

and parabolic mirrors are typically utilized rather than cheaper flat mirrors. As well, new transmission lines would be necessary to deploy either photovoltaics or solar thermal electricity-generating systems in remote regions with high direct insolation.

Figure 1.3. The parabolic trough power plant in California (left), a solar power tower in Nevada (center), and a solar dish concentrator (right). Images taken from Ref.[23]

1.2.4 Solar to Chemical Energy: Photocatalysis

In artificial photocatalytic solar to chemical energy conversion systems, semiconductors or photosensitizers act as light harvesters and charge separators, while catalysts facilitate the desired reactions. Upon photon absorption, electrons are excited from the highest occupied molecular orbital (HOMO) to the lowest unoccupied molecular orbital (LUMO), roughly, the equivalent energy levels in semiconductors are the valence and conduction bands, respectively. Electrons and holes then migrate to the semiconductor surface.[26] The conduction band electrons eventually reduce electron acceptors, while the holes oxidize electron donors. The relative positions of the valence band (VB) and conduction band (CB) in the semiconductor determine the redox potentials for oxidation and reduction reactions (Figure 1.4). For instance, in water oxidation, with n-type semiconductors, the VB position must be lower than the oxidation potential of water. In comparison, the CB position must be higher than the proton reduction potential or the reduction potential of the catalyst. Photoreduction of CO_2 is even more intricate, as the products can vary from CO to CH_4, CH_3OH, HCOOH, C_2H_4, etc. (Table 1.1), and typically is carried out in a p-type semiconductor.[27] Table 1.1 reflects the complexity of the CO_2 reduction reaction in aqueous conditions at different potentials and the impact of H^+ on the final product of the reduction. While photocatalytic systems hold promise for the large-scale production

of solar fuels, they face challenges of low efficiency and limited availability of band-matched photocatalysis.
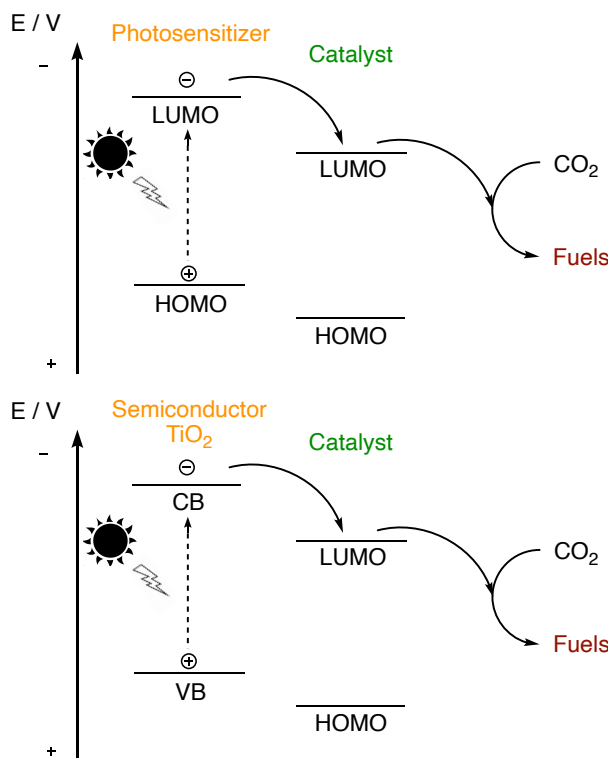
Figure 1.4. Schematic energy diagrams show the electron flow using a photosensitizer (left) or TiO_2 (right) for the reduction of CO_2 to prepare fuels.

Table 1.1. Selected CO_2 Reduction Processes and Corresponding Standard Redox Potentials E in Aqueous Conditions at pH 7[27]

Reaction	$E^{o'}$ vs SHE
$CO_2 + e^- \rightarrow CO_2^{-}$	−1.85 V
$CO_2(g) + 2\ H_2O(l) + 2\ e^- \rightarrow HCOO^-(l) + OH^-(l)$	−0.665 V
$CO_2(g) + 2\ H_2O(l) + 2\ e^- \rightarrow CO\ (g) + 2\ OH^-(l)$	−0.521 V
$CO_2(g) + 3\ H_2O(l) + 4\ e^- \rightarrow HCOH\ (l) + 4\ OH^-(l)$	−0.485 V
$CO_2(g) + 5\ H_2O(l) + 6\ e^- \rightarrow CH_3OH\ (l) + 6\ OH^-(l)$	−0.399 V
$CO_2(g) + 6\ H_2O(l) + 8\ e^- \rightarrow CH_4\ (g) + 8\ OH^-(l)$	−0.246 V
$2\ H_2O(l) + 2\ e^- \rightarrow 2\ OH^-(l)$	−0.414 V

This section of the dissertation will discuss mainly the photocatalytic systems in which discrete molecules instead of semiconductor materials carry out the light absorption process. Primarily, the two main types of photocatalytic reactions addressed here for storing solar energy into chemical bonds are the oxidation of water to form

hydrogen and oxygen, the so-called overall water splitting reaction (OWS), or the reduction of carbon dioxide with protons and electrons (from water oxidation) to form carbon monoxide and related fuels, the so-called CO_2 reduction reaction (CRR).

1.3 Solar Hydrogen

As stated above, solar energy can be stored by producing molecular hydrogen and oxygen (H_2 and O_2) through the OWS. From many points of view, this is among the most promising reactions to generate solar fuels (eq 1.1). Solar-generated H_2 could be used as a feedstock to produce ammonia, fertilizers, and drug-like precursors production, as well as in transportation. There is much study, for example, on photoelectrocatalytic N_2 reduction to NH_3. The NH_3 is utilized as a fertilizer, or it is reformed to generate H_2 after transport in ships and pipelines, or the NH_3 is oxidized directly in fuel cells or internal combustion engines. Alternatively, the solar H_2 can be combusted in a fuel cell to generate heat, water, and electricity. In other words, energy on demand.

$$2\ H_2O + 4\ hv \rightarrow 2\ H_2 + O_2 \qquad\qquad (1.1)$$
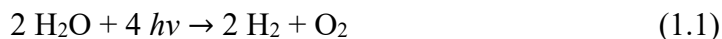
The OES typically is divided into oxidative and reductive redox reactions. The oxidation of water to oxygen, protons and electrons is called the oxygen evolution reaction or OER. This reaction is reviewed extensively, and this dissertation will focus on molecular systems. Several molecular catalysts have been developed for the oxidation of water to oxygen (called the oxygen evolution reaction, or OER). There are several reviews published on this topic.[28–35] The first was reported by Thomas Meyer in 1982, who disclosed a binuclear ruthenium complex that catalyzed the oxidation of water with low performance (TOF = 0.004 s^{-1}) using Ce(IV) as the stoichiometric oxidant.[36] The key O–O bond forming step with this system likely proceeded by coupling of two Ru(III)-oxide radical species (**Scheme 1.1**).

There are several reviews on the detailed mechanisms of the OWS.[37–41] As an example of recent development, the electrostatic coupling between Ru OER catalysts of opposite charges was utilized to enhance the rate of the slow O-O bond-forming reaction, increasing the TOF to 460 s^{-1}, with Ce(IV) as oxidant.[42] Many Earth-abundant molecular OER catalysts also have been developed. A recent example is a homogenous

pentanuclear iron catalyst with tricoordinate oxide and 3,5-bis(2-pyridyl)pyrazole. This complex catalyzed the electrochemical OER in acetonitrile/water (10:1 v/v) with TBAP (tetrabutylammonium perchlorate), reaching TOF = 1900 s^{-1}.[43]

$[Fe^{II}_4Fe^{III}(\mu_3-O)(\mu-L)_6]^{3+}$

● Oxygen   ● Hexa-coordinated Fe   ● Penta-coordinated Fe

LH
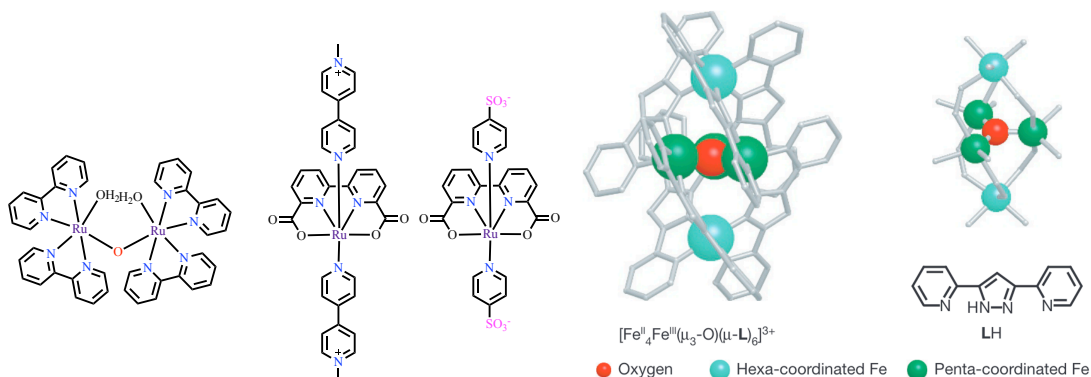
Scheme 1.1. Structures of Ruthenium complexes for water oxidation. Ball-and-stick representations of the molecular Fe$_5$O structure, $[Fe^{II}_4Fe^{III}(\mu_3-O)(\mu-L_6)]^{3+}$.

Photocatalysts also have been developed for the OWS reaction driven by visible light. Several recent reviews have been written on this area.[28,32,44,33,35] A representative recent example is a metal-free nanocomposite comprised of carbon nanodots (CDot) and carbon nitride (C$_3$N$_4$), which is a photocatalyst for overall solar water splitting (OWS). C$_3$N$_4$ is known to split water photocatalytically into hydrogen and peroxide, while CDots promote the decomposition of peroxide to oxygen. While many OWS photocatalysts operate at low quantum efficiencies (Φ < 0.1%), this CDot-C$_3$N$_4$ nanocomposite operated at Φ = 16%, 6.9%, 4.4% under 420, 580, and 600 nm light irradiation, respectively. The overall solar-to-chemical conversion efficiency (η_{STC}) with this nanocomposite is 2.0% (in this case solar-to-hydrogen).[45] The challenges encountered in this area of research include increasing the quantum efficiency in the visible range (they are typically less than 0.1%), reducing the dependence on expensive metals (e.g. Ru- and Ir-based photocatalysts), avoiding catalyst decomposition by oxidation, increasing the kinetics to reduce the large overpotentials typically encountered for OWS, and avoiding the formation of hydrogen peroxide.[46]

In a recent summary, Lewis estimated the levelized H$_2$ (LCH) cost from a solar-driven photoelectrochemical water-splitting system to be from $7 to $20/kg. In contrast, the LCH produced by steam reforming of natural gas is only $2/kg.[11] This LCH of H$_2$ from steam reforming does not, however, include the worldwide detrimental

costs of climate change brought on, in part, by CO_2 released by steam reforming and by natural gas leaks in the well to the steam reformer infrastructure. A serious challenge in the utilization of green hydrogen is the transport and storage of H_2, which would require extremely high pressures at room temperature.

1.4 Conversion of Solar Energy and CO_2 Fuels with Photocatalysis

The photocatalytic reduction (or recycling) of carbon dioxide to produce energy-rich, easily transported, and stored hydrocarbons, such as CO, C_2H_4, CH_4, CH_3OH, and HCOOH, is a strong strategy for renewable energy storage. The combustion of these fuels would, in principle, be net CO_2 neutral if the CO_2 was captured from the atmosphere. Carbon dioxide reduction can be achieved by different means, such as artificial photosynthesis, electrolysis using electricity provided by photovoltaics, and thermal CO_2 hydrogenation using renewable H_2. Typical artificial photosynthesis systems include a redox photosensitizer that promotes a photochemical one-electron transfer to a catalyst and the catalyst precursor that accepts electrons to reduce CO_2 to fuel molecules. The details of how each operates will be discussed in separate sections below. As well, this area has been reviewed heavily.[47–50] Many reports utilize separate, homogeneous Re(I) complexes as catalysts and Ru(II)-polypyridyl complexes as chromophores as photocatalytic systems for photochemical CO_2 reductions (Scheme 1.2.A).[47–50]

The first report of a supramolecular photocatalyst with the Ru and Re moieties covalently linked (RuRe) was by Ishitani and co-workers.[34] The system consisted of a $[Ru(bpy)_3]^{2+}$-type photosensitizer and a *fac*-Re(bpy)(CO)$_3$Cl-type catalyst bonded by 4-methyl-bpy moieties bridged by various aliphatic and aromatic chains. The use of -$CH_2CH(OH)CH_2$- as a linker and 1-benzyl-1,4-dihydronicotinamide (BNAH) as a sacrificial electron donor reduced CO_2 to CO under visible light at 460 nm with quantum yield (Φ_{co} = 0.12) and TON_{CO} = 170 (Scheme 1.2.C).[51] Ishitani and co-workers have dedicated significant time and effort to RuRe photosystems. Their most active system reached up to 3029 TON_{CO} and TOF = 35.7 min^{-1}, in high selectivity Γ >

99% in a CO_2-saturated DMF-TEOA (5:1 v/v) solution, under >500 nm light using a Hg lamp as a source. The general formula of the photocatalyst was [Ru(4,4'-Me$_2$bpy)$_3$]$^{2+}$-CH$_2$CH$_2$-[Re(bpy)(CO)$_2$(P(p-F-C$_6$H$_4$)$_3$)$_2$]$^+$ (Scheme 1.2.B), and 1,3-dimethyl-2-phenyl-2,3-dihydro-1H-benzo[d]imidazole (BIH) was the sacrificial electron donor.[52] This result demonstrates that high turnovers, yields, and selectivity can be obtained with supramolecular photocatalysts.
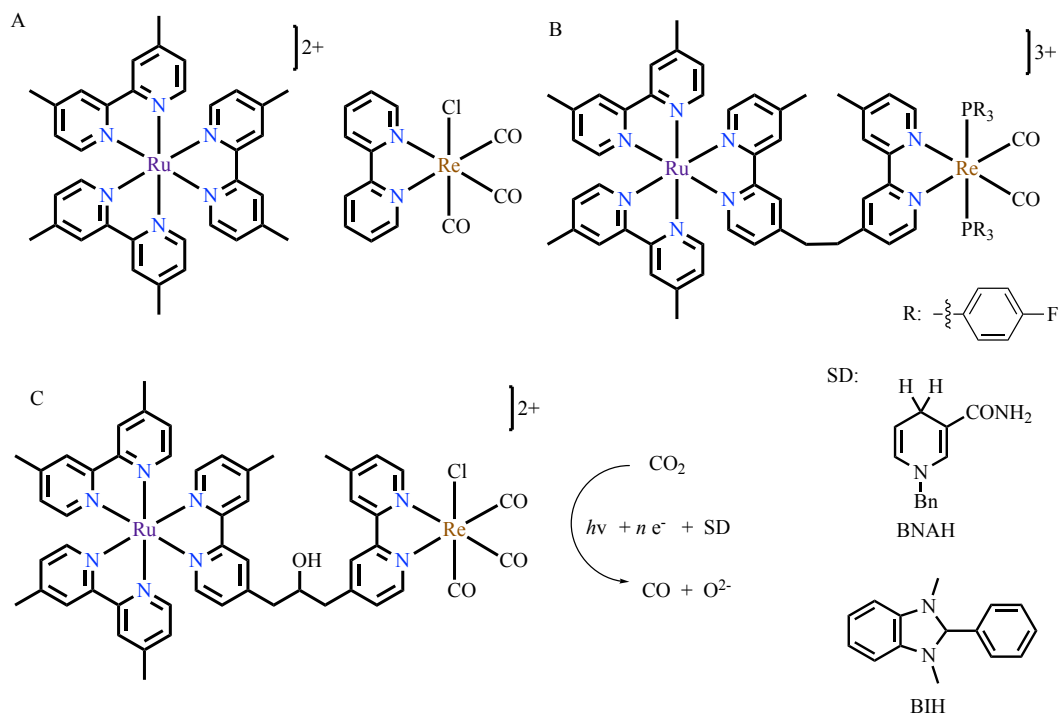
Scheme 1.2. Structures of Re(bpy)(CO)$_3$X- complexes and the reduction of CO_2

A supramolecular photocatalyst employing a Mn active site was prepared with one or two Ru polypyridine photosensitizers bridged through alkyl chains to a *fac*-MnBr(CO)$_3$bpy-type active site. This type of CO_2 reduction catalyst is discussed in more detail below. The ruthenium photosensitizers consisted of the [Ru(dmb)$_2$(BL)]$^{2+}$ units (dmb: 4,4'-dimethyl-2,2'bipyridine, BL: 4-(4-(2-(6'-(2,6-dimethoxyphenyl)[2,2'-bipyridin]-6yl)-3-methoxyphenoxy)butyl)-4'-methyl-2,2'-bipyridine) shown in Figure 1.5. These complexes photocatalyzed the reduction of CO_2 to HCOOH, CO and H$_2$ (Figure 1.5) in a CO_2-saturated DMF-triethanolamine (TEOA) (4:1) solution with 0.1 M BIH as a sacrificial electron donor. The reactions were irradiated at 546 nm (4.2x10^{-8} einstein s^{-1}) for 6 h to give the results summarized in Table 1.2.[53]
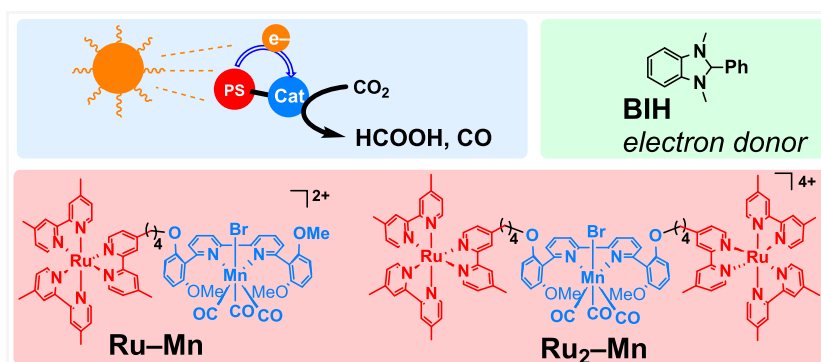
Figure 1.5. Ru-Mn photocatalytic system for CO_2 Reduction.

Table 1.2. Photocatalytic CO_2 Reduction with Ru–Mn complexes

| Entry | Complex | Products (TON) | | | Γ_{COOH} (Γ_{CO}) | Φ_{COOH} |
		HCOOH	CO	H$_2$	%	(Φ_{CO}) %
1	Ru-Mn	98	29	0.1	78 (21)	14 (0.64)
2	Ru$_2$-Mn	33	18	0.5	65 (34)	5.4 (0.43)
3	Ru + Mn	90	11	0.03	89 (10)	11 (0.24)

Light intensity: 546 nm (4.2×10^{-8} einstein s^{-1})

Interestingly, the compound with two Ru photosensitizers (2nd entry) was less effective than that with one (first entry) because the additional Ru centre is reduced before Mn. The total TON (~127), selectivity for formic acid (78%), and the incident light quantum yield (14%) for the mono-Ru species are appreciable for these types of photocatalysts. It is noted, that these values were similar to those obtained with the Mn catalyst and Ru sensitizer in discrete, separate molecules, suggesting that the supramolecular structure did not provide any performance advantages in this example.

Both monomolecular and supramolecular earth-abundant systems with Mn(I), Cu(I), and Fe(II) centres have been reported as photocatalysts for CO_2 reduction.[54] As an example of a high-activity system, the binuclear Cu complex [Cu$_2$(P$_2$bph)$_2$]$^{2+}$ (P$_2$bph = 4,7-diphenylphosphinetetramethylene-1,10-phenanthroline) was utilized as a photosensitizer with a variety of *fac*-Mn(X$_2$bpy)(CO)$_3$Br catalysts (X$_2$bpy = 4,4'-X$_2$-2,2'-bipyridine, X = H or MeO) (Figure 1.6) for CO_2 photoreduction.[55] The most efficient of the catalysts studied with this photosensitizer was *fac*-Mn((MeO)$_2$bpy)(CO)$_3$Br, which reduced CO_2 with an incident quantum yield = 57%

(CO + HCOOH), $TON_{CO} = 1300$, and the CO selectivity was 95% (conditions: *N,N*-dimethylacetamide-triethanolamine (DMA/TEOA) (4:1, v/v) solvent, 1,3-dimethyl-2-phenyl-2,3dihydro-1*H*-benzo[d]imidazole (BIH; 10 mM) as a sacrificial electron donor, 436 nm at 2.0 x 10^{-8} Einstein s^{-1}, 24 h, [Mn] = 0.05 mM , [Cu] = 0.25 mM)).[55] This latter example demonstrates that high TON and selectivity can be obtained with Earth-abundant photosensitizers and catalysts, albeit with excess photosensitizer and under relatively intense light.
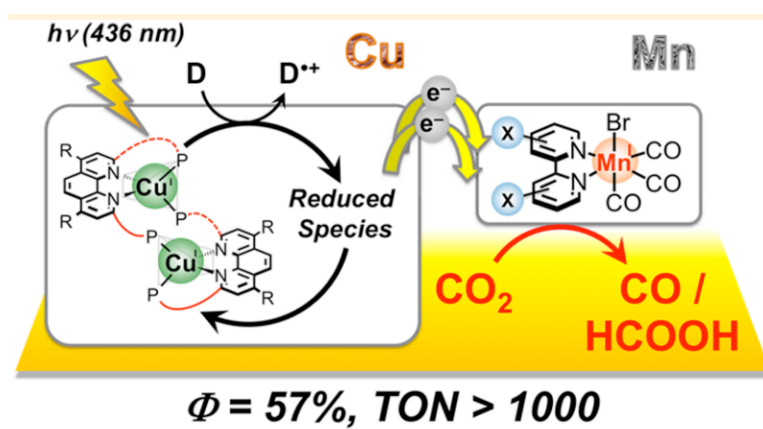
Figure 1.6. Cu-Mn photocatalytic system for CO_2 reduction.

1.5 Conversion of Solar Energy and CO_2 Fuels with Photoelectrocatalysis

The earliest report of photoelectrochemical overall water splitting dates back to 1972, with a report by Honda and Fujishima.[56] In that report, a TiO_2 photoanode catalyzed the oxygen evolution reaction in an electrochemical cell when illuminated with UV radiation. Carbon dioxide photoelectrochemical cells that utilize solar energy to drive the kinetically and thermodynamically uphill conversion of CO_2 to hydrocarbons.[57–60] The first example of a molecular photocatalyst utilized in a photoelectrochemical cell for visible-light-driven CO_2 reduction (using water as a reductant) was based on a Ru(II)-Re(I) supramolecular complex immobilized on a NiO electrode (NiO-RuRe).[60] This photocathode generated CO in high selectivity $\Gamma > 95\%$ and TON = 32, under radiation (12 h) at 460 nm light irradiation, with an applied bias of –0.7 V vs Ag/AgCl in an aqueous solution. The faradaic efficiency was 64% (Figure 1.7).
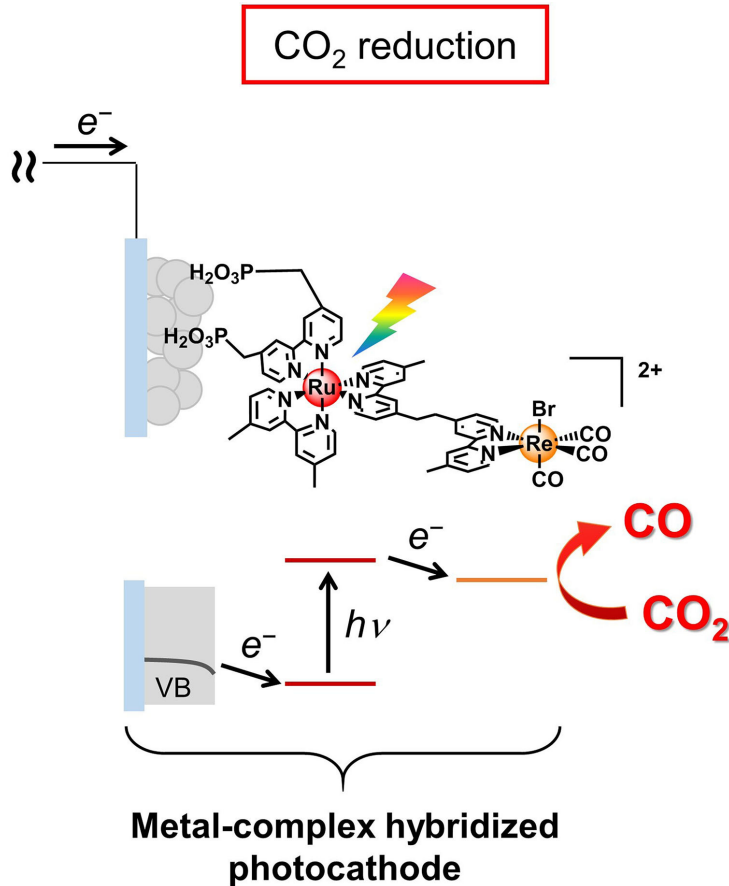
Figure 1.7. Hybrid photocathode for CO_2 comprising a Ru(II)-Re(I) supramolecular catalyst on a NiO electrode. Reproduced with permission from Ref. [60]

A recently reported molecular-based photocathode integrates chromophore-catalyst assemblies for long-term solar-driven CO_2 reduction in a stabilized polymeric film structure. The assembly, abbreviated as NiO-Si-poly(Ru^{II})-poly(Re^I), includes a silane surface-anchoring group, Ru(bpy)$_3$]$^{2+}$-type photosensitizer, and *fac*-[Re(bpy)(CO)$_3$Cl]-type catalyst (Figure 1.8). The silane group, Ru photosensitizer, and Re catalyst were all functionalized with vinyl groups to allow their electropolymerization. This photocathode was stable toward CO_2 reduction to CO for over 10 h in a CO_2-saturated NaHCO$_3$ (50 mM) aqueous buffer solution, at pH 7, with a FE of 65%, at –0.7 V vs Ag/AgCl, and TON = 58, under visible light irradiation (100 mW cm^{-2}, $\lambda \geq 400$ nm). The long-term stability, current density was maintained for ~10 h, was attributed to the electro-polymerization of the components.[61]
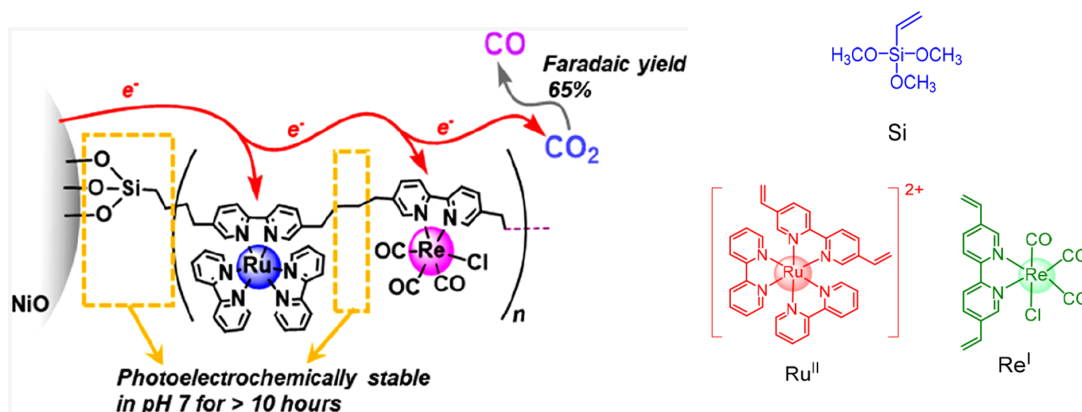
Figure 1.8. Possible surface assembly structures on $NiO|Si$-poly(Ru^{II})-poly(Re^I). Structures of molecular precursors derivatized with vinyl functional groups.[61]

A large amount of effort has been dedicated towards these academic-directed demonstration systems. There remains a considerable distance between these studies and large-scale commercial systems. Nevertheless, these studies have helped define the parameters, mechanisms, and strategies that eventually will lead to commercial photoelectrochemical systems for CO_2 reduction and water oxidation. This research also has trained many new researchers in this important area. The utilization of photoelectrochemical solar energy conversion into hydrocarbons or hydrogen will, in principle, minimize climate change while fulfilling the energy and chemical requirements of contemporary living and manufacturing.

1.6 Molecular Photosensitizers for Solar Energy Conversion

1.6.1 Ru(bpy)$_3$$^{2+}$ as a Photosensitizer for Solar Energy Conversion

As previous examples in this chapter illustrate, molecular photosensitizers are being investigated as components of visible-light-driven catalytic systems to prepare solar fuels. A molecular-based photocatalytic system typically possesses a photosensitizer (PS), a molecular catalyst (cat), and an electron donor (D). The electron donor is, typically, either an electrode or a sacrificial electron donor added to the solution.

The absorption of a photon initiates an electron transition within the photosensitizer (PS), resulting in the formation of an excited state (PS*) with two singly occupied molecular orbitals (SOMOs). Typically, the ^{1}S excited state undergoes

intersystem crossing (ISC) to form a lower energy, longer-lived ^{1}T excited state. It is the ^{1}T excited state that undergoes the electron transfer reactions typically encountered during solar fuel production. Precious metal photosensitizers, such as [Ru(bpy)$_3$]$^{2+}$, [Ir(bpy)(ppy)$_2$]$^+$, Ir(ppy)$_3$, and their derivatives, commonly were used in earlier studies on photocatalytic fuel generation. [62–67]

Ru(bpy)$_3$$^{2+}$ is the most studied transition metal complex for synthetic photocatalysis and solar energy conversion. The mechanism of operation by this chromophore is illustrative of how many operate in the literature. The absorption spectrum of Ru(bpy)$_3$$^{2+}$ contains a strong, broad band centered at 452 nm in the visible range. This absorption band corresponds to a metal-to-ligand-charge transfer (MLCT) transition to form the ^{1}S MLCT excited state with a high quantum efficiency ($\Phi \sim 1$). Because this characteristic absorption band is quite broad, a range of wavelengths of visible light can produce the catalytically relevant photoexcited state.[68] The ^{1}S excited state undergoes rapid intersystem crossing in (<20 fs), attributable to efficient spin-orbital coupling (SOC) brought about by the presence of the heavy Ru atom, leading to the long-lived ^{1}T MLCT excited state (Figure 1.9).[69]

Figure 1.9. Simplified Jablonsky diagram related to energy transfer (ET), intersystem crossing (ISC) and radiative and non-radiative de-excitation processes for Ru (II) polypyridyl complexes.

The ^{1}T MLCT state serves as either an electron donor or an electron acceptor in numerous intermolecular redox reactions.[69–71] One pathway (Figure 1.10, path i) involves oxidative quenching of the ^{1}T MLCT state by electron donation from the highest energy SOMO to an electron acceptor (e.g., CO_2 through a catalyst) to yield the

oxidized, d^5 Ru (III) complex $[Ru(bpy)_3]^{3+}$. Then, complex $[Ru(bpy)_3]^{3+}$ is reduced (e.g., by water through a catalyst) to regenerate the Ru(II)-bpy ground state. An alternative pathway (Figure 1.10, path ii) involves reductive quenching of the ^1T MLCT state by accepting an electron from a donor to generate the strongly reducing, anionic Ru(II) complex $[Ru^*(bpy)_3]^{2+}$, with an electron localized among the π^*-bpy orbitals. This strongly reducing compound then donates an electron (e.g., to CO_2 via a catalyst) to regenerate the Ru(II)-bpy ground state.

Figure 1.10. $Ru(bpy)_3^{2+}$ structure (A) and different energy transfer paths upon light excitation (B).

The low abundance of Ru and Ir limits their use in large-scale photocatalysis, especially for the scales required for solar fuel production. Developing organic photocatalysts offers more sustainable, cost-effective alternatives. This area has been extensively reviewed.[72–75] While the structure-property relationships are understood well for metal-based complexes, the molecular design principles for organic dyes are explored less. Recent reports highlight organic dyes for varied, specific catalytic purposes, focusing on either powerful reducing or oxidizing properties. [72,76,77]

1.6.2 4CzIPN as a Photosensitizer for Solar Energy Conversion.

The metal-free photosensitizer, 1,2,3,5-tetrakis(carbazol-9-yl)-4,6-dicyanobenzene (4CzIPN) is a donor-acceptor chromophore, with the carbazolyl (Cz) groups as electron donors and the dicyanobenzene (dcb) moiety as an electron acceptor. This class of

organic chromophores has emerged as a powerful organic photocatalyst since their discovery announcement in 2012.[75] Their excellent redox windows (redox potentials of the highest- and lowest-energy SOMOs in the T_1 excited state), good chemical stability and broad applicability make 4CzIPN and related compounds attractive metal-free photocatalysts and chromophores. The family of carbazolyl dicyanobenzenes (CDCBs) was reported first as highly efficient light harvesters for organic light-emitting diodes by Adachi and co-workers in 2012. This class of chromophore absorbs visible light (~430 nm) to undergo a push-pull displacement excitation of an electron mainly from a HOMO located on the carbazole rings to a π^* LUMO centered on the dicyanobenzene moiety. Steric crowding in these conformational restricted molecules results in the dihedral angles between the carbazolyl- and dicyanobenzene rings to be ~60º, minimizing the overlap between the LUMO and HOMO (frontier) orbitals. Density functional theory (DFT) calculations suggest there is a narrow energy gap between S_1 and T_1 excited states, facilitating ISC. The T_1 state is relatively long-lived (5.1 µs), and these molecules undergo efficient thermally activated delayed fluorescence (TADF) (Figure 1.11).

Figure 1.11. Energy diagram of a molecular chromophore illustrating fluorescence, phosphorescence and thermally activated delayed fluorescence (TADF).

More specifically, they undergo thermally activated reverse intersystem crossing (RISC) from T_1 to S_1, followed by relaxation through fluorescence from S_1 to S_0. The distinct localization of the HOMOs and LUMOs allows independent fine-tuning of both orbitals by modifying the electron donor and acceptor moieties on

the cyanobenzene scaffold, enabling adjustment of the photophysical and electrochemical properties of 4CzIPN (Figure 1.12).[75]

In addition to its cost-effective nature as an organic molecule, 4CzIPN presents several key photophysical characteristics shared by Ru- and Ir-polypyridyl catalysts. These include a prolonged excited state lifetime, a broad redox potential range, and a high fluorescence quantum yield.[78] Notably, 4CzIPN possesses oxidation and reduction potentials similar to those of the Ir-catalyst Ir[dF(CF$_3$)ppy]$_2$(dtbpy)(PF$_6$), making it an exceptionally desirable photocatalyst.[79]

Figure 1.12. Structure of 1,2,3,5-tetrakis(carbazol-9-yl)-4,6-dicyanobenzene (4CzIPN)

The exploration of 4CzIPN as a photocatalyst for organic reactions started in 2016.[75] This area is reviewed, and only representative examples will be discussed here. 4CzIPN is, for example, an active photoredox cocatalyst for both the decarboxylative arylation of carboxylic compounds by aryl halides and cross-couplings between alkyltrifluoroborates and aryl halides, both catalyzed by Ni complexes (Scheme 1.3).[80] The proposed reaction mechanisms for these transformations involve generating alkyl radicals through the oxidation of either an alkyl-carboxylate or an alkyl-trifluoroborate by SET to the lowest energy SOMO of the ^{1}T excited state of 4CzIPN. Such a step requires that the redox potential of this SOMO is at least +1.35 V vs SCE.

Scheme 1.3. Ni catalytic decarboxylative arylation of aryl halides driven by 4CzIPN.

Of relevance to the research in this dissertation is that 4CzIPN also has been utilized as a photocatalyst for CO_2 transformations.[81–83] For example, König and co-workers reported ligand-controlled selective Markovnikov and anti-Markovnikov hydrocarboxylation of styrenes with CO_2 under mild conditions (Scheme 1.4).[81] Specifically, irradiation of 4CzIPN under visible light yields the photoexcited state *4CzIPN, which, via two single electron transfer (SET) steps, regenerated the catalytic active Ni^0L_n species from $Ni^{II}L_n$, the entity directly responsible for the hydrocarboxylation. 4CzIPN uses a HEH (Hantzsch ester) as the electron donor. The reaction tolerates a wide range of functional groups and electron-poor, -neutral, and electron-rich styrene derivatives, providing the desired products in moderate to good yields.

Scheme 1.4. Scheme of catalytic hydrocarboxylation of styrene under CO_2 with 4CzIPN/Ni. Adapted with permission from Ref.[83]

Unlike metal-based chromophores, organic dyes are studied less in photocatalytic CO_2 reduction systems. In 2020, Wang and co-workers developed an earth-abundant photocatalytic CO_2 reduction system that is composed of a terpyridine–Fe(III) complex (FeTotpy) [10 μM] as a catalyst and 4CzIPN [50 μμM] as photosensitizer (Figure 1.13).[84]

Figure 1.13. Photocatalytic CO_2 reduction with 4CzIPN, FeTotpy and TEA. Reproduced with permission from Ref.[84]

The system produced 2250 TON of CO in 99.3% selectivity at TOF = 60 min^{-1} under visible light irradiation (420-650 nm, 3 w LEDs) in DMF/H_2O (3:2 v/v) solution, using 0.28 M of TEA [0.28 M] as the sacrificial electron donor. The presence of H_2O enhances the photocatalytic efficiency, presumably by acting as a proton source. The ruthenium photosensitizer [Ru(bpy)$_3$]$^{2+}$ activity was low, TON = 20 under the same conditions and timeframe. These results highlight the high activity of 4CzIPN as chromophores in photocatalytic CO_2 reduction, even in the presence of water.

1.7 Carbon Dioxide

CO_2 is a thermodynamically stable molecule ($\Delta G_f^o = -396$ kJ/mol) and the final product of many combustion processes. The reverse process, the electrochemical conversion of CO_2 into fuel or value-added molecules, requires a strong reducing potential, electrons, and protons. Table 1.3 lists the formal reduction potentials vs NHE (Normal Hydrogen Electrode) for the conversion of CO_2 into various hydrocarbon products, where $E^{o'}$ is the formal potential at 298 K, pH 7 and under 1 atm of pressure. According to this table, thermodynamics strongly influences product accessibility since electrochemical CO_2 reduction can follow multiple reduction routes. Note that, the single electron reduction of CO_2 to $CO_2^{.-}$ requires a very negative potential (–1.90 V vs NHE), This reaction is

utilized often to explain the high overpotentials encountered during CO_2 electroreduction. However, it is worth noting that solvated $CO_2^{-\cdot}$ is not formed during the electroreduction of CO_2. Instead, the species formed from the first one-electron reduction is bonded to the electrocatalyst surface, likely through multiple bonds and, perhaps, even stabilized by protonation by the solvent. As such, the often quoted –1.90 V potential for this step is of questionable relevance to a specific mechanism. In contrast, proton-coupled multielectron reactions are kinetically and thermodynamically more accessible. Still, significant overpotentials are encountered during experimental CO_2 electroreductions, higher than most of the normal reduction potentials in Table 1.3, leading to the formation of multiple products, often with significant amounts of hydrogen evolution as a common side reaction. Some products, like methanol or methane, are highly desirable, as they act as both raw chemicals and as fuel (in fuel cells and combustion engines).[85] Thus, electrocatalysts are necessary to overcome the inertness of CO_2 and to carry out the reductions selectively. Selective CO_2 electroreduction catalysts are rare and typically operate through kinetic selectivity, not thermodynamic.

Table 1.3. Thermodynamic Potentials of Competing Reactions for CO_2 Reduction in Non-aqueous Conditions. Reproduced with Permission from Ref.[86]

Reaction	$E^{o'}$ vs NHE
$CO_2(l) + 2\ H^+ + 2\ e^- \rightarrow CO_{(l)} + H_2O$	–0.53 V
$CO_2(l) + 2\ H^+ + 2\ e^- \rightarrow HCOOH$	–0.61 V
$CO_2(l) + 4\ H^+ + 4\ e^- \rightarrow HCHO + H_2O$	–0.48 V
$CO_2(l) + 6\ H^+ + 6\ e^- \rightarrow CH_3OH + H_2O$	–0.38 V
$CO_2(l) + 8\ H^+ + 8\ e^- \rightarrow CH_4 + H_2O$	–0.24 V
$CO_2(l) + e^- \rightarrow CO_2^{-\cdot}$	–1.90 V

Additionally, the CO_2 reductions shown in Table 1.3 can be carried out through catalysts driven by direct use of light (photocatalysis) or by preliminarily light conversion into electricity in photovoltaic cells, followed by electrocatalysis or a combination of both (photoelectrocatalysis).

One objective of the research described in this dissertation is to develop and study earth-abundant catalyst-chromophore systems for the photocatalytic- and photoelectrocatalytic reduction of CO_2 employing chromophores based upon new

derivatives of 4CzIPN. The next part of the dissertation will, therefore, discuss the relevant homogeneous catalysts for CO_2 electroreduction.

1.8 Homogeneous Catalytic Systems for CO_2 Reduction

Molecular catalysts are adaptable, well-defined systems to investigate the requirements for fast kinetics and long-term stability during CO_2 reduction. Almost uniquely, molecular catalysts offer direct observations and study of single, well-defined active sites, sometimes during the operation in the catalytic cycle. Molecular catalytic systems for CO_2 reduction are characterized and studied through electrochemistry. Studies on the electrocatalytic CO_2 reduction reaction (CRR) with homogeneous electrocatalysts typically are carried out in non-aqueous solvents, such as acetonitrile (MeCN) or dimethyl formamide (DMF) solvents with an added proton source. These mixtures provide three main advantages over an aqueous electrolyte: a broad potential window, the solubility of CO_2 is higher, and the concentration of protons is controllable.[87] For example, the solubility of CO_2 in acetonitrile is 0.28 M (298.15 K under 101.325 kPa), whereas in water it is lower than 0.03 M (298.15 K under 101.325 kPa).[87,88] In a typical electrochemical cell, a Glassy Carbon (GC) mounted on a rotating disk electrode (RDE) functions as the working electrode (WE), a platinum gauze is used as a counter electrode (CE), and for the reference electrode (RE) there are several options available with its advantages and disadvantages, depending on the solvents used and the nature of the catalytic system (Figure 1.14). The pseudo reference Ag/Ag^+ electrode is employed vastly for CO_2 reductions in organic solvents; it is calibrated with the internal reference of the ferrocene reversible redox couple (Fc/Fc^+). An electrolyte is added to the solution with the catalysts to facilitate the electron transfer. Tetrabutylammonium hexafluorophosphate ($TBAPF_6$) has arisen as the electrolyte of choice; however, variants of tetrabutylammonium with different anions (such as ClO_4^-) or $LiClO_4$ are still scattered across the literature.[89]

Figure 1.14. Schematic representation of a three-electrode electrochemical cell

The CRR performance is evaluated by controlled potential electrolysis (CPE, potentiostatic electrolysis) or by potentiodynamic experiments The Faradaic efficiency (FE) is the ratio of the moles of electrons (n) that formed CRR product to the total moles of electrons (eq 1.2, where F is the Faraday constant, Q is the charge in Coulombs, and z is the number of electrons involved in the process). The overpotential (η) = applied potential at a given current density (E_{app}) – thermodynamic potential for conversion (E^o) (eq 1.3, usually obtained from potentiodynamic experiments). Turnover number (TON) = moles of intended product/moles of catalyst (eq 1.4, usually obtained from CPE experiments). Catalytic selectivity = moles of intended product/(total moles of all products produced) (eq 1.5, from CPE). Turnover frequency (TOF) = catalytic turnovers per unit of time eq 1.6).

$$\text{FE}_{prod}\ (100\%) = 100 \text{ x } (zFn_{prod} / Q) \tag{1.2}$$

$$\eta = E_{app} - E^o \tag{1.3}$$

$$\text{TON} = n_{prod} / n_{cat} \tag{1.4}$$

$$\text{CS} = n_{prod} / n_{H_2} + n_{all\ products} \tag{1.5}$$

$$\text{TOF} = \text{TON} / \text{Time} \tag{1.6}$$

Note that TON and TOF can be reported based upon the total amount of catalyst precursor in solution, or they can be based upon the amount of active catalyst in the diffusion layer near the working electrode. In the homogeneous catalysis CRR

literature, the mechanisms most often are determined from cyclic voltammetric data using the foot of wave analysis (FOWA) pioneered by Savéant et al.[90,91] The fundamental components of the model are that the active catalyst (designated as Q) is generated from a reversible electron reduction of the oxidized catalyst (P). The ratio of Q to P is governed by the Nernst equation. As well, it is assumed that the $[CO_2]$ is constant and equal to the bulk $[CO_2]$, in other words, the rate of CO_2 diffusion is very high relative to the rate of reduction. Assumptions are then made regarding the mechanism. For example, for an EECC mechanism (two electron transfer steps followed by two chemical steps) in the first chemical step, the ratio of currents i_{cat} to i_p is given by eq 1.7. Here, i_p is the maximum current for density for a reversible 1 e⁻ redox couple of the catalyst. It can be determined by cyclic voltammetry of the catalyst in the absence of CO_2, or by utilizing a redox process in the catalyst that does not overlap with the catalytic wave in the cyclic voltammogram. The purpose of dividing i_{cat} by i_p is to normalize the data for the diffusion coefficient of the catalyst, electrode surface area, catalyst concentration, and scan rate. Here i_{cat} is the maximum current density measured during linear sweep voltammetry, i_p is the current density in the absence of CO_2, n is the number of electron transfers per mole of product per catalyst ($n = 2$ for CRR forming CO), n' is the catalyst equivalents required per turnover ($n' = 1$), υ is the scan rate, R is the universal gas constant, T is the temperature, F is Faraday's constant. From this equation, it follows that a plot of i_{cat}/i_p vs $1/(1 + \exp[(nF/RT)(E - E^o_{PQ})$ solves for the global rate constant k_{cat}. This global rate constant is typically an expression of rate constants leading up to the rate-determining step, and it includes the bulk $[CO_2]$. The FOWA analysis is a more representative measurement of the global rate constant because it is applied to the early stages of the CO_2 reduction peak in the cyclic voltammogram before other processes, such as catalyst deactivation, depletion of CO_2 near the electrode surface, etc., deviate the curve from ideal behaviour. The maximum TOF of the catalyst under these conditions (i.e., at the Nernst potential when all the catalyst is in the form of Q) is equal to k_{cat}. The FOWA analysis is a relatively recent development, and it is not applied commonly in the literature. A more common approach is utilizing the plateau region currents. Using the maximum i_{cat}, i.e., the region in the catalytic CV where the current is maximized or plateaued, at the potential where

all the catalyst precursor is converted to the active reduced catalyst, Q, eq 1.8 simplifies to eq 1.9. Like eq 1.8, 1.9. is based upon the assumption that $[CO_2]$ in the active zone near the electrode surface is equal to the bulk.

$$\frac{i_{cat}}{i_p} = \frac{2.24\sqrt{\frac{RT}{nFv}n'k_{cat}}}{1+\exp\left[\left(\frac{nF}{RT}\right)(E-E_{cat/2})\right]} \tag{1.7}$$

$$\frac{i_{cat}}{i_p} = \frac{1}{0.446}\sqrt{\frac{RT}{nFv}n'k_{cat}} \tag{1.8}$$

$$\text{TOF}_{max} = k_{cat} \tag{1.9}$$

The maximum turnover frequency of the catalyst is again = k_{cat}, eq 1.9, which includes the $[CO_2]$ and an expression of the rate constants up to and including the rate-determining step eq 1.8. The complications attending the use of the plateau method include catalyst deactivation, side reactions, and depletion of $[CO_2]$ at the maximum currents. As such, FOWA is more accurate.

A note on comparing the catalytic activity of molecular electrocatalysts CRR in the literature. In an attempt to compare literature catalyst performance for this dissertation, all potentials were converted to Fc/Fc^+ whenever possible, and emphasis was placed on product selectivity and Faradaic efficiencies. It is important to note that variations in the reported systems including [catalyst], [additives], type of solvent, CPE potentials, volumes, reactor size, number and type of side reactions, mechanisms, etc., render direct comparisons difficult, and the comparisons discussed here should be treated as tentative. In summary, there is a need for standard and more rigorous approaches across the literature.

1.8.1 Rhenium Electrocatalysts

The prototype Re complex for CO_2 electroreduction is *fac*-Re(bpy)(CO)$_3$Cl (Figure 1.15). This area has been reviewed extensively. [86,92–94] This complex is an octahedral, d^6, 18-electron selective electrocatalyst for the formation of CO. In their pioneering 1984 study, Hawecker and co-workers first reported electrocatalytic reduction of CO_2 using *fac*-Re(bpy)(CO)$_3$Cl (**1a**) [0.9 mM] at –1.25 V vs NHE (or –

1.97 V vs Fc/Fc$^+$) in DMF/Water (9:1) mixture as a solvent, with high Faradaic efficiencies (>98%), negligible amounts of H$_2$, with up to ~25 TON over 14 h.[93] Many related compounds have been investigated since then (Tables 1.2-1.5).[86,92–94] The major areas of research are the effects of variation of the electronic properties of bpy, the presence of inter- and intramolecular proton sources, and highly delocalized alternatives to bpy ligands.
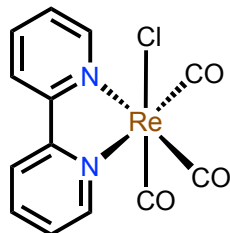
Figure 1 15. *fac*-Re(bpy)(CO)$_3$Cl **(1a).**

The synthetic versatility of the bpy ligand means that catalyst properties can be tailored to study and optimize activity. The Faradaic efficiencies (FE's) for the formation of CO by the series of compounds R= CH$_3$O- (**1b**), -CH$_3$- (**1c**), *t*Bu- (**1d**), -CF$_3$ (**1e**), -CN (**1f**) (Scheme 1.5, Table 1.4) were evaluated through controlled potential electrolysis (CPE) in CO$_2$-saturated acetonitrile solutions with TBAPF$_6$ as the electrolyte.
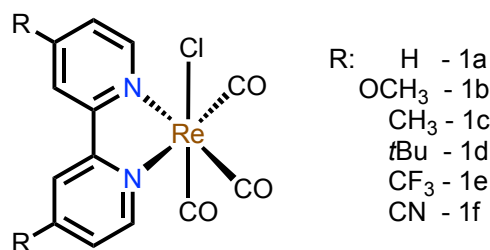
Scheme 1.5. General structure of Re catalyst for CO$_2$ to CO electrochemical reduction.

Table 1.4. CPE Reduction of CO_2 to CO with a Series Of $Re(R\text{-}bpy)(CO)_3Cl$ Catalysts

Entry	Catalyst	FEco (%)	Ref
1	**1a**	99	95
2	**1b**	59	95
3	**1c**	99	95
4	**1d**	99	95
5	**1e**	30	95
6	**1f**	18	95

FE determined after CPE for 1 hour in anhydrous CO_2-saturated MeCN with 0.1M TBAPF$_6$ and [Re] = 1 mM.

The FE's for R = ^{t}Bu (**1d**) and CH$_3$ (**1c**) were both high and the same as that reported in this publication for R = H, ~ 99 %. The Re(1/0) redox potentials for the complexes with electron-donating substituents ^{t}Bu- (–2.17 V, **1d**), and -CH$_3$ (–2.18 V, **1c**) were slightly more negative than the parent compound R= H (–2.16 V, **1a**). Interestingly, the methoxy is the most electron-donating group in this series (**1b**, Re (1/0) = –2.21 V) but had the lowest FE among the electron-rich compounds (59 %), suggesting that π- and σ- electron donation have different effects on the FE for this CRR, with σ- electron donation being more beneficial. The FE's with the electron-withdrawing ligands **1e** and **1f** were lower, 30 and 18 %, respectively. The Re(1/0) redox potentials for compounds with electron-withdrawing groups (-CF$_3$ (–1.79 V, **1e**) and -CN (–1.60 V, **1f**)) were more positive than **1a**, consistent with the notion that σ-electron donation enhances the FE for CRR with these complexes. The catalyst activities were investigated by comparing the cyclic voltammograms in MeCN with and without being saturated with CO_2 (0.28 M, sweep rate = 100 mV s^{-1}, 0.1 M TBAPF$_6$, GC working, Pt counter, Ag/AgCl reference). The ratio of the plateau currents i_{cat} to i_p decreased in the order R = OMe (40.7) > Me (32.6) ~ ^{t}Bu (32.1) > H (8.4) among the electron-donating series. The ratios were 15.0 (CF$_3$) and 8.3 (CN) among the electron-withdrawing series. Rate constants were estimated from these plateau currents as well as from FOWA data, with considerable variation in the constants obtained from the two methods. It is worth noting at this point that different groups report different performance data for the same compound. For example, the FE

for the CPE reduction of CO_2 to CO was reported recently to be 62% for **1a** (R = H) under nearly identical conditions.[96] This variation in the literature data is common, and groups have noted that electrode fouling is common in these systems; freshly polished glassy carbon disk electrodes must be used for each measurement.[95] Suffice it to say that the study of the exact nature and activities of these compounds is still evolving in the literature.

Another major contributor to CO_2 electroreduction with homogeneous electrocatalysts is the addition of a Brønsted acid. Re-bpy complexes have a second-order dependence on protons for the electrocatalytic reduction of CO_2 to CO and H_2O.[97] To illustrate, the addition of phenol, PhOH (1M, pK_a = 29.1) to MeCN solutions of **1a** (R=H) reduced the overpotential for CO_2 reduction in CV experiments and did not decrease the reported FE (96%) in CPE experiments.[95]

In line with these observations, researchers have investigated catalysts modified by the integration of an intramolecular proton source.[96] In one study, the position of the amine group (ortho-, meta-, and para-) was varied within an aniline ring situated on the 6-position of the 2,2'-bipyridine (Scheme 1.6). The Re(1/0) reduction within the meta-substituted aniline derivative **2b** occurs at a very similar potential to the parent, unsubstituted compound **1a**. In contrast, the Re(1/0) reduction potentials for **2a** (orth*o*-NH_2) and **2c** (para-NH_2) are more negative than the parent complex **1a** by 70 mV and 90 mV, respectively (Table 1.5). As expected from electrophilic substitution results with aniline and resonance models,[98] the meta-aniline group has a small electronic effect on Re. Cyclic voltammetry was used to investigate the performance of these compounds towards CO_2 reduction in CO_2-saturated MeCN with and without 4% trifluoroethanol (TFE) as a proton source. The turnover frequencies (TOFs) were estimated using eq 1.8 and 1.9. TFE increased the activity of all the compounds. The order in the absence of TFE was **1a** < **2c** (para-NH_2) < **2a** (ortho-NH_2) < **2b** (meta-NH_2). The order in the presence of TFE was **1a** < **2c** < **2a** < **2b** (**Table 1.5**). The meta-substituted catalyst was more active than all the compounds in the series, both in the absence and presence of TFE. A comparison of the Re (1/0) redox couples showed that the meta-substituted NH_2 had little electronic effect on the Re centre. The CPE faradaic efficiencies for CO formation were high (89–98%) for all the compounds in the

presence of TFE. The corresponding FEs were significantly lower for all the compounds except the *meta*-substituted aniline compound without TFE (Table 1.5).[96] Taken together, these results show that the meta-NH_2-substituted compound **2b** was superior and that the higher activity/selectivity does not result from a direct electronic influence of the meta-NH_2 group on the Re centre. The most likely explanation is that the second-sphere amine group is in the optimum position to hydrogen bond to the carboxylate group ligand formed by the reduction of CO_2 at the Re centre of the catalyst. This hydrogen bonding would, presumably, be stronger in the presence of TFE, and it would increase the rate of CO_2 reduction by stabilizing this intermediate and by facilitating C-O bond cleavage.
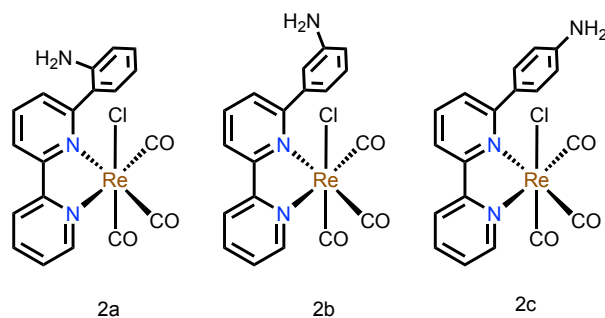
Scheme 1.6. Structures of the catalyst studied with a local proton source.

Table 1.5. Summary of the Electrocatalysis in CO_2 with *fac*-Re(nNH$_2$Ph-bpy)(CO)$_3$Cl.[96]

Entry	Catalyst	[Conc.]	Redox Potential vs Fc/Fc$^+$	FEco (%) No TFE	FEco (%) 4% TFE	TOF (s^{-1}) No TFE	TOF (s^{-1}) 4% TFE
1	**2a**	0.5 mM	–2.22 V	38	89	31.7	123
2	**2b**	0.5 mM	–2.14 V	83	93	98.8	239
3	**2c**	0.5 mM	–2.24 V	52	98	30.1	109
4	**1a**	0.5 mM	–2.15 V	62	92	14.6	72.9

Redox potential measured at v=100 mV s^{-1}. Glassy carbon disk working, platinum wire counter, and silver wire quasi-reference electrodes. In CH$_3$CN with TBAPF$_6$, 1 hour. The CPE potential applied for experiments with TFE is lower than no TFE conditions, ranging from 30 to 100 mV lower.

As another representative example of Re systems, the Portenkirchner group reported the synthesis, structure, and spectroscopic characterization of *fac*-Re(5,5'-bisphenylethylnyl-2,2'-bpy)(CO)$_3$Cl (**3a**) Scheme 1.7).[99] Cyclic voltammetry studies on the reduction of CO_2 in MeCN showed that the onset potential

for complex **3a** was 300 mV more positive than for **1a** (300 mV less overpotential). The catalytic rate constants for **3a** and **1a** determined using eq 1.8 were 220 $s^{-1}M^{-1}$ and 60 $s^{-1}M^{-1}$, respectively. The conjugation of the π-electron system is more extended in **3a** is than in **1a**, which may be a factor in the higher activity of **3a** vs **1a**. Additionally, CPE experiments indicated that the FE of **3a** (24–43%) was lower than **1a** (50%) under the conditions and times reported by the authors. Note that FE of **3a** measured by gas chromatography (43 %) was lower than that measured by Fourier Transform Infrared spectroscopy (FTIR, 24%) (Table 1.6). Homogeneous catalysis has advantages over heterogeneous catalysis, including more complete characterizations, easier modifications of the catalyst, and investigation of reaction mechanisms. The disadvantages to homogenous catalysis include possible solution-phase deactivation processes such as dimer formation that the solvent required to dissolve the catalyst may not be optimized for CO_2 reduction, or that isolation and reuse of homogeneous catalysts is typically impractical. A method to overcome these challenges is to immobilize the electrocatalyst on the electrode. The alkynyl-substituted Re complex **3a** was immobilized by electropolymerization onto a Pt electrode (complex **4a**, Scheme 1.7).[100] The FE of the polymer film (33%, measured by GC) was reported to be lower than that of the monomer in solution (43%), although the times and potentials of the CPE experiments were different. As well, traces of formate and oxalate (FEs < 1%) were formed by the polymeric catalyst. Cyclic voltammetric studies indicated that the current increases faster with applied potential over the polymeric catalyst and that the overpotential for CO_2-to-CO reduction is also lower for the polymeric catalyst.
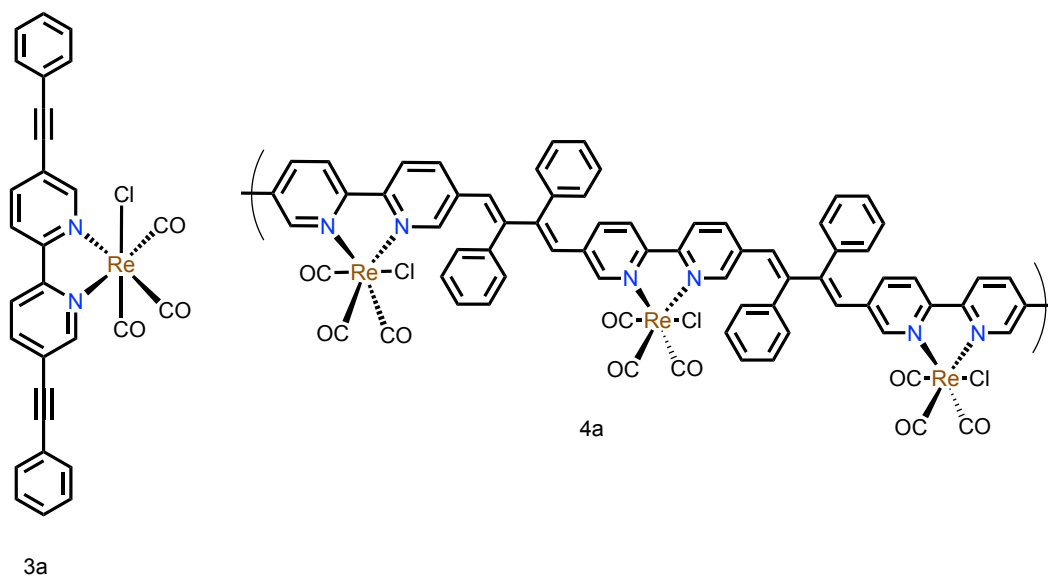
Scheme 1.7. Structure of *fac*-Re(5,5'-bisphenylethylnyl-2,2'-bpy)(CO)₃Cl 3a, and the putative structure of the polymer.

Table 1.6. Summary of the Electrocatalysis in CO_2 with *fac*-Re(5,5'-bisphenylethylnyl-2,2'-bpy)(CO)₃Cl and The Polymer Film

Entry	Catalyst	[Conc.]	Redox Potential vs Fc/Fc⁺	CPE Potential Applied (E_{app}) vs Fc/Fc⁺	Time of CPE (min)	FEco (%)	TOF (s⁻¹)	Ref
1	**3a**	1 mM	–2.39 V	–2.59 V	25	43	220	[99]
2	**3a**	1 mM	–2.39 V	–2.59 V	25	24[a]	220	[99]
3	**4a**	1.5 x 10⁻⁵ mol/cm²	–2.24 V	–2.24 V	60	33	NR	[100]
4	**1a**	1 mM	–2.17 V	-2.59 V	10	50	60	[99]

Redox potential under CO_2-saturated MeCN TBAPF6 solution. Pt was used as WE and CE, whereas Ag/AgCl as RE. The electrolysis was carried out without stirring, and gas chromatography was used to determine CO. [a]The method for detecting CO is FTIR, and the electrolysis was done with stirring. NR: not reported.

As a final representative example of Re systems, the large, conjugated ligand and redox-active moieties on the bpy ligand can serve as an electron reservoir for catalysis. These ligands lead to lower energy of the LUMO on the Re complex, decreasing the energy needed to reduce CO_2 into CO. Accordingly, an N-N bidentate ligand with a high degree of conjugation was introduced to the tricarbonyl rhenium complexes: dipyrido[3,2-*a*:2',3'-*c*]phenazine (dppz). A series of Re(I) with substituted dppz ligands with electron-donating (tBu) or electron-withdrawing (-CF₃) and redox-active (-NO₂) substituents have been evaluated as electrocatalysts for homogeneous

CO$_2$ reduction (Scheme 1.8, Table 1.7). Cyclic voltammetry studies on complexes **4a-d** showed the redox potential of the catalyst under N$_2$ was not affected significantly by the different groups on the dppz, showing the Re (1/0) potentials ranging from –2.01 V to –2.07 V vs Fc/Fc$^+$. Complex **4c** was the only 40 mV more negative overpotential than complex **1a**. In comparison, the cyclic voltammetry under CO$_2$ showed similar reduction potentials and similar reduction current densities. With the addition of phenol, under CO$_2$, the current density increased approximately double for complexes **4a** and **4b**, and for complex **4c,** the current density was six times higher, and complex **4d** showed the highest current density (~14 mA cm^{-2}), nearly five times higher than complex **4a**. The catalyst activity was evaluated by the ratio of the peak current in the presence (i_{cat}) and absence of CO$_2$ (i_p). The ratio of i_{cat} to i_p increased in the order R: H **4a** (1.8), ^{t}Bu **4c** (3.8), CF$_3$ **4b** (4.2) and N$_2$O **4d** (4.7). Usage of these data allowed the calculation of turnover frequencies. The TOF values were significantly higher for phenol-assisted experiments, and the TOF values are consistent with the catalytic current densities observed for cyclic voltammetry. Thus, **4d** presented the highest TOF (s^{-1}): 4.4, followed by CF$_3$ (3.6), ^{t}Bu (2.9) and H (0.7); however, it remains unclear how the redox active group -NO$_2$ plays its role in the CO$_2$ catalytic cycle. Further studies are required to understand its influence fully.

Additionally, the controlled potential electrolysis was performed at around –2.0 V vs Fc/Fc$^+$ for all complexes (**4a–d**), and PhOH (0.45 M) was added as a weak Brønsted acid in MeCN. GC confirmed CO as the product, and no other products than CO were detected in the gaseous phase. The results suggest that the ligand modification of dppz leads to a large conjugation and can aid in storing multiple electrons and lower the energy barrier for CO$_2$ reduction. However, it did not demonstrate a straightforward trend about the electron withdrawing/donating ability (CF$_3$/^{t}Bu) or the redox active/inert (NO$_2$/H) capabilities of the substituents in the 11-position of the dppz since the FE did show substantial improvements with different groups.

Notably, the -NO$_2$ group **4d** showed the highest FE (53%), whereas the -H group **4a** reached 48% under nearly the same conditions. Interestingly, under the same conditions, the FE for the parent compound **1a**, did show a low FE of 32%; another research group reported up to 92% FE with 0.5 mM of the catalyst and 4% of TFE

(Entry 5, Table 1.7).[96] These results highlight the importance of concentration and proton source drastically affecting the catalytic performance of Re complexes.

R = 4a (-H)
4b (CF$_3$)
4c (tBu)
4d (NO$_2$)
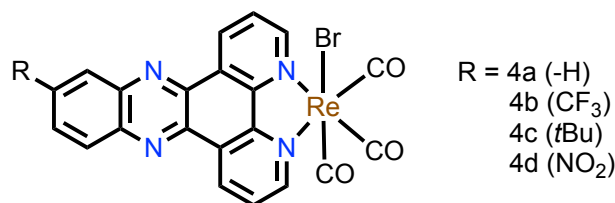
Scheme 1.8. Structures of Re(R-dppz)(CO)$_3$Br catalysts for CO$_2$ to CO electrochemical reduction

Table 1.7. Summary of Electrocatalysis of Re(R-dppz)(CO)$_3$Br Catalysts for The CO$_2$ to CO Reduction.[101]

Entry	Cat	Redox Potential under N$_2$	CPE Potential Applied (E_{app})	TOF (s^{-1}) No PhOH	TOF (s^{-1}) with PhOH	FE (%)
1	**4a**	–2.01 V	–2.0 V	0.3	0.7	48
2	**4b**	–2.03 V	–1.9 V	1.5	3.6	19
3	**4c**	–2.07 V	–2.0 V	0.4	2.9	27
4	**4d**	–2.02 V	–2.1 V	0.3	4.4	53
5	**1a**[a]	-.03 V	–2.1 V	1	-	32

All potentials reported vs Fc/Fc$^+$. CV was recorded in 0.1 mM [cat] in MeCN with 0.1 M TBAPF$_6$ under CO$_2$, at 100 mV s^{-1}. [a] Complex **1a**, with -Br instead of -Cl.

1.8.2 Manganese Electrocatalysts

Re-based homogeneous CRR catalysts are excellent for academic research and a fundamental understanding of the mechanistic and thermodynamic aspects of CO$_2$ activation-conversion.[92] More recently, transition metals from the first row of the periodic table, namely Mn, Fe, Co, and Ni, have emerged as a response for sustainable, affordable and efficient catalysts for CRR.[27,102,103] This area has been reviewed extensively, and mainly manganese complexes catalysts similar to their rhenium analogues, will be the focus of this section. In 2011, [*fac*-Mn(bpy)(CO)$_3$Br] (**5a**, Scheme 1.9) was found to be an active and selective catalyst for CO formation from CO$_2$ reduction in organic solvents.[104] Like its Re counterpart, Brønsted acids increase the activity of **5a** towards the CRR. CPE studies (–1.79 V vs Fc/Fc$^+$, CO$_2$-saturated acetonitrile, 0.1 M n-Bu$_4$NClO$_4$, 1 mM H$_2$O) show the FE of **5a** towards CO was 100 % after 4 h. Further, the TON$_{TOT}$ (based upon all the Mn in solution) was 13 (Entry 1,

Table 1.8). The FE dropped, however, to 85 % (15 % H_2) after 22 h (Entry 2, Table 1.8). The dimethyl derivative [*fac*-Mn(dmbpy)(CO)$_3$Br] (**5b**, dmbpy = 4,4'-dimethyl-2,2'-bipyridine) is more stable under CPE, with FE$_{CO}$ = 100 % and TON$_{TOT}$ = 34 after 18 h (Entry 3, Table 1.8).
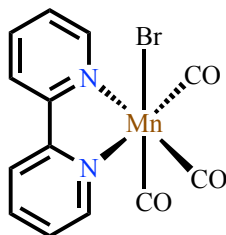
Scheme 1.9. Prototypal [*fac*-Mn(bpy)(CO)$_3$Br] (5a) complex for electrochemical CO_2 to CO reduction.

Table 1.8 Summary of Electrocatalytic CO_2 Reduction with Mn(R-bpy)(CO)$_3$Br Catalysts

Entry	Catalyst	CPE Potential Applied (V vs Fc/Fc$^+$)	Proton source [M]	Time (h)	Products (%FE)	Ref
1	**5a**	−1.79	1 mM H_2O	4	CO (100) H$_2$ (0)	104
2	**5a**	−1.79	1 mM H_2O	22	CO (85) H$_2$ (15)	104
3	**5b**	−1.79	1 mM H_2O	18	CO (100)	104
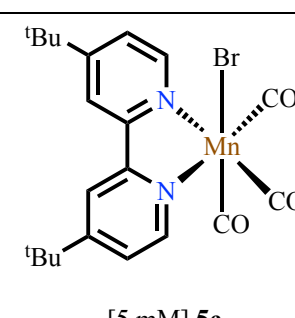
[cat]: 1 mM in CO_2-saturated MeCN solution with 0.1 M TBAP. GC was used as WE and Pt as CE, whereas 10 mM Ag/Ag$^+$ as RE. The electrolysis was carried out with stirring, and gas chromatography was used to determine CO.

Many synthetic strategies have been utilized to vary the structure of the bpy ligand to study structure-activity relationships. Modifications on the bpy ligand, such as placing electron-donating groups on positions 4,4', typically enhance the catalytic activity, such as in the case of the methyl groups on complex **5b** discussed above. The cyclic voltammetry studies of *fac*-Mn((^{t}Bu)$_2$bpy)(CO)$_3$Br (**5c**) (Table 1.9) were used to investigate the performance of this compound towards CO_2 reduction in MeCN with three different weak Brønsted acids (H_2O, MeOH and TFE) as a proton source. The catalyst activity was evaluated by the ratio of the peak current in the presence (i_{cat}) and absence of CO_2 (i_p). The ratio of i_{cat} to i_p increased in the order 3.1 M H_2O (25) > 5.8 M MeOH (26) > 1.6 M TFE (42). Usage of these data allowed the calculation of turnover frequencies. The turnover frequencies (TOFs) were estimated using eq 1.8 and

1.9 TOF increased the activity of **5c** for all the acids used. The TOF increased in the same order as the current density ratio, giving the highest 340 s-^{1} for TFE.

Additionally, the CPE of **5c** was carried out at -2.58 V vs Fc/Fc$^+$ in a CO_2-saturated acetonitrile solution, achieving 100% FE for CO in the presence of 0.8 M TFE, sustaining stable current density for a period of more than 3 h. The catalyst performance is likely due to the inhibition of the inactive Mn-dimer formation during catalysis. This activity is comparable to Re analogues at similar conditions.

Table 1.9. Electrocatalytic CO_2 Reduction with [*fac*-Mn(*t*Bu-bpy)(CO)₃Br] (5c).[105]

Catalyst	Proton source (M)	TOF (s^{-1})	Controlled Potential Electrolysis		
			Time (h)	Potential applied (V vs Fc/Fc$^+$)	Products (%FE)
	None	0			
	3.1 M H₂O	120	3	-2.58	CO (100)
	5.8 M MeOH	130			
	1.6 M TFE	340			

[TFE]: 0.8 M for the CPE.

In another study, the CPE FE$_{CO}$ (1 atm CO_2, CH₃CN, [Mn] = 1.0 mM, [H₂O] = 1.0 mM, 1.88V) after 4 h for a series of Mn compounds substituted at the 6-position of bpy with H (**5a**), 2-PhOH (**5d**), and 2-PhOMe (**5e**) were 75 %, 76 %, and 67 %, respectively (Scheme 1.10, Table 1.10).[106]
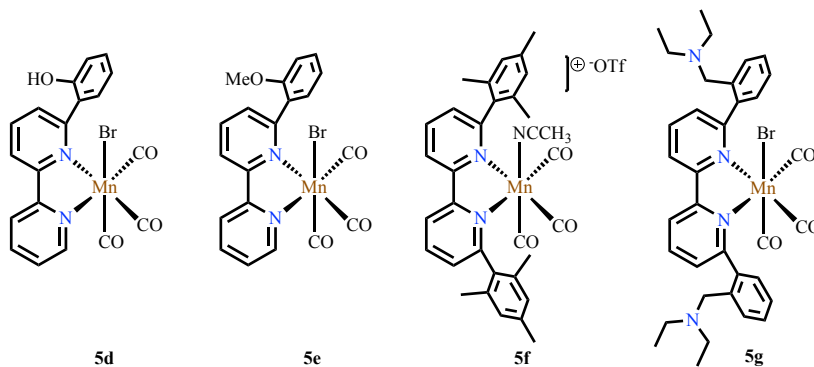
Scheme 1.10. Structures of *fac*-Mn(R-bpy)(CO)₃Br complexes for the CO_2-to-CO electroreduction.

Table 1.10. Electrocatalytic CO_2 Reduction with [*fac*-Mn(R-bpy)(CO)$_3$Br] Complexes

Entry	Catalyst	Conc. [M]	CPE Potential Applied	Proton source [M]	Time (h)	Products (%FE)	TOF (s^{-1})	Ref
1	**5d**	1 mM	–1.88 V	1 mM H$_2$O	4	CO (76)	-	[106]
2	**5e**	1 mM	–1.88 V	1 mM H$_2$O	4	CO (67)	-	[106]
3	**5f**	0.5 mM	–2.2 V	0.3 M TFE	1.2	CO (98) H$_2$ (0)	480	[107]
4	**5f**	0.5 mM	–1.6 V	1.4 M TFE	24	CO (96) H$_2$ (0)	5000	[107,108]
5	**5g**	1 mM	–2.17 V	2.0 M TFE	1	CO (35) HCOOH (25) H$_2$ (31)	7500	[109]
6	**5h**	1 mM	--2.17 V	2.0 M TFE	1	CO (4.8) HCOOH (71) H$_2$ (6.4)	5000	[109]
7		1 mM	–1.77 V	2.0 M TFE	1	CO (6.9) HCOOH (90) H$_2$ (7.3)	180	[109]
8		1 mM	–2.17 V	0.3 M *i*PrOH	1	CO (3.7) HCOOH (89) H$_2$ (0.2)	-	[109]
9		1 mM	–2.17 V	1.0 M PhOH	1	CO (0) HCOOH (63) H$_2$ (33)	-	[109]
10	**5i**	1 mM	–2.17 V	2.0 M TFE	1	CO (5.6) HCOOH (70) H$_2$ (5.9)	4000	[109]

CPE (V vs Fc/Fc$^+$), all CPE experiments were carried out in a CO_2-saturated MeCN solution.

Neither compound was stable under these conditions. The TON$_{TOT}$ was 1.2, 2.7, and 0.9, respectively. The low overpotential (~onset) current densities in CV experiments were higher for **5d** than **5a** or **5h**. The higher TON$_{TOT}$ and low overpotential current densities lead the authors to hypothesize that intramolecular H-bonding in **5d** promoted the CRR.

Increasing the steric hindrance further by substituting the bpy ligand at the 6,6'-positions with 2-mesityl groups, i.e. *fac*-Mn(6,6'-dimesityl-2,2'-bipyridine)(CO)$_3$Br (**5f**) increased the turnover frequency of the catalyst. More specifically, the TOF was 5000 s^{-1} for **5f**, compared to the previous best in class, *fac*-[Mn(^{t}Bu-bpy)(CO)$_3$Br] (**5c**) (TOF = 3000 s^{-1}) measured under the same conditions with the current plateau method.

The CPE FE_{CO} (96%) was as also high for the mesityl complex (1.6 V vs Fc/Fc$^+$, 24 h, TON$_{tot}$ = 30). As will be discussed in the mechanism section, a defining feature of this class of CRR electrocatalysts is the formation of Mn(0)-Mn(0) dimer. The apparent high activity of **5f** may arise from inhibition of dimer formation, or from increased rate of reduction of a Mn-carboxylic acid intermediate (see mechanism discussed below).

Taking the study of bulky substituents at the 6,6'-bpy positions further, a recent report prepared the 2,2'-(6,6'-(*N,N*)-diethylbenzylamine-2,2'-bipyridine) derivative **5h**. Electrochemical studies with in-situ characterization showed that this compound also does not form Mn(0)-Mn(0) dimers. And contrary to Mn-catalysts without amine groups at the ortho position of benzylamine, the main CPE product (MeCN, CO$_2$-saturated, 0.2 M TBABF$_4$, 2 M TFE) was formic acid (HCOOH). Two reaction regimes were identified, depending upon the applied potential. At relatively low potentials, –1.77 V vs Fc/Fc$^+$, the FE for HCOOH was 90%, with CO and H$_2$ as minor products. At higher potentials, –2.17 V vs Fc/Fc$^+$, The FE for HCOOH was 71%, again with CO and H$_2$ being minor products. DFT calculations and in situ NMR and IR observations led the authors to propose that the active catalyst is a Mn(I)-hydride species, formed by prior protonation of the pendant amine group, followed by protonation of the Mn centre. It is proposed that the formate group is formed by a nucleophilic-type addition of the hydride ligand to CO$_2$, followed by rearrangement to form a Mn-formate intermediate. Catalytic CV studies on the CRR using plateau potentials, i.e., maximum plateaued currents, suggest that the turnover frequency for the formation of HCOOH is quite high, 7500 s^{-1} at relatively high applied potentials, and 180 s^{-1} in the lower potential reaction regime.

1.8.3 Mechanism of Reduction for CO$_2$ with *fac*-M(bpy)(CO)$_3$X Catalysts

The cyclic voltammetry of these complexes is the subject of intense study. [110,95,97,111,112] Typically, the solvent is MeCN under an atmosphere of N$_2$. The parent, 18 e$^-$ compound **5a** undergoes two successive irreversible reduction reactions in the cathodic sweep (Complexes 1-3, Scheme 1.11). The first reduction at –1.65 V vs Fc/Fc$^+$ corresponds to the reduction of the Mn(I) centre to form, after the rapid loss of Br$^-$, the relatively

unstable 17 e⁻ monomer [Mn(0)(bpy)(CO)$_3$] (**2**). This species can undergo rapid dimerization through formation of a Mn–Mn bond to give the relatively stable 18 e⁻ dimer [Mn(0)(bpy)(CO)$_3$]$_2$ (**2D**). The second cathodic wave at –1.89 V vs Fc/Fc⁺ corresponds to a reduction of the dimer to form the anionic monomer [Mn(bpy)(CO)$_3$]⁻ (**3**). Interestingly, structural and DFT studies conclude that the more stable form of **3** is comprised of a Mn(0) centre and a bpy·⁻ anionic radical ligand, rather than the Mn(–1)/neutral bpy alternative. Note that some groups propose an alternative pathway where the reduction of the unstable 17 e⁻ Mn(0) monomer [Mn(0)(bpy)(CO)$_3$] to [Mn(bpy)(CO)$_3$]⁻ is more rapid than the dimer formation at –1.65 V vs Fc/Fc⁺, and the resulting 18 e⁻ anionic monomer **3** then undergoes a multi-step parent-child reaction with excess **5a** in solution to generate the Mn(0) dimer **2D**. Indeed, studies on the aforementioned compounds **5f** and **5g**, with large groups at the 6,6'-positions of the bipy ligand, are prohibited sterically from forming Mn(0) the dimers corresponding to **2D**. Instead, the unstable 17e⁻ Mn(0) monomers, formed by 1 e- reductions of **5f** and **5g** undergo rapid 1 e⁻ reductions to form the anionic monomers corresponding to **3**. Scheme 1.11. shows these reductive processes. The prevailing conclusion in the literature is that the anionic monomers with the same structure as **3** are the active catalysts in these electrocatalytic CRRs.
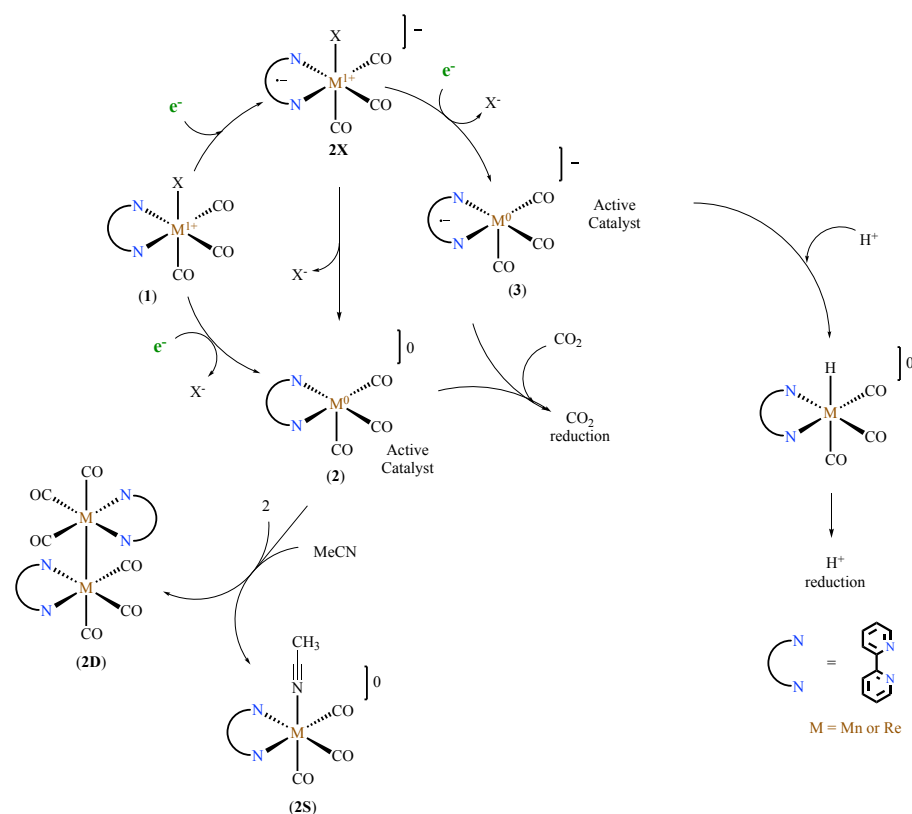
Scheme 1.11. Possible mechanism followed by M(bpy)(CO)₃X catalyst for the reduction of CO₂.

The species $[Mn^0(bpy^{\cdot-})(CO)_3(CO_2)]^-$ undergoes ligand-to-metal charge transfer, followed by electron injection from the d orbitals on the metal into the π^* orbitals on the C-O bonds from CO_2 (Complex **5**, Scheme 1.12). This species further reacts with a proton, forming $[Mn^0(bpy)(CO)_3(CO_2H)]$ (Complex **6**, Scheme 1.12). At this point, the applied potential and the proton source can determine two possible reaction pathways. Low overpotentials are responsible for a further protonation (protonation-first), followed by loss of H_2O and formation of $[Mn^I(bpy)(CO)_4]^+$ (Complex **7**, Scheme 1.12). High overpotentials are, instead, responsible for a further electron reduction (reduction-first) (Complex **8**, Scheme 1.12), followed by protonation and subsequent H_2O loss. Both scenarios lead to a further reduction and CO liberation (Complex **9**, Scheme 1.12). The main distinctive difference between manganese and rhenium carbonyl complexes is the tendency of Mn^0 species to dimerize (Complex **2D**, Scheme 1.11) This dimerization occurs after the first reduction wave and is accompanied by halide loss. To reduce the dimer to the catalytically active species

41

$[Mn(bpy^-)(CO)_3]^-$, a more negative potential is required than the potential required to reduce the unimolecular Mn^0 species.[97,105,113]
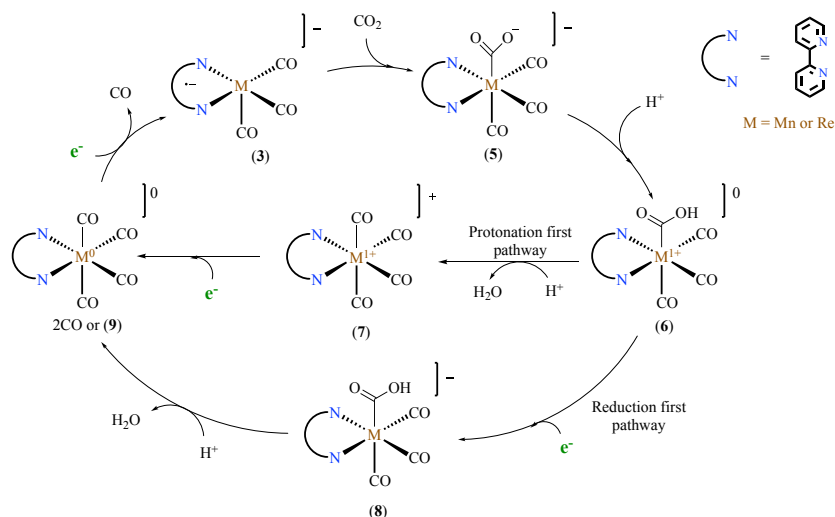
Scheme 1.12. Reaction mechanism proposed for the catalytic reduction of CO_2 catalyzed by $[M(bpy^-)(CO)_3]^-$ in the presence of weak Bronsted acids.

Despite all these findings, molecular catalysts are considered less durable than solid catalysts because only a few of them can convert CO_2 in aqueous conditions, and due to the lack of examples capable of reducing CO_2 beyond the two-electron reduction products (i.e., CO and HCOOH), research has been moving towards immobilization of catalyst.

1.9 Heterogeneous Systems for CO_2 Reduction

To combine the selectivity of molecular catalysts with heterogeneous systems, electrode surfaces have been modified with molecular catalysts to obtain selective and robust heterogeneous systems for electrochemical CO_2 reduction. Ultimately, the source of electrons and protons for the reduction of CO_2 to fuel molecules will be water oxidation to oxygen, protons, and electrons, the oxygen evolution reaction (ORR). Given that ultimate condition, any CO_2 reduction photocatalyst must have a component that also effects the ORR or is heterogenized to the cathode surface of an electrochemical or photoelectrochemical cell with the ORR occurring at the anode. Heterogenization of CRR catalysts to electrodes is likely the easier of the two routes.

As well, heterogenization offers advantages such as avoiding catalyst dimerization, direct electronic connection between the catalyst and electrode, long-term stabilization, avoiding rate limitations from catalyst diffusion; catalyst loadings are not limited by solubility, and operating in solvents where the isolated catalyst would otherwise be insoluble.[114–116] Also, grafting molecular catalysts onto surfaces presents an opportunity to create a tailored synthetic environment around the catalytic site, allowing for the modification of its properties through secondary interactions.

The field of heterogenization of molecular electrocatalysts and photosensitizers is vast and has been reviewed. Apart from those examples previously discussed in this chapter, only representative examples will be discussed in this section. Surface functionalization of carbon surfaces with rhenium CRR catalysts is a common approach. For a recent example, a graphite-conjugated catalyst-rhenium species was prepared by condensation of fac-Re(phen-$(NH_2)_2$)$(CO)_3$Cl with o-quinone moieties on the surface of glassy carbon. The glassy carbon was anodized in aqueous acid to generate the surface o-quinone groups. The catalyst performance was evaluated through controlled current electrolysis (CCE). The CCE at 1.0 mA/cm^2 in acetonitrile with 0.1 M TBAPF$_6$ as the supporting electrolyte over 1.4 h produced CO in 96% FE (Scheme 1.13, left). Proton sources were not added to these solutions. Based upon the moles of Re on the electrode surface, the TON was 12000, a substantially higher value than that observed during CPE experiments with homogeneous Re complexes in solution (140). While the TOF (2.5 s^{-1}), was not as high as that estimated by FOWA analysis of homogeneous systems in diffusion layers, the utilization (TON$_{tot}$) and stability of the catalysts were significantly higher upon heterogenization.[117]

In another representative example, Re(4-NH$_2$-2,2'-bpy)$(CO)_3$Cl onto graphene oxide electrodes was anchored covalently to graphene-oxide electrodes via diazonium electrografting. The resulting system was investigated for syngas production in a CO$_2$-saturated MeCN that was 3.1 M in H$_2$O as the proton source (Scheme 1.13, center). This system is an example of a Re-type CRR electrocatalyst operating in the presence of high amounts of H$_2$O. CPE with this heterogenized catalyst resulted in the generation of syngas (CO/H$_2$) in a ratio of 7:5, TOF = 4.44 s^{-1}, TON = 8000, and FE = 25% at –

1.766 V vs NHE.[114] This result again illustrates the high TON that is achieved by heterogenization.

In another example, the bis(diazonium) compound [Re(5,5'-(N$_2$)$_2$-2,2'-bpy)(CO)$_3$Cl](BF$_4$)$_2$ was electrografted first to carbon paper, TiO$_2$, FTO, or even gold, and then electropolymerized (Scheme 1.13, right). CO$_2$ electroreduction by CPE at – 2.25 V vs Fc/Fc$^+$ for 2 h in acetonitrile (0.1 M TBAPF$_6$) produced CO with FE$_{CO}$ = 99%, TON$_{CO}$ = 3606, and TOF = 0.5 s^{-1},[116] again illustrating the significantly higher TON that can be obtained by heterogenizing this class of CRR electrocatalyst.
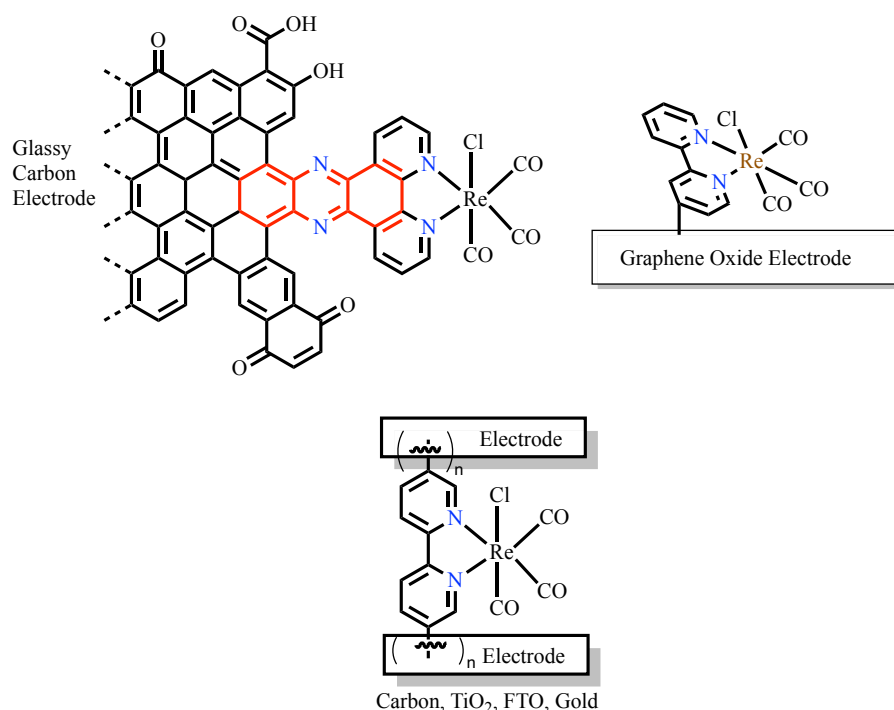
Scheme 1.13. Structures of Re catalyst for the CO$_2$ to CO electrochemical reduction.

In an example employing Mn, *fac*-Mn(bpy)(CO)$_3$Br was entrapped within Nafion on a GC electrode (Scheme 1.14, left). CPE CO$_2$ electroreduction in a relatively rare example of an aqueous pH 7 phosphonate buffer electrolyte at –1.7 V vs Fc/Fc$^+$ formed CO with TON$_{CO}$ = 471, and FE$_{CO}$ = 51% after 4 h.[118] Thus, higher TONs were obtained, and an aqueous electrolyte could be utilized by heterogenizing the homogeneous electrocatalyst.

In another example, a *fac*-Mn(bpy)(CO)$_3$Br-type catalyst was immobilized on multi-wall carbon nanotubes (MWCNT) via electrostatic interactions through a pyrene

anchoring group present as a substituent on the bpy ligand (Scheme 1.14, right). Through this modification, it was possible to control the catalyst loading on the surface of the electrode, and different loadings led to the different major products from CPE CO_2 electroreduction. CO was the main product (FE = 30%) at relatively high catalyst loadings (Γ > 30 nmol cm^{-2}) at –1.5 V (vs Fc/Fc$^+$) with TON$_{CO}$ > 1000 in aqueous 0.5 M KHCO$_3$ solution saturated with CO_2. H$_2$ and HCOOH were the major products at lower loadings (Γ < 20 nmol cm^{-2}) with TON$_{HCOOH}$ > 3000) (Scheme 1.14). The difference in selectivity was attributed to Mn-Mn dimer formation on the surface at higher loadings of Mn.[119] This result again illustrates heterogenizing the homogeneous electrocatalyst results in higher TON and allows the use of aqueous electrolytes.
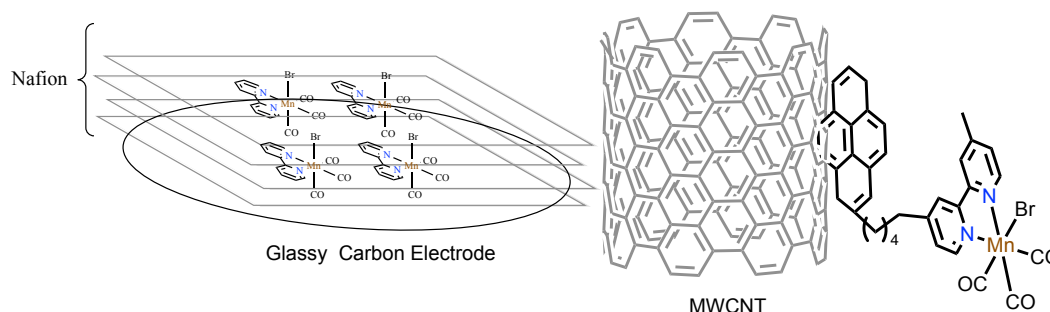
Scheme 1.14. Representation of structures of Mn catalysts immobilized on electrodes through electrostatic interactions.

Early studies have described the integration of Co (phthalocyanines and porphyrins) on carbon surfaces for CO_2 electroreduction. One of the most active immobilized abundant CRR electrocatalysts was prepared by first anodizing glassy carbon, followed by a reaction of the surface carboxylic acid groups with SOCl$_2$. Then, the resulting surface acyl chlorides were amidized by a reaction with 4-aminopyridine, followed by coordination of the py ligands to Co(II)-tetraphenylporphyrin (CoTPP) (Scheme 1.15). Remarkably, this catalyst effected the CPE reduction of CO_2 to CO at –0.5 V vs RHE with TON$_{CO}$ = 10^7, and FE$_{CO}$: > 90 % under aqueous conditions (phosphate buffer, saturated with CO_2, pH 6).[120]

Glassy Carbon Electrode
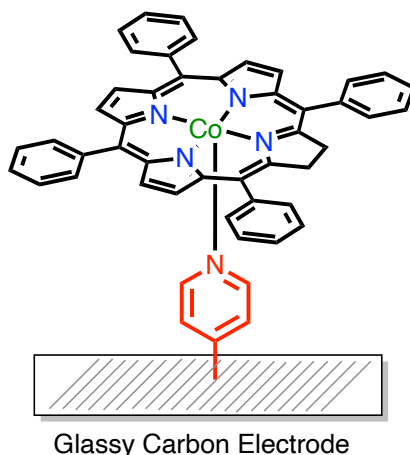
Scheme 1.15. Structures of CO_2 reduction Co catalysts immobilized on electrodes.

Taken together, these results demonstrate that substantial TONs and FE's can be obtained from immobilizing CRR electrocatalysts. As well, the CRR reactions can be carried out under aqueous solvents, which is more compatible with the oxygen evolution reaction as a large-scale source of protons and electrons.

1.10 Research Objectives

According to the literature, the field of solar CO_2 conversion and utilization is too extensive to be addressed by a single project; thus, the research of this dissertation project is focused on the design and synthesis of molecular architectures of selective and efficient systems. Early studies are based on the most common photosensitizer $Ru(bpy)_3^{2+}$, coupled to the most well-studied CRR catalysts, $Re(bpy)(CO)_3Cl$, for benchmarking. The evidence in the literature suggests that supramolecular systems are more efficient for photocatalytic CO_2 reduction, as found in Section 1.4.

Chapter 2 addresses the synthesis and catalytic performance evaluation of the RuRe supramolecular system as a homogeneous photocatalyst. In consideration of the large disconnection between TON obtained from CPE, and TOF obtained from FOWA and the plateau current analysis found in the literature (Section 1.8), the Ru-Re heterogenization is studied as a strategy to overcome this inconsistency. Additionally, the difficulty of synthesizing RuRe in solution, poor solubility, and stability, also led to a stepwise Ru-Re assembly, via diazonium anchorage, on various semiconductor surfaces (GC, NiO, TiO_2) for the photochemical and photoelectrochemical CRR

comparison. This heterogenization aims to increase the TON, avoid the use of a sacrificial electron donor, and may allow for water oxidation to obtain the electrons for CRR, as is explored in Chapter 3.

To emphasize the transition from $Ru(bpy)_3^{2+}$ to Earth-abundant components for CRR, Chapter 3 focuses on developing 4CzIPN derivatives since it has been proven a strong alternative as a photosensitizer. Some examples include imidazole-3CzIPN, imidazolium-3CzIPN and NHC-3CzIPN, followed by the integration to the semiconductor surfaces, specifically (TiO_2). The surface chemistry of the 4CzIPN derivatives, via diazonium, or NHC-H bonding to TiO_2 or polymerization/heterogenization on GC are studied. The photoactivity of NHC-3CzIPN on TiO_2 electrodes is evaluated as well.

The demonstration of the photocatalytic activity of 4CzIPN derivatives on TiO_2 is the first step towards a sustainable solar-driven CRR system. To continue in this direction, the 3CzIPN-imidazole compound is coordinated with the Earth-abundant complex, *fac*-Mn(bpy)(CO)$_3$Br. Chapter 4 describes the synthesis, and homogeneous photocatalytic activity evaluation for CO_2 reduction of 3CzIPN-imidazole-Mn and steady-state and time-resolved photoluminescence for a better understanding of the electron transfer processes.

1.11 References

(1) Statistical Review of World Energy 2022. **2022**.

(2) Brennaman, M. K.; Dillon, R. J.; Alibabaei, L.; Gish, M. K.; Dares, C. J.; Ashford, D. L.; House, R. L.; Meyer, G. J.; Papanikolas, J. M.; Meyer, T. J. Finding the Way to Solar Fuels with Dye-Sensitized Photoelectrosynthesis Cells. *J. Am. Chem. Soc.* **2016**, *138* (40), 13085–13102. https://doi.org/10.1021/jacs.6b06466.

(3) Blankenship, R. E.; Tiede, D. M.; Barber, J.; Brudvig, G. W.; Fleming, G.; Ghirardi, M.; Gunner, M. R.; Junge, W.; Kramer, D. M.; Melis, A.; Moore, T. A.; Moser, C. C.; Nocera, D. G.; Nozik, A. J.; Ort, D. R.; Parson, W. W.; Prince, R. C.; Sayre, R. T. Comparing Photosynthetic and Photovoltaic Efficiencies and Recognizing the Potential for Improvement. *Science* **2011**, *332* (6031), 805–809. https://doi.org/10.1126/science.1200165.

(4) Haegel, N. M.; Verlinden, P.; Victoria, M.; Altermatt, P.; Atwater, H.; Barnes, T.; Breyer, C.; Case, C.; De Wolf, S.; Deline, C.; Dharmrin, M.; Dimmler, B.; Gloeckler, M.; Goldschmidt, J. C.; Hallam, B.; Haussener, S.; Holder, B.; Jaeger, U.; Jaeger-Waldau, A.; Kaizuka, I.; Kikusato, H.;

Kroposki, B.; Kurtz, S.; Matsubara, K.; Nowak, S.; Ogimoto, K.; Peter, C.; Peters, I. M.; Philipps, S.; Powalla, M.; Rau, U.; Reindl, T.; Roumpani, M.; Sakurai, K.; Schorn, C.; Schossig, P.; Schlatmann, R.; Sinton, R.; Slaoui, A.; Smith, B. L.; Schneidewind, P.; Stanbery, B.; Topic, M.; Tumas, W.; Vasi, J.; Vetter, M.; Weber, E.; Weeber, A. W.; Weidlich, A.; Weiss, D.; Bett, A. W. Photovoltaics at Multi-Terawatt Scale: Waiting Is Not an Option. *Science* **2023**, *380* (6640), 39–42. https://doi.org/10.1126/science.adf6957.

(5) Geisz, J. F.; France, R. M.; Schulte, K. L.; Steiner, M. A.; Norman, A. G.; Guthrey, H. L.; Young, M. R.; Song, T.; Moriarty, T. Six-Junction III–V Solar Cells with 47.1% Conversion Efficiency under 143 Suns Concentration. *Nat Energy* **2020**, *5* (4), 326–335. https://doi.org/10.1038/s41560-020-0598-5.

(6) *Best Research-Cell Efficiency Chart*. https://www.nrel.gov/pv/cell-efficiency.html (accessed 2023-05-30).

(7) Polman, A.; Knight, M.; Garnett, E. C.; Ehrler, B.; Sinke, W. C. Photovoltaic Materials: Present Efficiencies and Future Challenges. *Science* **2016**, *352* (6283), aad4424. https://doi.org/10.1126/science.aad4424.

(8) O'Regan, B.; Gratzelt, M. A Low-Cost, High-Efficiency Solar Cell Based on Dye-Sensitized Colloidal Ti02 Films. **1991**, *353*.

(9) Mathew, S.; Yella, A.; Gao, P.; Humphry-Baker, R.; Curchod, B. F. E.; Ashari-Astani, N.; Tavernelli, I.; Rothlisberger, U.; Nazeeruddin, Md. K.; Grätzel, M. Dye-Sensitized Solar Cells with 13% Efficiency Achieved through the Molecular Engineering of Porphyrin Sensitizers. *Nature Chem* **2014**, *6* (3), 242–247. https://doi.org/10.1038/nchem.1861.

(10) *Photovoltaics Report - Fraunhofer ISE*. Fraunhofer Institute for Solar Energy Systems ISE. https://www.ise.fraunhofer.de/en/publications/studies/photovoltaics-report.html (accessed 2023-05-31).

(11) Lewis, N. S. Research Opportunities to Advance Solar Energy Utilization. *Science* **2016**, *351* (6271), aad1920. https://doi.org/10.1126/science.aad1920.

(12) Park, N.-G. Perovskite Solar Cells: An Emerging Photovoltaic Technology. *Materials Today* **2015**, *18* (2), 65–72. https://doi.org/10.1016/j.mattod.2014.07.007.

(13) Cui, Y.; Yao, H.; Zhang, J.; Zhang, T.; Wang, Y.; Hong, L.; Xian, K.; Xu, B.; Zhang, S.; Peng, J.; Wei, Z.; Gao, F.; Hou, J. Over 16% Efficiency Organic Photovoltaic Cells Enabled by a Chlorinated Acceptor with Increased Open-Circuit Voltages. *Nat Commun* **2019**, *10* (1), 2515. https://doi.org/10.1038/s41467-019-10351-5.

(14) Meng, L.; Zhang, Y.; Wan, X.; Li, C.; Zhang, X.; Wang, Y.; Ke, X.; Xiao, Z.; Ding, L.; Xia, R.; Yip, H.-L.; Cao, Y.; Chen, Y. Organic and Solution-Processed Tandem Solar Cells with 17.3% Efficiency. *Science* **2018**, *361* (6407), 1094–1098. https://doi.org/10.1126/science.aat2612.

(15) Zhang, G.; Zhao, J.; Chow, P. C. Y.; Jiang, K.; Zhang, J.; Zhu, Z.; Zhang, J.; Huang, F.; Yan, H. Nonfullerene Acceptor Molecules for Bulk Heterojunction Organic Solar Cells. *Chem. Rev.* **2018**, *118* (7), 3447–3507. https://doi.org/10.1021/acs.chemrev.7b00535.

(16) Lu, L.; Zheng, T.; Wu, Q.; Schneider, A. M.; Zhao, D.; Yu, L. Recent Advances in Bulk Heterojunction Polymer Solar Cells. *Chem. Rev.* **2015**, *115* (23), 12666–12731. https://doi.org/10.1021/acs.chemrev.5b00098.

(17) Lee, C.; Lee, S.; Kim, G.-U.; Lee, W.; Kim, B. J. Recent Advances, Design Guidelines, and Prospects of All-Polymer Solar Cells. *Chem. Rev.* **2019**, *119* (13), 8028–8086. https://doi.org/10.1021/acs.chemrev.9b00044.

(18) Chen, L. X. Organic Solar Cells: Recent Progress and Challenges. *ACS Energy Lett.* **2019**, *4* (10), 2537–2539. https://doi.org/10.1021/acsenergylett.9b02071.

(19) Yao, H.; Bai, F.; Hu, H.; Arunagiri, L.; Zhang, J.; Chen, Y.; Yu, H.; Chen, S.; Liu, T.; Lai, J. Y. L.; Zou, Y.; Ade, H.; Yan, H. Efficient All-Polymer Solar Cells Based on a New Polymer Acceptor Achieving 10.3% Power Conversion Efficiency. *ACS Energy Lett.* **2019**, *4* (2), 417–422. https://doi.org/10.1021/acsenergylett.8b02114.

(20) Gibson, T. L.; Kelly, N. A. Solar Photovoltaic Charging of Lithium-Ion Batteries. *Journal of Power Sources* **2010**, *195* (12), 3928–3932. https://doi.org/10.1016/j.jpowsour.2009.12.082.

(21) Tian, Z.; Sun, Z.; Shao, Y.; Gao, L.; Huang, R.; Shao, Y.; Kaner, R. B.; Sun, J. Ultrafast Rechargeable Zn Micro-Batteries Endowing a Wearable Solar Charging System with High Overall Efficiency. *Energy Environ. Sci.* **2021**, *14* (3), 1602–1611. https://doi.org/10.1039/D0EE03623D.

(22) Lv, J.; Abbas, S. C.; Huang, Y.; Liu, Q.; Wu, M.; Wang, Y.; Dai, L. A Photo-Responsive Bifunctional Electrocatalyst for Oxygen Reduction and Evolution Reactions. *Nano Energy* **2018**, *43*, 130–137. https://doi.org/10.1016/j.nanoen.2017.11.020.

(23) *Solar thermal power plants - U.S. Energy Information Administration (EIA)*. https://www.eia.gov/energyexplained/solar/solar-thermal-power-plants.php (accessed 2023-07-10).

(24) *HTST: High-Temperature Solar Thermal*. Solar Power Authority. https://www.solarpowerauthority.com/high-temperature-solar-thermal/ (accessed 2023-06-05).

(25) *Renewable heat consumption, 2007-2024 – Charts – Data & Statistics*. IEA. https://www.iea.org/data-and-statistics/charts/renewable-heat-consumption-2007-2024 (accessed 2023-06-05).

(26) Wang, Q.; Domen, K. Particulate Photocatalysts for Light-Driven Water Splitting: Mechanisms, Challenges, and Design Strategies. *Chem. Rev.* **2020**, *120* (2), 919–985. https://doi.org/10.1021/acs.chemrev.9b00201.

(27) Francke, R.; Schille, B.; Roemelt, M. Homogeneously Catalyzed Electroreduction of Carbon Dioxide—Methods, Mechanisms, and Catalysts. *Chem. Rev.* **2018**, *118* (9), 4631–4701. https://doi.org/10.1021/acs.chemrev.7b00459.

(28) Nishioka, S.; Osterloh, F. E.; Wang, X.; Mallouk, T. E.; Maeda, K. Photocatalytic Water Splitting. *Nat Rev Methods Primers* **2023**, *3* (1), 42. https://doi.org/10.1038/s43586-023-00226-x.

(29) Dalle, K. E.; Warnan, J.; Leung, J. J.; Reuillard, B.; Karmel, I. S.; Reisner, E. Electro- and Solar-Driven Fuel Synthesis with First Row Transition Metal Complexes. *Chem. Rev.* **2019**, *119* (4), 2752–2875. https://doi.org/10.1021/acs.chemrev.8b00392.

(30) Matheu, R.; Ertem, M. Z.; Gimbert-Suriñach, C.; Sala, X.; Llobet, A. Seven Coordinated Molecular Ruthenium–Water Oxidation Catalysts: A Coordination Chemistry Journey: Focus Review. *Chem. Rev.* **2019**, *119* (6), 3453–3471. https://doi.org/10.1021/acs.chemrev.8b00537.

(31) Wang, Y.; Suzuki, H.; Xie, J.; Tomita, O.; Martin, D. J.; Higashi, M.; Kong, D.; Abe, R.; Tang, J. Mimicking Natural Photosynthesis: Solar to Renewable H $_2$ Fuel Synthesis by Z-Scheme Water Splitting Systems. *Chem. Rev.* **2018**, *118* (10), 5201–5241. https://doi.org/10.1021/acs.chemrev.7b00286.

(32) Brereton, K. R.; Bonn, A. G.; Miller, A. J. M. Molecular Photoelectrocatalysts for Light-Driven Hydrogen Production. *ACS Energy Lett.* **2018**, *3* (5), 1128–1136. https://doi.org/10.1021/acsenergylett.8b00255.

(33) Blakemore, J. D.; Crabtree, R. H.; Brudvig, G. W. Molecular Catalysts for Water Oxidation. *Chem. Rev.* **2015**, *115* (23), 12974–13005. https://doi.org/10.1021/acs.chemrev.5b00122.

(34) Kärkäs, M. D.; Verho, O.; Johnston, E. V.; Åkermark, B. Artificial Photosynthesis: Molecular Systems for Catalytic Water Oxidation. *Chem. Rev.* **2014**, *114* (24), 11863–12001. https://doi.org/10.1021/cr400572f.

(35) Sala, X.; Romero, I.; Rodríguez, M.; Escriche, L.; Llobet, A. Molecular Catalysts That Oxidize Water to Dioxygen. *Angewandte Chemie International Edition* **2009**, *48* (16), 2842–2852. https://doi.org/10.1002/anie.200802659.

(36) Gersten, S. W.; Samuels, G. J.; Meyer, T. J. Catalytic Oxidation of Water by an Oxo-Bridged Ruthenium Dimer. *J. Am. Chem. Soc.* **1982**, *104* (14), 4029–4030. https://doi.org/10.1021/ja00378a053.

(37) Kumar, M.; Meena, B.; Subramanyam, P.; Suryakala, D.; Subrahmanyam, C. Recent Trends in Photoelectrochemical Water Splitting: The Role of Cocatalysts. *NPG Asia Mater* **2022**, *14* (1), 88. https://doi.org/10.1038/s41427-022-00436-x.

(38) Marwat, M. A.; Humayun, M.; Afridi, M. W.; Zhang, H.; Abdul Karim, M. R.; Ashtar, M.; Usman, M.; Waqar, S.; Ullah, H.; Wang, C.; Luo, W. Advanced Catalysts for Photoelectrochemical Water Splitting. *ACS Appl. Energy Mater.* **2021**, *4* (11), 12007–12031. https://doi.org/10.1021/acsaem.1c02548.

(39) Kang, D.; Kim, T. W.; Kubota, S. R.; Cardiel, A. C.; Cha, H. G.; Choi, K.-S. Electrochemical Synthesis of Photoelectrodes and Catalysts for Use in Solar Water Splitting. *Chem. Rev.* **2015**, *115* (23), 12839–12887. https://doi.org/10.1021/acs.chemrev.5b00498.

(40) Walter, M. G.; Warren, E. L.; McKone, J. R.; Boettcher, S. W.; Mi, Q.; Santori, E. A.; Lewis, N. S. Solar Water Splitting Cells. *Chem. Rev.* **2010**, *110* (11), 6446–6473. https://doi.org/10.1021/cr1002326.

(41) Concepcion, J. J.; Zhong, D. K.; Szalda, D. J.; Muckerman, J. T.; Fujita, E. Mechanism of Water Oxidation by [Ru(Bda)(L) $_2$]: The Return of the "Blue Dimer." *Chem. Commun.* **2015**, *51* (19), 4105–4108. https://doi.org/10.1039/C4CC07968J.

(42) Yi, J.; Zhan, S.; Chen, L.; Tian, Q.; Wang, N.; Li, J.; Xu, W.; Zhang, B.; Ahlquist, M. S. G. Electrostatic Interactions Accelerating Water Oxidation Catalysis via Intercatalyst O–O Coupling. *J. Am. Chem. Soc.* **2021**, *143* (6), 2484–2490. https://doi.org/10.1021/jacs.0c07103.

(43) Okamura, M.; Kondo, M.; Kuga, R.; Kurashige, Y.; Yanai, T.; Hayami, S.; Praneeth, V. K. K.; Yoshida, M.; Yoneda, K.; Kawata, S.; Masaoka, S. A Pentanuclear Iron Catalyst Designed for Water Oxidation. *Nature* **2016**, *530* (7591), 465–468. https://doi.org/10.1038/nature16529.

(44) Takanabe, K. Photocatalytic Water Splitting: Quantitative Approaches toward Photocatalyst by Design. *ACS Catal.* **2017**, *7* (11), 8006–8022. https://doi.org/10.1021/acscatal.7b02662.

(45) Liu, J.; Liu, Y.; Liu, N.; Han, Y.; Zhang, X.; Huang, H.; Lifshitz, Y.; Lee, S.-T.; Zhong, J.; Kang, Z. Metal-Free Efficient Photocatalyst for Stable Visible Water Splitting via a Two-Electron Pathway. *Science* **2015**, *347* (6225), 970–974. https://doi.org/10.1126/science.aaa3145.

(46) Balzani, V.; Credi, A.; Venturi, M. Photochemical Conversion of Solar Energy. *ChemSusChem* **2008**, *1* (1–2), 26–58. https://doi.org/10.1002/cssc.200700087.

(47) Kumagai, H.; Tamaki, Y.; Ishitani, O. Photocatalytic Systems for CO $_2$ Reduction: Metal-Complex Photocatalysts and Their Hybrids with Photofunctional Solid Materials. *Acc. Chem. Res.* **2022**, *55* (7), 978–990. https://doi.org/10.1021/acs.accounts.1c00705.

(48) Tamaki, Y.; Ishitani, O. Supramolecular Photocatalysts for the Reduction of CO $_2$. *ACS Catal.* **2017**, *7* (5), 3394–3409. https://doi.org/10.1021/acscatal.7b00440.

(49) Kuramochi, Y.; Ishitani, O.; Ishida, H. Reaction Mechanisms of Catalytic Photochemical CO2 Reduction Using Re(I) and Ru(II) Complexes. *Coordination Chemistry Reviews* **2018**, *373*, 333–356. https://doi.org/10.1016/j.ccr.2017.11.023.

(50) Yamazaki, Y.; Takeda, H.; Ishitani, O. Photocatalytic Reduction of CO2 Using Metal Complexes. *Journal of Photochemistry and Photobiology C: Photochemistry Reviews* **2015**, *25*, 106–137. https://doi.org/10.1016/j.jphotochemrev.2015.09.001.

(51) Gholamkhass, B.; Mametsuka, H.; Koike, K.; Tanabe, T.; Furue, M.; Ishitani, O. Architecture of Supramolecular Metal Complexes for Photocatalytic CO $_2$ Reduction: Ruthenium−Rhenium Bi- and Tetranuclear Complexes. *Inorg. Chem.* **2005**, *44* (7), 2326–2336. https://doi.org/10.1021/ic048779r.

(52) Koike, K.; Naito, S.; Sato, S.; Tamaki, Y.; Ishitani, O. Architecture of Supramolecular Metal Complexes for Photocatalytic CO2 Reduction. *Journal of Photochemistry and Photobiology A: Chemistry* **2009**, *207* (1), 109–114. https://doi.org/10.1016/j.jphotochem.2008.12.014.

(53) Fabry, D. C.; Koizumi, H.; Ghosh, D.; Yamazaki, Y.; Takeda, H.; Tamaki, Y.; Ishitani, O. A Ru(II)–Mn(I) Supramolecular Photocatalyst for CO_2 Reduction. *Organometallics* **2020**, *39* (9), 1511–1518. https://doi.org/10.1021/acs.organomet.9b00755.

(54) Roger, I.; Shipman, M. A.; Symes, M. D. Earth-Abundant Catalysts for Electrochemical and Photoelectrochemical Water Splitting. *Nat Rev Chem* **2017**, *1* (1), 0003. https://doi.org/10.1038/s41570-016-0003.

(55) Takeda, H.; Kamiyama, H.; Okamoto, K.; Irimajiri, M.; Mizutani, T.; Koike, K.; Sekine, A.; Ishitani, O. Highly Efficient and Robust Photocatalytic Systems for CO_2 Reduction Consisting of a Cu(I) Photosensitizer and Mn(I) Catalysts. *J. Am. Chem. Soc.* **2018**, *140* (49), 17241–17254. https://doi.org/10.1021/jacs.8b10619.

(56) Fujishima, A.; Honda, K. Electrochemical Photolysis of Water at a Semiconductor Electrode. *Nature* **1972**, *238* (5358), 37–38. https://doi.org/10.1038/238037a0.

(57) Nandal, N.; Jain, S. L. A Review on Progress and Perspective of Molecular Catalysis in Photoelectrochemical Reduction of CO2. *Coordination Chemistry Reviews* **2022**, *451*, 214271. https://doi.org/10.1016/j.ccr.2021.214271.

(58) Tang, B.; Xiao, F.-X. An Overview of Solar-Driven Photoelectrochemical CO_2 Conversion to Chemical Fuels. *ACS Catal.* **2022**, *12* (15), 9023–9057. https://doi.org/10.1021/acscatal.2c01667.

(59) Castro, S.; Albo, J.; Irabien, A. Photoelectrochemical Reactors for CO_2 Utilization. *ACS Sustainable Chem. Eng.* **2018**, *6* (12), 15877–15894. https://doi.org/10.1021/acssuschemeng.8b03706.

(60) Sahara, G.; Abe, R.; Higashi, M.; Morikawa, T.; Maeda, K.; Ueda, Y.; Ishitani, O. Photoelectrochemical CO_2 Reduction Using a Ru(II)–Re(I) Multinuclear Metal Complex on a p-Type Semiconducting NiO Electrode. *Chem. Commun.* **2015**, *51* (53), 10722–10725. https://doi.org/10.1039/C5CC02403J.

(61) Li, T.-T.; Shan, B.; Meyer, T. J. Stable Molecular Photocathode for Solar-Driven CO_2 Reduction in Aqueous Solutions. *ACS Energy Lett.* **2019**, *4* (3), 629–636. https://doi.org/10.1021/acsenergylett.8b02512.

(62) Chen, Z.; Chen, C.; Weinberg, D. R.; Kang, P.; Concepcion, J. J.; Harrison, D. P.; Brookhart, M. S.; Meyer, T. J. Electrocatalytic Reduction of CO2 to CO by Polypyridyl Ruthenium Complexes. *Chem. Commun.* **2011**, *47* (47), 12607. https://doi.org/10.1039/c1cc15071e.

(63) Kuramochi, Y.; Ishitani, O. Iridium(III) 1-Phenylisoquinoline Complexes as a Photosensitizer for Photocatalytic CO_2 Reduction: A Mixed System with a Re(I) Catalyst and a Supramolecular

Photocatalyst. *Inorg. Chem.* **2016**, *55* (11), 5702–5709. https://doi.org/10.1021/acs.inorgchem.6b00777.

(64) Kuramochi, Y.; Kamiya, M.; Ishida, H. Photocatalytic CO $_2$ Reduction in *N* , *N* - Dimethylacetamide/Water as an Alternative Solvent System. *Inorg. Chem.* **2014**, *53* (7), 3326– 3332. https://doi.org/10.1021/ic500050q.

(65) Tamaki, Y.; Morimoto, T.; Koike, K.; Ishitani, O. Photocatalytic CO $_2$ Reduction with High Turnover Frequency and Selectivity of Formic Acid Formation Using Ru(II) Multinuclear Complexes. *Proc. Natl. Acad. Sci. U.S.A.* **2012**, *109* (39), 15673–15678. https://doi.org/10.1073/pnas.1118336109.

(66) Ashford, D. L.; Song, W.; Concepcion, J. J.; Glasson, C. R. K.; Brennaman, M. K.; Norris, M. R.; Fang, Z.; Templeton, J. L.; Meyer, T. J. Photoinduced Electron Transfer in a Chromophore– Catalyst Assembly Anchored to TiO $_2$. *J. Am. Chem. Soc.* **2012**, *134* (46), 19189–19198. https://doi.org/10.1021/ja3084362.

(67) Yoshitomi, F.; Sekizawa, K.; Maeda, K.; Ishitani, O. Selective Formic Acid Production via CO $_2$ Reduction with Visible Light Using a Hybrid of a Perovskite Tantalum Oxynitride and a Binuclear Ruthenium(II) Complex. *ACS Appl. Mater. Interfaces* **2015**, *7* (23), 13092–13097. https://doi.org/10.1021/acsami.5b03509.

(68) Juris, A.; Balzani, V.; Barigelletti, F.; Campagna, S.; Belser, P.; Zelewsky, A. V. COMPLEXES: PHOTOPI3YSICS, ELECl?ROCHEMISTRY, SCENCE.

(69) Lemercier, G.; Bonne, A.; Four, M.; Lawson-Daku, L. M. 3MLCT Excited States in Ru(II) Complexes: Reactivity and Related Two-Photon Absorption Applications in the near-Infrared Spectral Range. *Comptes Rendus Chimie* **2008**, *11* (6–7), 709–715. https://doi.org/10.1016/j.crci.2007.11.012.

(70) Thompson, D. W.; Ito, A.; Meyer, T. J. [Ru(Bpy)3]2+* and Other Remarkable Metal-to-Ligand Charge Transfer (MLCT) Excited States. *Pure and Applied Chemistry* **2013**, *85* (7), 1257–1305. https://doi.org/10.1351/PAC-CON-13-03-04.

(71) Lumpkin, R. S.; Kober, E. M.; Worl, L. A.; Murtaza, Zakir.; Meyer, T. J. Metal-to-Ligand Charge-Transfer (MLCT) Photochemistry: Experimental Evidence for the Participation of a Higher Lying MLCT State in Polypyridyl Complexes of Ruthenium(II) and Osmium(II). *J. Phys. Chem.* **1990**, *94* (1), 239–243. https://doi.org/10.1021/j100364a039.

(72) Leung, C.-F.; Lau, T.-C. Organic Photosensitizers for Catalytic Solar Fuel Generation. *Energy Fuels* **2021**, *35* (23), 18888–18899. https://doi.org/10.1021/acs.energyfuels.1c02675.

(73) Du, Y.; Pearson, R. M.; Lim, C.; Sartor, S. M.; Ryan, M. D.; Yang, H.; Damrauer, N. H.; Miyake, G. M. Strongly Reducing, Visible-Light Organic Photoredox Catalysts as Sustainable Alternatives to Precious Metals. *Chemistry A European J* **2017**, *23* (46), 10962–10968. https://doi.org/10.1002/chem.201702926.

(74) Rybicka-Jasińska, K.; Shan, W.; Zawada, K.; Kadish, K. M.; Gryko, D. Porphyrins as Photoredox Catalysts: Experimental and Theoretical Studies. *J. Am. Chem. Soc.* **2016**, *138* (47), 15451–15458. https://doi.org/10.1021/jacs.6b09036.

(75) Shang, T.-Y.; Lu, L.-H.; Cao, Z.; Liu, Y.; He, W.-M.; Yu, B. Recent Advances of 1,2,3,5-Tetrakis(Carbazol-9-Yl)-4,6-Dicyanobenzene (4CzIPN) in Photocatalytic Transformations. *Chem. Commun.* **2019**, *55* (38), 5408–5419. https://doi.org/10.1039/C9CC01047E.

(76) Poelma, S. O.; Burnett, G. L.; Discekici, E. H.; Mattson, K. M.; Treat, N. J.; Luo, Y.; Hudson, Z. M.; Shankel, S. L.; Clark, P. G.; Kramer, J. W.; Hawker, C. J.; Read De Alaniz, J. Chemoselective Radical Dehalogenation and C–C Bond Formation on Aryl Halide Substrates Using Organic Photoredox Catalysts. *J. Org. Chem.* **2016**, *81* (16), 7155–7160. https://doi.org/10.1021/acs.joc.6b01034.

(77) Luo, J.; Zhang, J. Donor–Acceptor Fluorophores for Visible-Light-Promoted Organic Synthesis: Photoredox/Ni Dual Catalytic C(Sp^3)–C(Sp^2) Cross-Coupling. *ACS Catal.* **2016**, *6* (2), 873–877. https://doi.org/10.1021/acscatal.5b02204.

(78) Uoyama, H.; Goushi, K.; Shizu, K.; Nomura, H.; Adachi, C. Highly Efficient Organic Light-Emitting Diodes from Delayed Fluorescence. *Nature* **2012**, *492* (7428), 234–238. https://doi.org/10.1038/nature11687.

(79) Speckmeier, E.; Fischer, T. G.; Zeitler, K. A Toolbox Approach To Construct Broadly Applicable Metal-Free Catalysts for Photoredox Chemistry: Deliberate Tuning of Redox Potentials and Importance of Halogens in Donor–Acceptor Cyanoarenes. *J. Am. Chem. Soc.* **2018**, *140* (45), 15353–15365. https://doi.org/10.1021/jacs.8b08933.

(80) Karakaya, I.; Primer, D. N.; Molander, G. A. Photoredox Cross-Coupling: Ir/Ni Dual Catalysis for the Synthesis of Benzylic Ethers. *Org. Lett.* **2015**, *17* (13), 3294–3297. https://doi.org/10.1021/acs.orglett.5b01463.

(81) Meng, Q.-Y.; Wang, S.; Huff, G. S.; König, B. Ligand-Controlled Regioselective Hydrocarboxylation of Styrenes with CO_2 by Combining Visible Light and Nickel Catalysis. *J. Am. Chem. Soc.* **2018**, *140* (9), 3198–3201. https://doi.org/10.1021/jacs.7b13448.

(82) Choi, J.; Martín-Gago, P.; Fu, G. C. Stereoconvergent Arylations and Alkenylations of Unactivated Alkyl Electrophiles: Catalytic Enantioselective Synthesis of Secondary Sulfonamides and Sulfones. *J. Am. Chem. Soc.* **2014**, *136* (34), 12161–12165. https://doi.org/10.1021/ja506885s.

(83) Seo, H.; Liu, A.; Jamison, T. F. Direct β-Selective Hydrocarboxylation of Styrenes with CO_2 Enabled by Continuous Flow Photoredox Catalysis. *J. Am. Chem. Soc.* **2017**, *139* (40), 13969–13972. https://doi.org/10.1021/jacs.7b05942.

(84) Wang, Y.; Gao, X.-W.; Li, J.; Chao, D. Merging an Organic TADF Photosensitizer and a Simple Terpyridine–Fe(III) Complex for Photocatalytic CO_2 Reduction. *Chem. Commun.* **2020**, *56* (81), 12170–12173. https://doi.org/10.1039/D0CC05047D.

(85) Ponnada, S.; Kiai, M. S.; Gorle, D. B.; Nowduri, A.; Sharma, R. K. Insight into the Role and Strategies of Metal–Organic Frameworks in Direct Methanol Fuel Cells: A Review. *Energy Fuels* **2021**, *35* (19), 15265–15284. https://doi.org/10.1021/acs.energyfuels.1c02010.

(86) Grice, K. A.; Kubiak, C. P. Recent Studies of Rhenium and Manganese Bipyridine Carbonyl Catalysts for the Electrochemical Reduction of CO2. In *Advances in Inorganic Chemistry*; Elsevier, 2014; Vol. 66, pp 163–188. https://doi.org/10.1016/B978-0-12-420221-4.00005-6.

(87) Moura De Salles Pupo, M.; Kortlever, R. Electrolyte Effects on the Electrochemical Reduction of CO_2. *ChemPhysChem* **2019**, *20* (22), 2926–2935. https://doi.org/10.1002/cphc.201900680.

(88) Lucile, F.; Cézac, P.; Contamine, F.; Serin, J.-P.; Houssin, D.; Arpentinier, P. Solubility of Carbon Dioxide in Water and Aqueous Solution Containing Sodium Hydroxide at Temperatures from (293.15 to 393.15) K and Pressure up to 5 MPa: Experimental Measurements. *J. Chem. Eng. Data* **2012**, *57* (3), 784–789. https://doi.org/10.1021/je200991x.

(89) König, M.; Vaes, J.; Klemm, E.; Pant, D. Solvents and Supporting Electrolytes in the Electrocatalytic Reduction of CO2. *iScience* **2019**, *19*, 135–160. https://doi.org/10.1016/j.isci.2019.07.014.

(90) Costentin, C.; Drouet, S.; Passard, G.; Robert, M.; Savéant, J.-M. Proton-Coupled Electron Transfer Cleavage of Heavy-Atom Bonds in Electrocatalytic Processes. Cleavage of a C–O Bond in the Catalyzed Electrochemical Reduction of CO_2. *J. Am. Chem. Soc.* **2013**, *135* (24), 9023–9031. https://doi.org/10.1021/ja4030148.

(91) Costentin, C.; Savéant, J. Multielectron, Multistep Molecular Catalysis of Electrochemical Reactions: Benchmarking of Homogeneous Catalysts. *ChemElectroChem* **2014**, *1* (7), 1226–1236. https://doi.org/10.1002/celc.201300263.

(92) Mukherjee, J.; Siewert, I. Manganese and Rhenium Tricarbonyl Complexes Equipped with Proton Relays in the Electrochemical CO_2 Reduction Reaction. *Eur. J. Inorg. Chem.* **2020**, *2020* (46), 4319–4333. https://doi.org/10.1002/ejic.202000738.

(93) Hawecker, J.; Lehn, J.-M.; Ziessel, R. Electrocatalytic Reduction of Carbon Dioxide Mediated by Re(Bipy)(CO)&I (Bipy = 2,2'-Bipyridine).

(94) Guyot, M.; Lalloz, M.-N.; Aguirre-Araque, J. S.; Rogez, G.; Costentin, C.; Chardon-Noblat, S. Rhenium Carbonyl Molecular Catalysts for CO_2 Electroreduction: Effects on Catalysis of Bipyridine Substituents Mimicking Anchorage Functions to Modify Electrodes. *Inorg. Chem.* **2022**, *61* (40), 16072–16080. https://doi.org/10.1021/acs.inorgchem.2c02473.

(95) Clark, M. L.; Cheung, P. L.; Lessio, M.; Carter, E. A.; Kubiak, C. P. Kinetic and Mechanistic Effects of Bipyridine (Bpy) Substituent, Labile Ligand, and Brønsted Acid on Electrocatalytic CO_2 Reduction by Re(Bpy) Complexes. *ACS Catal.* **2018**, *8* (3), 2021–2029. https://doi.org/10.1021/acscatal.7b03971.

(96) Talukdar, K.; Sinha Roy, S.; Amatya, E.; Sleeper, E. A.; Le Magueres, P.; Jurss, J. W. Enhanced Electrochemical CO_2 Reduction by a Series of Molecular Rhenium Catalysts Decorated with

Second-Sphere Hydrogen-Bond Donors. *Inorg. Chem.* **2020**, *59* (9), 6087–6099. https://doi.org/10.1021/acs.inorgchem.0c00154.

(97) Riplinger, C.; Sampson, M. D.; Ritzmann, A. M.; Kubiak, C. P.; Carter, E. A. Mechanistic Contrasts between Manganese and Rhenium Bipyridine Electrocatalysts for the Reduction of Carbon Dioxide. *J. Am. Chem. Soc.* **2014**, *136* (46), 16285–16298. https://doi.org/10.1021/ja508192y.

(98) Vakula, N. I.; Kuramshina, G. M.; Makhmutova, S. F.; Pentin, Yu. A. DFT Theoretical Studies of Anions of Aniline and Its Several Derivatives. *Struct Chem* **2011**, *22* (2), 345–356. https://doi.org/10.1007/s11224-010-9724-5.

(99) Portenkirchner, E.; Oppelt, K.; Ulbricht, C.; Egbe, D. A. M.; Neugebauer, H.; Knör, G.; Sariciftci, N. S. Electrocatalytic and Photocatalytic Reduction of Carbon Dioxide to Carbon Monoxide Using the Alkynyl-Substituted Rhenium(I) Complex (5,5′-Bisphenylethynyl-2,2′-Bipyridyl)Re(CO)3Cl. *Journal of Organometallic Chemistry* **2012**, *716*, 19–25. https://doi.org/10.1016/j.jorganchem.2012.05.021.

(100) Portenkirchner, E.; Gasiorowski, J.; Oppelt, K.; Schlager, S.; Schwarzinger, C.; Neugebauer, H.; Knör, G.; Sariciftci, N. S. Electrocatalytic Reduction of Carbon Dioxide to Carbon Monoxide by a Polymerized Film of an Alkynyl-Substituted Rhenium(I) Complex. *ChemCatChem* **2013**, *5* (7), 1790–1796. https://doi.org/10.1002/cctc.201200904.

(101) Liang, Y.; Nguyen, M. T.; Holliday, B. J.; Jones, R. A. Electrocatalytic Reduction of CO2 Using Rhenium Complexes with Dipyrido[3,2-a:2′,3′-c]Phenazine Ligands. *Inorganic Chemistry Communications* **2017**, *84*, 113–117. https://doi.org/10.1016/j.inoche.2017.08.002.

(102) Takeda, H.; Cometto, C.; Ishitani, O.; Robert, M. Electrons, Photons, Protons and Earth-Abundant Metal Complexes for Molecular Catalysis of CO$_2$ Reduction. *ACS Catal.* **2017**, *7* (1), 70–88. https://doi.org/10.1021/acscatal.6b02181.

(103) Bizzarri, C. Homogeneous Systems Containing Earth-Abundant Metal Complexes for Photoactivated CO$_2$ Reduction: Recent Advances. *European J Organic Chem* **2022**, *2022* (24). https://doi.org/10.1002/ejoc.202200185.

(104) Bourrez, M.; Molton, F.; Chardon-Noblat, S.; Deronzier, A. [Mn(Bipyridyl)(CO)3Br]: An Abundant Metal Carbonyl Complex as Efficient Electrocatalyst for CO2 Reduction. *Angew. Chem. Int. Ed.* **2011**, *50* (42), 9903–9906. https://doi.org/10.1002/anie.201103616.

(105) Smieja, J. M.; Sampson, M. D.; Grice, K. A.; Benson, E. E.; Froehlich, J. D.; Kubiak, C. P. Manganese as a Substitute for Rhenium in CO$_2$ Reduction Catalysts: The Importance of Acids. *Inorg. Chem.* **2013**, *52* (5), 2484–2491. https://doi.org/10.1021/ic302391u.

(106) Agarwal, J.; Shaw, T. W.; Schaefer, H. F.; Bocarsly, A. B. Design of a Catalytic Active Site for Electrochemical CO$_2$ Reduction with Mn(I)-Tricarbonyl Species. *Inorg. Chem.* **2015**, *54* (11), 5285–5294. https://doi.org/10.1021/acs.inorgchem.5b00233.

(107) Sampson, M. D.; Nguyen, A. D.; Grice, K. A.; Moore, C. E.; Rheingold, A. L.; Kubiak, C. P. Manganese Catalysts with Bulky Bipyridine Ligands for the Electrocatalytic Reduction of

Carbon Dioxide: Eliminating Dimerization and Altering Catalysis. *J. Am. Chem. Soc.* **2014**, *136* (14), 5460–5471. https://doi.org/10.1021/ja501252f.

(108) Sampson, M. D.; Kubiak, C. P. Manganese Electrocatalysts with Bulky Bipyridine Ligands: Utilizing Lewis Acids To Promote Carbon Dioxide Reduction at Low Overpotentials. *J. Am. Chem. Soc.* **2016**, *138* (4), 1386–1393. https://doi.org/10.1021/jacs.5b12215.

(109) Rønne, M. H.; Cho, D.; Madsen, M. R.; Jakobsen, J. B.; Eom, S.; Escoudé, É.; Hammershøj, H. C. D.; Nielsen, D. U.; Pedersen, S. U.; Baik, M.-H.; Skrydstrup, T.; Daasbjerg, K. Ligand-Controlled Product Selectivity in Electrochemical Carbon Dioxide Reduction Using Manganese Bipyridine Catalysts. *J. Am. Chem. Soc.* **2020**, *142* (9), 4265–4275. https://doi.org/10.1021/jacs.9b11806.

(110) Grills, D. C.; Ertem, M. Z.; McKinnon, M.; Ngo, K. T.; Rochford, J. Mechanistic Aspects of CO2 Reduction Catalysis with Manganese-Based Molecular Catalysts. *Coordination Chemistry Reviews* **2018**, *374*, 173–217. https://doi.org/10.1016/j.ccr.2018.05.022.

(111) Agarwal, J.; Fujita, E.; Schaefer, H. F.; Muckerman, J. T. Mechanisms for CO Production from CO_2 Using Reduced Rhenium Tricarbonyl Catalysts. *J. Am. Chem. Soc.* **2012**, *134* (11), 5180–5186. https://doi.org/10.1021/ja2105834.

(112) Agarwal, J.; Johnson, R. P.; Li, G. Reduction of CO_2 on a Tricarbonyl Rhenium(I) Complex: Modeling a Catalytic Cycle. *J. Phys. Chem. A* **2011**, *115* (13), 2877–2881. https://doi.org/10.1021/jp111342r.

(113) Grills, D. C.; Farrington, J. A.; Layne, B. H.; Lymar, S. V.; Mello, B. A.; Preses, J. M.; Wishart, J. F. Mechanism of the Formation of a Mn-Based CO_2 Reduction Catalyst Revealed by Pulse Radiolysis with Time-Resolved Infrared Detection. *J. Am. Chem. Soc.* **2014**, *136* (15), 5563–5566. https://doi.org/10.1021/ja501051s.

(114) Zhou, X.; Micheroni, D.; Lin, Z.; Poon, C.; Li, Z.; Lin, W. Graphene-Immobilized *Fac*-Re(Bipy)(CO)$_3$Cl for Syngas Generation from Carbon Dioxide. *ACS Appl. Mater. Interfaces* **2016**, *8* (6), 4192–4198. https://doi.org/10.1021/acsami.5b11958.

(115) Bullock, R. M.; Das, A. K.; Appel, A. M. Surface Immobilization of Molecular Electrocatalysts for Energy Conversion. *Chem. Eur. J.* **2017**, *23* (32), 7626–7641. https://doi.org/10.1002/chem.201605066.

(116) Orchanian, N. M.; Hong, L. E.; Skrainka, J. A.; Esterhuizen, J. A.; Popov, D. A.; Marinescu, S. C. Surface-Immobilized Conjugated Polymers Incorporating Rhenium Bipyridine Motifs for Electrocatalytic and Photocatalytic CO_2 Reduction. *ACS Appl. Energy Mater.* **2019**, *2* (1), 110–123. https://doi.org/10.1021/acsaem.8b01745.

(117) Oh, S.; Gallagher, J. R.; Miller, J. T.; Surendranath, Y. Graphite-Conjugated Rhenium Catalysts for Carbon Dioxide Reduction. *J. Am. Chem. Soc.* **2016**, *138* (6), 1820–1823. https://doi.org/10.1021/jacs.5b13080.

(118) Walsh, J. J.; Neri, G.; Smith, C. L.; Cowan, A. J. Electrocatalytic CO $_2$ Reduction with a Membrane Supported Manganese Catalyst in Aqueous Solution. *Chem. Commun.* **2014**, *50* (84), 12698–12701. https://doi.org/10.1039/C4CC06404F.

(119) Reuillard, B.; Ly, K. H.; Rosser, T. E.; Kuehnel, M. F.; Zebger, I.; Reisner, E. Tuning Product Selectivity for Aqueous CO $_2$ Reduction with a Mn(Bipyridine)-Pyrene Catalyst Immobilized on a Carbon Nanotube Electrode. *J. Am. Chem. Soc.* **2017**, *139* (41), 14425–14435. https://doi.org/10.1021/jacs.7b06269.

(120) Atoguchi, T.; Aramata, A.; Kazusaka, A.; Enyo, M. Electrocatalytic Activity of Co II TPP-Pyridine Complex Modified Carbon Electrode for CO2 Reduction. *1991 318*, 309–320.

Chapter 2

Solid-Phase Synthesis and Photoactivity of Ru-Polypyridyl Visible Light Chromophores and RuRe Photocatalyst Bonded through Carbon to Semiconductor Surfaces[1]

2.1 Introduction

Anthropogenic climate change is the greatest challenge faced by our society.[1] Intense, worldwide efforts are underway to develop energy sources that do not emit greenhouse gases.[2,3] The amount of solar energy that strikes Earth in one hour equals the amount of energy consumed by humankind in one year.[4,5] In principle, solar energy can fulfill most of humankind's energy requirements, but it is intermittent and diffuse. Efficient, large-scale energy storage, that also delivers the stored energy on demand, is required for the widespread adoption of solar and renewable energy.[5–8]

A promising method to store solar energy is artificial photosynthesis of either hydrogen from water and sunlight, or hydrocarbons from CO_2, water, and sunlight. [2,8] In essence, solar energy is stored in the resulting fuel (and O_2). Hydrocarbons have enormous gravimetric energy densities, and they can deliver vast amounts of energy over extended periods.[9,10] Hydrocarbons made by artificial photosynthesis are ideally suitable for applications with these requirements (e.g., transportation, large-scale storage for power or heat),[7,9,10] and their utilization would be net CO_2 emission neutral. In principle, the CO_2 emissions from a conventional power plant can be captured and converted back into hydrocarbons in a zero-emission, solar-fuel cycle.[9,10] Carbon dioxide also can, in principle, be removed from the atmosphere and converted into solar fuels or commodity chemicals.

Artificial photosynthesis often is carried out in a photoelectrochemical cell.[11] Water splitting occurs at the photoanode to produce oxygen, protons, and electrons,

---

either protons are reduced to hydrogen or CO_2 and protons are reduced to hydrocarbons at the photocathode. A potential typically is applied to prevent back transfer at the electrodes. Systems based upon Z-schemes that operate without applied bias by transferring electrons from the conductance band of the photoanode to the valence band of the photocathode are also under investigation.[12]

Photocatalytic water splitting was reported first by Fujishima and Honda in 1972, who utilized TiO_2 as a photoanode to oxidize H_2O to form O_2, protons, and electrons under UV irradiation.[13] Narrow band gap semiconductors, such as $CuWO_4/CoPi$,[14] and $Ta_3N_5/KTaO_3$[15] have been studied as photocatalysts for water splitting that absorb in the visible light range.[16] Dye-sensitized photoelectrochemical cells (DSPECs) are an alternative to using one material for both light absorption and water-splitting catalysis.[5] In DSPECs, the light-absorbing material (dye or chromophore) and the catalyst are typically different materials.[17] Thereby, both can be optimized for their specific function independently to tune and understand the overall performance of the DSPEC better.[18,19]

The chromophores that have been investigated in DSPEC's include Zn, Os, Ir, or Ru metal complexes.[20–23] Ru-polypyridyl compounds are the most studied[24–27] because they possess relatively strong, tunable metal-to-ligand charge transfer absorbances in the visible range, and their triplet excited states are relatively long-lived.[28,29] Further, the ligands can be varied to tune relevant characteristics, such as chemical stability, the rates of injection and back electron transfer, excited state potential, and light-absorption range.[30,31] Ru-polypyridyl chromophores typically are attached to semiconductor (SC) electrodes through phosphonate- or carboxylate-SC linkages in DSPECs. While these linkages are stable under acidic conditions, they undergo rapid hydrolysis at pHs above 7 and 5, respectively.[32] Basic pHs are more desired because most earth-abundant catalysts are stable under these conditions.[33] Also, kinetics favour CO_2 reduction to H_2 evolution at higher pH values.[34] Atomic layer deposition of Al_2O_3 or TiO_2 has improved the stability of chromophore/catalyst assemblies.[35] A common method to graft a desired organic compound through a covalent bond to an electrode is via electrografting of the corresponding diazonium salt.[36–43] Several groups,[27,44,45] including our own,[46] have reported that Ru- polypyridine

chromophores grafted to various surfaces by diazonium ions demonstrate good stability under basic conditions.

The majority of Ru-polypyridyl chromophores undergo one electron processes under light, whereas the reduction of CO_2, and related reactions require multiple electron transfers. Dinuclear Ru(II) polypyridyl complexes, such as $[(phen)_2Ru(tatpq)Ru(phen)_2]^{4+}$ (phen = 1,10-phenanthroline, and tatpq = 9,11,20,22-tetraazatetrapyrido[3,2-a:2'3'c:3'',2''-l:2''',3'''-n]-pentacene-10,21-quinone),[47] or tetranuclear Ru(II) complex $[(Ru(phen)_2)_4(ditatpp)]^{8+}$ (ditatpp = dimer of 9,11,20,22-tetra-aza-tetrapyrido[3,2-a:2'3'-c:3'',2''-l:2''',3''']-pentacene linked by a carbon–carbon bond along the central benzene ring)[48] can store up to 4 electrons upon irradiation with visible light in presence of triethylamine (Et_3N) as the sacrificial electron donor. Each one-electron reduction of the bridging ligand is accompanied by protonation to prevent the build-up of negative charge. As well, chromophores with multiple Ru and other metal centers absorb light deeper into the visible range than monomeric chromophores.[49,50] Multinuclear chromophores often have poor solubility, however, hampering their purification, characterization, activity measurements, and attachment to electrode surfaces.[51,52]

A modular synthesis of complex chromophores/catalysts in a step-by-step manner with the starting group covalently bonded to the surface, much like solid-phase synthesis,[53] would simplify the construction of complex systems on electrode surfaces. Specifically, insolubility is not a limitation because the target is bonded already to the electrode, and it is constructed by a sequence of reactions with smaller components dissolved in solution. This simplification of the procedure would allow for rapid optimization by varying the reactants in each step of the sequence. Another advantage of attaching a small component molecule to the semiconductor surface first is that higher surface coverages may be obtained than if the larger molecule was attached to the surface in one step.[54]

In a recent publication in our group, it was established the stepwise synthesis of a SC-$[(phen)Ru(bpy)_2]^{2+}$ photoanode (SC = semiconductors, phen = 1,10-phenanthroline), with the ruthenium-polypyridyl chromophore covalently bonded to the semiconductor at C5 of the phen ligand. The bond between the SC and C5 was

more robust under neutral and basic conditions than phosphonate- or carboxylate linkages.[46] This chapter describes the preparation of a series of monomeric- and dimeric Ru-polypyridine chromophores to demonstrate the versatility of this synthetic strategy (Scheme 2.1-2.4). As well, it describes the light absorption range, $Ru^{2+/3+}$ redox potential, and the photoactivity of the resulting photoanodes towards the photoelectrochemical oxidation of hydroquinone or triethylamine under a wide pH, wavelength, and potential range. Include here the CO_2 reduction and photochemical CO_2 reduction with RuRe.

2.2 Results and Discussion

The diazonium derivative of 1,10-phenanthroline-5-amine was used to electrograft phenanthroline to flat FTO or TiO_2 nanoparticles pasted on FTO (referred to here as TiO_2) electrodes using cyclic voltammetry (CV), as was reported previously (1 mM phen and 2 mM $NaNO_2$ in 0.1 M H_2SO_4, –0.20 to 0.15 V vs SCE, 50 mV s^{-1}, five cycles) (Scheme 2.1).[46,55] Figures 2.1A and 2.1B show the deposition voltammograms. The high cathodic current in the first cycle, followed by the significantly lower values in the remaining cycles indicates that the majority of the electrochemically active sites are occupied after the first cycle. As expected, the cathodic deposition current over the higher surface area TiO_2 electrode was ~10 larger than over flat FTO.
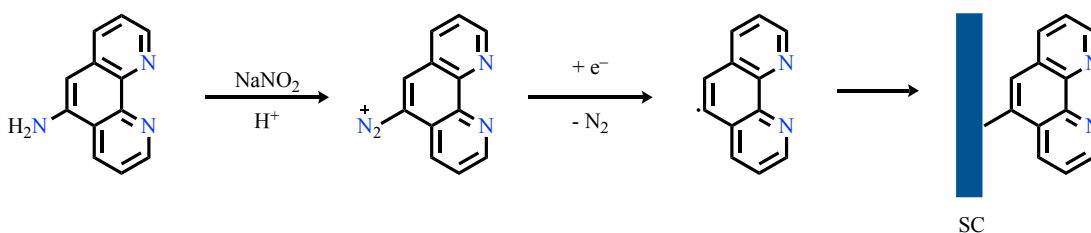
Scheme 2.1. Route for the solid-phase synthesis. Electrografting of 5-diazo-1,10-phenanthroline cation on the surface of various semiconductors.
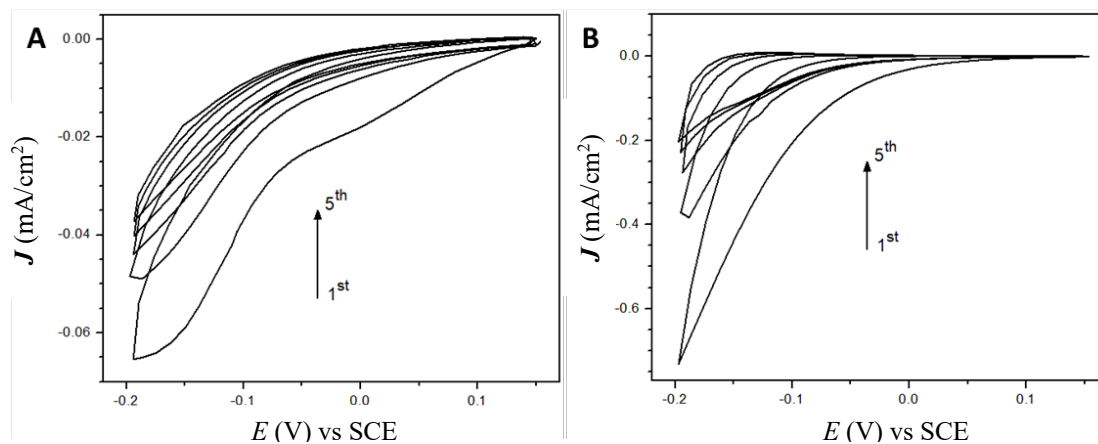
Figure 2.1. Cyclic voltammogram of the (A) FTO, and (B) TiO$_2$ electrodes in 0.1 M H$_2$SO$_4$ solution containing 5-amino-1,10-phenanthroline (1 mM) and NaNO$_2$ (2 mM), scan rate 50 mV s^{-1}.

The high-resolution XPS spectra (Figure 2.2) show the N1s region (~400 eV) of FTO, TiO$_2$, FTO-phen, and TiO$_2$-phen. The N1s peaks at 400 eV for FTO-phen and TiO$_2$-phen, confirming that nitrogen is only present after electrografting, and indicating that the nitrogen is sp^2-hybridized in an aromatic phen-type structure.[56] Additionally, the cyclic voltammogram (CV) (Figure 2.3) of FTO-phen shows that sweeping to a lower potential limit than during the electrografting (0.1 M Na$_2$SO$_4$, 0 to –1.0 V vs SCE, 50 mV s^{-1}). Similar to ITO-phen reported previously,[46] the cathodic peak at about –0.85 V in the first cathodic sweep is absent in subsequent sweeps. This peak is attributed to two proton-coupled, electron transfers to phen, forming species resembling 1,4-dihydro-1,10-phenanthroline grafted at C5 to the electrode surfaces.[55,57] Charge integration of this peak estimates the electrochemically accessible surface coverage to be 3.8×10^{-10} mol cm^{-2}. As expected, this charge is slightly less than those for the corresponding electrografting by reduction of the diazonium (equivalent to 4.45 $\times$ 10^{-9} mol cm^{-2} assuming it involves 1 e$^-$ transfer). Specifically, it is reasonable to expect that a portion of the phen radicals formed during the electrografting of the diazonium does not bond to ITO or TiO$_2$ at electrochemically accessible sites.
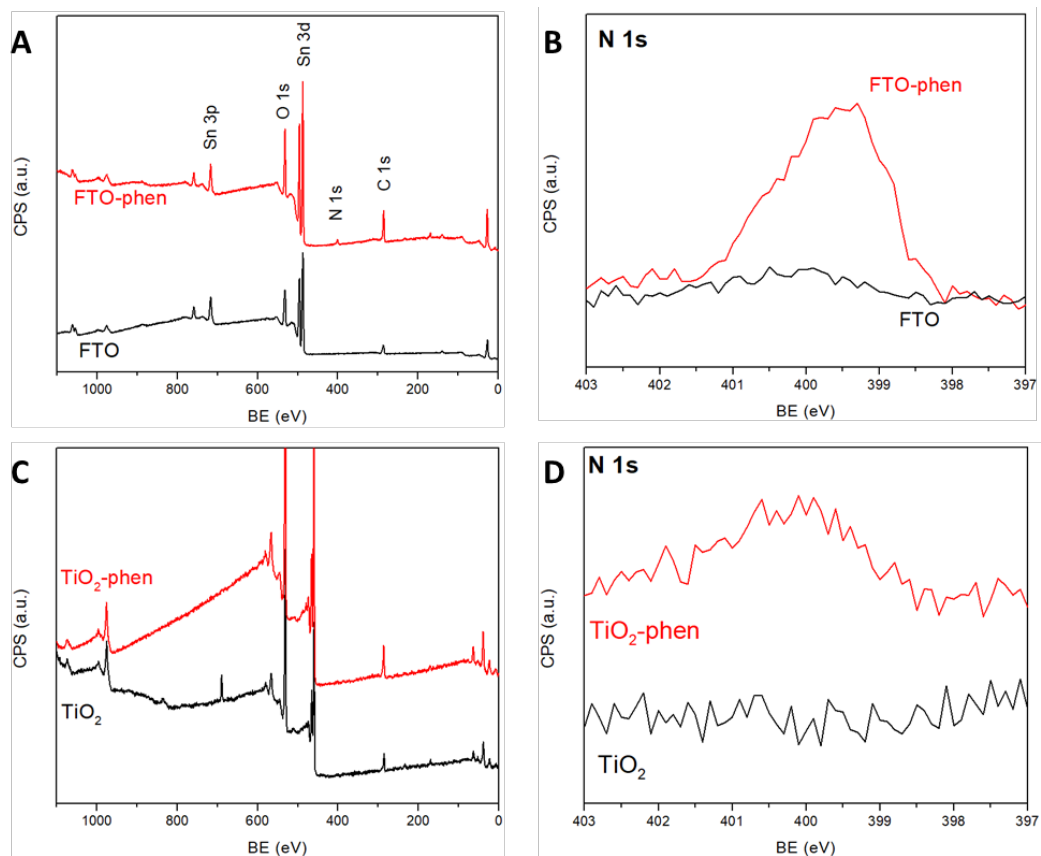
Figure 2.2. XPS survey scan (A and C), and high-resolution N 1s region spectra (B and D) of bare and phen-modified FTO and TiO_2, respectively.
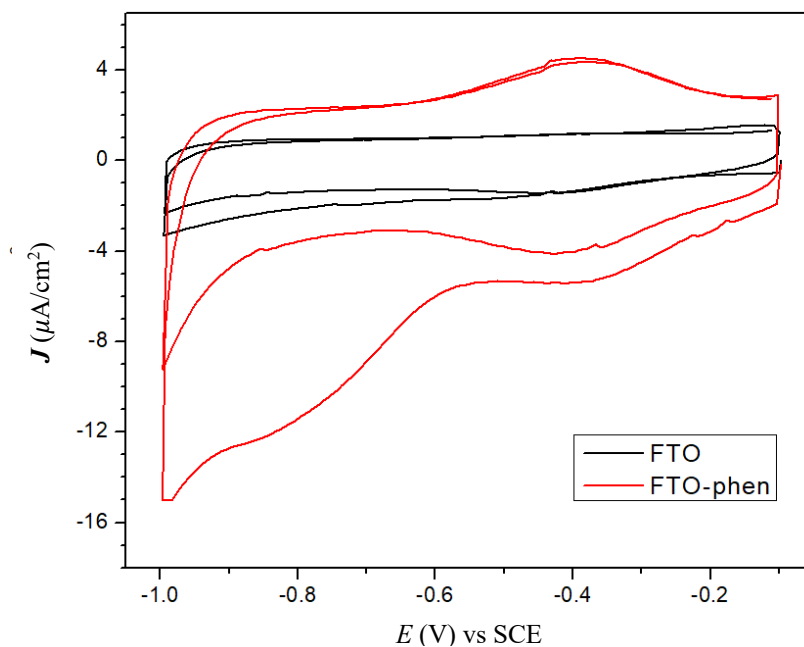
Figure 2.3. Cyclic voltammograms of the bare FTO and 1,10-phenanthroline modified FTO electrodes in N_2-saturated 0.1 M Na_2SO_4 solution and scan rate of 50 mV s^{-1}.

The heterogeneous ITO-phen, FTO-phen, and TiO$_2$-phen ligands react to completion over 4 h at 70 °C with either *cis*-[Ru(Mebpy)$_2$(CH$_3$CN)$_2$](BF$_4$)$_2$ (MeBpy = 4,4'-methyl 2,2'-bipyridine), *cis*-[Ru('Bubpy)$_2$(CH$_3$CN)$_2$](BF$_4$)$_2$ ('Bubpy = 4,4'-tert-butyl 2,2'-bipyridine), or *cis*-[Ru(PhenO)(bpy)(CH$_3$CN)$_2$](OTf)$_2$ (PhenO = 1,10-phenanthroline-5,6-dione; bpy = 2,2'-bipyridine) dissolved in THF/CH$_2$Cl$_2$ (5:1) by displacing the CH$_3$CN ligands to form the corresponding surface-bound, heterogeneous SC-[(phen)Ru(polypyridyl)$_2$]$^{2+}$ complexes (Scheme 2.2).[46]
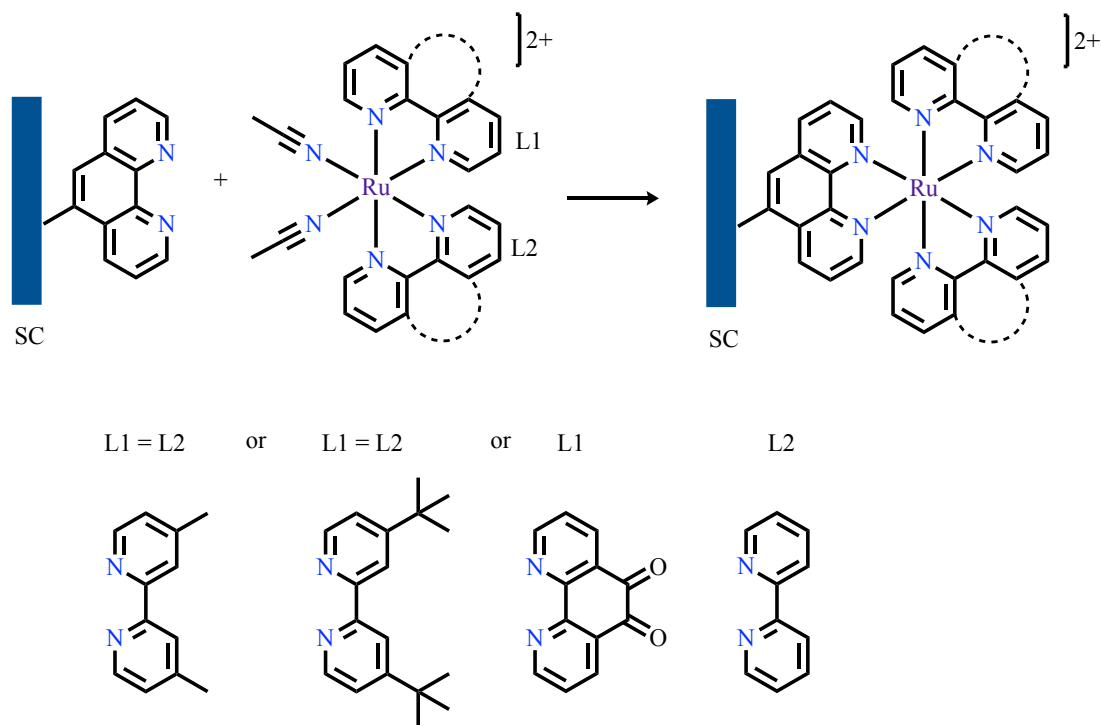
Scheme 2.2. Metalation of SC-Phen with different Ru polypyridyl complexes.

The precursor *cis*-[Ru(PhenO)(bpy)(CH$_3$CN)$_2$](OTf)$_2$ was prepared by first reacting *cis*-RuCl$_2$(PhenO)(DMSO)$_2$ (DMSO = dimethylsulfoxide) with bpy in DCB (reflux for 12 h) to prepare *cis*-RuCl$_2$(PhenO)(bpy), followed by reaction with AgOTf in CH$_3$CN to form the target. The synthesis for this complex was complicated to develop, mainly due to solubility issues of the precursors as well as the products, multiple products/isomers formation, and product isolation issues. Scheme 2.3 shows the synthesis of *trans*-Ru(PhenO)(DMSO)$_2$Cl$_2$, which started from *trans*-Ru(DMSO)$_4$Cl$_2$, a commercially available complex. The displacement of DMSO

in CHCl$_3$ at 60 ºC for 18 h is reported to proceed in 55% yield.[58] I found however that 88% yield was obtained with EtOH as solvent at 100 ºC for 16 h.
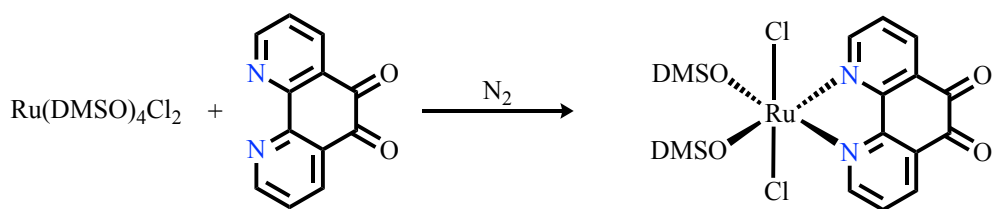
Conditions: 1. CDCl$_3$, 60 ºC, 18 h
2. EtOH, 100 ºC, 16 h

Scheme 2.3. Reaction and conditions for the synthesis of *trans*-Ru(PhenO)(DMSO)$_2$Cl$_2$

The displacement of the DMSO ligands from Ru(PhenO)(DMSO)$_2$Cl$_2$ by bpy was reported previously by Pinczewska et al.[58] Scheme 2.4 shows the reaction and the conditions explored for the synthesis of *trans*-Ru(PhenO)(bpy)Cl$_2$. Unfortunately, the literature procedure (DMF, 160 ºC, 4 h) failed to provide the desired product in the reported yield and purity. By changing the solvent to 1,4-dichlorobenzene (DCB) and heating for 16 h at 160 ºC, the desired product was obtained in 95% yield. The product is an orange solid that can be used further after washing with hexanes.
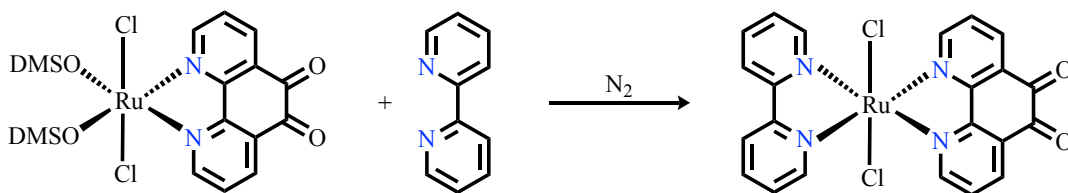
Conditions: 1. NO$_3$CH$_3$, 100 ºC, 24 h
2. DMF, 160 ºC, 4 h
3. DCB, 160 ºC, 16 h

Scheme 2.4. Reaction and conditions for the synthesis of Ru(PhenO)(bpy)Cl$_2$

Once the *trans*-Ru(PhenO)(bpy)Cl$_2$ complex was synthesized, it was only necessary to replace the Cl anions with acetonitrile ligands. That reaction was carried out with AgOTf simply because the counterion ($^-$OTf) makes the complex more soluble in DCM (as compared to $^-$BF$_4$ or $^-$PF$_6$), a solvent that is employed in the metalation of the ITO-Phen electrodes (vide infra). Scheme 2.5 shows the reaction for the synthesis

of [*trans*-Ru(PhenO)(bpy)(CH$_3$CN)$_2$]$^{2+}$($^-$OTf)$_2$, the product was synthesized in 98% yield in acetonitrile, at 75 ºC for 2.5 h.
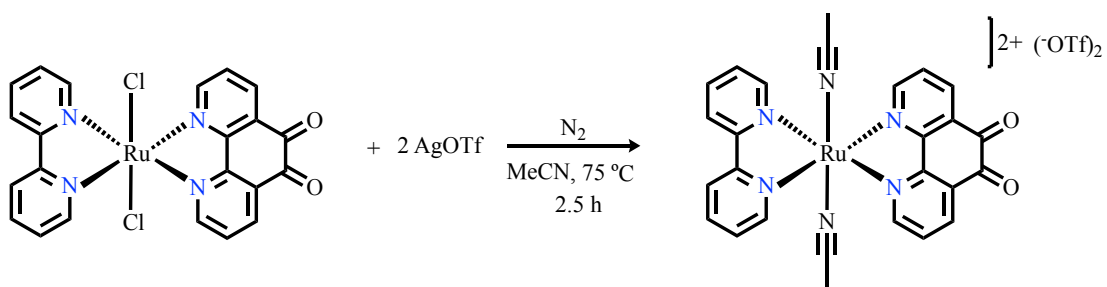
Scheme 2.5. Synthesis of [*trans*-Ru(PhenO)(bpy)(CH$_3$CN)$_2$]$^{2+}$($^-$OTf)$_2$.

Figure 2.4 shows the CVs of ITO, ITO-phen, and the ITO-[(phen)Ru(polypyridyl)$_2$]$^{2+}$ photoanodes recorded in CH$_3$CN (0.1 M NBu$_4$PF$_6$, −1.75 to 1.4 V Fc$^+$/Fc (Fc = ferrocene; 100 mV s^{-1}, from here on all potentials are referenced vs Fc$^+$/Fc, unless otherwise stated, Ag wire as a reference electrode). The first sweep is in the positive direction, starting at 0 V Fc$^+$/Fc. The ITO was a low specific surface area transparent film on a glass slide. The CV of bare ITO contained only the onset of solvent oxidation at potentials >1 V.[59] The CV of ITO-phen contains a strong anodic peak at ~0.45 V that is assigned to a largely destructive oxidation of SC-Phen.[55] The CVs of the ITO-[(phen)Ru(polypyridyl)$_2$]$^{2+}$ photoanodes contain large anodic peaks ranging from 0.75 to 0.96 V in the first positive-going sweep with much smaller cathodic peaks. There are no corresponding large cathodic peaks, showing that these oxidations are irreversible. These are in the range of known potentials for the Ru(II)/(III) oxidation for Ru-polypyridyl chromophores, both in solution and as we reported previously for ITO-RuPhen.[24,31] It is well-known that the oxidation of Ru(II) to Ru(III) is largely destructive for Ru-polypyridyl compounds under these conditions.[46] The peak current potentials for ITO-RuMePhen, ITO-Ru^{t}BuPhen, and ITO-RuOPhen were 0.75, 0.83, and 0.96 V, respectively. The CV of ITO- RuOPhen contained evidence of PhenO ligand redox peaks (vide infra).
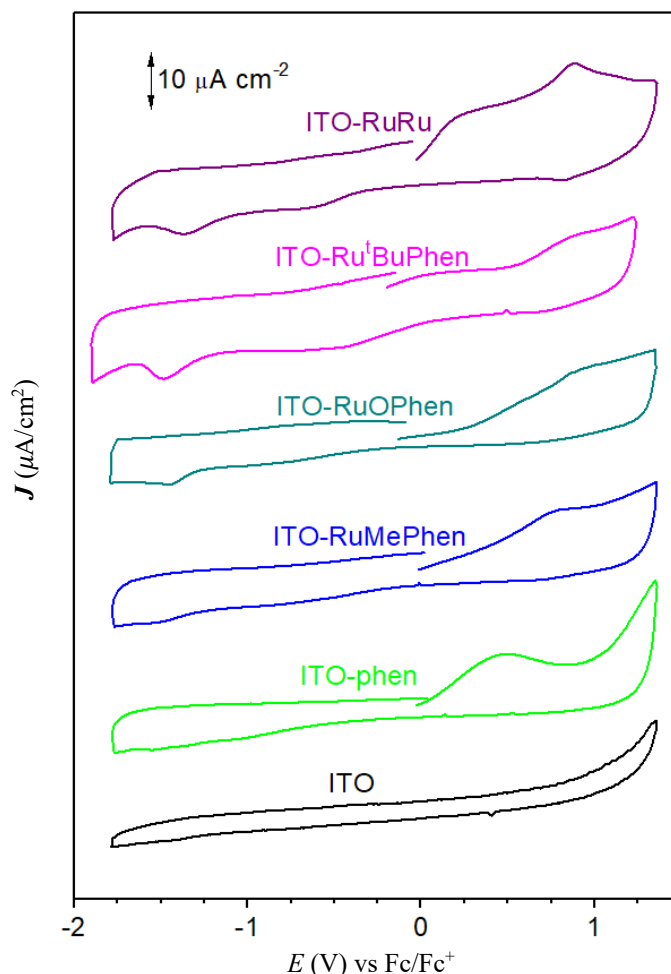
Figure 2.4. Cyclic voltammograms of the ITO-based electrodes in N_2-saturated CH_3CN (0.1 M NBu_4PF_6, 100 mV s^{-1}; the first sweep is in the positive direction, starting at 0 V Fc$^+$/Fc).

We also found that the PhenO carbonyl groups in the ITO-RuPhenO photoanode readily undergo solid-phase condensation with the amine groups in $[Ru(bpy)_2(phendiamine)]^{2+}$ (phendiamine = 1,10-phenanthroline-4,5-diamine) dissolved in ethanol after 1 h at 80 °C to form the dimeric chromophore bridged by a tetrapyrido[3,2-a:2',3'-c:3",2"-h:2''',3'''-j]phenazine (tpphz) ligand grafted to ITO (Scheme 2.6). The charge under the Ru(II)/Ru(III) redox peak in the CV of ITO-$[(phen)(bpy)Ru(tpphz)Ru(bpy)_2]^{4+}$ (denoted as SC-RuRu) is ~2x that of the monomeric Ru chromophores. The estimated $E_{1/2}$ is 0.85 V. Similar to ITO-RuPhenO, there appear to be redox peaks from the bridging tpphz ligand in the CV of ITO-RuRu.
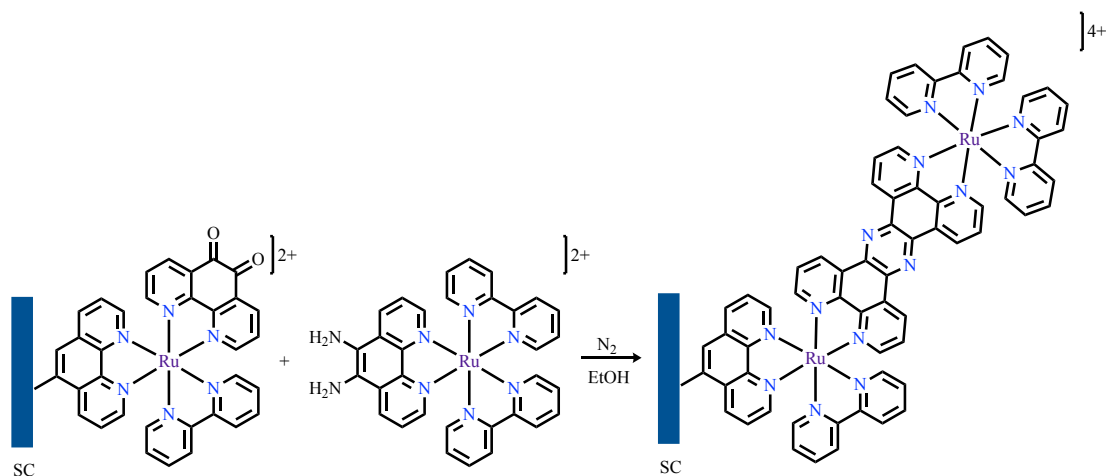
Scheme 2.6. Condensation of second nuclei on SC-[(phen)Ru(PhenO)(bpy)]$^{2+}$ chromophore forming SC-[(phen)(bipy)Ru(tpphz)Ru(bpy)$_2$]$^{4+}$.

Similarly, the solid-phase condensation with the amine groups in Re(CO)$_3$(phendiamine)Cl (phendiamine = 1,10-phenanthroline-5,6-diamine) following the same conditions as for the dimeric chromophore formed the SC-[(phen)(bpy)Ru(tpphz)Re(CO)$_3$Cl]$^{2+}$ (denoted as SC-RuRe), which is grafted on ITO, Scheme 2.7.
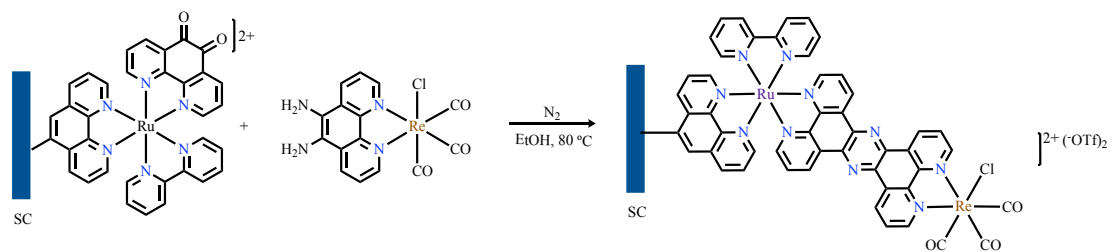
Scheme 2.7. Condensation of second nuclei on SC-[(phen)Ru(PhenO)(bpy)]$^{2+}$ chromophore forming SC-[(phen)(bpy)Ru(tpphz)Re(CO)$_3$Cl]$^{2+}$.

Figure 2.5 shows the expanded CVs of the free ligand PhenO (a), of ITO-RuPhenO (b), and of ITO-RuRu (b) in MeCN. The CV of the ITO-RuPhenO electrode contains two redox peaks at –0.62 and –1.43 V. This CV was measured with $E_{initial} = 0$ V and with the first sweep in the cathodic direction to avoid the destructive oxidation that occurs at higher potentials. These peaks likely arise from two 1-electrons redox processes at the carbonyl groups of the PhenO ligand, sequentially and reversibly forming the semi-quinone and then the catecholate derivatives. These redox processes are known for the free- and palladium-coordinated PhenO ligand.[60] The presence of these peaks in the

CV of ITO- RuPhenO is more evidence for the successful metalation of ITO-phen by *cis*-[Ru(PhenO)(bpy)(CH$_3$CN)$_2$]$^{2+}$. Consistent with the observations of Yellowlees,[60] coordination to Ru shifts these peaks to more positive potentials from those of the free ligand PhenO (Figure 2.2A).
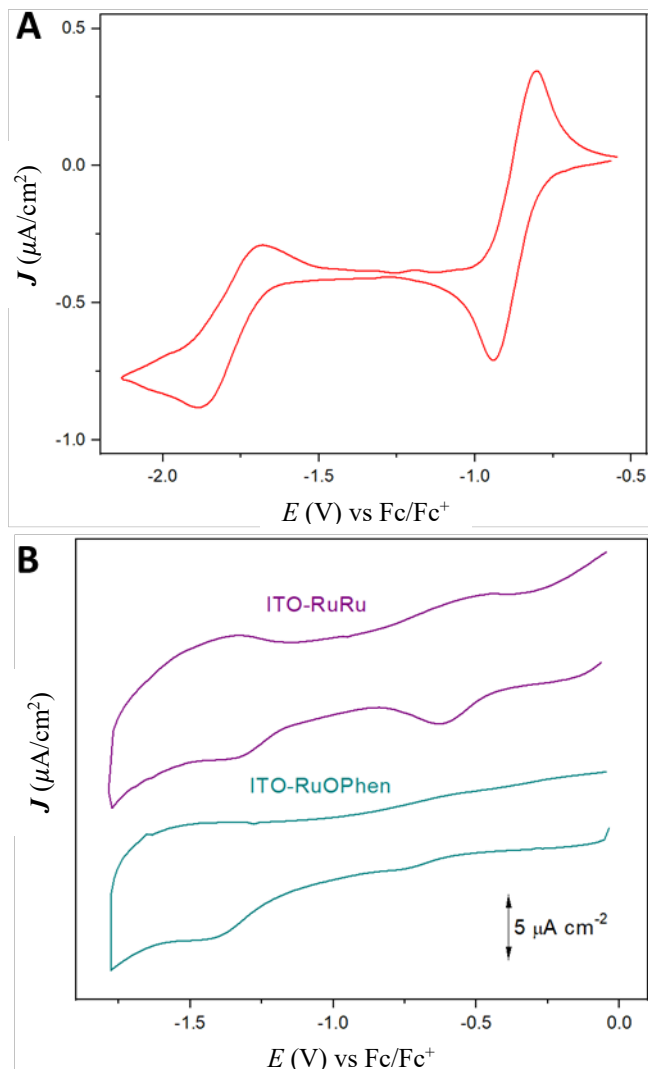
Figure 2.5. Cyclic voltammograms of the (A) 2.5 mM PhenO; and (B) ITO-RuPhenO and ITO-RuRu electrodes in N$_2$-saturated CH$_3$CN solution containing 0.1 M NBu$_4$PF$_6$, scan rate: 100 mV s^{-1}.

The expanded CV of ITO-RuRu electrode contained two redox peaks at –0.53 and at –1.36 V (Figure 2.2.B). As for ITO-RuPhenO, the CV of ITO-RuRu was recorded with $E_{initial}$ = 0 V and with the first sweep in the cathodic direction to avoid the destructive oxidation that occurs at higher potentials. These peaks likely result from two 1-electron redox processes at the nitrogen centers of the pyrazine group. These

redox processes are known for related pyrazine ligands both free- and bonded to ruthenium in solution.[60] Converting the carbonyl groups on the PhenO ligand into a bridging pyrazine group shifted the peaks to less negative values.

Figure 2.6 shows the cathodic CV of SC-RuRe attached to the ITO electrode. The CV shows the first two cathodic sweeps, it shows two redox peaks at –0.8 V and at –1.2 V. These peaks likely arise from the two 1-electron reduction processes.   At –0.8 V the peak is likely the reduction at the nitrogen centers of the pyrazine group, as seen before for SC-RuRu, and the peak at –1.2 V also likely is associated with the reduction of Re(I) to Re(0), as has been reported previously.[61] As can be noticed from the initial sweep, it is a non-reversible 1-electron reduction process. Although the reduction of the pyrido unit on the phenazine ligand also can be associated with this potential, it can be seen from the second sweep that the prominent peak around –1.2 V has decreased significantly, showing that even after the initial reduction of phenazine it is possible that the complex experience ligand-to-metal charge transfer (LMCT) thus reducing the Re center. Additionally, from this CV it can be seen that the presence of CO_2 in the solution did not increase the current generated, which may be attributed to the lack of a proton source to facilitate the electron transfer to the CO_2 adduct formed with Re.
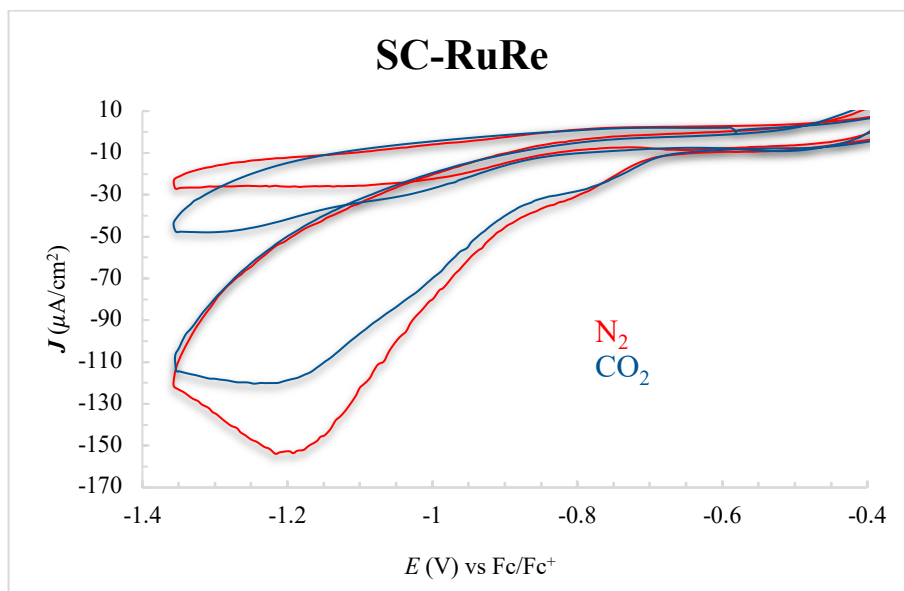
Figure 2.6. Cyclic voltammograms of ITO-RuRe electrodes in N_2- and CO_2-saturated CH_3CN solution containing 0.1 M $LiClO_4$, scan rate: 100 mV s^{-1}.

Figure 2.7 shows the CVs of the chromophores attached to TiO_2 nanoparticles (pasted onto FTO slides). The electrochemically accessible surface area of the TiO_2 is notably higher than that of the ITO or FTO films. Potentials below –0.2 V were avoided to prevent the reduction of the TiO_2 substrate. The CVs of both TiO_2 and TiO_2-phen are quite featureless over the potential range. The first sweep started at 0 V and was in the positive-going direction. The large peaks in the first positive going sweep in the CVs of the TiO_2-[(phen)Ru(polypyridyl)$_2$]$^{2+}$ electrodes are substantially larger and better defined than those over flat ITO. As well, although the Ru(II)/Ru(III) oxidations were destructive, there was clear evidence of a smaller cathodic peak in the reverse sweep. $E_{1/2}$ for (in increasing order) TiO_2-Ru^{t}BuPhen, TiO_2-RuMePhen, TiO_2-RuRu, and TiO_2-RuOPhen were 0.67, 0.75, 1.04, and 1.09 V, respectively.
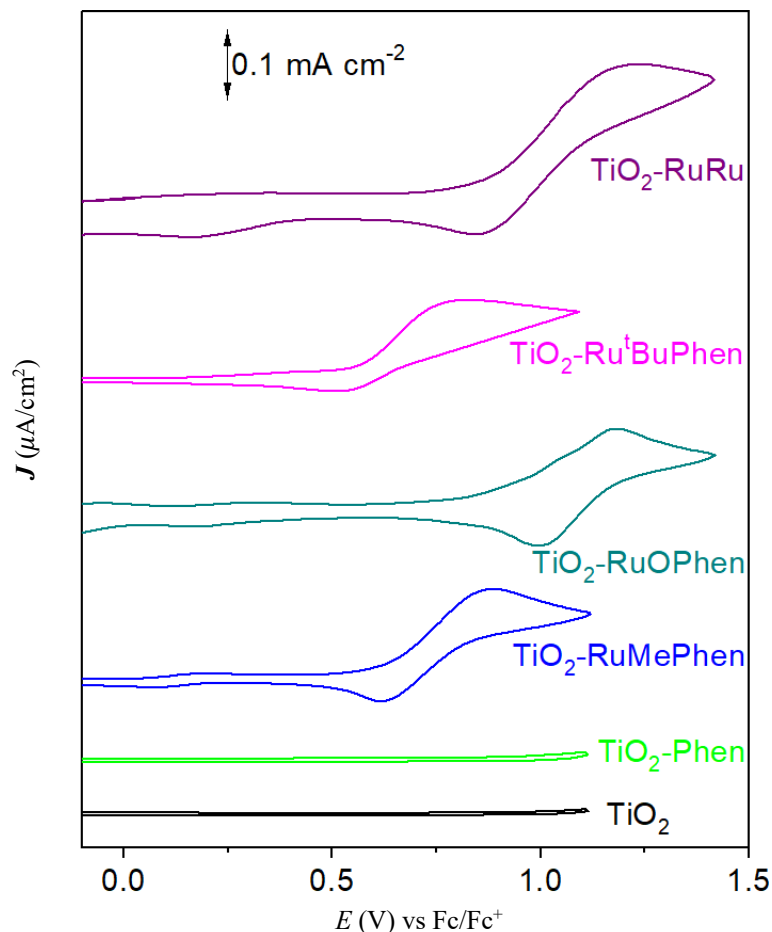
Figure 2.7. Cyclic voltammograms of the TiO_2-based electrodes after each step of chromophore synthesis in N_2-saturated CH_2Cl_2 solution containing 0.1 M NBu$_4$PF$_6$, scan rate: 100 mV s^{-1}.

A study of related Ru chromophores attached by phosphonic acid to TiO_2 found the $E_{1/2}$ was similar for Mebpy and ^{t}Bubpy.[30] The more positive $E_{1/2}$ for the PhenO-Bpy complex is consistent with these ligands being less electron donating than the Me- and ^{t}Bubpy derivatives. This order is expected based on the relative electron-donating ability of these ligands/groups. Using integration of the oxidation peak, the surface coverages (geometric surface area) of Ru were estimated to be 5.2×10^{-9}, 5.2×10^{-9}, 1.1×10^{-8}, and 5.1×10^{-9} mol cm^{-2}, respectively. As expected, there is roughly twice as much Ru in TiO_2-RuRu.

Figure 2.8 shows the Ru 3d and C 1s region of the high-resolution XPS of the FTO and TiO_2-based photoanodes. The binding energies of C 1s and Ru 3d sometimes overlap in the 280–290 eV range. The Ru 3d$_{5/2}$ peak, however, is located easily at 281.4 eV and is assigned to ruthenium in the 2+ oxidation state.[62] As expected, this peak is absent in the XPS spectra of the phen controls. Deconvolution of the C 1s peak reveals the Ru 3d$_{3/2}$ peak at 285.5 eV (peak separation = 4.1 eV), a position also consistent with Ru being present in the 2+ oxidation state.[63] The atomic ratios of N:Ru in all the photoanodes except TiO_2-RuRu (ratio ~7) were estimated from XPS to be ~6, indicating that the majority of the SC-phen reacted with the cis-[Ru(polypyridyl)$_2$(CH$_3$CN)$_2$]$^{2+}$ precursors during the metalation step.[64] The XPS peaks centered at 285.0 and 286.1 eV (C 1s region) can be attributed to C-C/C-H and C-N bonds, respectively.[65]
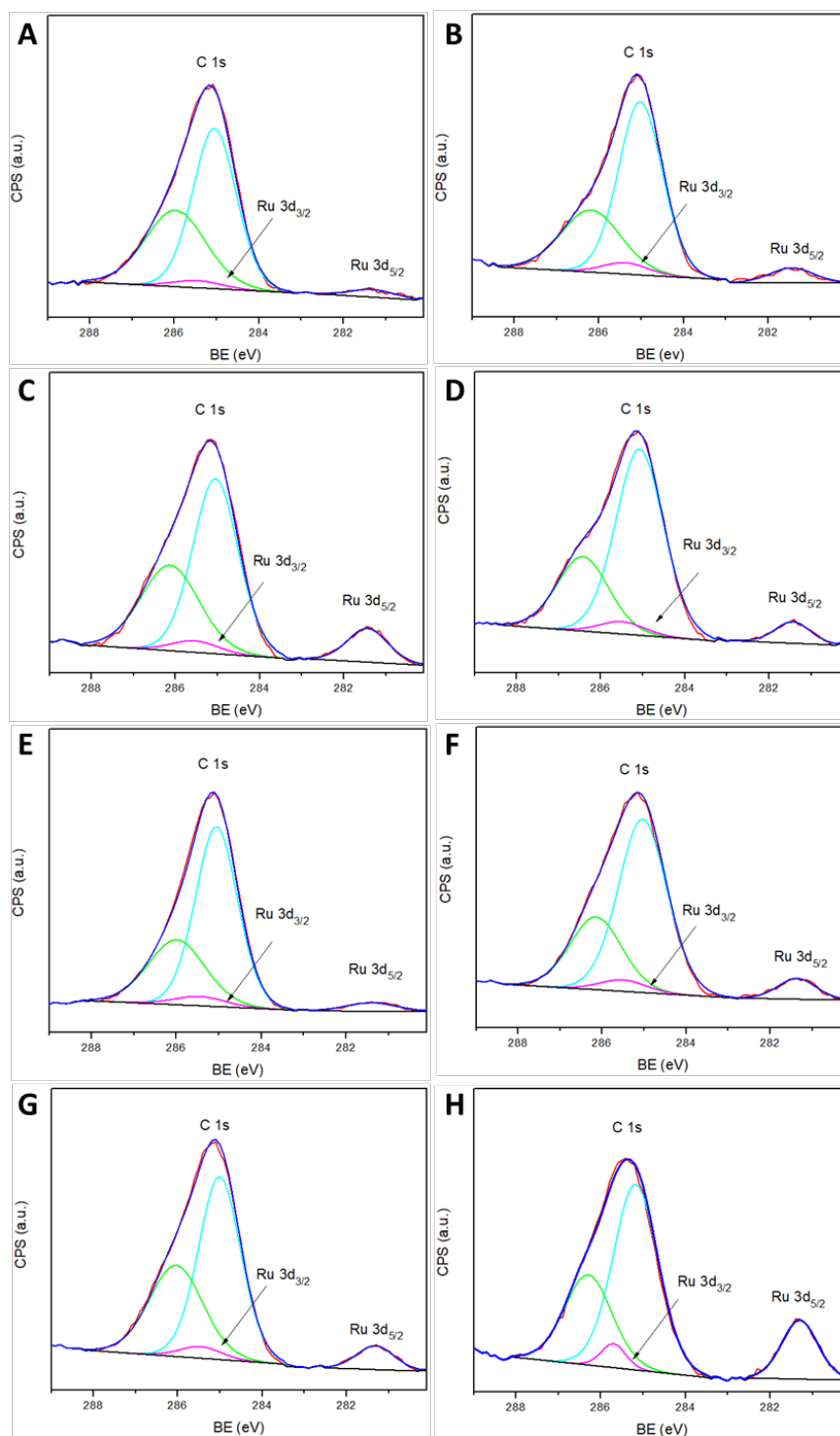
Figure 2.8. High resolution C 1s and Ru 3d region XPS spectra of (A) FTO-[(phen)Ru(Mebipy)$_2$]$^{2+}$; (B) TiO$_2$-[(phen)Ru(Mebipy)$_2$]$^{2+}$; (C) FTO-[(phen)Ru(pheno)(bipy)]$^{2+}$; (D) TiO$_2$-[(phen)Ru(PhenO)(bipy)]$^{2+}$; (E) FTO-[(phen)Ru(^{t}Bubipy)$_2$]$^{2+}$; (F) TiO$_2$-[(phen)Ru(^{t}Bubipy)$_2$]$^{2+}$; (G) FTO-[(phen)(bipy)Ru(tpphz)Ru(bipy)$_2$]$^{4+}$; and (H) TiO$_2$-[(phen)(bipy)Ru(tpphz)Ru(bipy)$_2$]$^{4+}$electrodes.

Figure 2.9 shows the solid-state UV-vis absorption spectra from 400–700 nm of the Ru-polypyridyl photoanodes using TiO$_2$ as the blank. The insets show the molar

extinction coefficient vs. wavelength spectra of the corresponding Ru-polypyridyl chromophores (containing phen as a model for SC-phen) dissolved in CH_2Cl_2.
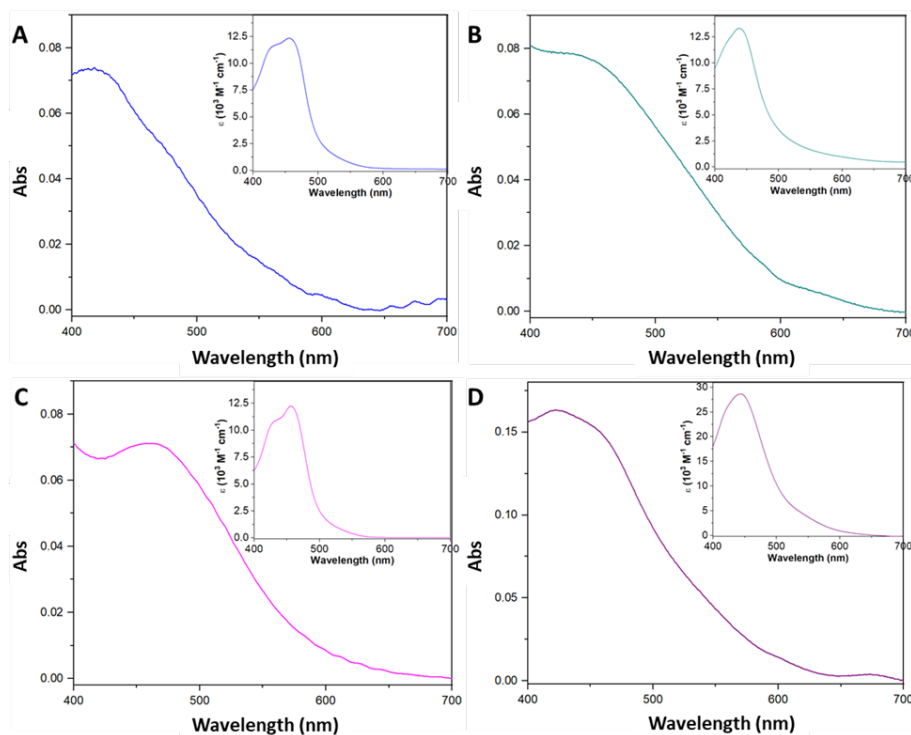
Figure 2.9. UV-vis spectra of (A) TiO_2-RuMePhen; (B) TiO_2-RuOPhen; (C) TiO_2-Ru^{t}BuPhen; and (D) TiO_2-RuRu electrodes with TiO_2 absorption subtracted. (Insets are ε vs. wavelength plots for homogeneous chromophores in CH_2Cl_2).

The solid-state UV-vis spectra resemble those of the model chromophores dissolved in solution. There is typically a slight blue shift and broadening of the peaks in the spectra of the SC-chromophores. These shifts and broadening likely result from interactions between the surface and the chromophore bonded at C5. An investigation into the nature of these interactions is beyond the scope of the present study. The UV-vis spectra of Ru(II)-polypyridyl chromophores are well-understood. The major absorptions in the visible region are due to metal-to-ligand charge transfer (MLCT), with lesser contributions from ligand-to-ligand charge transfer (LLCT), and ligand-centered (LC) transitions.[66] The molar extinction coefficients for the MLCT of the monomeric analogs dissolved in CH_2Cl_2 were similar. Perhaps not surprisingly, the molar extinction coefficient of RuRu was ~2x those of the monomeric analogs. As well,

the absorptions of RuRu and RuPhenO extended to longer wavelengths than the others.[49,67]

The surface coverages (Γ) of the Ru-based chromophores on the photoanode were estimated using the ~450 nm molar extinction coefficient measured for the dissolved chromophore analogs and eq 2.1.[68]

$$\Gamma = A_\lambda /(10^3 \times \varepsilon_\lambda) \tag{2.1}$$

Where A_λ is the absorption at a specific wavelength (λ), and ε_λ is the molar extinction coefficient at the same wavelength in M^{-1} cm^{-1}. The Γ was calculated to be 5.6×10^{-9}, 5.7×10^{-9}, 5.9×10^{-9}, and 5.6×10^{-9} mol cm^{-2} for TiO_2-RuMePhen, TiO_2-Ru^{t}BuPhen, TiO_2-RuOPhen, and TiO_2-RuRu, respectively. These values are consistent with the coverages estimated from their CVs, indicating that most of the SC-phen sites reacted with the cis-$[Ru(polypyridyl)_2(CH_3CN)_2]^{2+}$ precursors and that most of the resulting SC-$[(phen)Ru(II)(polypyridyl)_2]^{2+}$ chromophores were electrochemically accessible.

ICP-MS analysis of the Ru solutions obtained by digesting the photoanodes in aqua regia showed that the coverage of TiO_2 (geometric surface area) by the chromophores was 5.8×10^{-9}, 5.8×10^{-9}, 5.1×10^{-9}, and 5.7×10^{-9} mol cm^{-2} (considering 2 Ru for each chromophore) for the TiO_2-RuMePhen, TiO_2-Ru^{t}BuPhen, TiO_2-RuOPhen, and TiO_2-RuRu electrodes, respectively. These loadings are consistent with coverages obtained using CV and solid-state UV-vis absorption.

Taken together, the results from the CV, solid-state UV-vis absorption, XPS, and ICP-MS analyses show that the SC-phen ligands were converted into the target monomeric- and dimeric-Ru(II)-polypyridyl chromophores. As well, control experiments show that 1-naphthylene grafted with diazonium chemistry passivates the TiO_2 surface towards reaction with the Ru-bis(acetonitrile precursors) under our conditions. The chromophores are anchored by a covalent bond to C5 at electrochemically accessible sites on the semiconductor.

In addition to the characterization of ITO and TiO_2-based electrodes, the photoelectrocatalytic activity of ITO-RuRe was briefly explored. Specifically, the photoelectrocatalytic CO_2 reduction under controlled potentials with ITO-RuRe was investigated. As discussed in Chapter 1, the photocatalytic and photoelectrocatalytic

reduction of CO_2 (usually to CO) by *fac*-Re(bpy)(CO)$_3$Cl and related complexes has been studied extensively.[69–72] As discussed in Section 1.4, supramolecular complexes comprising Ru and Re centres are excellent candidates to demonstrate the advantages of combining the chromophore and catalyst attached to a semiconductor surface.[73–77] Since ITO-RuRe is anchored to the surface via covalent bonding (O-C bond), it is expected to promote fast electron injection into the LUMO orbital of the Ru complex upon light excitation (π^* orbitals on bpy). It is noted that ITO is an N-type semiconductor, and a better match would utilize a p-type; nevertheless, the in-hand ITO-RuRe was investigated for this preliminary study in 0.1 M LiClO$_4$ MeCN solutions saturated with CO_2. As discussed in Section 1.4, the negative going sweep in the CV of ITO-RuRe contains cathodic waves at –0.8 and –1.2 V, assigned to the reduction of the pyrido bridging group and the reduction of Re^1 to Re^0, respectively. Two potentials were initially investigated for the photoelectrocatalytic CO_2 reductions, –0.65 V and at –0.9 V. These potentials were chosen because they are not sufficiently reductive to affect the pyrido$^{0/-1}$ and Re$^{1/0}$ redox transformations in the dark. The light used was a simple white LED flashlight (~4.6 mW cm^{-2}) with 400 and 900 nm cut-off filters. Figure 2.10. Under similar conditions, when a commercial flashlight is employed to excite the Ru chromophore, there is a sudden change in the current density, about 10 µA cm^{-2} It is surprising to note that the light intensity was sufficient to produce the same current density increments independent of the voltage applied, whether –0.9 V or –1.1 V (Scheme 2.8). Despite these preliminary results, it is necessary to analyze the gas phase to confirm the CO presence and quantify the number of moles to be able to estimate the TON (turnover numbers). Controlled light sources and additives were not investigated for this preliminary study. Attempts to prepare the free dinuclear complex (phen)(bpy)Ru(tpphz)Re(bpy)(CO)$_3$Cl in solution produced mixtures that were difficult to purify. This project was abandoned in favour of the development of more stable, active, and abundant photosensitizers and electrocatalysts.
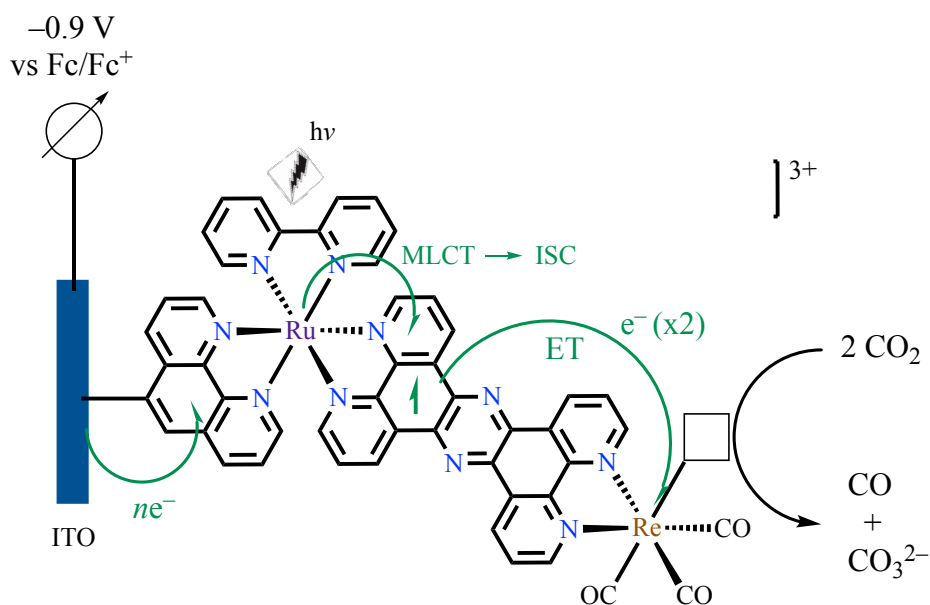
Scheme 2.8. Photoelectrochemical reduction of CO_2 with ITO-RuRe.
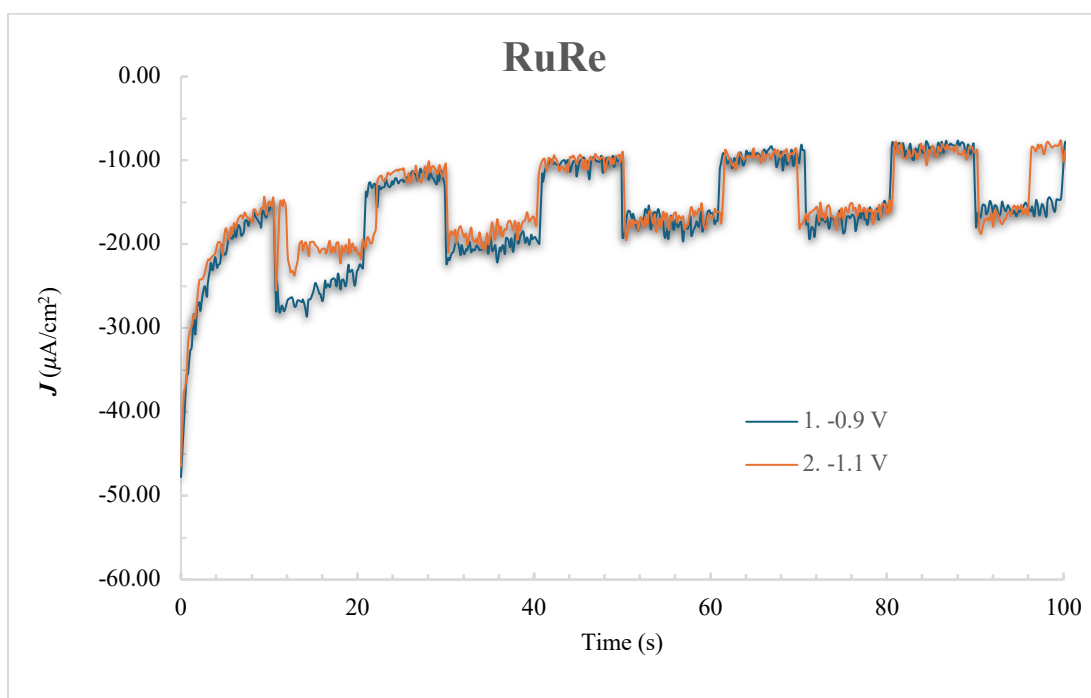
Figure 2.10. Controlled potential photoelectrolysis of CO_2 with ITO-RuRe in CO_2-saturated 0.1 M $LiClO_4$ MeCN solution. Using a commercial flashlight (~4.6 mW/cm^2), using >400, <900 nm filters.

2.3 Conclusions

This chapter described an adaptable, stepwise, solid-phase type synthesis of several semiconductor-chromophore assemblies. The prepared chromophores were attached to the semiconductor by a direct covalent bond to C5 of a phen ligand, presumably to an

oxygen atom in the semiconductor. This attachment has appreciable stability in basic conditions, providing a means to study to base-stable, abundant metal catalysts for water splitting and CO_2 reduction. The chromophores were well-characterized, and they largely are situated at electrochemically accessible sites on the semiconductor. In general, more electron-donating ligands (i.e. methyl and tert-butyl) to Ru decreased the redox potential of the chromophores relative to the unsubstituted bipy parent complex, while replacing a bpy with phendione ligand and causing a potential shift to higher values. An interesting future direction would be to vary the structure of the ligands within the dimer systematically and investigate the effect on hole transfer between the Ru centres and the overall photoactivity of the bonded chromophore. Detailed photophysical studies are required to determine the origins of the differences in photoactivity between these systems. As well, this solid-phase synthesis can, in principle, be used to prepare high molecular weight chromophores with multiple, mixed metal centers in a controlled, stepwise manner, while avoiding difficulties arising from insolubility.

2.4 Experimental

Materials

Chemicals were used without any further treatment unless mentioned otherwise. The following compounds were purchased from Sigma Aldrich: 1,10-phenanthroline-5-amine (97%), $NaNO_2$ ($\geq$97.0%), TiO_2 nanoparticles (anatase, nanopowder <25 nm particle size, 99.7% trace metals basis), $TiCl_4$ ($\geq$99.995%, trace metals basis), 2,4-pentadione ($\geq$99%), hydroquinone (ReagentPlus, $\geq$99.5%), $NaClO_4$ (ACS reagent, $\geq$98.0%), sulfuric acid (99.999%), triethylamine, distilled (Et$_3$N, $\geq$99.0%), tetrahydrofuran, distilled (ACS reagent, $\geq$99.0%), dichloromethane, distilled (ACS reagent, $\geq$99.5%), triply distilled water; dichloromethane, distilled (Sigma Aldrich, ACS reagent, $\geq$99.5%); hexanes, distilled (Caledon, ACS); acetonitrile, distilled ($\geq$99.5%); methanol (Sigma Aldrich, ACS reagent, $\geq$99.8%); silver trifluoromethanesulfonate (Sigma Aldrich, 99%); silver tetrafluoroborate (Sigma Aldrich, 98%); tetrahydrofuran, distilled (Sigma Aldrich, ACS reagent, $\geq$99.0%). $Ru(COD)Cl_2$ (Strem Chemicals, polymer, $\geq$97%); 4,4'-methyl 2,2'-bipyridine (Sigma

Aldrich, 99%); 4,4'-tert-butyl 2,2'-bipyridine (Sigma Aldrich, 98%); 1,10-phenanthroline (Sigma Aldrich, ≥99%); Ru(DMSO)$_4$Cl$_2$ (Sigma Aldrich, 96%); Hydrochloric acid (Caledon, 37%); diethyl ether (Anachemia, ≥99.0%); 1,10-phenanthroline-5,6-diamine (**Shanghai Uchem,** ≥98%); 1,10-phenanthroline-5,6-dione (Sigma Aldrich, 97%); dimethylformamide (Fisher Chemicals, 99.9%). Anhydrous ethanol, Triton X-100, and perchloric acid were purchased from Commercial Alcohols, EMD Millipore Corporation, and GFS Chemicals (ACS reagent, 70%), respectively. Triply distilled water was used in the preparation of aqueous solutions.

Instrumentation

Electrochemical studies were done using Solartron SI 1287 Electrochemical Interface controlled by CorrWare for Windows Version 2-3d software (without iR compensation). The X-ray photoelectron spectroscopy (XPS) measurements were done using a Kratos Axis 165. A monochromatized Al Kα source (hv = 1486.6 eV) was used at 12 mA and 14 kV, while the pressure in the sample analytical chamber was <1 × 10^{-9} torr. Survey scans covered the binding energy of 1100 to 0 eV, with 160 eV analyzer pass energy and 0.3 eV steps. For deconvolution, the spectra are calibrated by C-C binding energy at 285.0 eV. UV-vis spectra were collected using a Cary 5000 UV-vis spectrometer for chromophores dissolved in CH$_2$Cl$_2$ or on TiO$_2$ (with TiO$_2$ absorption subtracted). Inductively coupled plasma–mass spectrometry (ICP-MS) was performed to obtain the surface coverage of each chromophore using Perkin Elmer Elan 6000.

Fabrication of FTO/TiO$_2$ Electrodes

Fluorine-doped tin oxide slides (FTO, Sigma Aldrich, surface resistivity ~7 Ω/sq, cut into 1 × 2.5 cm^2) were sonicated in ethanol, followed by water for 15 min each. Then they were heated in 50 mM TiCl$_4$ solution at 70 ºC for 30 min. TiO$_2$ paste was prepared following the reported literature procedure.[41,46] The paste was applied on FTO surfaces using the doctor-blade technique (4 layers of scotch tape and TiO$_2$ thickness of ~10 μm). After drying in air, the electrodes were heated at 500 ºC for 2 h in a muffle

furnace, followed by treatment in 50 mM TiCl$_4$ solution at 70 °C for 30 min. They were rinsed thoroughly with water and heated at 450 °C for 30 min.

Electrochemical Grafting of 1,10-phenanthroline

Electrochemical grafting of 1,10-phenanthroline onto FTO (or indium doped tin oxide slides (ITO, Sigma Aldrich, surface resistivity 8–12 Ω/sq, cut into 0.8 × 2.5 cm^2)) or FTO/TiO$_2$ slides (referred to here as TiO$_2$) was done following our previous report,[46] adapted from Ekinci and Belanger studies.[55,57,785] FTO (or ITO) electrodes were cleaned by sonication in ethanol and water, for 15 min each before the experiments. Briefly, 0.1 M H$_2$SO$_4$ solution (10 mL) containing 1 mM 1,10-phenanthroline-5-amine (1.9 mg) was bubbled with N$_2$ for 15 min. Once 2 mM NaNO$_2$ (1.4 mg) was added, ~1 cm^2 of the FTO slide was immersed into the solution as the working electrode. The potential was swept between 0.15 and –0.20 V$_{SCE}$ at 50 mV s^{-1} for five cycles using cyclic voltammetry technique. Coiled platinum wire and saturated calomel electrode (SCE) were used as counter and reference electrodes. Phen electrografted electrodes (referred to as SC-phen; SC = FTO, ITO or TiO$_2$) were rinsed with abundant water followed by ethanol and dried in air.

Synthesis of Ru(MeBpy)$_2$Cl$_2$ and Ru(^{t}Bubpy)$_2$Cl$_2$ Complexes

A literature procedure with slight modification was used to prepare both Ru(MeBpy)$_2$Cl$_2$ and Ru(^{t}Bubpy)$_2$Cl$_2$ complexes.[79] Ru(COD)Cl$_2$ (1 equivalent) and ligand (2 equivalents) were weighed into a 100 ml side-arm flask. Then the flask was connected to a Schlenk line, and then evacuated and refilled with N$_2$ (3 cycles). 1,2-Dichlorobenzene (0.04 M based on [Ru(COD)Cl$_2$]), bubbled with N$_2$ for 30 min, was added to the flask, then connected to a condenser. The flask was placed in an oil bath preheated to 140 °C and stirred overnight. During the reaction, the colour of the solution turned to dark purple with precipitate forming. After 16 hours, the flask was cooled to room temperature, 20 mL of hexane were added and allowed for precipitates to settle down. The dark purple product was collected by filtration through a Buchner funnel and by washing with copious amounts of hexane. The yield of the product after drying under suction was >90% with some 1,2-dichlorobenzene present, which was used for

the next step without further purifications. The ^{1}H NMR data were consistent with the reported values:[80]

Ru(Mebpy)$_2$Cl$_2$ **^{1}H NMR** (399.978 MHz, CD$_2$Cl$_2$, 27.0 °C): 2.41 (s, 6H), 2.61 (s, 6H), 6.72 (d, 2H, J = 5.0 Hz), 7.39 (d, 2H, J = 4.9 Hz), 7.47 (s, 2H), 7.82 (s, 2H), 7.95 (s, 2 H), 10.12 (d, 2H, J = 4.8 Hz).

Ru(^{t}Bubpy)$_2$Cl$_2$ **^{1}H NMR** (498.119 MHz CDCl$_3$, 27.0 °C): 1.31 (s, 18H), 1.51 (s, 18H), 6.95 (d, 2H, J = 4.5 Hz), 7.55–7.59 (m, 4H), 7.95 (d, 2H, J = 1.5 Hz), 8.09 (d, 2H, J = 1.0 Hz), 10.17 (d, 2H, J = 3.9 Hz).

General Procedure for the Synthesis of [Ru(bpy)$_2$(CH$_3$CN)$_2$](BF$_4$)$_2$ Complexes

Both Ru(bpy)$_2$Cl$_2$ (1 equivalent) and AgBF$_4$ (2 equivalents) were weighed into a 100 mL side arm flask inside the glove box. The flask was wrapped in aluminum foil, connected to a Schlenk line, and then evacuated and refilled with N$_2$ (three cycles). Then, freshly distilled MeCN (0.02 M based on Ru(bpy)$_2$Cl$_2$) was added using a gas-tight syringe and the resulting suspension was stirred at room temperature overnight. After 20 h, the stirring was stopped, and the precipitates were allowed to settle down. After an hour, the orange-reddish solution was transferred into another side-arm flask by cannula filtration. The greyish-white precipitate was washed with additional MeCN (2 × 10 mL), and the filtrate was transferred to the same flask. The combined filtrate was concentrated using rotavapor, and a reddish-orange product was obtained, dissolved using minimum DCM. Upon dissolving in DCM, a greyish-white precipitate (AgCl) started to form again, which was removed by filtering through a Celite plug. Additional DCM was passed until no more orange/reddish colour was observed on the Celite plug. The filtrate was then concentrated again using rotavapor and purified by crystallization with DCM/Et$_2$O.

[Ru(MeBpy)$_2$(CH$_3$CN)$_2$](BF$_4$)$_2$:**^{1}H NMR** (498.121 MHz, CD$_3$CN, 27.0 °C): δ 2.26 (6H, s, CH$_3$), 2.45 (6H, s, CH$_3$), 2.69 (6H, s, CH$_3$), 7.08 (2H, dd J = 5.5 Hz, aromatic CH), 7.37 (2H, d, J = 6.0 Hz, aromatic CH), 7.66 (2H, d, J = 5.5 Hz, aromatic CH), 8.21 (2H, s, aromatic CH), 8.35 (2H, s, aromatic CH), 9.09 (2H, d, J = 6.0 Hz, aromatic CH). **^{13}C{^{1}H} NMR** (125.686 MHz, CD$_3$CN, 27.0 °C): δ 3.5 (CH$_3$), 20.1 (CH$_3$), 20.4 (CH$_3$), 124.2 (CH), 124.5 (CH), 125.4 (C), 127.4 (CH), 128.2 (CH), 150.4 (C), 150.7

(C), 151.0 (CH), 152.5 (CH), 156.7 (C), 157.6 (C). **HRMS (ESI)** m/z Calcd. for $C_{28}H_{30}N_6{}^{102}Ru$ (M^{2+}): 276.0782. Found: 276.0787. Figure 2.11 shows the 1H NMR spectrum and Figure 2.12 shows the 13C spectrum for this compound.
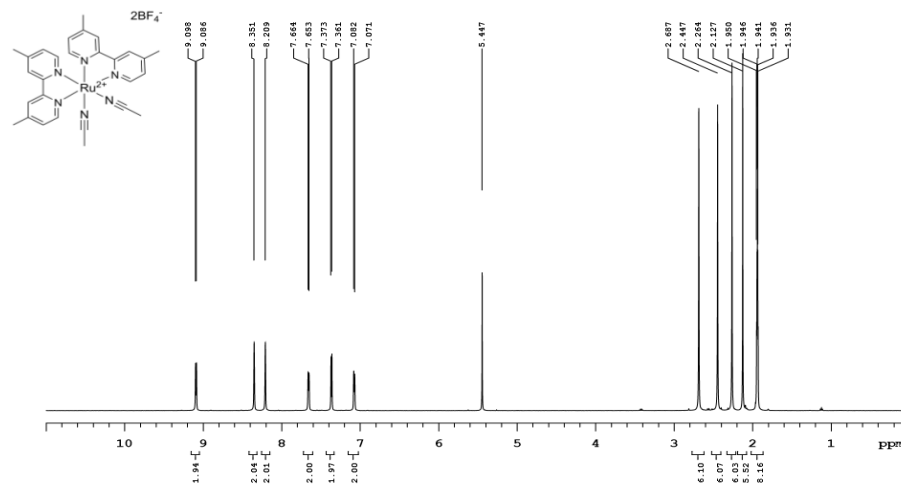
Figure 2.11. ^{1}H NMR spectra of [Ru(Mebpy)$_2$(CH$_3$CN)$_2$](BF$_4$)$_2$.
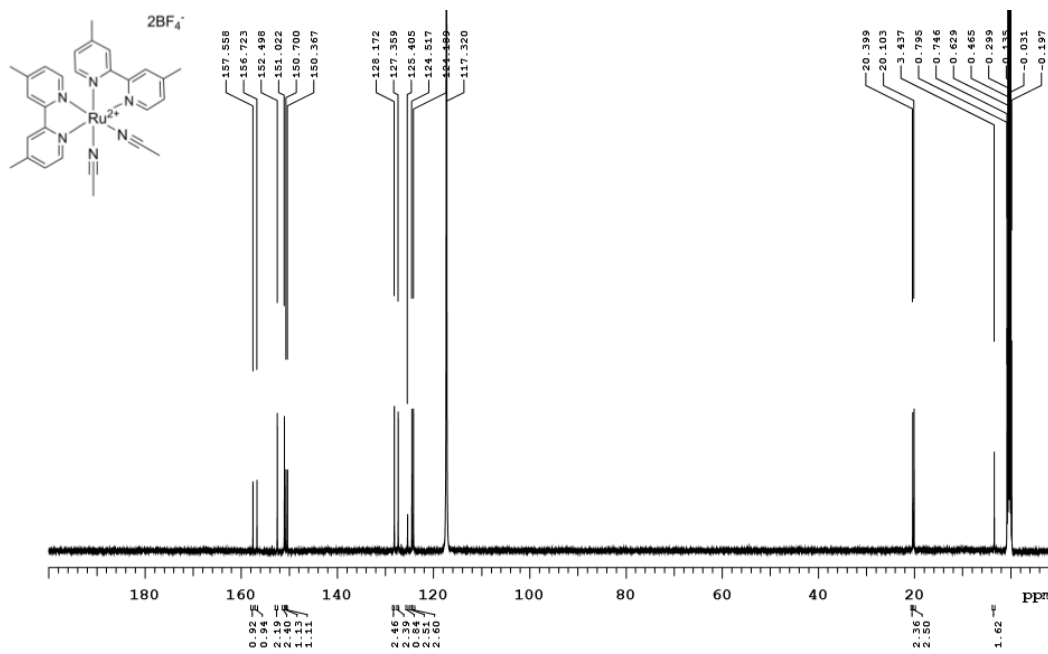
Figure 2.12. ^{13}C NMR spectra of [Ru(Mebpy)$_2$(CH$_3$CN)$_2$](BF$_4$)$_2$.

[Ru(^{t}Bubpy)$_2$(CH$_3$CN)$_2$](BF$_4$)$_2$:^{1}**H NMR** (498.121 MHz, CD$_3$CN, 27.0 °C): δ 1.34 (18H, s, CH$_3$), 1.55 (18H, s, CH$_3$), 2.29 (6H, s, CH$_3$), 7.26 (2H, dd, J = 6.0 Hz,

$J = 2.0$ Hz aromatic CH), 7.42 (2H, d, $J = 6.0$ Hz, 2 aromatic CH), 7.83 (2H, dd, $J = 6.0$ Hz, $J = 2.0$ Hz, 2 aromatic CH), 8.34 (2H, d, $J = 1.5$ Hz, 2 aromatic CH), 8.48 (2H, d, $J = 1.5$ Hz, 2 aromatic CH), 9.18 (2H, d, $J = 8.1$ Hz, 2 aromatic CH). **^{13}C{^{1}H}** **NMR** (125.685 MHz, CD$_3$CN, 27.0 °C): δ 3.5 (CH$_3$), 29.4 (CH$_3$), 29.6 (CH$_3$), 35.2 (aliphatic C), 35.5 (aliphatic C), 120.8 (CH), 121.1 (CH), 123.6 (CH), 124.5 (CH), 125.3 (C), 151.3 (CH), 152.7 (CH), 156.9 (C), 157.8 (C), 162.7 (C), 163.1 (C). **HRMS (ESI)** m/z Calcd. for C$_{40}$H$_{54}$N$_6$^{102}Ru (M^{2+}): 360.1712. Found: 360.1724. Figure 2.13 shows the ^{1}H NMR spectrum and Figure 2.14 shows the ^{13}C NMR spectrum.
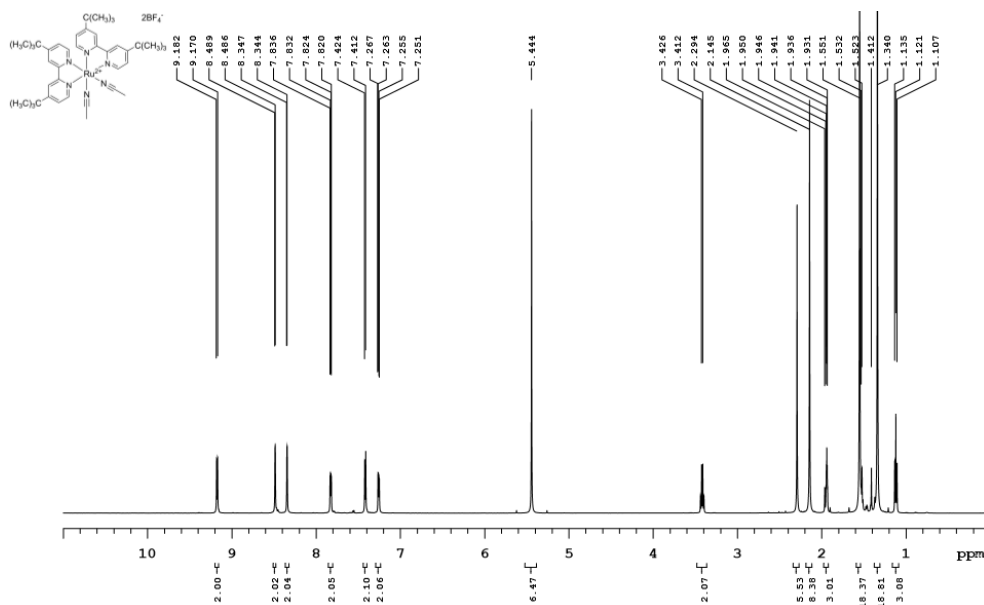
Figure 2.13. ^{1}H NMR spectra of [Ru(^{t}Bubpy)$_2$(CH$_3$CN)$_2$](BF$_4$)$_2$.
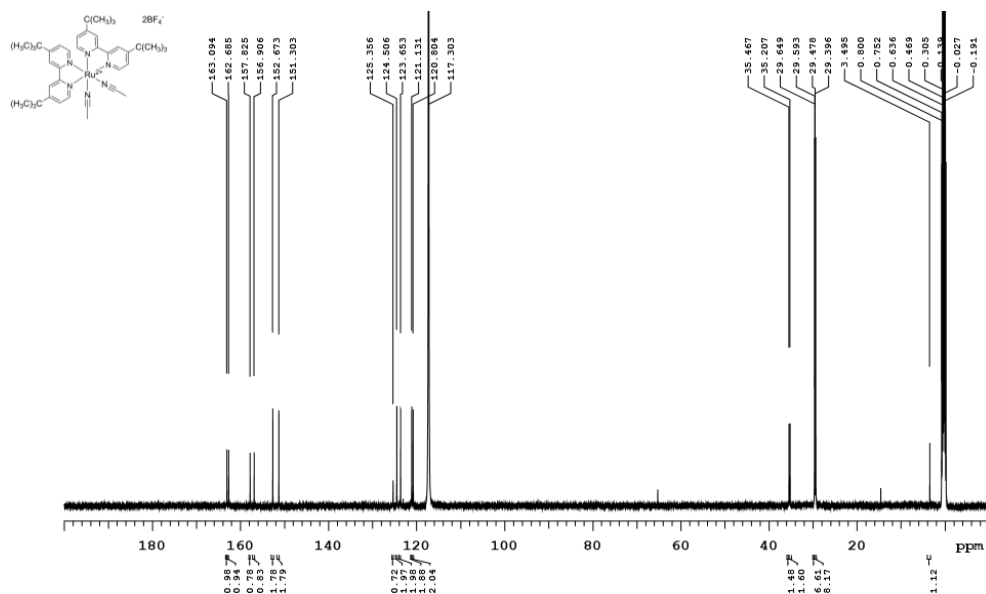
Figure 2.14. ^{13}C NMR spectra of [Ru(^{t}Bubpy)$_2$(CH$_3$CN)$_2$](BF$_4$)$_2$.

Synthesis of Ru(1,10-phenanthroline-5,6-dione)(bpy)Cl$_2$

Following a literature procedure,[58] Ru(PhenO)(DMSO)$_2$Cl$_2$ (590.2 mg, 1.1 mmol, 1 equiv.) and 2,2'-bipyridine (194.1 mg, 1.2 mmol, 1.1 equiv.) were added to 30 mL of DCB under N$_2$ atmosphere in a dry Schlenk flask. The yellow suspension was refluxed at 160 ºC for 12 h under N$_2$ and minimum exposure to light by covering the reaction mixture with aluminum foil. After cooling the reaction mixture to room temperature, a dark purple solid precipitated. Then, the solvent was removed using a cannula and the solid was thoroughly washed with hexanes (3 x 20 mL), followed by diethyl ether (3 x 20 mL) and dried under high vacuum. The dark purple microcrystalline solid needed no further purification (560.6 mg, 95% yield), the ^{1}H NMR data confirmed the product. The **^{1}H NMR** data is as follows and consistent with reported values: (ppm, in DMSO-d_6, 599.929 MHz, J-values in Hz): 7.12 (t, 1 H, J = 6.6), 7.28 (dd, 1 H, J = 6.0), 7.49 (d, 1 H, J = 6), 7.71 (t, 1 H, J = 7.8), 7.81–7.79 (m, 1 H), 7.95 (dd, 1 H, J = 5.4), 8.10– 8.04 (m, 2 H), 8.42 (d, 1 H, J = 7.8), 8.50–8.46 (m, 1 H), 8.65 (d, 1 H, J = 7.8), 9.99 (d, 1 H, J = 5.4), 10.06 (d, 1 H, J = 5.4). (ppm, in CD$_3$CN, 399.98 MHz, J-values in Hz): 10.09 (d, 1 H, J = 5.2), 7.05 (t, 1 H, J = 5.6), 7.20 (dd, 1 H, J = 6.0, 1.6), 7.70– 7.66 (m, 2 H), 7.74 (t, 1 H, J = 6.4), 7.89 (dd, 1 H, J = 6.0, 2.0), 7.95 (d, 1 H,

$J = 5.6$), 8.03–8.08 (m, 2 H), 8.25 (d, 1 H, $J = 8.0$), 8.44 (dd, 2 H, $J = 7.2, 6.4$), 10.28 (d, 1 H, $J = 4.8$). Figure 2.15 shows the ^{1}H NMR in DMSO-$d6$.
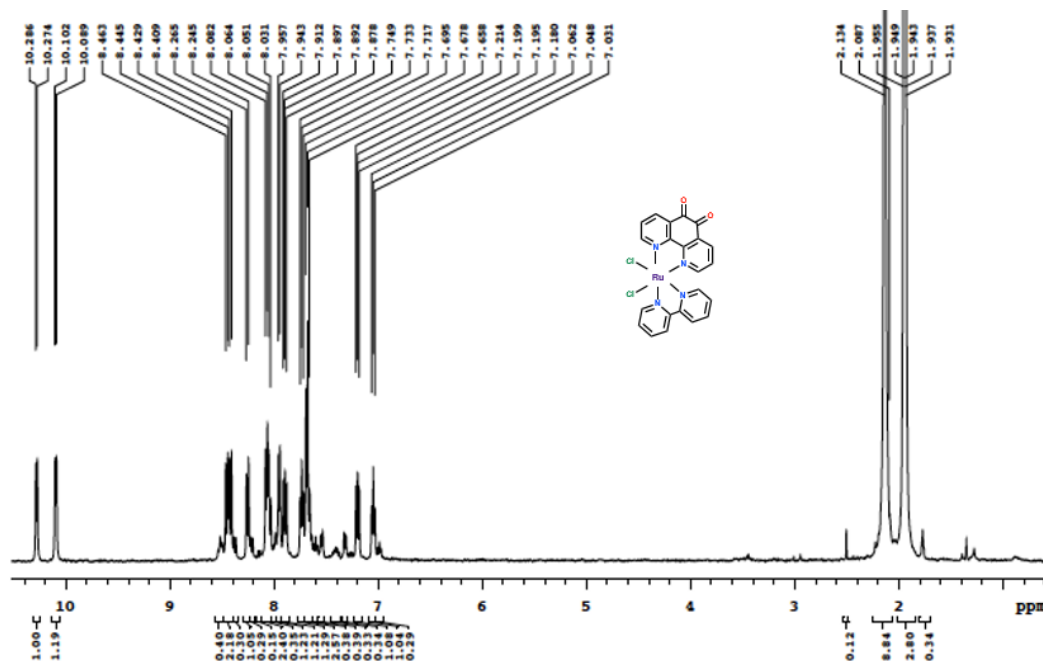
Figure 2.15. 1H NMR spectra of [Ru(bpy)(PhenO)]Cl$_2$ in DMSO-$d6$.

Synthesis Ru(PhenO)(bpy)(CH$_3$CN)$_2$](OTf)$_2$

Ru(PhenO)(bpy)Cl$_2$ (165.0 mg, 0.3 mmol, 1 equiv.) and AgOTf (181.1 mg, 0.7 mmol, 2.3 equiv.) were dissolved in 10 mL acetonitrile, forming a black-purple solution, and refluxed for 16 h under N$_2$. After cooling to room temperature, the red brick solution was cannula filtered into a different flask to separate it from the white precipitate, AgCl. The mixture reaction was passed through a Celite column into a dry and clean flask three times. The last Celite filtration column was washed with DCM to collect all remaining products. Then, the solvents were removed using high vacuum. The red-brown solid was washed with ether (3 × 30 mL) and vacuum-dried again. The solid was recrystallized from acetonitrile/diethyl ether (249.0 mg, 98% yield). The **^{1}H NMR** data is as follows: (ppm, CD$_3$CN-d_3, 498.121 MHz, J-values in Hz): 2.29 (s, 3 H), 2.31 (s, 3 H), 7.30 (t, 1 H, $J = 12.9$), 7.47 (dd, 1 H, $J = 6.0, 2.0$), 7.76 (d, 1 H, $J = 5.5$), 7.83 (d, 1 H, $J = 5.0$), 7.87 (t, 1 H, $J = 6.0$), 7.98 (t, 1 H, $J = 7.5$), 8.10–8.04 (m, 1 H), 8.31

(t, 1 H, $J = 7.5$), 8.41 (t, 2 H, $J = 8.5$), 8.56 (d, 1 H, $J = 8.0$), 8.71 (d, 1 H, $J = 8.0$), 9.33 (d, 1 H, $J = 5.5$), 9.53 (d, 1 H, $J = 5.5$). **^{13}C{^{1}H} NMR** (ppm, CD$_3$CN-d$_3$, 125 MHz): δ =175.2, 158.0, 157.9, 157.2, 156.9, 153.6, 152.7, 138.7, 138.4, 136.5, 136.2, 128.8, 127.8, 127.6, 126.7, 124.0, 123.7, 117.4, 3.5, 3.4. Figure 2.16 shows the ^{1}H NMR and Figure 2.17 shows the ^{13}C NMR spectra.
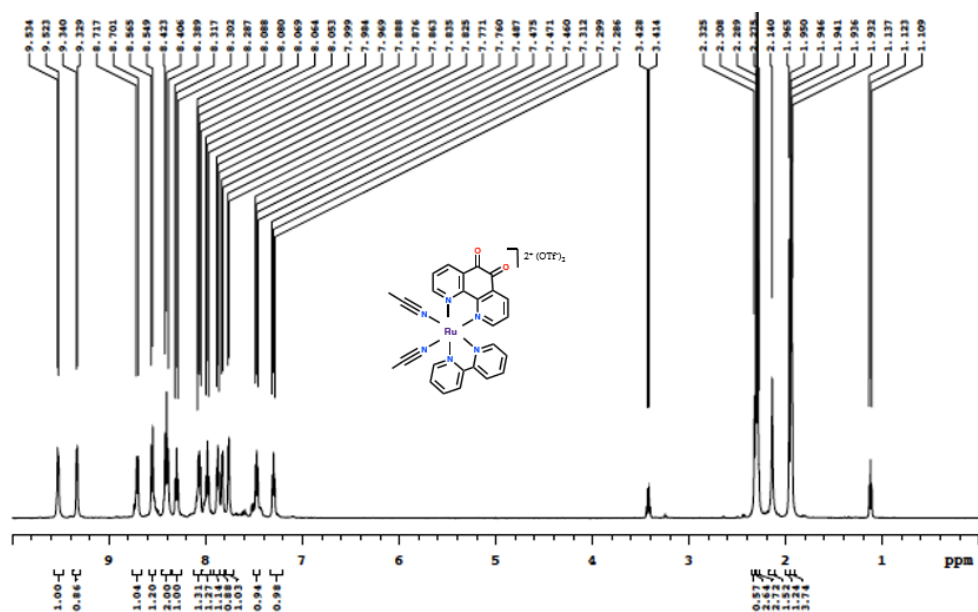
Figure 2.16. ^{1}H NMR spectra of [Ru(Bpy)(PhenO)(CH$_3$CN)$_2$](OTf)$_2$
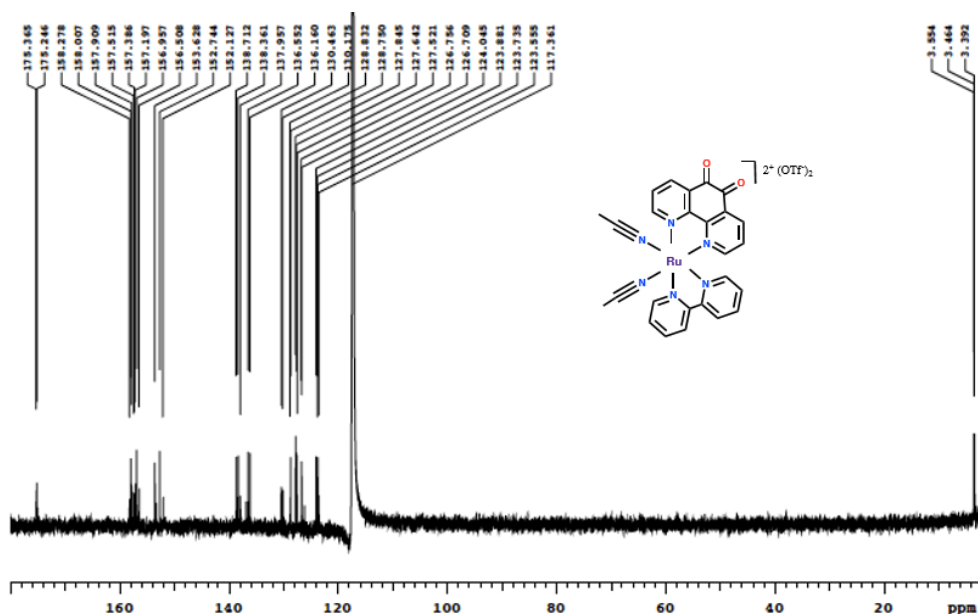
Figure 2.17. ^{13}C NMR spectra of [Ru(Bpy)(PhenO)(CH$_3$CN)$_2$](OTf)$_2$

Synthesis of Ru(bpy)₂(5,6-diamino-1,10-phenanthroline)(OTf)₂

Inside a glove box, [Ru(CH₃CN)₂(bipy)₂](OTf)₂ (made following the procedure reported in our previous paper, 199.5 mg, 0.2514 mmol) and 1,10-phenanthroline-5,6-diamine (52.8 mg, 0.251 mmol, 1 equivalent) were weighed into a 500 mL Schlenk flask. The flask was sealed with a 24/40 septum, brought out of the box, and attached to an Argon Schlenk line. A minimum volume of anhydrous, bubbled MeOH was added, and the solution was transferred through a double-ended needle to a triply evacuated and refilled screw-top Schlenk flask. The flask was heated to 75 ºC under Argon bubbler line pressure. The flask was sealed, and the temperature was set to 70 ºC. The reaction was stirred for 3 days, cooled to room temperature, and solvent was removed under reduced pressure. The crude product was sonicated in DCM, and the black liquid was removed via filtration through a double-ended needle to leave a reddish-orange solid (129.6 mg, 56.0 %).

¹H NMR (399.796 MHz, CD₃OD, 27.0 °C): δ 7.30 (ddd, J = 7.6, 5.6, 1.1 Hz, 2H), 7.50 (ddd, J = 7.6, 5.6, 1.1 Hz, 2H), 7.56 (d, J = 5.6 Hz, 2H), 7.63 (dd, J = 8.7, 5.1 Hz, 2H), 7.84 (d, J = 5.1 Hz, 2H), 7.91 (d, J = 5.6 Hz, 2H), 8.03 (ddd, J = 7.9, 7.6, 1.4 Hz, 2H), 8.13 (ddd, J = 7.9, 7.6, 1.4 Hz, 2H), 8.66–8.71 (m, 6H). **¹³C{¹H} NMR** (125.688 MHz, CDCl₃, 27.0 °C): δ 125.4, 125.5, 125.6, 128.7, 128.8, 131.0, 138.9, 139.0, 143.2, 148.5, 152.5, 152.8, 158.6, 158.8. **HRMS (ESI)** *m/z*: Calcd for $C_{33}H_{26}F_3N_8O_3RuS$ [M]⁺: 773.0847. Found: 773.0835. Figure 2.18 shows the ¹H NMR and Figure 2.19 shows the ¹³C NMR spectra.
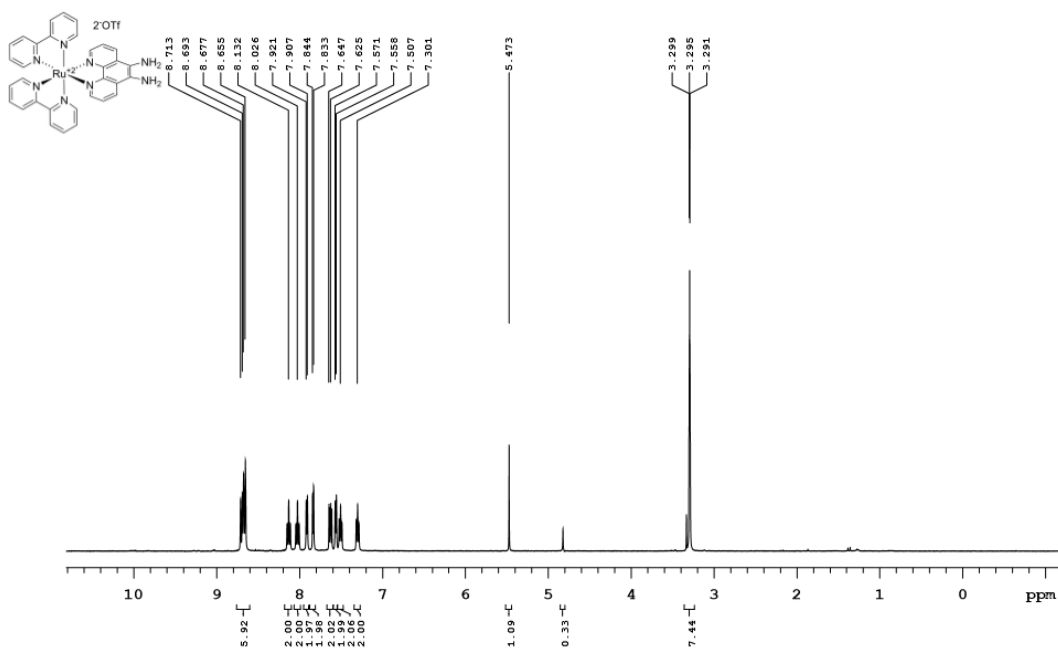
Figure 2.18. ^{1}H NMR spectra of [Ru(Bpy)$_2$(phendiamine)](OTf)$_2$.
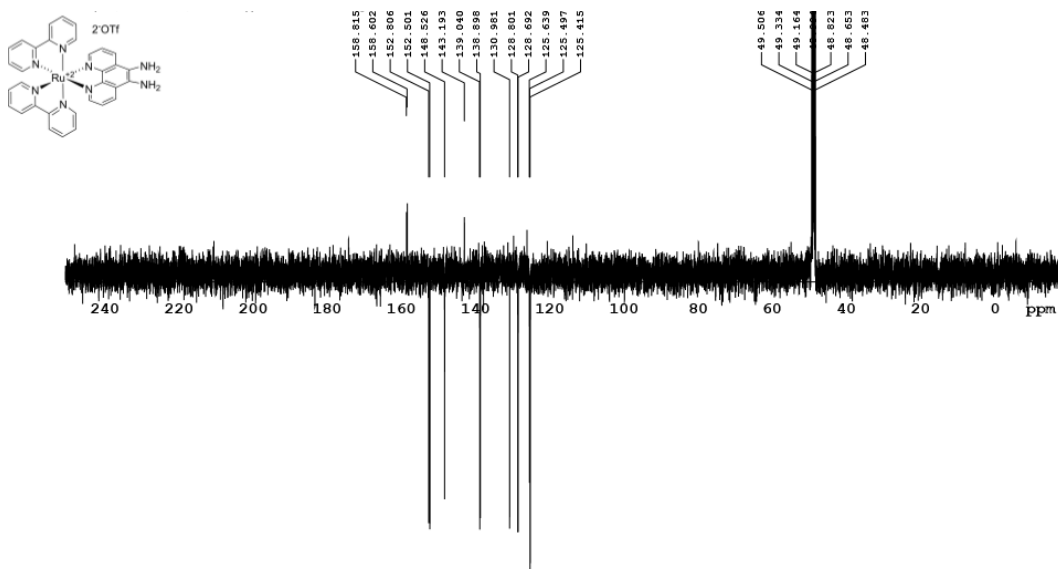
Figure 2.19. ^{13}C NMR spectra of [Ru(Bpy)$_2$(phendiamine)](OTf)$_2$.

Synthesis of Ru(PhenO)(Phen)Cl$_2$

Ru(PhenO)(DMSO)$_2$Cl$_2$ was prepared according to a reported procedure.[58] Ru(PhenO)(DMSO)$_2$Cl$_2$ (1 equivalent) and phen ligand (1 equivalent) were weighed into a 100 mL side-arm flask. The flask was then connected to a Schlenk line, evacuated; and refilled with N$_2$ (three cycles). 1,2-dichlorobenzene (0.016 M based on Ru(PhenO)(DMSO)$_2$Cl$_2$) bubbled with N$_2$ for 30 min was added to the flask, and the

flask was connected to a condenser. Then the flask was placed in an oil bath preheated to 150 °C and stirred overnight. During the reaction, the color of the solution turned brownish black with precipitate forming. After 18 h, the flask was cooled to room temperature, and 20 mL of hexane was added, and the precipitates were allowed to settle down. The dark purple product was collected by filtration through a Buchner funnel and by washing with copious amounts of hexane. The yield of the product after being dried under suction was >85% with some 1,2-dichlorobenzene still present, which was used for the next step without further purifications: **^{1}H NMR** (498.120 MHz, DMSO, 27.0 °C): δ 7.14 (1H, dd, J = 6.0 Hz, J = 6.0 Hz, aromatic CH), 7.50 (1H, dd, J = 5.4 Hz, J = 5.5 Hz, aromatic CH), 7.69 (1H, d, J = 5.5 Hz, aromatic CH), 7.86 (1H, d J = 5.1 Hz, aromatic CH), 7.98–8.00 (2H, m, aromatic CH), 8.14 (1H, d, J = 8.9 Hz, aromatic CH), 8.19 (1H, dd, J = 5.3 Hz, J = 5.3 Hz, aromatic CH), 8.27 (1H, d, J = 8.8 Hz, aromatic CH), 8.32 (1H, d, J = 8.0 Hz, aromatic CH), 8.46 (1H, d, J = 7.1 Hz, aromatic CH), 8.70 (1H, d, J = 7.8 Hz, aromatic CH), 10.15 (1H, d, J = 4.8 Hz, aromatic CH), 10.20 (1H, d, J = 4.7 Hz, aromatic CH). **^{13}C{^{1}H} NMR** (125.686 MHz, DMSO, 27.7 °C): δ 124.4, 124.9, 126.1, 126.2, 127.1, 127.5, 129.5, 129.6, 130.4, 130.6, 130.7, 132.1, 132.8, 134.0, 148.9, 150.2, 153.1, 153.9, 156.0, 157.0, 157.8, 159.4, 174.8, 175.0. **HRMS (ESI)** m/z Calcd. for $C_{24}H_{14}Cl_2N_4O_2{}^{102}Ru$ (M$^+$): 561.9532. Found: 561.9529. Figure 2.20 shows the ^{1}H NMR and Figure 2.21 shows the ^{13}C NMR spectra.
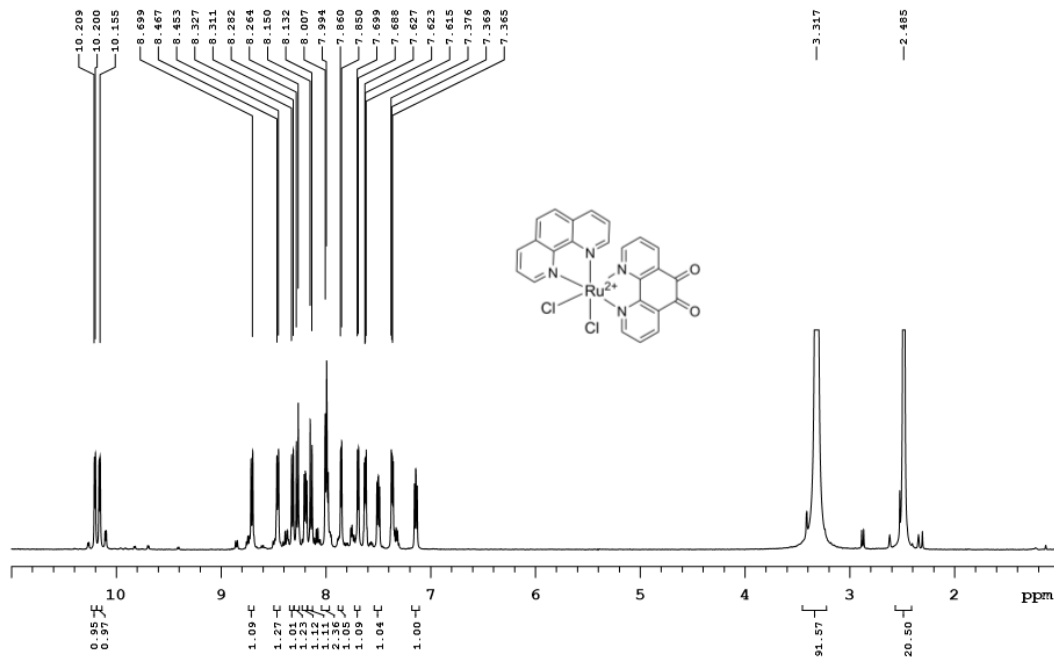
Figure 2.20. ^{1}H NMR spectra of [Ru(Phen)(PhenO)]Cl$_2$.
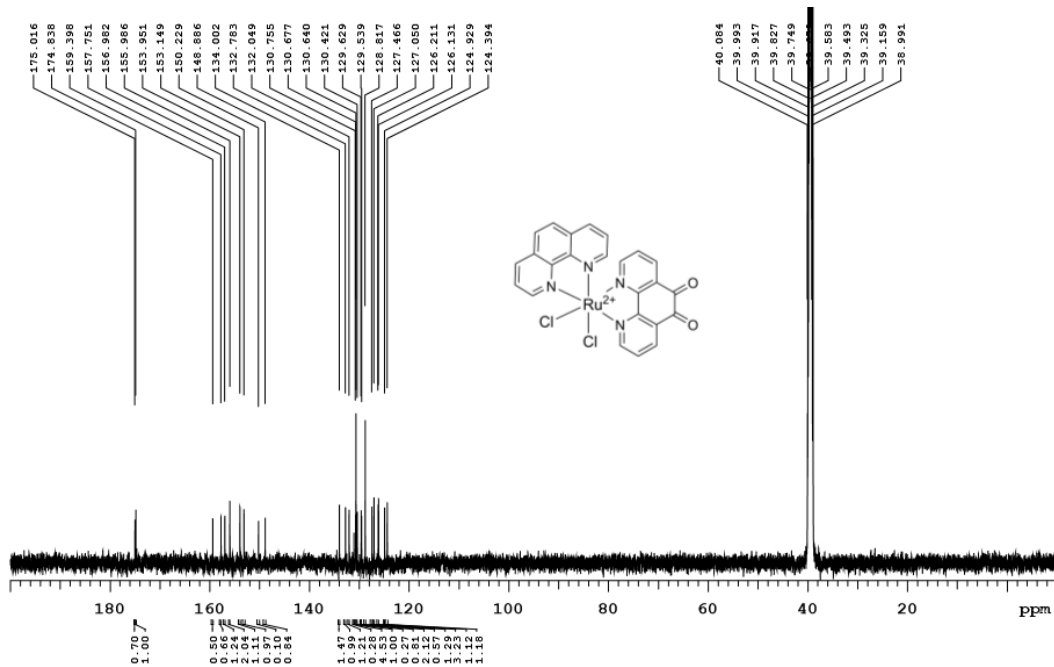
Figure 2.21. ^{13}C NMR spectra of [Ru(Phen)(PhenO)]Cl$_2$.

Synthesis of [Ru(PhenO)(Phen)(MeCN)$_2$](BF$_4$)$_2$

Both Ru(PhenO)(phen)Cl$_2$ (1 equivalent) and AgBF$_4$ (2 equivalents) were weighed into a 100 ml side arm flask inside the glove box. The flask was wrapped in aluminum foil, connected to a Schlenk line, and then evacuated and refilled with N$_2$ (three cycles). Then, freshly distilled MeCN (0.02 M based on Ru-(bis-bipyridine)$_2$Cl$_2$) was added using a gas tight syringe, and the resulting suspension was stirred at room temperature. After 48 h, the stirring stopped, and the precipitates were allowed to settle down. After an hour, the dark reddish-brown solution was transferred into another side arm flask by cannula filtration. The grayish-white precipitate was washed with additional MeCN (2 × 10 mL), and the filtrate was transferred to the same flask. Combined filtrate was concentrated using rotavapor, resulting in a dark brown product, which was dissolved using minimum MeCN and passed through a Celite plug. Additional MeCN was passed until no further brown color on the Celite plug was observed. The filtrate was concentrated again using rotavapor, and purified by crystallization with MeCN/Et$_2$O to give 83% of the target compound: **^{1}H NMR** (498.120 MHz, CD$_3$CN, 27.0 °C): δ 2.19 (3H, s, CH$_3$), 2.35 (3H, s, CH$_3$), 7.30–7.33 (1H, m, aromatic CH), 7.62–7.65 (1H, m, aromatic CH), 7.68 (1H, d, J = 5.3 Hz, aromatic CH), 8.08–8.12 (2H, m, aromatic CH), 8.19–8.23 (2H, m, aromatic CH), 8.31 (1H, d, J = 8.8 Hz, aromatic CH), 8.35 (1H, d, J = 7.8 Hz, aromatic CH), 8.55 (1H, d, J = 8.1 Hz, aromatic CH), 8.76 (1H, d, J = 7.7 Hz, aromatic CH), 8.88 (1H, d, J = 8.1 Hz, aromatic CH), 9.63 (1H, d, J = 5.1 Hz, aromatic CH), 9.67 (1H, d, J = 5.1 Hz, aromatic CH). **^{13}C{^{1}H} NMR** (125.685 MHz, CD$_3$CN, 27.0 °C): δ 3.5 (2 CH$_3$), 125.3, 126.2, 126.4, 126.7, 127.7, 127.8, 127.9, 128.7, 130.1, 130.6, 131.0, 136.1, 136.6, 137.4, 137.7, 147.8, 148.5, 153.5, 154.2, 156.7, 157.4, 158.3, 175.2, 175.4. **HRMS (ESI)** m/z Calcd. for C$_{28}$H$_{20}$N$_6$O$_2$^{102}Ru (M^{2+}): 287.034. Found: 287.034. Figure 2.22 shows the ^{1}H NMR and Figure 2.23 shows the ^{13}C NMR spectra.
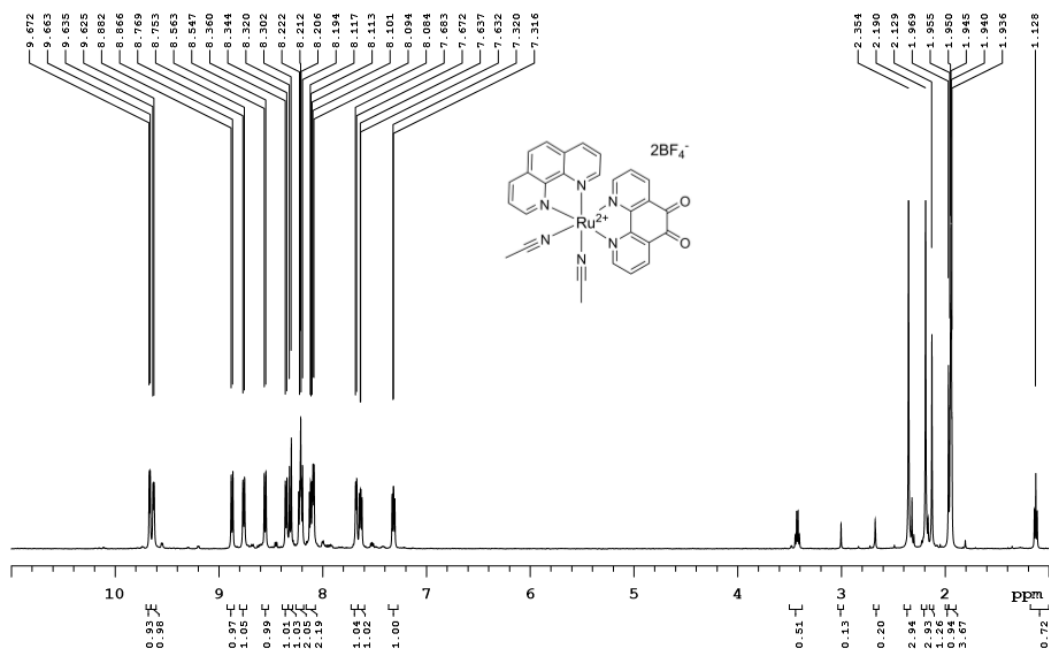
Figure 2.22. ^{1}H NMR spectra of [Ru(Phen)(PhenO)(CH$_3$CN)$_2$](BF$_4$)$_2$.
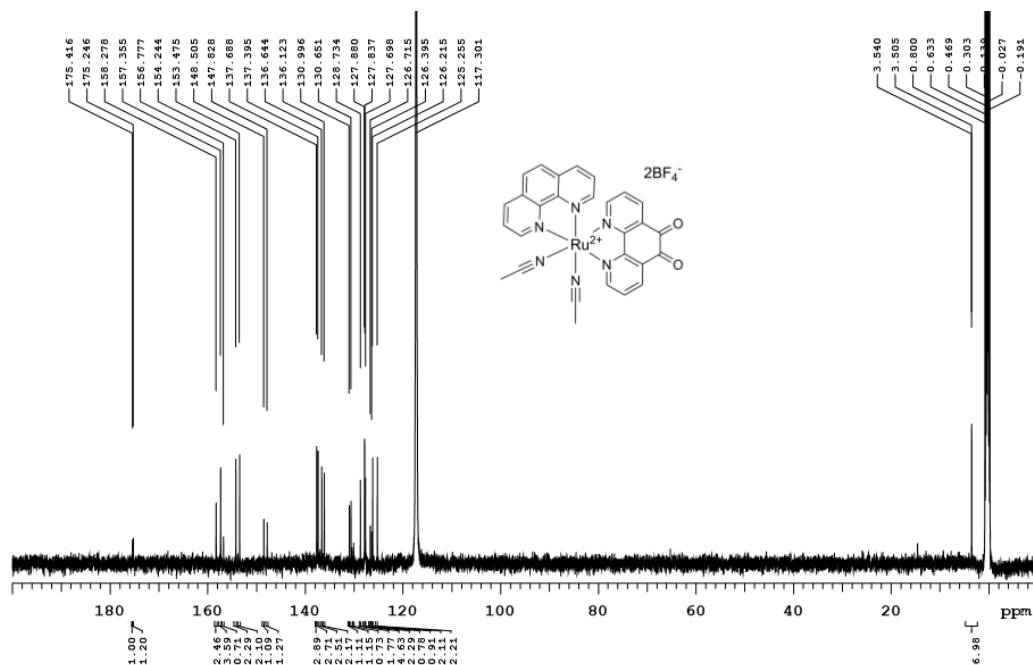
Figure 2.23. ^{13}C NMR spectra of [Ru(Phen)(PhenO)(CH$_3$CN)$_2$](BF$_4$)$_2$.

Synthesis of [Ru(PhenO)(Phen)(Bpy)](BF$_4$)$_2$

[Ru(PhenO)(phen)(MeCN)$_2$](BF$_4$)$_2$ (31 mg, 0.0402 mmol) and bpy ligand (6.1 mg, 0.0402 mmol) were weighed into a 15 mL side arm flask. Then the flask was connected to a Schlenk line, evacuated, and refilled with N$_2$ (three cycles). To the flask, 3.0 mL

of absolute ethanol and 1.0 mL of distilled water (both solvents were bubbled with N_2 before use) were added and then connected to a condenser. The content in the flask was refluxed overnight under N_2 atmosphere. After 16 h, the heating was stopped, and the reaction mixture was cooled down. The content was concentrated under reduced pressure using rotavapor, giving a reddish-brown solid product.

^{1}H NMR (498.120 MHz, CD$_3$CN, 26.9 °C): δ 7.25 (1H, t J = 6.4 Hz m, aromatic CH), 7.43 (1H, dd, J = 5.7 Hz, J=5.7 Hz, aromatic CH), 7.49 (1H, t, J = 6.6 Hz aromatic CH), 7.57 (1H, d, J = 5.4 Hz, aromatic CH), 7.61–7.63 (1H, m, aromatic CH), 7.67 (1H, dd, J = 5.8 Hz, J = 5.7 Hz, aromatic CH), 7.76–7.79 (2H, m, aromatic CH), 7.98– 8.04 (2H, m, aromatic CH), 8.10–8.16 (4H, m, aromatic CH), 8.22 (1H, d, J = 7.9 Hz, aromatic CH), 8.44–8.45 (2H, m, aromatic CH), 8.52–8.58 (3H, m, aromatic CH), 8.66 (1H, d, J = 8.1 Hz, aromatic CH), 8.74 (1H, d, J = 4.5 Hz, aromatic CH). **^{13}C{^{1}H} NMR** (125.685 MHz, CD$_3$CN, 27.7 °C): δ 121.6, 124.3, 124.4, 125.3, 126.1, 126.2, 127.5, 128.6, 128.7, 130.6, 130.7, 131.2, 135.8, 135.9, 137.3, 137.4, 138.1, 138.3, 139.5, 147.4, 147.5, 148.1, 152.1, 152.5, 152.7, 153.0, 156.3, 156.6, 156.7, 156.8, 157.0, 157.3, 175.3, 175.4. **HRMS (ESI)** m/z Calcd. for C$_{34}$H$_{22}$N$_6$O$_2$^{102}Ru (M^{2+}): 324.0418. Found: 324.0415. Figure 2.24 shows the ^{1}H NMR and Figure 2.25 shows the ^{13}C NMR spectra.
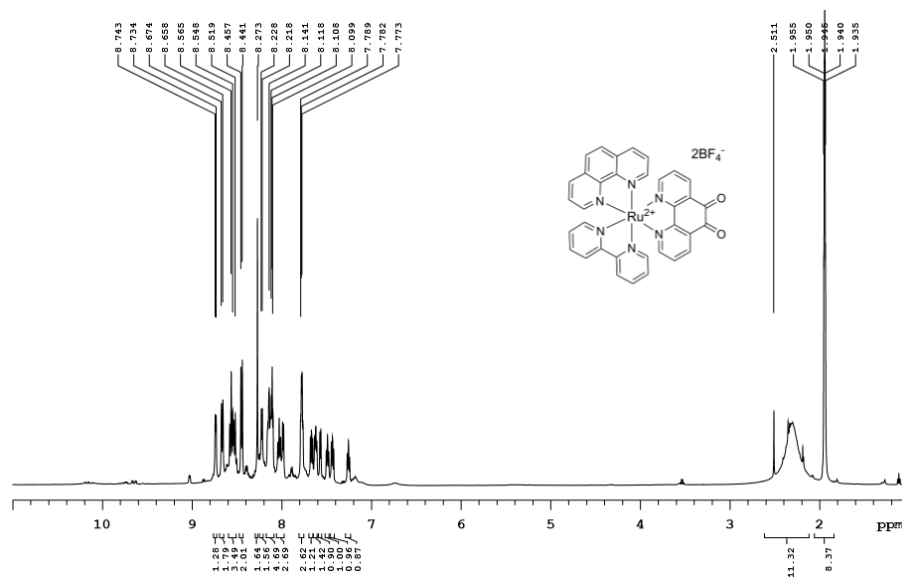
Figure 2.24. ^{1}H NMR spectra of [Ru(phen)(PhenO)(bpy)](BF$_4$)$_2$.
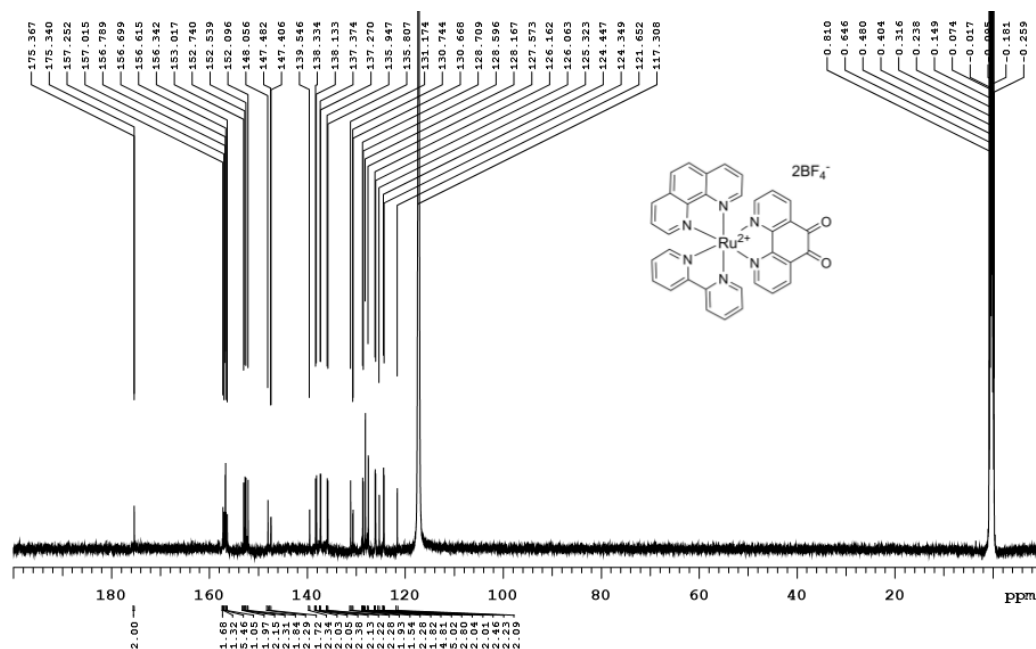
Figure 2.25. ^{13}C NMR spectra of [Ru(phen)(PhenO)(bpy)](BF$_4$)$_2$.

Metalation of Chromophore onto SC-phen.

[Ru(Mebpy)$_2$(CH$_3$CN)$_2$]$^{2+}$ (6.0 mg, 0.007 mmol), [Ru(^{t}Bubpy)$_2$(CH$_3$CN)$_2$]$^{2+}$ (6.0 mg, 0.006 mmol), or [Ru(PhenO)(bpy)(CH$_3$CN)$_2$]$^{2+}$ (6.0 mg, 0.006 mmol) were weighed out into a screw cap Schlenk tube inside the glovebox. Distilled dichloromethane (0.8 mL) and THF (4.0 mL) were added to the Schlenk tube. SC-phen electrodes were placed in the Schlenk tube after being kept in the nitrogen flow for a minute. Schlenk tube was heated at 70 °C for 4 hours using a paraffin oil bath. The Schlenk tube was removed from the oil bath and allow to cool down to room temperature. The electrodes were rinsed by cannulating ~5 ml CH$_2$Cl$_2$ into the flask and repeated two more times. The metalated electrodes were kept under N$_2$ and in the dark and tested within 24 h. The prepared electrodes in this manner are labelled SC-[(phen)Ru(Mebpy)$_2$]$^{2+}$, SC-[(phen)Ru(^{t}Bubpy)$_2$]$^{2+}$, and SC-[(phen)Ru(PhenO)(bpy)]$^{2+}$, which contain Mebpy, ^{t}Bubpy, or PhenO ligands (hereon denoted as SC-RuMePhen, SC-Ru^{t}BuPhen, and SC-RuOPhen), respectively.

Synthesis of dimeric chromophore onto SC-RuOPhen.

4.8 mL anhydrous ethanol containing [Ru(bipy)$_2$(phen-diamine)]$^{2+}$ (phen-diamine = 1,10-phenanthroline-5,6-diamine; 5.0 mg, 0.006 mmol) were cannulated into a screw

cap Schlenk tube with SC-RuOPhen electrodes. The flask was heated at 80 °C for 1h. Then, the electrodes were rinsed with anhydrous ethanol (~5.0 mL each) three times after the flask cooled down to room temperature.

Photoelectrochemistry.

For photoelectrochemistry studies, a 0.1 M $HClO_4$ solution containing hydroquinone (pH = 1.0), or a 0.1 M $NaClO_4$ solution containing either hydroquinone (pH = 7.0) or Et_3N (pH = 12.6) were used. Synthesized TiO_2-Ru-polypyridyl electrodes were the working electrode. Photoanodes were synthesized and tested at least 2–3 times for each medium (except for SC-Ru^{t}BuPhen under basic conditions due to its poor performance), and the results presented here are illustrative. The reference and counter electrodes were saturated calomel electrode (SCE) and platinum gauze, respectively. A homemade 100 mL four-neck quartz flask with a flat window was used as the reaction flask. The electrolyte was stirred using a magnetic bar at 500 rpm throughout the measurements. Prior to each measurement, the solution was purged with argon for 30 min, followed by maintaining an argon blanket on top of the solution. The light source was a Newport QEPVSI-b system (300 W Xe lamp with Cornerstone M 260 monochromator), and the incident light intensity was measured with a Thorlab S121C light meter, eq 2.2 was used for calculating the IPCE at any specific wavelength:[81,82]

$$IPCE\ (\%) = (1240 \text{ x } i) / (P \text{ x } \lambda) \tag{2.2}$$

where i is the obtained photocurrent density (mA cm^{-2}), P is light power density (mW cm^{-2}), and λ is the specific wavelength (nm).

2.5 References

(1) Tilley, S. D. Recent Advances and Emerging Trends in Photo-Electrochemical Solar Energy Conversion. *Advanced Energy Materials* **2019**, *9* (2), 1802877. https://doi.org/10.1002/aenm.201802877.

(2) Chu, S.; Cui, Y.; Liu, N. The Path towards Sustainable Energy. *Nature Mater* **2017**, *16* (1), 16–22. https://doi.org/10.1038/nmat4834.

(3) Lewis, N. S. Research Opportunities to Advance Solar Energy Utilization. *Science* **2016**, *351* (6271), aad1920. https://doi.org/10.1126/science.aad1920.

(4) Zhu, X.-G.; Long, S. P.; Ort, D. R. What Is the Maximum Efficiency with Which Photosynthesis Can Convert Solar Energy into Biomass? *Current Opinion in Biotechnology* **2008**, *19* (2), 153–159. https://doi.org/10.1016/j.copbio.2008.02.004.

(5) Zhang, B.; Sun, L. Artificial Photosynthesis: Opportunities and Challenges of Molecular Catalysts. *Chem. Soc. Rev.* **2019**, *48* (7), 2216–2264. https://doi.org/10.1039/C8CS00897C.

(6) Niu, F.; Wang, D.; Li, F.; Liu, Y.; Shen, S.; Meyer, T. J. Hybrid Photoelectrochemical Water Splitting Systems: From Interface Design to System Assembly. *Advanced Energy Materials* **2020**, *10* (11), 1900399. https://doi.org/10.1002/aenm.201900399.

(7) Yan, Z.; Hitt, J. L.; Turner, J. A.; Mallouk, T. E. Renewable Electricity Storage Using Electrolysis. *Proc. Natl. Acad. Sci. U.S.A.* **2020**, *117* (23), 12558–12563. https://doi.org/10.1073/pnas.1821686116.

(8) Lewis, N. S. A Prospective on Energy and Environmental Science. *Energy Environ. Sci.* **2019**, *12* (1), 16–18. https://doi.org/10.1039/C8EE90070A.

(9) Concepcion, J. J.; House, R. L.; Papanikolas, J. M.; Meyer, T. J. Chemical Approaches to Artificial Photosynthesis. *Proc. Natl. Acad. Sci. U.S.A.* **2012**, *109* (39), 15560–15564. https://doi.org/10.1073/pnas.1212254109.

(10) Davis, S. J.; Caldeira, K.; Matthews, H. D. Future CO_2 Emissions and Climate Change from Existing Energy Infrastructure. *Science* **2010**, *329* (5997), 1330–1333. https://doi.org/10.1126/science.1188566.

(11) Zhang, J. Z.; Reisner, E. Advancing Photosystem II Photoelectrochemistry for Semi-Artificial Photosynthesis. *Nat Rev Chem* **2019**, *4* (1), 6–21. https://doi.org/10.1038/s41570-019-0149-4.

(12) Low, J.; Jiang, C.; Cheng, B.; Wageh, S.; Al-Ghamdi, A. A.; Yu, J. A Review of Direct Z-Scheme Photocatalysts. *Small Methods* **2017**, *1* (5), 1700080. https://doi.org/10.1002/smtd.201700080.

(13) Fujishima, A.; Honda, K. Electrochemical Photolysis of Water at a Semiconductor Electrode. *Nature* **1972**, *238* (5358), 37–38. https://doi.org/10.1038/238037a0.

(14) Chen, S.; Hossain, M. N.; Chen, A. Significant Enhancement of the Photoelectrochemical Activity of $CuWO_4$ by Using a Cobalt Phosphate Nanoscale Thin Film. *ChemElectroChem* **2018**, *5* (3), 523–530. https://doi.org/10.1002/celc.201700991.

(15) Wang, Z.; Inoue, Y.; Hisatomi, T.; Ishikawa, R.; Wang, Q.; Takata, T.; Chen, S.; Shibata, N.; Ikuhara, Y.; Domen, K. Overall Water Splitting by Ta3N5 Nanorod Single Crystals Grown on the Edges of KTaO3 Particles. *Nat Catal* **2018**, *1* (10), 756–763. https://doi.org/10.1038/s41929-018-0134-1.

(16) Agbe, H.; Nyankson, E.; Raza, N.; Dodoo-Arhin, D.; Chauhan, A.; Osei, G.; Kumar, V.; Kim, K.-H. Recent Advances in Photoinduced Catalysis for Water Splitting and Environmental Applications. *Journal of Industrial and Engineering Chemistry* **2019**, *72*, 31–49. https://doi.org/10.1016/j.jiec.2019.01.004.

(17) Wu, L.; Eberhart, M.; Shan, B.; Nayak, A.; Brennaman, M. K.; Miller, A. J. M.; Shao, J.; Meyer, T. J. Stable Molecular Surface Modification of Nanostructured, Mesoporous Metal Oxide Photoanodes by Silane and Click Chemistry. *ACS Appl. Mater. Interfaces* **2019**, *11* (4), 4560–4567. https://doi.org/10.1021/acsami.8b17824.

(18) Xu, P.; McCool, N. S.; Mallouk, T. E. Water Splitting Dye-Sensitized Solar Cells. *Nano Today* **2017**, *14*, 42–58. https://doi.org/10.1016/j.nantod.2017.04.009.

(19) Brennaman, M. K.; Dillon, R. J.; Alibabaei, L.; Gish, M. K.; Dares, C. J.; Ashford, D. L.; House, R. L.; Meyer, G. J.; Papanikolas, J. M.; Meyer, T. J. Finding the Way to Solar Fuels with Dye-Sensitized Photoelectrosynthesis Cells. *J. Am. Chem. Soc.* **2016**, *138* (40), 13085–13102. https://doi.org/10.1021/jacs.6b06466.

(20) Orbelli Biroli, A.; Tessore, F.; Di Carlo, G.; Pizzotti, M.; Benazzi, E.; Gentile, F.; Berardi, S.; Bignozzi, C. A.; Argazzi, R.; Natali, M.; Sartorel, A.; Caramori, S. Fluorinated Zn II Porphyrins for Dye-Sensitized Aqueous Photoelectrosynthetic Cells. *ACS Appl. Mater. Interfaces* **2019**, *11* (36), 32895–32908. https://doi.org/10.1021/acsami.9b08042.

(21) Shaw, G. B.; Styers-Barnett, D. J.; Gannon, E. Z.; Granger, J. C.; Papanikolas, J. M. Interligand Electron Transfer Dynamics in [Os(Bpy) 3] 2+ : Exploring the Excited State Potential Surfaces with Femtosecond Spectroscopy. *J. Phys. Chem. A* **2004**, *108* (23), 4998–5006. https://doi.org/10.1021/jp0363850.

(22) Lanoë, P.-H.; Chan, J.; Groué, A.; Gontard, G.; Jutand, A.; Rager, M.-N.; Armaroli, N.; Monti, F.; Barbieri, A.; Amouri, H. Cyclometalated N-Heterocyclic Carbene Iridium(III) Complexes with Naphthalimide Chromophores: A Novel Class of Phosphorescent Heteroleptic Compounds. *Dalton Trans.* **2018**, *47* (10), 3440–3451. https://doi.org/10.1039/C7DT04369D.

(23) Shan, B.; Nayak, A.; Brennaman, M. K.; Liu, M.; Marquard, S. L.; Eberhart, M. S.; Meyer, T. J. Controlling Vertical and Lateral Electron Migration Using a Bifunctional Chromophore Assembly in Dye-Sensitized Photoelectrosynthesis Cells. *J. Am. Chem. Soc.* **2018**, *140* (20), 6493–6500. https://doi.org/10.1021/jacs.8b03453.

(24) Zigler, D. F.; Morseth, Z. A.; Wang, L.; Ashford, D. L.; Brennaman, M. K.; Grumstrup, E. M.; Brigham, E. C.; Gish, M. K.; Dillon, R. J.; Alibabaei, L.; Meyer, G. J.; Meyer, T. J.; Papanikolas, J. M. Disentangling the Physical Processes Responsible for the Kinetic Complexity in Interfacial Electron Transfer of Excited Ru(II) Polypyridyl Dyes on TiO 2. *J. Am. Chem. Soc.* **2016**, *138* (13), 4426–4438. https://doi.org/10.1021/jacs.5b12996.

(25) Amthor, S.; Braun, H.; Gröne, J.; Nauroozi, D.; Jacob, T.; Rau, S. Tailored Protective Groups for Surface Immobilization of Ruthenium Dyes. *Dalton Trans.* **2020**, *49* (12), 3735–3742. https://doi.org/10.1039/C9DT03591E.

(26) Troian-Gautier, L.; Marcélis, L.; De Winter, J.; Gerbaux, P.; Moucheron, C. Two Ruthenium Complexes Capable of Storing Multiple Electrons on a Single Ligand – Photophysical, Photochemical and Electrochemical Properties of [Ru(Phen) 2 (TAPHAT)] 2+ and [Ru(Phen) 2

(TAPHAT)Ru(Phen) $_2$] $^{4+}$. *Dalton Trans.* **2017**, *46* (44), 15287–15300. https://doi.org/10.1039/C7DT03232C.

(27) Bangle, R.; Sampaio, R. N.; Troian-Gautier, L.; Meyer, G. J. Surface Grafting of Ru(II) Diazonium-Based Sensitizers on Metal Oxides Enhances Alkaline Stability for Solar Energy Conversion. *ACS Appl. Mater. Interfaces* **2018**, *10* (3), 3121–3132. https://doi.org/10.1021/acsami.7b16641.

(28) Evans, R. C.; Douglas, P.; Winscom, C. J. Coordination Complexes Exhibiting Room-Temperature Phosphorescence: Evaluation of Their Suitability as Triplet Emitters in Organic Light Emitting Diodes. *Coordination Chemistry Reviews* **2006**, *250* (15–16), 2093–2126. https://doi.org/10.1016/j.ccr.2006.02.007.

(29) Yuan, Y.-J.; Yu, Z.-T.; Chen, D.-Q.; Zou, Z.-G. Metal-Complex Chromophores for Solar Hydrogen Generation. *Chem. Soc. Rev.* **2017**, *46* (3), 603–631. https://doi.org/10.1039/C6CS00436A.

(30) Purnama, I.; Salmahaminati, S.; Abe, M.; Hada, M.; Kubo, Y.; Mulyana, J. Y. Factors Influencing the Photoelectrochemical Device Performance Sensitized by Ruthenium Polypyridyl Dyes. *Dalton Trans.* **2019**, *48* (2), 688–695. https://doi.org/10.1039/C8DT03502D.

(31) Raber, M. M.; Brady, M. D.; Troian-Gautier, L.; Dickenson, J. C.; Marquard, S. L.; Hyde, J. T.; Lopez, S. J.; Meyer, G. J.; Meyer, T. J.; Harrison, D. P. Fundamental Factors Impacting the Stability of Phosphonate-Derivatized Ruthenium Polypyridyl Sensitizers Adsorbed on Metal Oxide Surfaces. *ACS Appl. Mater. Interfaces* **2018**, *10* (26), 22821–22833. https://doi.org/10.1021/acsami.8b04587.

(32) Materna, K. L.; Crabtree, R. H.; Brudvig, G. W. Anchoring Groups for Photocatalytic Water Oxidation on Metal Oxide Surfaces. *Chem. Soc. Rev.* **2017**, *46* (20), 6099–6110. https://doi.org/10.1039/C7CS00314E.

(33) Surendranath, Y.; Kanan, M. W.; Nocera, D. G. Mechanistic Studies of the Oxygen Evolution Reaction by a Cobalt-Phosphate Catalyst at Neutral pH. *J. Am. Chem. Soc.* **2010**, *132* (46), 16501–16509. https://doi.org/10.1021/ja106102b.

(34) Watanabe, M.; Motoo, S. Electrocatalysis by Ad-Atoms. *Journal of Electroanalytical Chemistry and Interfacial Electrochemistry* **1975**, *60* (3), 275–283. https://doi.org/10.1016/S0022-0728(75)80262-2.

(35) Alibabaei, L.; Dillon, R. J.; Reilly, C. E.; Brennaman, M. K.; Wee, K.-R.; Marquard, S. L.; Papanikolas, J. M.; Meyer, T. J. Chromophore-Catalyst Assembly for Water Oxidation Prepared by Atomic Layer Deposition. *ACS Appl. Mater. Interfaces* **2017**, *9* (44), 39018–39026. https://doi.org/10.1021/acsami.7b11905.

(36) Combellas, C.; Kanoufi, F.; Pinson, J.; Podvorica, F. I. Sterically Hindered Diazonium Salts for the Grafting of a Monolayer on Metals. *J. Am. Chem. Soc.* **2008**, *130* (27), 8576–8577. https://doi.org/10.1021/ja8018912.

(37) Cao, C.; Zhang, Y.; Jiang, C.; Qi, M.; Liu, G. Advances on Aryldiazonium Salt Chemistry Based Interfacial Fabrication for Sensing Applications. *ACS Appl. Mater. Interfaces* **2017**, *9* (6), 5031–5049. https://doi.org/10.1021/acsami.6b16108.

(38) Volatron, F.; Noël, J.-M.; Rinfray, C.; Decorse, P.; Combellas, C.; Kanoufi, F.; Proust, A. Electron Transfer Properties of a Monolayer of Hybrid Polyoxometalates on Silicon. *J. Mater. Chem. C* **2015**, *3* (24), 6266–6275. https://doi.org/10.1039/C5TC00074B.

(39) Leroux, Y. R.; Fei, H.; Noël, J.-M.; Roux, C.; Hapiot, P. Efficient Covalent Modification of a Carbon Surface: Use of a Silyl Protecting Group To Form an Active Monolayer. *J. Am. Chem. Soc.* **2010**, *132* (40), 14039–14041. https://doi.org/10.1021/ja106971x.

(40) Malmos, K.; Dong, M.; Pillai, S.; Kingshott, P.; Besenbacher, F.; Pedersen, S. U.; Daasbjerg, K. Using a Hydrazone-Protected Benzenediazonium Salt to Introduce a Near-Monolayer of Benzaldehyde on Glassy Carbon Surfaces. *J. Am. Chem. Soc.* **2009**, *131* (13), 4928–4936. https://doi.org/10.1021/ja809816x.

(41) Menanteau, T.; Levillain, E.; Downard, A. J.; Breton, T. Evidence of Monolayer Formation via Diazonium Grafting with a Radical Scavenger: Electrochemical, AFM and XPS Monitoring. *Phys. Chem. Chem. Phys.* **2015**, *17* (19), 13137–13142. https://doi.org/10.1039/C5CP01401H.

(42) Cao, L.; Fang, G.; Wang, Y. Electroreduction of Viologen Phenyl Diazonium Salts as a Strategy To Control Viologen Coverage on Electrodes. *Langmuir* **2017**, *33* (4), 980–987. https://doi.org/10.1021/acs.langmuir.6b04317.

(43) Tran, QuangT.; Pellon, P.; Jeannin, O.; Geneste, F.; Lagrost, C. Multi-Modal Surface Grafting of [Trans-Bis(Aminodiphenylphosphine) Terpyridine-Ru(II)Cl]+Cl− Complex onto Glassy Carbon Electrode. *Electrochimica Acta* **2018**, *259*, 151–160. https://doi.org/10.1016/j.electacta.2017.10.142.

(44) Nguyen, V. Q.; Sun, X.; Lafolet, F.; Audibert, J.-F.; Miomandre, F.; Lemercier, G.; Loiseau, F.; Lacroix, J.-C. Unprecedented Self-Organized Monolayer of a Ru(II) Complex by Diazonium Electroreduction. *J. Am. Chem. Soc.* **2016**, *138* (30), 9381–9384. https://doi.org/10.1021/jacs.6b04827.

(45) Kim, Y.; Fournier, S.; Lau-Truong, S.; Decorse, P.; Devillers, C. H.; Lucas, D.; Harris, K. D.; Limoges, B.; Balland, V. Introducing Molecular Functionalities within High Surface Area Nanostructured ITO Electrodes through Diazonium Electrografting. *ChemElectroChem* **2018**, *5* (13), 1625–1630. https://doi.org/10.1002/celc.201800418.

(46) Wang, C.; Amiri, M.; Endean, R. T.; Martinez Perez, O.; Varley, S.; Rennie, B.; Rasu, L.; Bergens, S. H. Modular Construction of Photoanodes with Covalently Bonded Ru- and Ir-Polypyridyl Visible Light Chromophores. *ACS Appl. Mater. Interfaces* **2018**, *10* (29), 24533–24542. https://doi.org/10.1021/acsami.8b06605.

(47) Konduri, R.; Ye, H.; MacDonnell, F. M.; Serroni, S.; Campagna, S.; Rajeshwar, K. Ruthenium Photocatalysts Capable of Reversibly Storing up to Four Electrons in a Single Acceptor Ligand:

A Step Closer to Artificial Photosynthesis. *Angew. Chem.* **2002**, *114* (17), 3317–3319. https://doi.org/10.1002/1521-3757(20020902)114:17<3317::AID-ANGE3317>3.0.CO;2-R.

(48) Aslan, J. M.; Yousufuddin, M.; Boston, D. J.; MacDonnell, F. M. Quadruple Electron Storage Using Visible Light with Nitrogen-Heterocycles under Metal-Free Conditions. *Inorganica Chimica Acta* **2017**, *454*, 216–221. https://doi.org/10.1016/j.ica.2016.06.025.

(49) Hayes, D.; Kohler, L.; Hadt, R. G.; Zhang, X.; Liu, C.; Mulfort, K. L.; Chen, L. X. Excited State Electron and Energy Relays in Supramolecular Dinuclear Complexes Revealed by Ultrafast Optical and X-Ray Transient Absorption Spectroscopy. *Chem. Sci.* **2018**, *9* (4), 860–875. https://doi.org/10.1039/C7SC04055E.

(50) Tsuji, Y.; Yamamoto, K.; Yamauchi, K.; Sakai, K. Near-Infrared Light-Driven Hydrogen Evolution from Water Using a Polypyridyl Triruthenium Photosensitizer. *Angew Chem Int Ed* **2018**, *57* (1), 208–212. https://doi.org/10.1002/anie.201708996.

(51) Zhang, L.-J.; Wang, Y.-H.; Liu, J.; Xu, M.-C.; Zhang, X.-M. Efficient and Environmentally Friendly Glaser Coupling of Terminal Alkynes Catalyzed by Multinuclear Copper Complexes under Base-Free Conditions. *RSC Adv.* **2016**, *6* (34), 28653–28657. https://doi.org/10.1039/C6RA01262K.

(52) Rathnayaka, S. C.; Lindeman, S. V.; Mankad, N. P. Multinuclear Cu(I) Clusters Featuring a New Triply Bridging Coordination Mode of Phosphaamidinate Ligands. *Inorg. Chem.* **2018**, *57* (15), 9439–9445. https://doi.org/10.1021/acs.inorgchem.8b01422.

(53) Palomo, J. M. Solid-Phase Peptide Synthesis: An Overview Focused on the Preparation of Biologically Relevant Peptides. *RSC Adv.* **2014**, *4* (62), 32658–32672. https://doi.org/10.1039/C4RA02458C.

(54) Wang, J. C.; Hill, S. P.; Dilbeck, T.; Ogunsolu, O. O.; Banerjee, T.; Hanson, K. Multimolecular Assemblies on High Surface Area Metal Oxides and Their Role in Interfacial Energy and Electron Transfer. *Chem. Soc. Rev.* **2018**, *47* (1), 104–148. https://doi.org/10.1039/C7CS00565B.

(55) Shul, G.; Weissmann, M.; Bélanger, D. Electrochemical Formation of an Ultrathin Electroactive Film from 1,10-Phenanthroline on a Glassy Carbon Electrode in Acidic Electrolyte. *Langmuir* **2014**, *30* (22), 6612–6621. https://doi.org/10.1021/la500349t.

(56) Gunasekar, G. H.; Park, K.; Ganesan, V.; Lee, K.; Kim, N.-K.; Jung, K.-D.; Yoon, S. A Covalent Triazine Framework, Functionalized with Ir/N-Heterocyclic Carbene Sites, for the Efficient Hydrogenation of CO_2 to Formate. *Chem. Mater.* **2017**, *29* (16), 6740–6748. https://doi.org/10.1021/acs.chemmater.7b01539.

(57) Shul, G.; Weissmann, M.; Bélanger, D. Electrochemical Characterization of Glassy Carbon Electrode Modified with 1,10-Phenanthroline Groups by Two Pathways: Reduction of the Corresponding Diazonium Ions and Reduction of Phenanthroline. *Electrochimica Acta* **2015**, *162*, 146–155. https://doi.org/10.1016/j.electacta.2014.12.116.

(58) Pinczewska, A.; Sosna, M.; Bloodworth, S.; Kilburn, J. D.; Bartlett, P. N. High-Throughput Synthesis and Electrochemical Screening of a Library of Modified Electrodes for NADH Oxidation. *J. Am. Chem. Soc.* **2012**, *134* (43), 18022–18033. https://doi.org/10.1021/ja307390x.

(59) Buzzeo, M. C.; Hardacre, C.; Compton, R. G. Extended Electrochemical Windows Made Accessible by Room Temperature Ionic Liquid/Organic Solvent Electrolyte Systems. *ChemPhysChem* **2006**, *7* (1), 176–180. https://doi.org/10.1002/cphc.200500361.

(60) Murphy, D. M.; McNamara, K.; Richardson, P.; Sanchez-Romaguera, V.; Winpenny, R. E. P.; Yellowlees, L. J. Electrochemical and Spectroelectrochemical Studies of Complexes of 1,10-Phenanthroline-5,6-Dione. *Inorganica Chimica Acta* **2011**, *374* (1), 435–441. https://doi.org/10.1016/j.ica.2011.02.050.

(61) Liang, Y.; Nguyen, M. T.; Holliday, B. J.; Jones, R. A. Electrocatalytic Reduction of CO2 Using Rhenium Complexes with Dipyrido[3,2-a:2′,3′-c]Phenazine Ligands. *Inorganic Chemistry Communications* **2017**, *84*, 113–117. https://doi.org/10.1016/j.inoche.2017.08.002.

(62) Agnès, C.; Arnault, J.-C.; Omnès, F.; Jousselme, B.; Billon, M.; Bidan, G.; Mailley, P. XPS Study of Ruthenium Tris-Bipyridine Electrografted from Diazonium Salt Derivative on Microcrystalline Boron Doped Diamond. *Phys. Chem. Chem. Phys.* **2009**, *11* (48), 11647. https://doi.org/10.1039/b912468c.

(63) Singh, J.; Gusain, A.; Saxena, V.; Chauhan, A. K.; Veerender, P.; Koiry, S. P.; Jha, P.; Jain, A.; Aswal, D. K.; Gupta, S. K. XPS, UV–Vis, FTIR, and EXAFS Studies to Investigate the Binding Mechanism of N719 Dye onto Oxalic Acid Treated TiO$_2$ and Its Implication on Photovoltaic Properties. *J. Phys. Chem. C* **2013**, *117* (41), 21096–21104. https://doi.org/10.1021/jp4062994.

(64) Lund, T.; Nguyen, P. T.; Ruhland, T. Electrochemical Grafting of TiO2-Based Photo-Anodes and Its Effect in Dye-Sensitized Solar Cells. *Journal of Electroanalytical Chemistry* **2015**, *758*, 85–92. https://doi.org/10.1016/j.jelechem.2015.10.021.

(65) Jama, C.; Al Khawwam, A.; Loir, A.; Goudmand, P.; Dessaux, O.; Gengembre, L.; Grimblot, J. X-ray Photoelectron Spectroscopy Study of Carbon Nitride Coatings Deposited by IR Laser Ablation in a Remote Nitrogen Plasma Atmosphere. *Surface & Interface Analysis* **2001**, *31* (9), 815–824. https://doi.org/10.1002/sia.1110.

(66) Tang, H.; Li, Y.; Chen, Q.; Chen, B.; Qiao, Q.; Yang, W.; Wu, H.; Cao, Y. Efficient Yellow–Green Light-Emitting Cationic Iridium Complexes Based on 1,10-Phenanthroline Derivatives Containing Oxadiazole-Triphenylamine Unit. *Dyes and Pigments* **2014**, *100*, 79–86. https://doi.org/10.1016/j.dyepig.2013.07.029.

(67) Goss, C. A.; Abruna, H. D. Spectral, Electrochemical and Electrocatalytic Properties of 1,10-Phenanthroline-5,6-Dione Complexes of Transition Metals. *Inorg. Chem.* **1985**, *24* (25), 4263–4267. https://doi.org/10.1021/ic00219a012.

(68) Brennaman, M. K.; Patrocinio, A. O. T.; Song, W.; Jurss, J. W.; Concepcion, J. J.; Hoertz, P. G.; Traub, M. C.; Murakami Iha, N. Y.; Meyer, T. J. Interfacial Electron Transfer Dynamics

Following Laser Flash Photolysis of [Ru(Bpy) $_2$ ((4,4′-PO $_3$ H $_2$) $_2$ Bpy)] $^{2+}$ in TiO $_2$ Nanoparticle Films in Aqueous Environments. *ChemSusChem* **2011**, *4* (2), 216–227. https://doi.org/10.1002/cssc.201000356.

(69) Saito, D.; Yamazaki, Y.; Tamaki, Y.; Ishitani, O. Photocatalysis of a Dinuclear Ru(II)–Re(I) Complex for CO $_2$ Reduction on a Solid Surface. *J. Am. Chem. Soc.* **2020**, *142* (45), 19249–19258. https://doi.org/10.1021/jacs.0c09170.

(70) Kamata, R.; Kumagai, H.; Yamazaki, Y.; Sahara, G.; Ishitani, O. Photoelectrochemical CO $_2$ Reduction Using a Ru(II)–Re(I) Supramolecular Photocatalyst Connected to a Vinyl Polymer on a NiO Electrode. *ACS Appl. Mater. Interfaces* **2019**, *11* (6), 5632–5641. https://doi.org/10.1021/acsami.8b05495.

(71) Sahara, G.; Abe, R.; Higashi, M.; Morikawa, T.; Maeda, K.; Ueda, Y.; Ishitani, O. Photoelectrochemical CO $_2$ Reduction Using a Ru(Ⅱ)–Re(Ⅰ) Multinuclear Metal Complex on a p-Type Semiconducting NiO Electrode. *Chem. Commun.* **2015**, *51* (53), 10722–10725. https://doi.org/10.1039/C5CC02403J.

(72) Li, T.-T.; Shan, B.; Meyer, T. J. Stable Molecular Photocathode for Solar-Driven CO $_2$ Reduction in Aqueous Solutions. *ACS Energy Lett.* **2019**, *4* (3), 629–636. https://doi.org/10.1021/acsenergylett.8b02512.

(73) Koike, K.; Naito, S.; Sato, S.; Tamaki, Y.; Ishitani, O. Architecture of Supramolecular Metal Complexes for Photocatalytic CO2 Reduction. *Journal of Photochemistry and Photobiology A: Chemistry* **2009**, *207* (1), 109–114. https://doi.org/10.1016/j.jphotochem.2008.12.014.

(74) Gholamkhass, B.; Mametsuka, H.; Koike, K.; Tanabe, T.; Furue, M.; Ishitani, O. Architecture of Supramolecular Metal Complexes for Photocatalytic CO $_2$ Reduction: Ruthenium−Rhenium Bi- and Tetranuclear Complexes. *Inorg. Chem.* **2005**, *44* (7), 2326–2336. https://doi.org/10.1021/ic048779r.

(75) Tamaki, Y.; Ishitani, O. Supramolecular Photocatalysts for the Reduction of CO $_2$. *ACS Catal.* **2017**, *7* (5), 3394–3409. https://doi.org/10.1021/acscatal.7b00440.

(76) Tamaki, Y.; Koike, K.; Morimoto, T.; Ishitani, O. Substantial Improvement in the Efficiency and Durability of a Photocatalyst for Carbon Dioxide Reduction Using a Benzoimidazole Derivative as an Electron Donor. *Journal of Catalysis* **2013**, *304*, 22–28. https://doi.org/10.1016/j.jcat.2013.04.002.

(77) Tamaki, Y.; Watanabe, K.; Koike, K.; Inoue, H.; Morimoto, T.; Ishitani, O. Development of Highly Efficient Supramolecular CO $_2$ Reduction Photocatalysts with High Turnover Frequency and Durability. *Faraday Discuss.* **2012**, *155*, 115–127. https://doi.org/10.1039/C1FD00091H.

(78) Yeşildağ, A.; Ekinci, D. Covalent Attachment of Pyridine-Type Molecules to Glassy Carbon Surfaces by Electrochemical Reduction of in Situ Generated Diazonium Salts. Formation of Ruthenium Complexes on Ligand-Modified Surfaces. *Electrochimica Acta* **2010**, *55* (23), 7000–7009. https://doi.org/10.1016/j.electacta.2010.06.020.

(79) Mack, J. B. C.; Walker, K. L.; Robinson, S. G.; Zare, R. N.; Sigman, M. S.; Waymouth, R. M.; Du Bois, J. Mechanistic Study of Ruthenium-Catalyzed C–H Hydroxylation Reveals an Unexpected Pathway for Catalyst Arrest. *J. Am. Chem. Soc.* **2019**, *141* (2), 972–980. https://doi.org/10.1021/jacs.8b10950.

(80) Viala, C.; Coudret, C. An Expeditious Route to Cis-Ru(Bpy)2C12 (Bpy=2,2′-Bipyridine) Using Carbohydrates as Reducers. *Inorganica Chimica Acta* **2006**, *359* (3), 984–989. https://doi.org/10.1016/j.ica.2005.07.019.

(81) O'Regan, B.; Gratzelt, M. A Low-Cost, High-Efficiency Solar Cell Based on Dye-Sensitized Colloidal Ti02 Films. **1991**, *353*.

(82) Sabuzi, F.; Tiravia, M.; Vecchi, A.; Gatto, E.; Venanzi, M.; Floris, B.; Conte, V.; Galloni, P. Deposition of Tetraferrocenylporphyrins on ITO Surfaces for Photo-Catalytic O $_2$ Activation. *Dalton Trans.* **2016**, *45* (37), 14745–14753. https://doi.org/10.1039/C6DT01821A.

Chapter 3

N-Heterocyclic Carbene Organic Dyes Derived from 2,4,5,6-tetra(9*H*-carbazol-9-yl)isophthalonitrile (4CzIPN) Bonded to TiO$_2$ Surfaces[2]

3.1 Introduction

One hour of solar illumination of the planet contains the same amount of energy that Earth's population consumes in one year.[1–4] Solar energy is diffuse, intermittent, and must be stored for practical applications. Dye-sensitized photoelectrochemical cells (DSPEC) are being developed as solar energy conversion devices where sunlight is stored in chemical bonds through artificial photosynthesis.[5–11] The photoelectrodes in DSPECs typically consist of a photosensitizer (also called chromophore or dye), an electrocatalyst, and a semiconductor. These components operate together at the DSPEC photoanode to utilize solar energy to oxidize water, forming oxygen, protons, and electrons (OER = oxygen evolution reaction). Photocathodes in DSPEC typically convert the protons and electrons into hydrogen, or they utilize them to reduce CO$_2$ (COR = CO$_2$ reduction reaction).[5–7,11] An ideal DSPEC operates with high efficiencies in the visible light range, as this range makes up ~44% of the solar spectrum.[12,13]

Ru-polypyridyl complexes are among the most studied molecular chromophores in photoelectrochemical applications because they have strong, tunable metal-to-ligand charge transfer absorbances and because their excited singlet states undergo intersystem crossing (ISC) to form triplet states with useful lifetimes and redox potentials.[14–16] Organic chromophores offer metal-free alternatives that are composed of abundant, less-toxic elements.[17,18] Molecular chromophores typically are bonded to semiconductor surfaces via carboxylate- or phosphonate anchor groups.[19-21] These bonds are stable at pH below 5 and 7, respectively, but hydrolyze under alkaline

conditions.[19] The rates of the OER and COR can be higher under alkaline conditions than they are in acid.[20] As well, a wider range of earth-abundant electrocatalysts are more stable under alkaline and neutral conditions than they are in acid.[22,23] Thus, developing earth-abundant chromophores that are stable under alkaline conditions is an important strategy for constructing efficient, low-cost, visible light-driven OER- and COR-photoelectrodes.

Electrografting diazonium-modified chromophores to semiconductors has been reported by several groups.[24,25] Our group reported a stepwise construction of photoelectrodes that begins with electrografting 5-amino-1,10-phenanthroline (phen-NH$_2$) to semiconductor surfaces using standard diazonium electrochemistry. For example, TiO$_2$ was decorated with phen in this matter to prepare TiO$_2$-phen. The reaction between TiO$_2$-phen and dissolved *cis*-[Ru(bipy)$_2$(MeCN)$_2$]$^{2+}$ (bipy = 2,2-bipyridine) proceeds by displacement of the MeCN ligands to form the photoelectrode TiO$_2$-[(phen)Ru(bipy)$_2$]$^{2+}$, with the Ru-polypyridyl chromophore bonded to the semiconductor surface through the C5 carbon in the phen ligand.[26,27] This chapter describes the complex chromophore-semiconductor photoelectrodes containing multiple metal centers by utilizing linking groups in a manner like the solid-phase synthesis of proteins.[27] This methodology avoids difficulties such as preparing and purifying insoluble, high molecular-weight chromophores before they are attached to semiconductor surfaces. The photoanodes prepared by diazonium electrografting were more stable under alkaline conditions (pH 12) than those constructed with phosphonic acid linkages, Scheme 3.1.[27]

Hydrolyze under basic conditions   Stable under basic conditions (pH: 12)
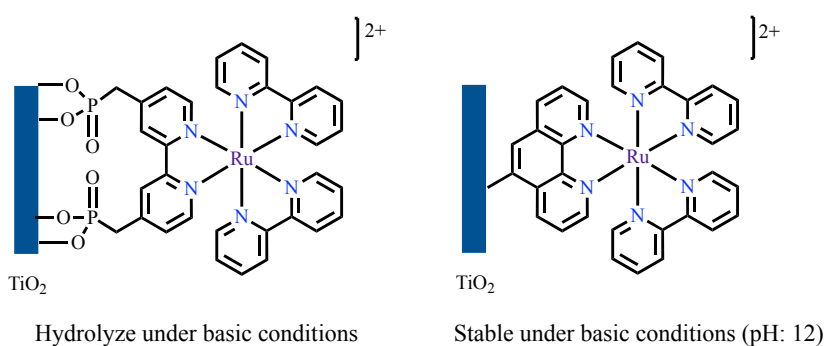
Scheme 3.1. Structures of [Ru((PO$_3$H$_2$-CH$_2$)bpy))(bpy)$_2$]$^{2+}$ and [Ru(phen)(bpy)$_2$]$^{2+}$ on TiO$_2$ electrodes.

The recently developed organic chromophore 2,4,5,6-tetra(9*H*-carbazol-9-yl)benzene-1,3-dicarbonitrile (4CzIPN) absorbs visible light to form a singlet excited state that undergoes facile intersystem crossing (ISC) to a triplet state.[28,29] The triplet state has sufficient lifetime and energy to undergo energy transfer and redox organic photoreactions.[30–34] Also, the facile ISC between the singlet and triplet excited states of 4CzIPN derivatives is being investigated as a method to overcome the 1:3 ratio of singlet to triplet states formed by ion-ion annihilation in organic light emitting diode (OLED) displays.[30] 4CzIPN and related chromophores had not been incorporated into photoelectrodes until our group recently reported a simple procedure to prepare 4CzIPN derivatives with one carbazole ring functionalized by an amine group at C4.[35] The in-situ prepared diazonium derivative of this amine is electrografted readily to semiconductors to prepare base-resilient earth-abundant photoelectrodes. For example, the derivative 4-NH_2Cz-3CzIPN was able to functionalize the surface of ITO or carbon electrodes, forming ITO-4CzIPN or Carbon-4CzIPN, respectively. These heterogenized dyes are also high turnover number photocatalysts for Dexter energy-transfer trans- to cis-olefin photoisomerization reactions.[36]

NHCs are molecules featuring a ring structure with at least one nitrogen atom and contain a divalent carbon atom with a six-electron valence shell (Scheme 3.2), which originally were incorporated as ligands in catalytically active transition metals. Tailor-made NHCs were designed for highly sophisticated catalytic reactions such as the ruthenium-catalysed olefin metathesis.[37–39] More recently, NHC have found many applications across chemical sciences, ranging from organocatalysis, earth-abundant transition metal catalysis, main group chemistry to on-surface chemistry.[40]
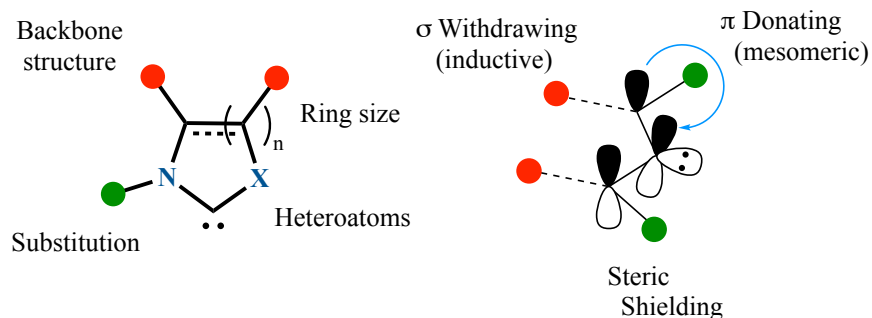
Scheme 3.2. Key structural features of N-heterocyclic carbenes (NHCs).

Additionally, NHCs are intrinsically reactive entities, presenting many structural features contributing to their kinetic and thermodynamic stability as well as to their characteristic reactivity and binding patterns. In this regard, four distinctive features contribute (Scheme 3.2): (1) the presence and location of heteroatoms (N and others); (2) substituents at proximal positions; (3) backbone structure (e.g., unsaturation); (4) ring size. Adjacent nitrogen atoms, due to high electronegativity, withdraw electron density from the non-bonding lone pair at the carbenic carbon (HOMO, σ-electron withdrawing), while the available lone pairs can overlap with the empty *p*-orbital (LUMO, π-electron-donating). Steric bulk on the *N*-substituents protects the reactive center from dimerization or other decomposition processes. The presence of unsaturation on the cyclic backbone can contribute to the aromatic character of the heterocyclic system and offer enhanced thermodynamic stability.

The development of NHCs has inspired new avenues toward the modification of surfaces (Scheme 3.3).[40–42]
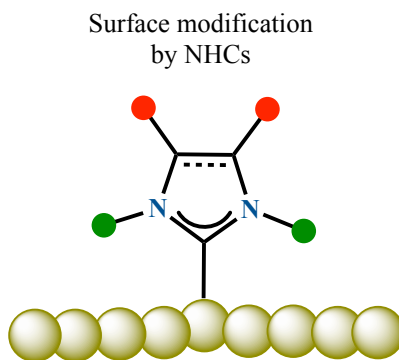
Scheme 3.3. Surface modification by NHCs.

Particularly, research has aimed at broadening the understanding of NHCs binding modes on metallic surfaces and other applications. NHC-coordinated surfaces can form stable self-assembled monolayers with promising electrochemical and biosensing applications.[43,44] Among the different binding modes, vertical is found for classical NHC complexes, and a flat-lying or tilted arrangement have been proposed. Also, NHCs have been investigated as supported nanoparticles, nanorods, and clusters.[45–50] Although early studies on NHC-modified surfaces in catalysis were focused on the stabilization of these surfaces, more recently, research has been directed

toward an activating effect that NHCs can offer for supported catalysts, as demonstrated for the improved Faradaic efficiency and current density in CO_2 reduction by Cao et al.[51,52]

This chapter describes the first high-yield route to N-heterocyclic carbene (NHC) derivatives of 2,4,5,6-tetra(9*H*-carbazol-9-yl)benzene-1,3-dicarbonitrile (4CzIPN). The NHC-dye was studied in solution by NMR, infrared- and UV-vis spectroscopy, cyclic voltammetry, and photoluminescence. The NHC group bonds to the surface of TiO_2 forming a semiconductor/chromophore system that was characterized by cyclic voltammetry, XPS, infrared and UV-vis spectroscopy, as well as photoluminescence. The bonding between the NHC group and TiO_2 is quite stable towards the photooxidation of sacrificial electron donors under alkaline conditions without applying any protective layers.

3.2 Results and Discussion

Scheme 3.5 shows the synthesis of (1-(2,4,6-tri(9*H*-carbazol-9-yl)benzene-1,3-dicarbonitrile)-3-benzyl-1,3-dihydro-2H-imidazol-2-ylidene (**6**). Our group previously reported that the displacement of the fluorides at the 2,4,6-positions of tetrafluoroisophthalonitrile by three equivalents of sodium carbazolate in THF is facile and selective at low temperatures.[35,53–55] This chapter describes that the remaining fluoride in 5-fluoro-2,4,6-tris(carbazole-9-yl)benzene-1,3-dicarbonitrile (**2**) is replaced by the imidazolate anion generated in MeCN solution by deprotonation of imidazole with Cs_2CO_3 to give 1-(2,4,6-tri(9*H*-carbazol-9-yl)benzene-1,3-dicarbonitrile)-imidazole in 95% yield (**3**, 3CzIPNIm). Reaction with neat benzyl bromide at 120 °C then gives the target imidazolium **4** in 95% yield. Imidazoliums like **4** are reported to undergo deprotonation to form the corresponding N-heterocyclic carbene.[56] We found that the bromide **4** is deprotonated by strong bases (KO′Bu, KN(Si(Me)$_3$)$_2$) at low temperatures in THF to generate the target NHC-dye **6** (Scheme 3.4).
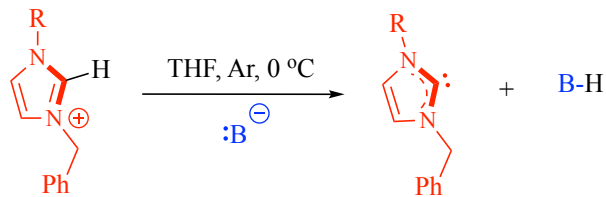
Scheme 3.4. NHC formation from the corresponding imidazolium deprotonation in THF.
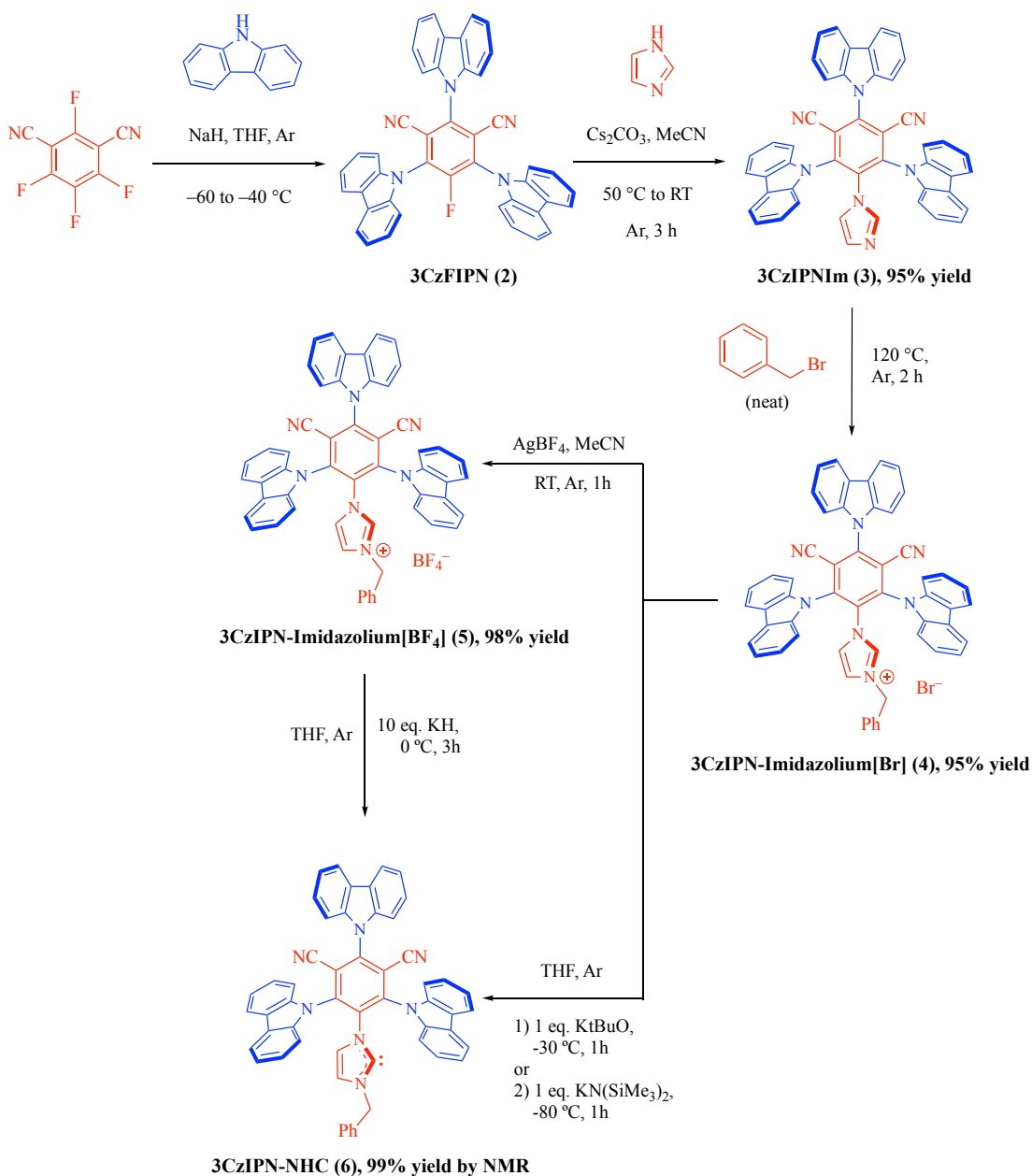
Scheme 3.5. Synthetic route of (1-(2,4,6-tri(9*H*-carbazol-9-yl)benzene-1,3-dicarbonitrile)-3-benzyl-1,3-dihydro-2H-imidazol-2-ylidene (**6**).

It was found, however, that any excess of base, even transient excesses that result from the relatively low solubility of **4** in THF, decompose the NHC target. To address this limitation, the bromide counterion was exchanged with BF_4^- (giving **5** in 98% yield) using $AgBF_4$ to increase the solubility in THF. Further, a more convenient and reliable method to deprotonate **5** is by stirring over excess (10 equivalents) KH in THF for 3 h at 0 °C. The target NHC-dye, 3CzIPN-NHC **6**, is prepared by this latter method with 99% NMR yield. The excess KH can be removed by simple filtration. While the dark red NHC-dye **6** cannot be isolated without decomposition, THF solutions of **6** were stable for long periods at temperatures below ~0 °C.

Figure 3.1A shows the aromatic region in the ^{1}H NMR spectrum of imidazolium **4** and highlights the signal for the proton at the 2-position of the imidazolium ring (δ 9.24 ppm). *g*HSQC NMR correlation experiments show that this hydrogen is coupled directly to the signal at 137.1 ppm in the ^{13}C NMR spectrum, which we assign to C2 of the imidazolium ring (Figure 3.11). Figure 3.1B shows the aromatic region in the ^{13}C{^{1}H} NMR spectrum of **4**. As stated above, the yellow imidazolium **4** can be deprotonated by one equiv. of ^{t}BuOK or $KN(SiCH_3)_3$ to form the red NHC compound **6** at low temperatures in THF-d_8. Upon deprotonation, the aromatic signals in the ^{1}H NMR spectrum shift, and the signal at 9.24 ppm corresponding to the hydrogen on C2 of the imidazolium group disappears (Figure 3.1C). Similarly, the ^{13}C{^{1}H} NMR signal at 137.2 ppm (corresponding to C3 in imidazolium **4**) shifts to 219.2 ppm upon deprotonation to form the NHC dye **6**. This chemical shift is typical for NHC carbene carbon centers (Figure 3.1D).[57,58] Typically, ^{13}C chemical shifts for the carbenic carbon appear ranging from 158 to 182 ppm, depending on the electron-donating ability of the carbon. For instance, the 1,3-bis(2,4,6-trimethylphenyl)-1,3-dihydro-2*H*-imidazole-2-ylidene presents a ^{13}C chemical shift at 177.2 ppm.[59] These NMR experiments provide conclusive evidence for the formation of the NHC dye **6**. The dissolved NHC dye **6** was stable at 0 °C but attempts to isolate it as solid resulted in decomposition.
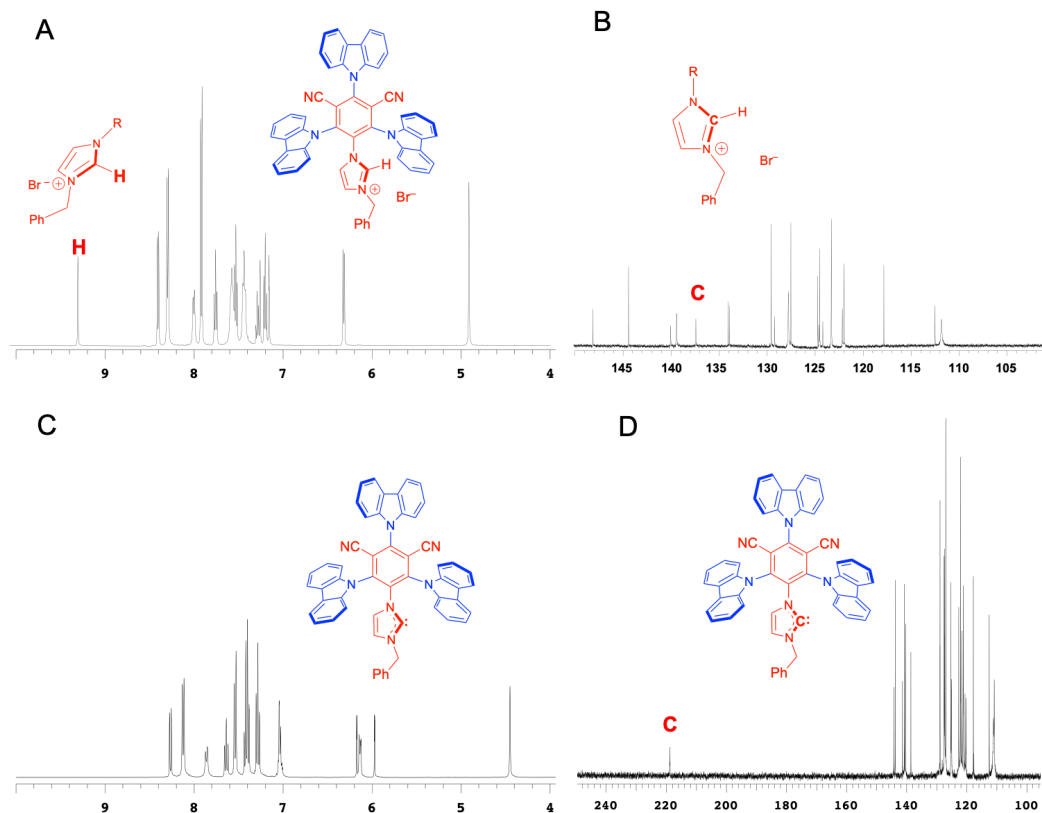
Figure 3.1. ^{1}H (A, C) and ^{13}C NMR (B, D) spectra of 4 (A, B) and 6 (C, D).

To our surprise, the red NHC dye **6** bonds to the surface of anatase TiO$_2$ nanoparticle electrodes. Specifically, the reaction between TiO$_2$ and **6** dissolved in THF was complete after 1 h at 0 ºC, forming TiO$_2$-**6** as a yellow solid. To our knowledge, this is the first observation of bonding between an NHC group and the surface of TiO$_2$. Figure 3.2 shows the cyclic voltammogram (CV) of the pale yellow TiO$_2$-**6** electrode recorded in dichloromethane (0 to 1.6 V vs. Fc/Fc$^+$ (ferrocene; all non-aqueous potentials in this manuscript are reported vs. a Fc/Fc$^+$ internal standard, 100 mV s^{-1}, 0.1 M nBu$_4$PF$_6$). The first sweep was in the positive-going direction because TiO$_2$ is reduced at lower potentials, resulting in large currents that obscure any redox peaks from **6**. Figure 3.2 also shows the baseline CV of the bare TiO$_2$ electrode, which did not contain prominent features over this potential range. The CV of TiO$_2$-**6** contains an anodic wave that begins at ~0.6 V, followed by a strong, largely irreversible anodic peak starting at ~0.99 V due to oxidation of the carbazole rings.[31,35] Using the charge

under oxidation of the carbazole rings, a very rough estimate of the surface coverage of TiO_2 by **6** is 4.4×10^{-9} mol cm^{-2}.
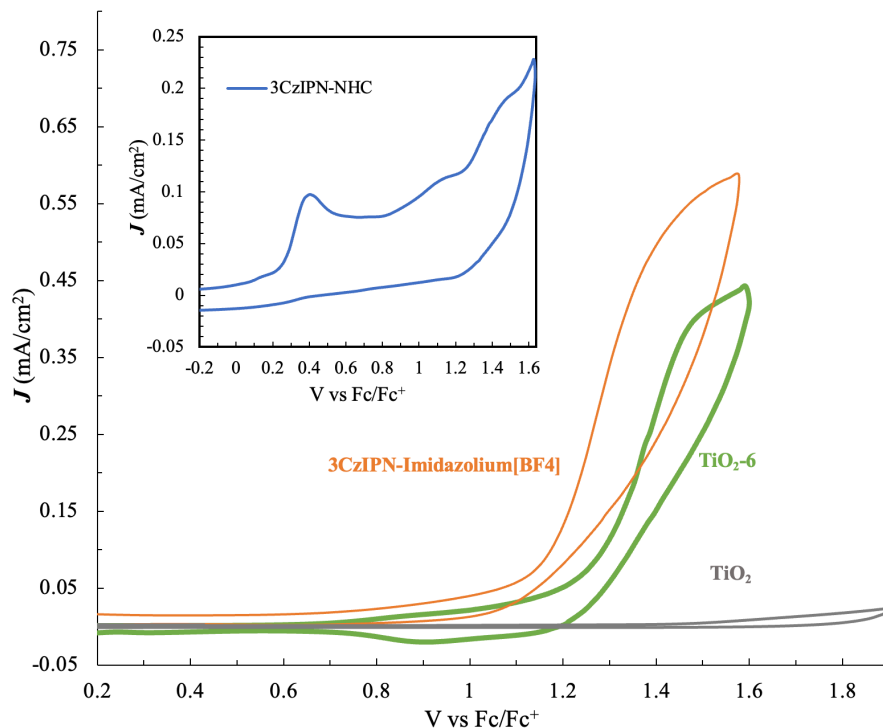
Figure 3.2. CVs of blank TiO_2, 3CzIPN-Imidazolium[BF_4] 5 (0.1mM) and of the TiO_2-6 electrodes in N_2-saturated DCM (0.1 M nBu_4PF_6). Inset: CV of 3CzIPN-NHC 6 (0.1mM) using a glassy carbon as working electrode in N_2-saturated THF containing (0.1 M nBu_4PF_6). Scan rate 100 mV.

For comparison, Figure 3.2 also shows the CV of the imidazolium **5** in CH_2Cl_2 solution recorded with a TiO_2 working electrode. The CV contains an anodic wave onset at 0.8 V, followed by a strong irreversible peak at 1.15 V assigned to the oxidation of carbazole rings (Scheme 3.6).[35]

The positive going sweeps contain peaks that are like those in the CV of TiO_2-**6**, suggesting that the dye is present on the surface of TiO_2 in a form similar to **5**. Figure 3.2 (inset) also shows the CV of the free NHC-dye **6** dissolved in THF solution, recorded with a glassy carbon working electrode at 0 ºC under the strict absence of air (N_2 atmosphere). Solution CVs of free NHCs are uncommon in the literature.[53–55] The CV of **6** contains a new irreversible anodic peak at 0.4 V, which is characteristic of the one-electron oxidation of the NHC carbene center to form a radical cation. Similar NHC-based radical cations are reported to undergo rapid dimerization to form

113

dications. (Scheme 3.7). [53–55] The oxidation peaks for the carbazole rings in **6** at 1.1 V and 1.4 V occur at slightly more cathodic potentials than the corresponding peaks in the imidazolium **5**, as expected for an electron-rich species. A comparison of the solution-phase CVs of **6**, **5**, and TiO$_2$-**6** suggests the structure of the NHC group bonded to TiO$_2$ resembles **5.**
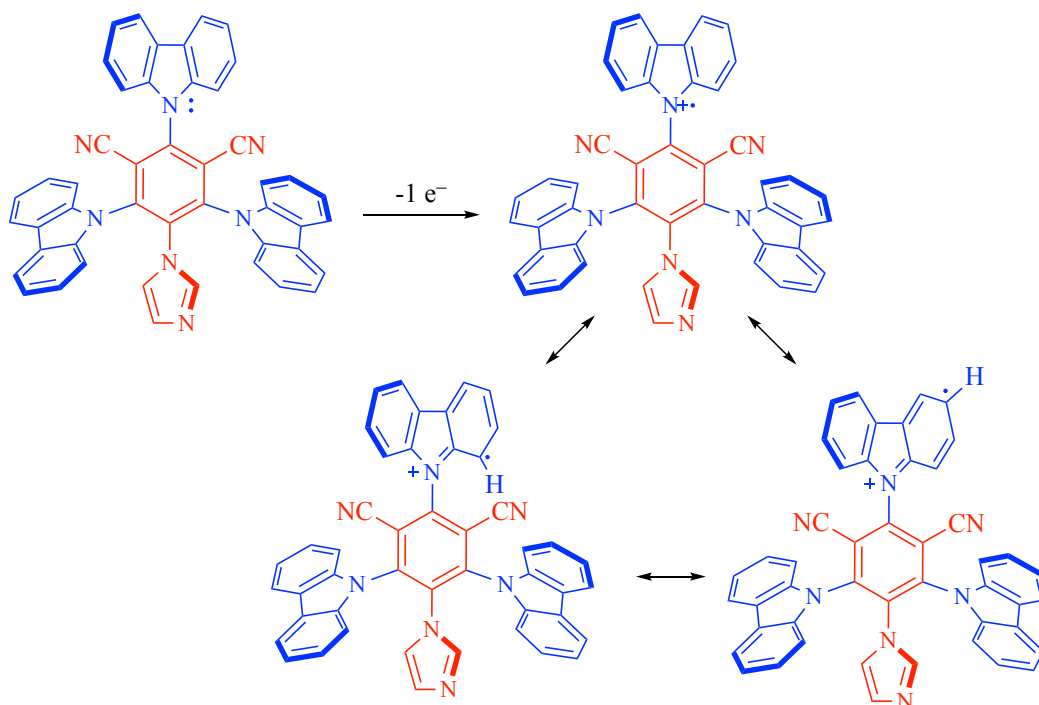
Scheme 3.6. Electrochemical oxidation of the carbazole in 3CzIPN-Imidazolium[BF$_4$].
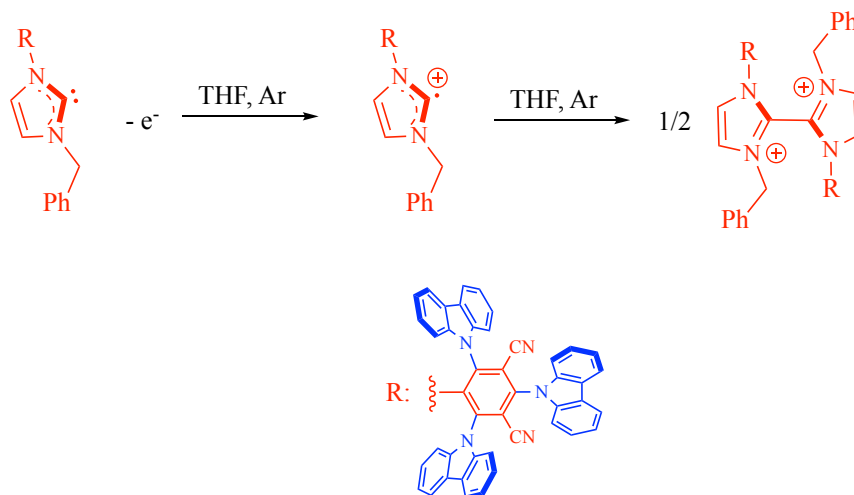
Scheme 3.7. Proposal for the NHC dimerization process.

114

Figure 3.3 shows the N1s region of the XPS high-resolution spectra of the blank TiO₂ and TiO₂-**6** electrodes. Deconvolution of this region indicates there are three types of N peaks in the XPS spectrum of TiO₂-**6**. There is a peak in the region for aromatic N atoms at ~400 eV[35,58,60] that likely arises from the carbazole rings, there is a peak that arises from imidazole-type N atoms at ~401.5 eV that likely arises from the NHC group, and there is a peak at ~399.6 eV that likely arises from the nitrogen atoms in the nitrile groups.[60,61] The ratio of the pyridine to imidazole nitrogen signals is ~2:3 for the TiO₂-**6** electrode, as expected for the structure of **6**. The XPS spectrum of the TiO₂ blank did not contain peaks in this region. In the experimental section, Figure 3.16 shows the high-resolution XPS spectra in O1s region for the TiO₂ and TiO₂-**6** electrodes. Deconvolution indicates there are peaks at ~530, 531, and 532 eV in the XPS spectrum of TiO₂-**6** that can be ascribed to oxygen in a metal oxide (TiO₂), in a metal hydroxide group,[61–63] and bonded to carbon (C-O),[26,27] respectively. The signal from O bonded to C is present in the TiO₂ blank, however, and it is likely due to adventitious impurities, perhaps present in the air.
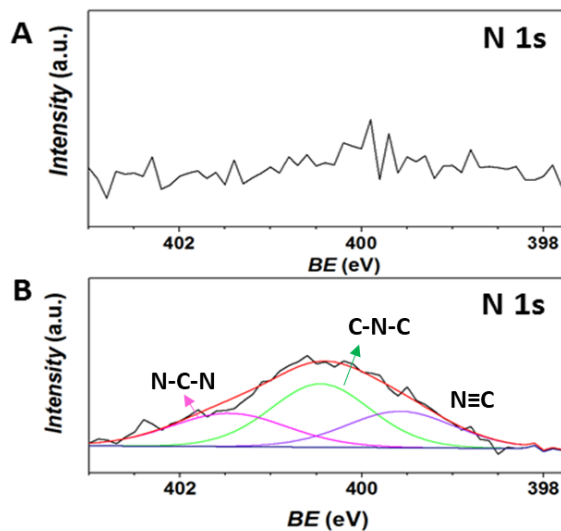
Figure 3.3. The high-resolution XPS spectra in N1s region for bare TiO₂(A) and grafted TiO₂-6 (B) electrodes.

Figure 3.4A shows the solid-state and UV-vis absorption spectrum of TiO₂-**6** in the 350–800 nm range using TiO₂ as the blank. The inset shows the solution UV-vis

spectrum of the parent imidazolium **5** in CH$_2$Cl$_2$, and of the free NHC-**6** in THF solution under N$_2$.
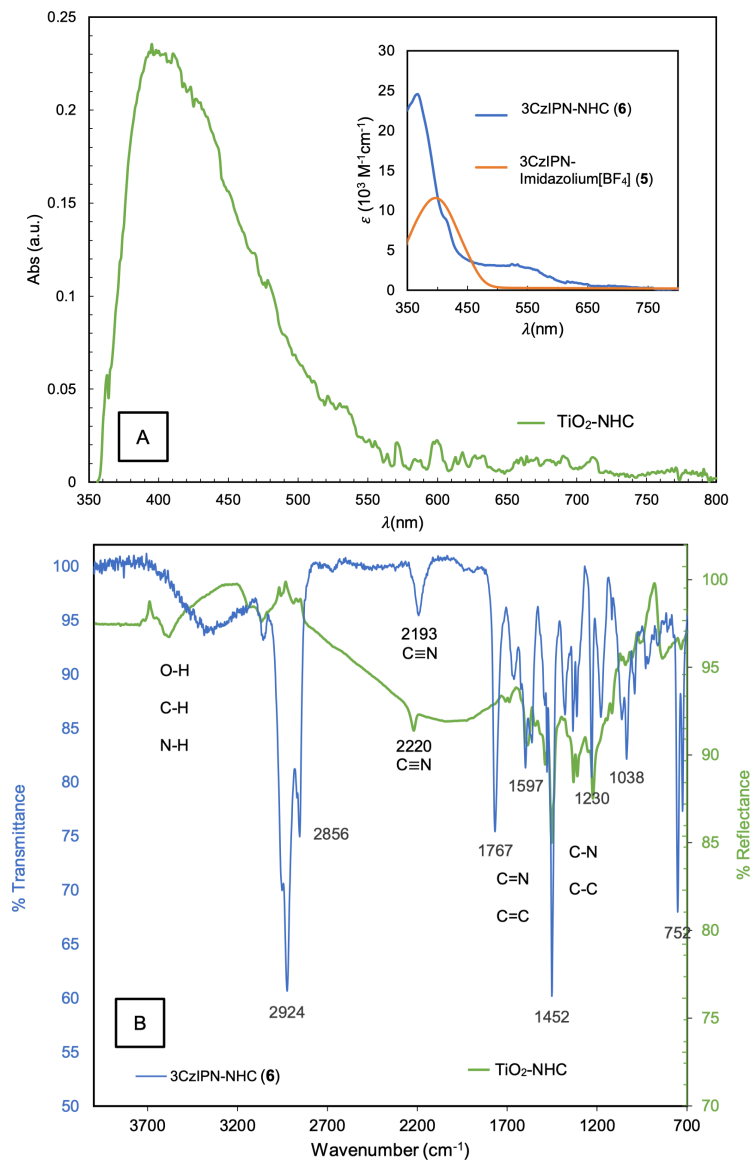
Figure 3.4. (A) UV-vis spectra of TiO$_2$-NHC-**6** with TiO$_2$ absorption subtracted (Inset is molar extinction coefficient vs. wavelength plots for homogeneous solutions of the imidazolium **5** (in CH$_2$Cl$_2$) and the free NHC-dye 6 in THF. (B) Infrared reflectance spectra of TiO$_2$-**6** electrode with TiO$_2$ as blank, and the IR transmittance spectrum of the free NHC-dye **6** in THF solution.

The solid-state UV-vis spectrum of TiO$_2$-**6** resembles more that of the imidazolium **5** in solution, apart from broadening and a slight blue shift (about 25 nm) that it does of the free NHC **6**. The maximum absorbance wavelength of the free NHC-

6 is blue-shifted from both **5** and TiO$_2$-**6**, and it contains an extra broad peak with a maximum at ~540 nm. Conclusive speciation of TiO$_2$-**6** is not possible from these UV-vis spectra alone. The surface coverage (Γ) of TiO$_2$ by **6** is, therefore, only roughly estimated as 3.7×10^{-8} mol cm^{-2} using the molar extinction coefficient of **5** dissolved in CH$_2$Cl$_2$.

The estimated coverage obtained from the UV-vis measurement is higher than that estimated from the CV data. A similar trend was reported for Ru-bipyridyl chromophores bonded to TiO$_2$ through phosphonate groups[63–65] and indicates that only a portion of the NHC-dye attached to the TiO$_2$ surface is electrochemically accessible. The difference in estimated surface coverages, based on solid-state UV-vis and CV measurements, was much smaller in our previous reports of chromophores attached to surfaces by diazonium electrografting.[26,27,66] We expect that the diazonium-chromophore binds in the vicinity of the electrochemically accessible sites on the TiO$_2$ surface during electrografting, while the reaction between NHC-**6** and the TiO$_2$ surface is less specific.

Figure 3.4B shows the solid-state reflectance infrared spectrum of TiO$_2$-**6** and the solution spectra of the parent NHC **6**. There are similarities between the spectra, including in the C-H, the C=Y, and C-Y vibration regions (Y= N, C). Perhaps the most indicative similarity is the C≡N stretches at 2220 and 2193 cm^{-1} for TiO$_2$-**6**, and NHC **6**, respectively. The corresponding peak in the solution spectrum of the imidazolium **5** occurs at 2239 cm^{-1} (Figure 3.15, in the experimental section). The C≡N stretching frequency for **5** is closer to TiO$_2$-**6** than to the free NHC **6**. As well, the order of stretching frequencies (**5** > TiO$_2$-**6** > **6**) shows that there is more electron density in the C$_6$ ring in **6** than in **5** or TiO$_2$-**6**. The greater electron density in **6** undoubtedly results from deprotonation of the cationic imidazolium group in **5** to form the NHC group in **6**. As a final comparison, the corresponding CN stretch in the IR spectrum of the tetracarbazole dye 4CzIPN is 2233 cm^{-1},[67] closer to **5** and TiO$_2$-**6**, and higher than the free NHC **6**. Figure 3.5 summarizes the differences in stretching frequencies.
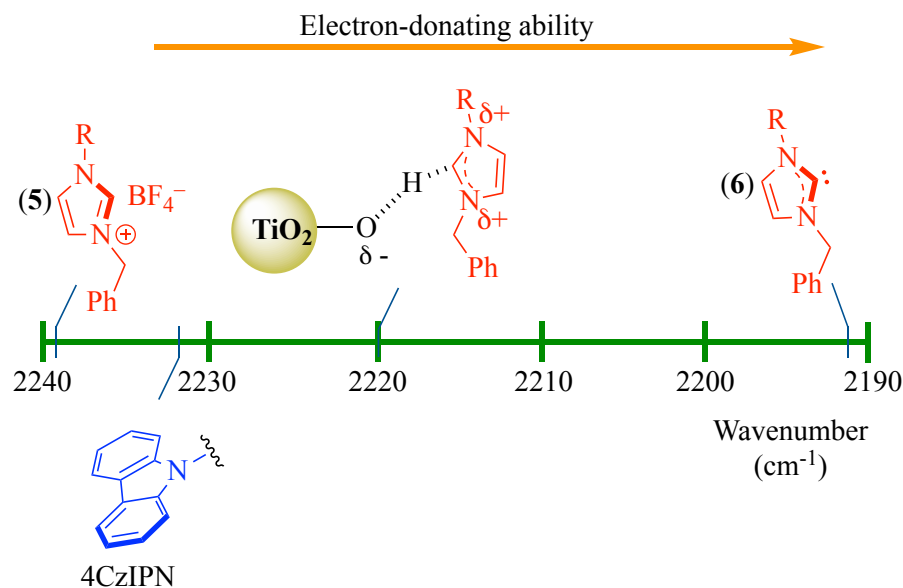
Figure 3.5. Comparison of the –C≡N stretching frequencies and electron densities in the dicyanobenzene moieties of the dicyanocarbazoles.

Figure 3.6 shows the photoluminescence spectra of TiO_2-**6**, the imidazolium **5**, and the free NHC **6**. TiO_2-**6** has an intense yellow-orange emission with a maximum at 568 nm. The wavelengths of the maximum excitation and emission peaks, the Stokes shifts, and their intensities in the spectrum of TiO_2-**6** resemble those of the imidazolium **5** more closely than of the NHC **6**. Interestingly, the maximum absorption peak of the NHC **6** is shifted to higher energies than **5** and TiO_2-**6** (400 vs 421 nm), and the Stokes shift for **6** is also quite a bit smaller (57.5 nm) than **5** (159 nm) and TiO_2-6 (146 nm). Although these absorptions and emissions cannot be assigned with certainty without detailed study, based on comparisons to carbazole dicyanobenzenes-carbazoles in the literature,[67] we tentatively assign the absorbances between 400 and 421 nm to the S_0 → S_1 intermolecular charge transfer between the highest energy occupied natural transition orbital (NTO) centered on the carbazole rings to the lowest energy unoccupied NTO centered on the dicyanobenzene moiety (Scheme 3.8). The relatively small Stokes shift for NHC **6** suggests that the intramolecular rearrangement that occurs between S_0 and S_1 is more restrained in the free NHC **6** than they are in the imidazolium **5** and TiO_2-**6**.[67]
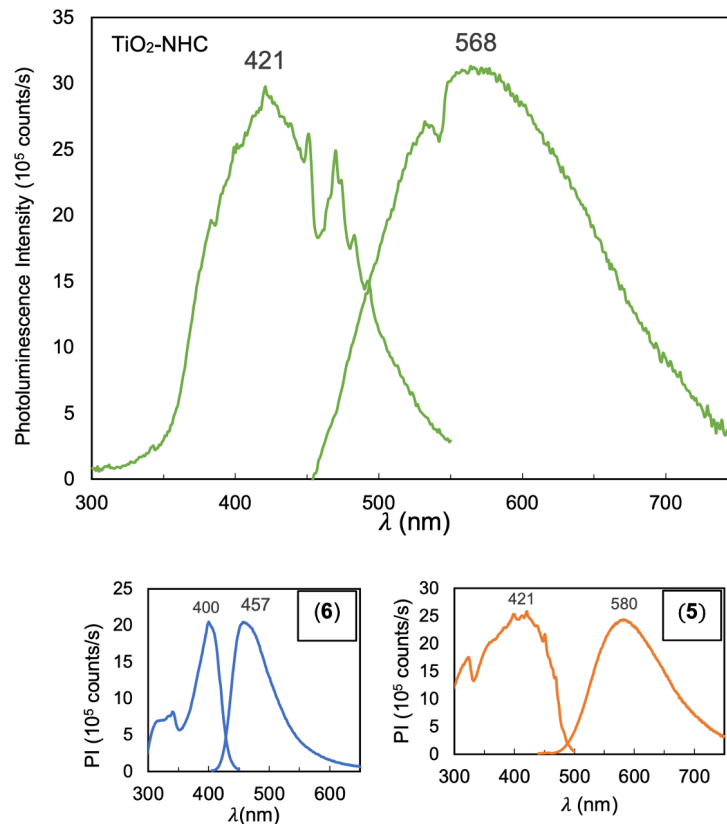
Figure 3.6. Photoluminescence spectra of TiO$_2$-NHC, 3CzIPN-Imidazolium[BF$_4$] and 3CzIPN-NHC **(6).**
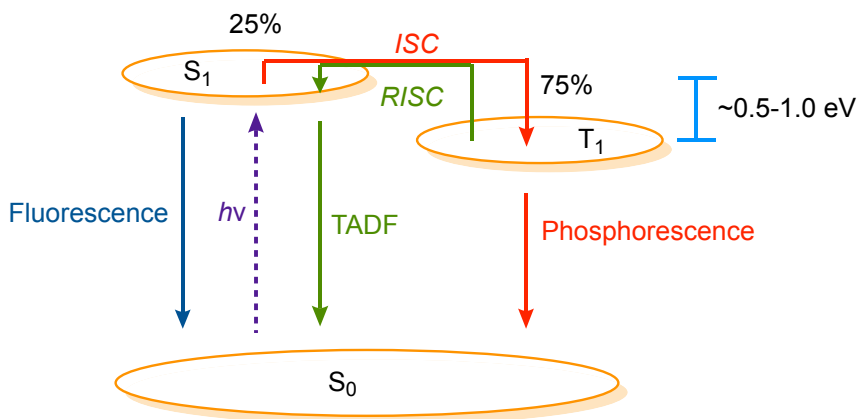
Scheme 3.8. Simplified energy diagram illustrating energy transfer (ET) processes upon light excitation of 4CzIPN derivatives like **5**, **6**, and TiO$_2$-**6**.

The CV, solid-state IR, XPS, UV-vis, and photoluminescence data for TiO$_2$-**6** all resemble the solution data of imidazolium **5** more than they do of the free NHC **6**. Taken together, we propose that bonding between the free NHC 6 and the TiO$_2$ involves hydrogen bonding between the NHC carbon and a protic hydrogen within an -OH, or

H₂O group on the TiO₂ surface.[54] Scheme 3.9 shows the proposed structure. It is well-known that NHC groups engage in hydrogen bonding with protic hydrogen atoms.[68,69] It is also well-known that water and O-H groups exist on the surface of TiO₂.[70] This bonding would result in the formation of a partial negative charge at oxygen in the hydroxyl group, forming a partial ion pair between the NHC-**6** and the surface hydroxyl group (Scheme 3.9). Another possibility is the direct coordination of the NHC group to a Ti centre in TiO₂. This second mode seems less likely because the Ti centres are not easily accessible in TiO₂. More study is required, however, to determine the exact nature of the bonding between TiO₂ and **6**. Attempts to measure the solid-state ^{1}H NMR of TiO₂-NHC were inconclusive because of the low amounts of **6** present on the surface of TiO₂ as well as the inhomogeneity of the surface sites on TiO₂ nanoparticles.
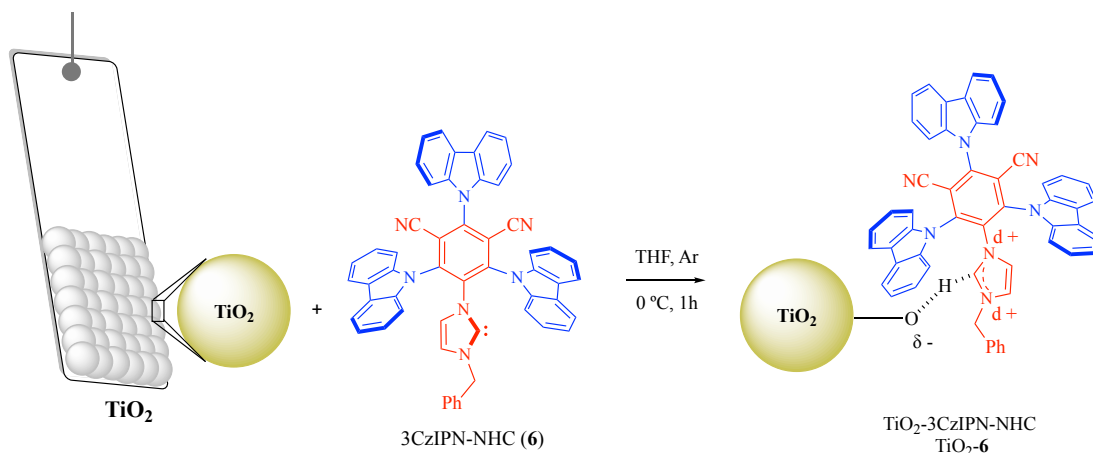
Scheme 3.9. Functionalization of TiO₂ with 3CzIPN-NHC (**6**) for the formation of TiO₂-**6**.

Figure 3.7A shows the incident photon to current conversion efficiencies (IPCEs) and the photoelectrochemical activities of TiO₂-6 and TiO₂ under neutral conditions with hydroquinone (H₂Q) as the sacrificial electron donor (E = 0 $V_{SCE,}$ 0.1 M NaClO₄, 0.02 M H₂Q, pH = 7.0). The TiO₂-**6** photoelectrode was photoactive at wavelengths below ≤540 nm, reaching 1.6% and 0.9% efficiency at 400 and 420 nm, respectively. Figure 3.7B shows the potentiostatic photocurrent response of TiO₂-**6** and TiO₂ under illumination at 450 nm at 0 V_{SCE}. The initial photocurrent from the TiO₂-**6** photoanode was 4.6 µA cm⁻², and it was appreciably stable, decreasing to 4.1 µA cm⁻²

(89%) after 1000 s. The blank TiO_2 electrode showed very little photoactivity (1.1 µA cm^{-2}), which dropped to 72% of its original value after 1000 s.
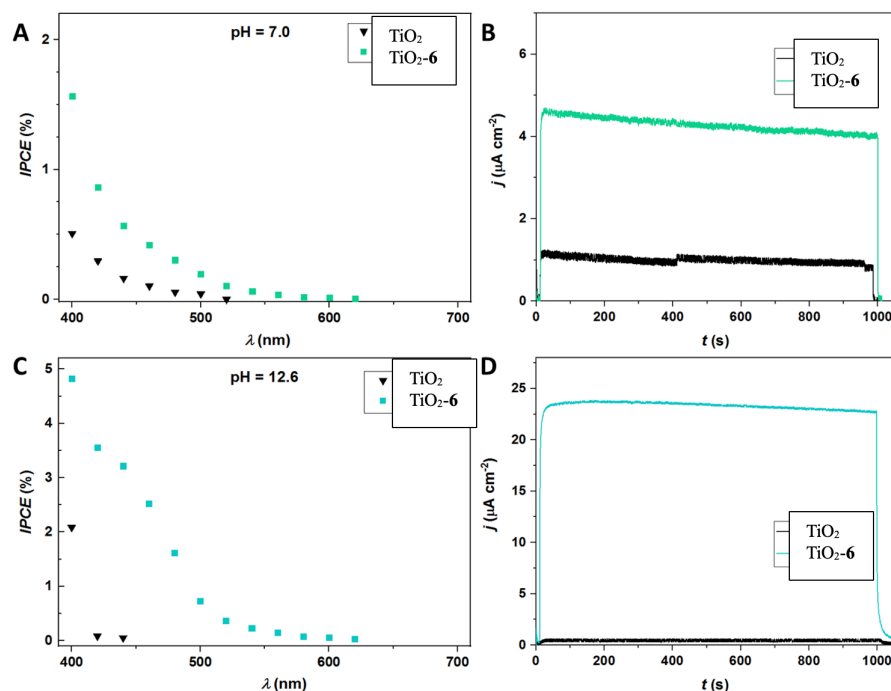
Figure 3.7. The IPCE measurements (A and C) and photoelectrochemical responses (B and D) of TiO_2 and TiO_2-6 electrodes in 0.1 M $NaClO_4$ containing 0.02 M H_2Q (pH = 7.0) (A and B) at a constant potential of 0 V or containing 0.5 M Et_3N (pH = 12.6) at a constant potential of –0.2 V (C and D), illumination of 450 nm, under Ar atmosphere.

Figure 3.7C shows the IPCE activities of the TiO_2-**6** and TiO_2 photoanodes in the visible range (400–700 nm) under basic conditions, with Et_3N as the sacrificial electron donor (pH = 12.6, 0.5 M Et_3N, 0.1 M $NaClO_4$, E = –0.2 V_{SCE}) (Scheme 3.10). The TiO_2-**6** electrode was quite a bit more active under alkaline conditions with Et_3N as an electron donor than under neutral conditions with H_2Q as a donor. The IPCE increased as the wavelength decreased under alkaline conditions, reaching 3.6% and 4.8% at 420 and 400 nm, respectively. The photoanode was not significantly photoactive at wavelengths >550 nm, in agreement with the UV-vis spectra of TiO_2-**6**, and **5** (in solution).
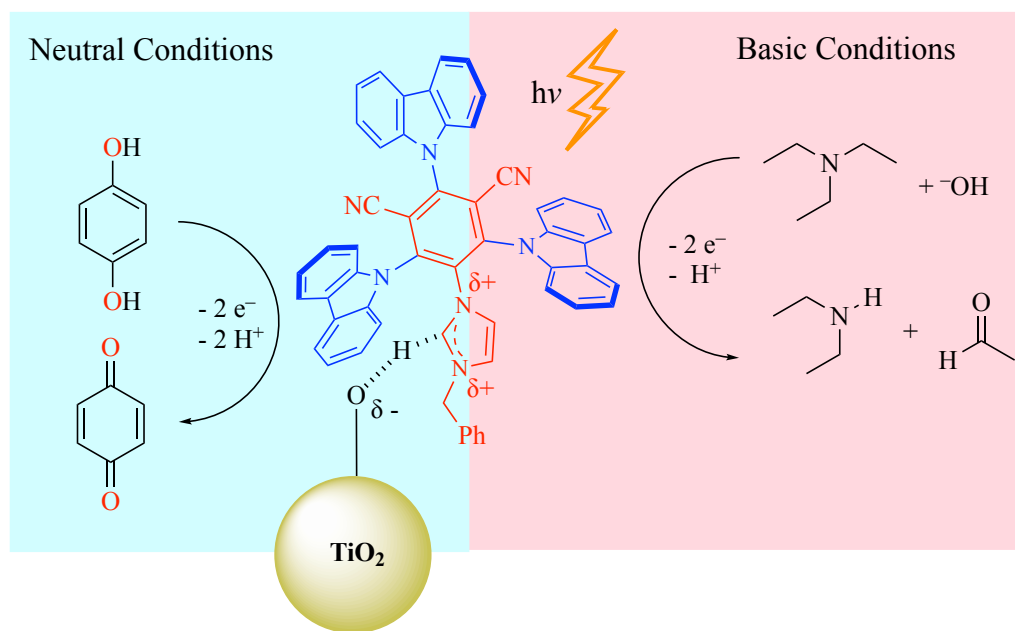
Scheme 3.10. Photooxidation of H_2Q under neutral conditions (left) and Et_3N under basic conditions (right) with the TiO_2-**6** electrode.

Figure 3.7D shows the potentiostatic photocurrent responses of the TiO_2-**6** and TiO_2 photoanodes under irradiation at 450 nm towards the light-driven oxidation of Et_3N. The TiO_2 photoanode was not noticeably photoactive under these conditions (photocurrent of a mere 0.3 µA cm^{-2}). The TiO_2-**6** electrode was appreciably active and stable, giving a photocurrent density of 23.4 µA cm^{-2}, with ~97% retention over 1000 s irradiation at 450 nm. The increase in IPCE, photocurrent, and stability of the TiO_2-**6** photoelectrode with the increase in pH is interesting and somewhat unprecedented. Factors such as differences in the nature of the sacrificial electron donors (kinetics or overpotentials)[64] or changes in the quasi-Fermi level of semiconductor (TiO_2) caused by variation of pH likely play a role in the change in activity.[66] The apparent stability under such high pH, without protective oxide layers (e.g., Al_2O_3 ALD), suggests that systems like TiO_2-**6** should be explored for photo-driven OER under these conditions.

Table 3.1 compares the IPCE (%), and photoelectrochemical activities (µA cm^{-2}) of various electrodes functionalized with comparable Ru- or Ir-polypyridyl chromophores and TiO_2-**6** in neutral and alkaline conditions. The IPCE value for the photoelectrooxidation of H_2Q under neutral conditions (1.6%) was modest over TiO_2-**6**. The IPCE value for the photoelectrooxidation Et_3N under alkaline conditions (pH

12.6) over TiO$_2$-**6** was among the highest (4.8%), while generating relatively high photocurrents. The relatively high performance under alkaline conditions may lead to systems that operate with a wider range of earth-abundant electrocatalysts than under acidic conditions.

Table 3.1. IPCE and Photocurrent Density for Different Electrodes under Neutral and Alkaline Conditions.[26,27,35]

Electrode	pH 7		pH 12.6	
	IPCE (%)[a]	Photocurrent density (μA cm^{-2})[b]	IPCE (%)[c]	Photocurrent density (μA cm^{-2})[b]
TiO$_2$-(phen)Ru(bpy)$_2^{2+}$	5.5	25	3.8	4.2
TiO$_2$-(phen)Ru(dmbpy)$_2^{2+}$	12.7	22.4	6.6	4
TiO$_2$-[Ru(bpy)$_2$ ((4,4'-PO$_3$H$_2$)$_2$bpy)$^{2+}$	5.6	35	0.5	1
TiO$_2$-[(phen)Ir(ppy)$_2$]$^+$	4	15	2	2.5
ITO-4CzIPN	-	-	3.5	15
TiO$_2$-**6** (this work)	1.6	4	4.8	23.4

[a] IPCE for the photooxidation of H$_2$Q under neutral conditions [0 V$_{SCE}$, 0.02 M H$_2$Q, 0.1 M NaClO$_4$, 400 nm]. [b] Photoactivity measured under the illumination of 450 nm light. [c] IPCE for the photooxidation of TEA under basic conditions [0 V$_{SCE}$, 0.1 M NaClO$_4$, 0.5 M TEA, 400 nm].

3.3 Conclusions

The purpose of this discovery report is to detail the preparation and characterization of the first 4-CzIPN chromophore functionalized with an NHC ligand. As well, the manuscript details the bonding of an NHC group to the surface of TiO$_2$. To our knowledge, this is the first report of this type of bonding. Steady-state photoluminescence studies show that the light absorption properties of the ligand are maintained upon coordination to TiO$_2$. As well, preliminary studies show that the TiO$_2$-**6** surface functions as a visible-light-driven photoanode for the oxidation of sacrificial electron donors under neutral and alkaline conditions, demonstrating that this new system has applications in the fundamental study of solar fuel processes. The range of practical applications of this new ligand-type and bonding mode (e.g., solar fuels, photocatalysis, OLED displays, photodynamic therapy) is under investigation in our research group.

3.4 Experimental

Materials

Chemicals were used without any further treatment, unless mentioned otherwise. Following chemicals were obtained from Sigma Aldrich: TiO_2 nanoparticles (anatase, nanopowder <25 nm particle size, 99.7% trace metals basis), $TiCl_4$ ($\geq$99.995%, trace metals basis), 2,4-pentadione ($\geq$99%), $NaClO_4$ (ACS reagent, $\geq$98.0%), hydroquinone (ReagentPlus, $\geq$99.5%), triethylamine, distilled (Et_3N, $\geq$99.0%), tetrabutylammonium hexafluorophosphate (NBu_4PF_6; for electrochemical analysis, $\geq$99.0%), acetonitrile, distilled (MeCN for HPLC, gradient grade, $\geq$99.9%), dichloromethane, distilled (DCM; ACS reagent, $\geq$99.5%), tetrahydrofuran, distilled (THF; ACS reagent, $\geq$99.0%), potassium tert-butoxide (95%), potassium hydride (from 60% oil suspension, THF washed, dried). FTO (surface resistivity ~7 Ω/sq, 10×10 cm pieces). Triton X-100 was purchased from EMD Millipore Corporation. Triply distilled water was used to prepare aqueous solutions. Tetrafluoroisophthalonitrile (>98.0%) and imidazole were obtained from TCI and Baker, respectively. When possible, the liquid reagents were distilled before use. The solvents DCM (CaH_2), acetonitrile (CaH_2), toluene (CaH_2), and tetrahydrofuran-d_8/tetrahydrofuran (Na/benzophenone) were distilled from the appropriate drying agent under N_2. Argon or N_2 gas was bubbled through solvents for a minimum of 30 min before use unless noted otherwise.

Instrumentation

Electrochemical studies were carried out using a Solartron SI 1287 Electrochemical Interface. The X-ray photoelectron spectroscopy (XPS) measurements were done using a Kratos Axis 165. A monochromatized Al Kα source (hν =1486.6 eV) was used at 12 mA and 14 kV, while the pressure in the sample analytical chamber was maintained <1 $\times 10^{-9}$ torr. Survey scans ran in the binding energy of 1100 to 0 eV, with analyzer pass energy of 160 eV and 0.3 eV steps. For deconvolution, the spectra are calibrated by C–C binding energy at 285.0 eV. UV-vis spectra were collected using Cary 5000 UV-vis spectrometer for chromophores dissolved in CH_2Cl_2 or on TiO_2 (with TiO_2 absorbance subtracted). ^1H NMR spectra were acquired using 400 MHz and 500 MHz Varian Inova, and Varian DD2 M2 400 MHz NMR spectrometers. ^{13}C NMR spectra were

acquired using a Varian VNMRS 500 MHz NMR spectrometer. The ^{19}F NMR spectra were acquired on a 400 MHz Varian DD2 MR spectrometer. The chemical shifts are reported in parts per million relative to TMS with the solvent as internal standard. Abbreviations used in reporting NMR data are s (singlet), d (doublet), t (triplet), q (quartet), dd (doublet of doublet), dq (doublet of quartet), and m (multiplet). HRMS spectra were acquired using either electrospray ionization in an Agilent 6220 ao TOF mass spectrometer, or electron ionization on a Kratos Analytical MS50G double focusing sector mass spectrometer. Powder X-ray diffraction (pXRD) patterns of the ground samples were collected on a Bruker D8 Advance powder diffractometer, equipped with a SSD160 detector and a Cu Kα radiation source operated at 40 kV and 40 mA. The Scanning Electron Microscope (SEM) images were recorded with a Zeiss Sigma 300 VP-FESEM.Photoluminescence spectra were collected using a Horiba-PTI QM-8075-11 Fluorescence System.

Fabrication of FTO/TiO$_2$ Electrodes

The electrodes were fabricated according to a previous publication with minor modifications.[35] Shortly, FTO coated glasses (1 × 2.5 cm piece) were sonicated in ethanol for 15 min followed by water for another 15 min, and rinsed with water. They were heated in a 50 mM TiCl$_4$ solution at 70 ºC for 30 min and washed with water thoroughly. In order to make TiO$_2$ paste, 0.5 g nanoparticles, 50 μl Triton X-100 (as surfactant), and 50 μl 2,4-pentanedione were mixed in a 3 ml ethanol/water 1:1 for 2 h and sonicated for 30 min using the doctor-blade method (four layers of scotch tape), the paste was applied on FTO slides (~10 μm thickness). After the slides were dried in air, they were heated at 500 ºC in a muffle furnace for 2 h, followed by treatment in 50 mM TiCl$_4$ solution at 70 ºC for 30 min. The slides were rinsed thoroughly with water and heated at 450 ºC for 30 min. Slides were transferred from the oven at 90 ºC into the glovebox to keep them dry.

Synthesis of 5-fluro-2,4,6-tri(9H-carbazol-9-yl)benzene-1,3-dicarbonitrile (2)
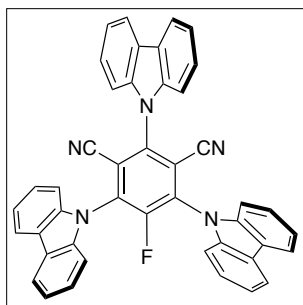
Carbazole (2.505 g, 15 mmol) and NaH (60% dispersion in mineral oil, 0.9 g, 22.5 mmol) were weighed into a flask that was evacuated and refilled with argon 3x, cooled to –80 °C, and charged with 30 mL of freshly distilled, dry THF (30 mL). The cooling bath was removed, and the reaction mixture stirred for 30 min upon reaching room temperature. The flask was cooled to –80 °C, and a solution of tetrafluoroisophthalonitrile (1.02 g, 5 mmol) in 15 mL of freshly distilled, dry THF was added slowly at –80 °C. Additional THF (10 mL) was used for quantitative transfer of tetrafluoroisophthalonitrile. The reaction mixture was stirred at temperatures between –60 °C and –40 °C. An aliquot after 2 h showed (NMR) the presence of **1** with no starting materials remaining. The reaction was stopped after 3 h by adding distilled water (3 mL) drop wise under argon, then warming to room temperature, and stirring for an additional 30 min. The precipitate that formed during the addition of water was removed by filtration. The precipitate was washed with an additional 40 mL of THF. The combined filtrates and washings were concentrated under reduced pressure using a rotavap to yield **2** as a fluffy yellow solid. The solid was dissolved in 100 mL of DCM and washed with water (3 × 50 mL), saturated NaCl (1 x 50 mL), and the organic layer was dried over anhydrous Na_2SO_4 and concentrated using a rotavap to give a yellow oily product. Then, the oily product was dissolved in the minimum amount of DCM and precipitated with diethyl ether to give the tricarbazole-fluoride (**2**) as a yellow powder in 90% yield.
^{1}H NMR (498.120 MHz, CD_3CN, 26.9 °C): δ 7.44–7.50 (6H, m), 7.62–7.69 (10H, m), 7.75 (2H, d, J = 8.2 Hz), 8.24 (4H, d, J = 7.7 Hz), 8.28 (2H, d, J = 7.8 Hz). **^{19}F NMR** (468.664 MHz, CD_3CN, 26.9 °C): δ –116.07 (1F, s). **^{13}C{^{1}H} NMR** (125.686 MHz, CD_3CN_3, 27.0 °C): δ 110.3, 110.8, 111.7 (d, $^4J_{C,F}$ = 3.4 Hz), 115.8 (d, $^3J_{C,F}$ = 3.4 Hz), 120.9, 121.0, 122.1, 122.3, 124.0, 124.3, 127.0, 127.2, 135.5 (d, $^2J_{C,F}$ = 15.2 Hz), 139.4, 140.2, 142.5 (d, $^4J_{C,F}$ = 4.4 Hz), 155.6 (d, $^1J_{C,F}$ = 262.2 Hz). **HRMS (ESI)** m/z Calcd. for $C_{44}H_{24}FN_5$ (M+Na)$^+$: 664.1908. Found: 664.1909. Figure 3.8 (a), (b), and (c) show the ^{1}H, ^{13}C, and ^{19}F NMR spectra of (**2**).
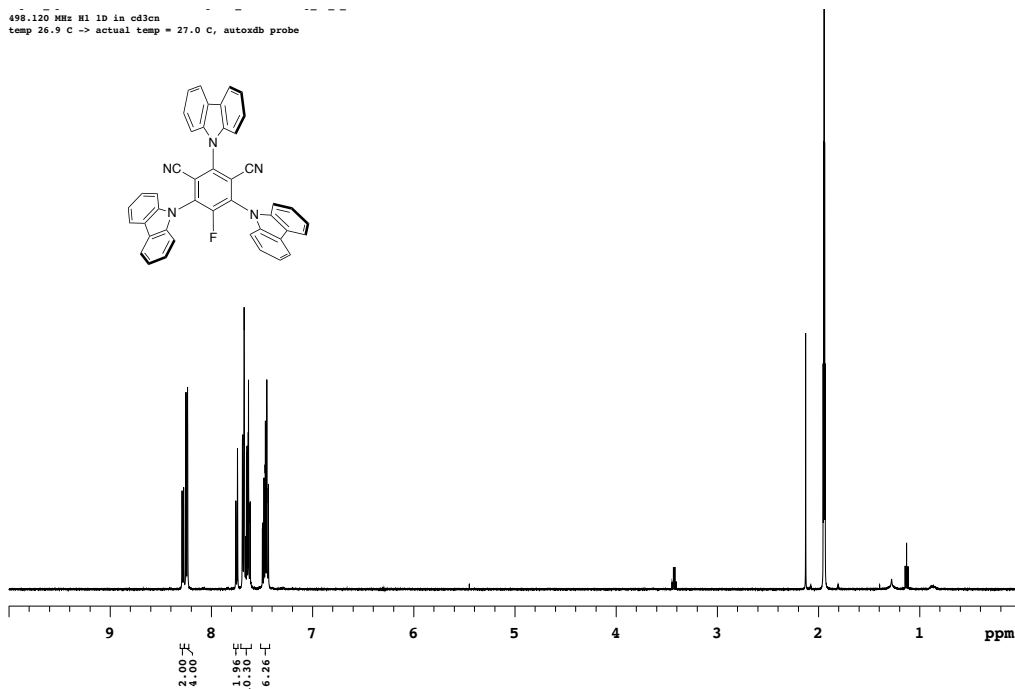
Figure 3.8. ^{1}H NMR (a) of 5-fluro-2,4,6-tri(9*H*-carbazol-9-yl)benzene-1,3-dicarbonitrile (**2**) in MeCN-*d₃*.
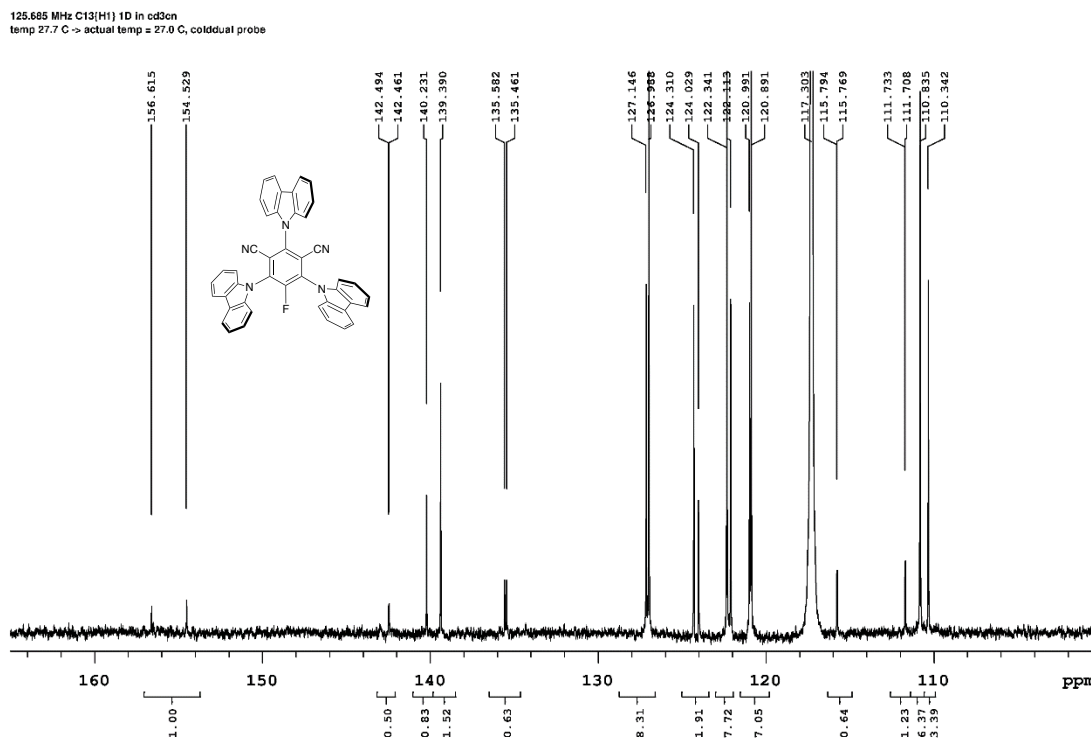
Figure 3.8. ^{13}C NMR (b) of 5-fluro-2,4,6-tri(9*H*-carbazol-9-yl)benzene-1,3-dicarbonitrile (2) in MeCN-*d₃*.
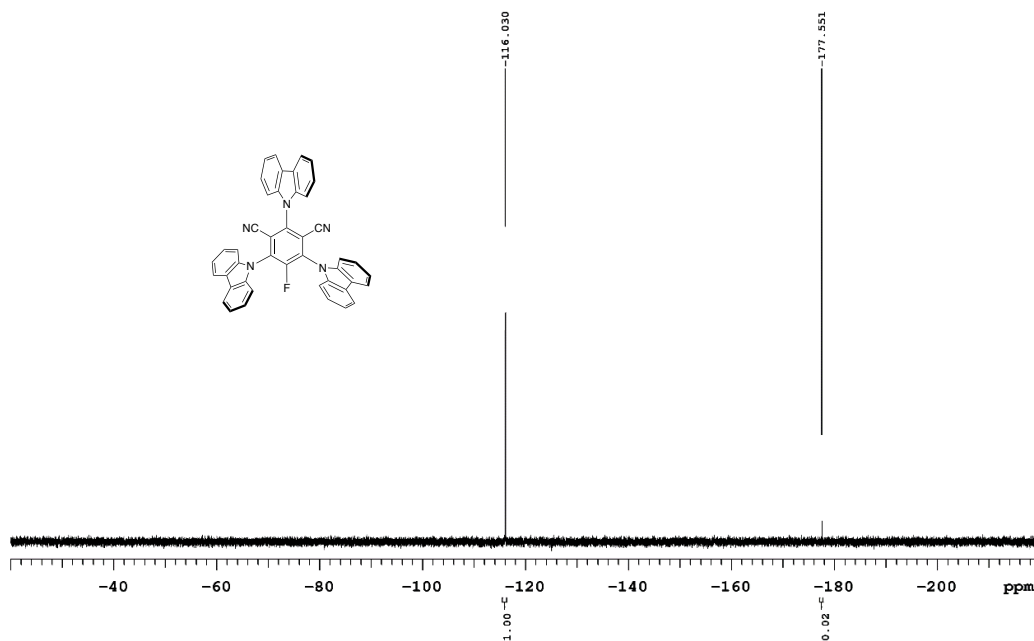
Figure 3.8. ^{19}F NMR (c) of 5-fluro-2,4,6-tri(9*H*-carbazol-9-yl)benzene-1,3-dicarbonitrile (2) in MeCN-*d₃*.

Synthesis of 1-(2,4,6-tri(9*H*-carbazol-9-yl)benzene-1,3-dicarbonitrile)imidazole (3)
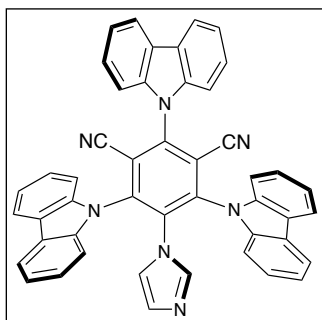
Imidazole (106.1 mg, 1.56 mmol) and Cs_2CO_3 (1.52 g, 4.67 mmol) were weighed into a side arm flask, evacuated, and refilled with argon for three cycles. Then, acetonitrile (30 mL, dried over molecular sieves and bubbled with N_2 for 30 min) was added into the flask and the resulting suspension was stirred at 50 °C for 30 min. A solution of 3CzFIPN (**2**, 1.06 g, 1.56 mmol) in 10 mL of CH_3CN and was added slowly into the flask containing imidazole and Cs_2CO_3 at room temperature. CH_3CN (10 mL) was used for quantitative transfer of the 3CzFIPN. The reaction was stirred at 50 °C. An aliquot showed (NMR) that the reaction was complete after 3 h. The reaction was allowed to cool to room temperature and then filtered using 100 mL of CH_3CN for transfer and washing. The combined filtrates were concentrated under reduced pressure using a rotavap to give a yellow solid. The crude product was dissolved in DCM (50 mL) and

the organic layer was washed with water (3 × 50 mL), brine, and dried over anhydrous Na$_2$SO$_4$. Filtration and concentration using a rotavap gave the imide **3** as a yellow powder in 95% yield. **^{1}H NMR** (499.789 MHz, CD$_3$CN, 27.7 °C): δ 6.11 (1H, s), 6.21 (1H, t, J = 1.3 Hz), 6.73 (1H, s), 7.39 (4H, t, J = 7.5 Hz), 7.49–7.55 (6H, m), 7.62 (4H, d, J = 8.1 Hz), 7.73 (1H, dt, J = 8.0 Hz, J = 1.1 Hz), 7.86 (1H, d, J = 8.2 Hz), 8.17 (2H, d, J = 7.8 Hz), 8.30 (2H, d, J = 7.8 Hz). **^{13}C{^{1}H} NMR** (125.685 MHz, CD$_3$CN, 27.7 °C): δ 110.1, 110.6, 111.8, 117.8, 118.2, 120.8, 121.0, 122.1, 122.4, 123.9, 124.2, 126.9, 127.1, 129.3, 135.4, 137.3, 139.4, 139.7, 143.2, 145.3. **HRMS (ESI)** m/z Calcd. for C$_{47}$H$_{27}$N$_7$ (M+H)$^+$: 690.2401. Found: 690.2404. Figure 3.9 (a) and (b) show the ^{1}H and ^{13}C NMR spectra of (**3**).
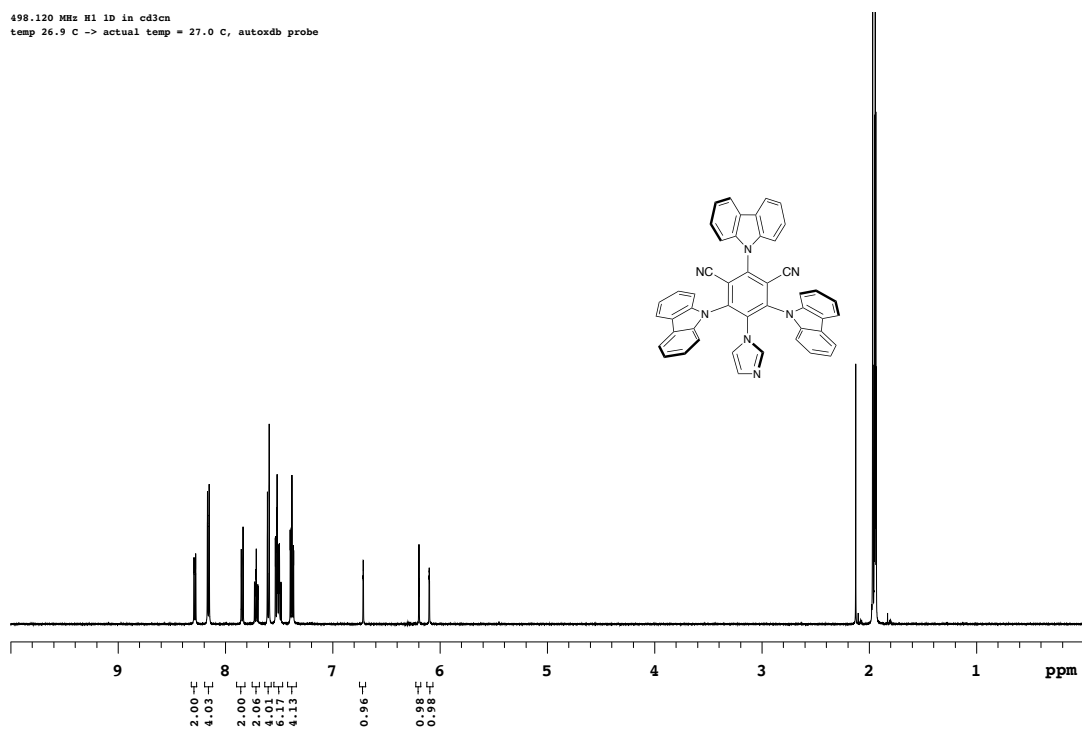
Figure 3.9. ^{1}H NMR (a) of 1-(2,4,6-tri(9*H*-carbazol-9-yl)benzene-1,3-dicarbonitrile)imidazole (**3**) in MeCN-*d$_3$*.
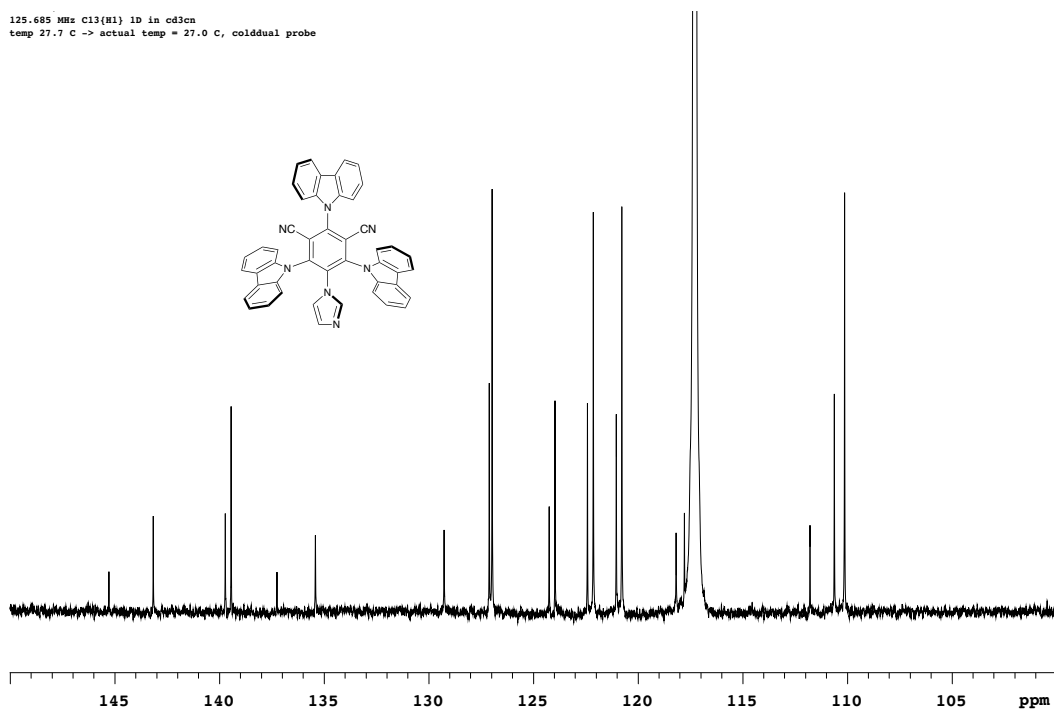
Figure 3.9. ^{13}C NMR (b) of 1-(2,4,6-tri(9*H*-carbazol-9-yl)benzene-1,3-dicarbonitrile)imidazole (**3**) in MeCN-*d₃*.

Synthesis of 1-(2,4,6-tri(9*H*-carbazol-9-yl)benzene-1,3-dicarbonitrile)-3-benzyl-Imidazolium Bromide (4)
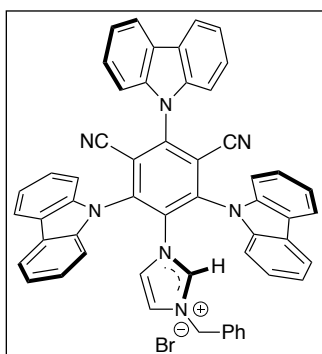
The imidazole (**3**, 400 mg, 0.58 mmol) was weighed into a 15 mL side-arm flask that was evacuated and refilled with argon 3 times. Distilled benzyl bromide (2 mL) was added using a gas-tight syringe under argon, and the resulting suspension was immersed into a 120 °C oil bath. The imidazole dissolved upon heating, then a yellow precipitate formed over the next two hours. The yellow solid was collected by filtration and washed with 50 mL of Et₂O (2 x 25 ml) to give the imidazolium bromide **4** in 95% yield. **¹H NMR** (499.789 MHz, DMSO, 27.7 °C): δ 4.90 (2H, s), 6.29 (2H, d, *J* = 7.3 Hz), 7.12 (1H, t, *J* = 1.7 Hz), 7.16 (2H, t, *J* = 7.5 Hz), 7.22 (1H, t, *J* = 1.6 Hz), 7.25 (1H, t, *J* = 7.4 Hz), 7.40 (4H, t, *J* = 6.9 Hz), 7.45–7.57 (6H, m), 7.71 (2H, t, *J* = 7.8 Hz), 7.87 (4H, d, *J* = 8.2 Hz), 7.95 (2H, d, *J* = 8.1 Hz), 8.24 (4H, d, *J* = 7.8 Hz), 8.35 (2H, d, *J* = 7.8 Hz), 9.24 (1H, s). **¹³C{¹H} NMR** (125.686

130

MHz, DMSO, 27.0 °C): δ 51.9, 111.3, 111.9, 117.3, 121.5, 121.7, 122.9, 123.8, 124.1, 124.2, 124.3, 127.1, 127.4, 128.8, 129.2, 133.6, 133.8, 137.1, 139.2, 139.8, 144.2, 148.0. **HRMS (ESI)** m/z Calcd. for $C_{54}H_{34}N_7$ (M)$^+$: 780.2870. Found: 780.2870. Figure 3.10 (a) and (b) show the ^{1}H and ^{13}C NMR spectra of (**4**), Figure 3.11 show the H1 gHSQCAD correlations.
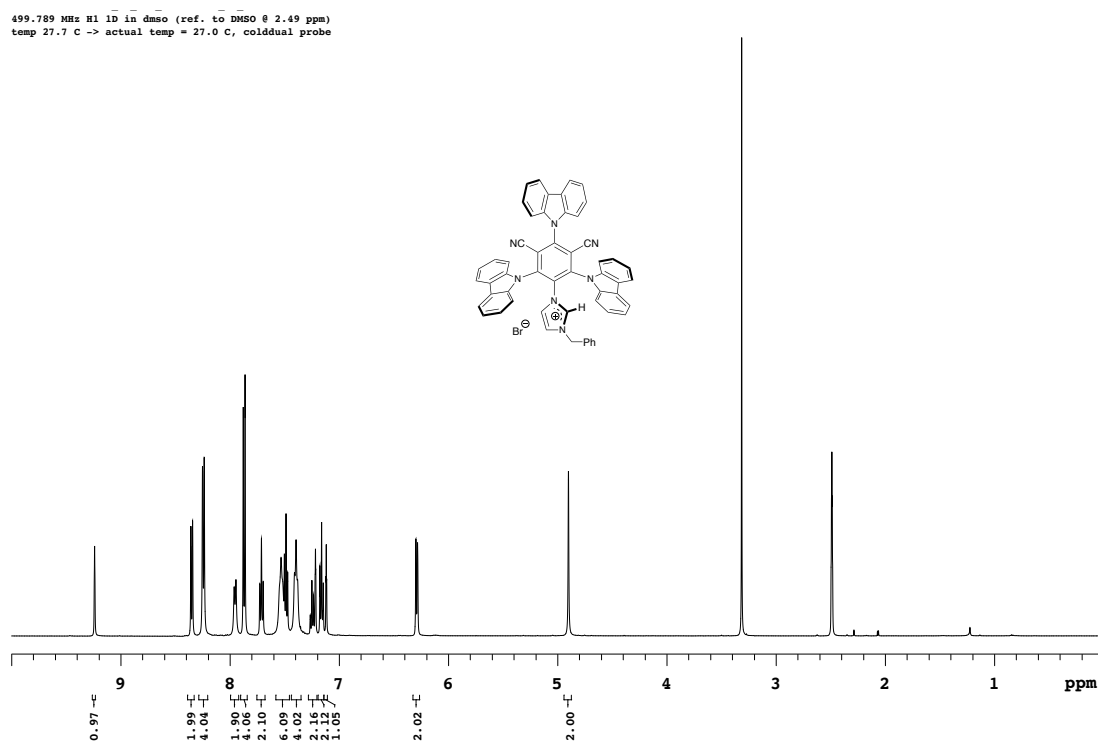
Figure 3.10. ^{1}H NMR (a) of 1-(2,4,6-tri(9H-carbazol-9-yl)benzene-1,3-dicarbonitrile)-3-benzyl-Imidazolium bromide (**4**) in DMSO-d_6.
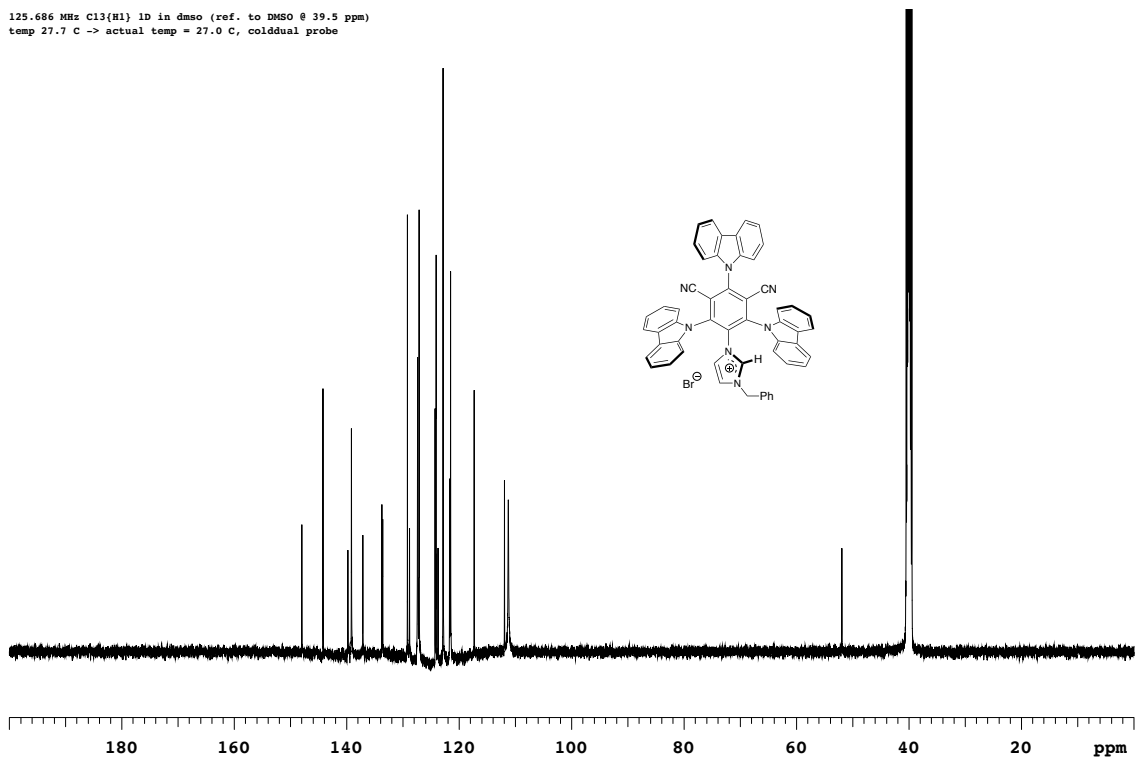
Figure 3.10. ^{13}C NMR (b) of 1-(2,4,6-tri(9H-carbazol-9-yl)benzene-1,3-dicarbonitrile)-3-benzyl-Imidazolium bromide (4) in DMSO-*d6*.
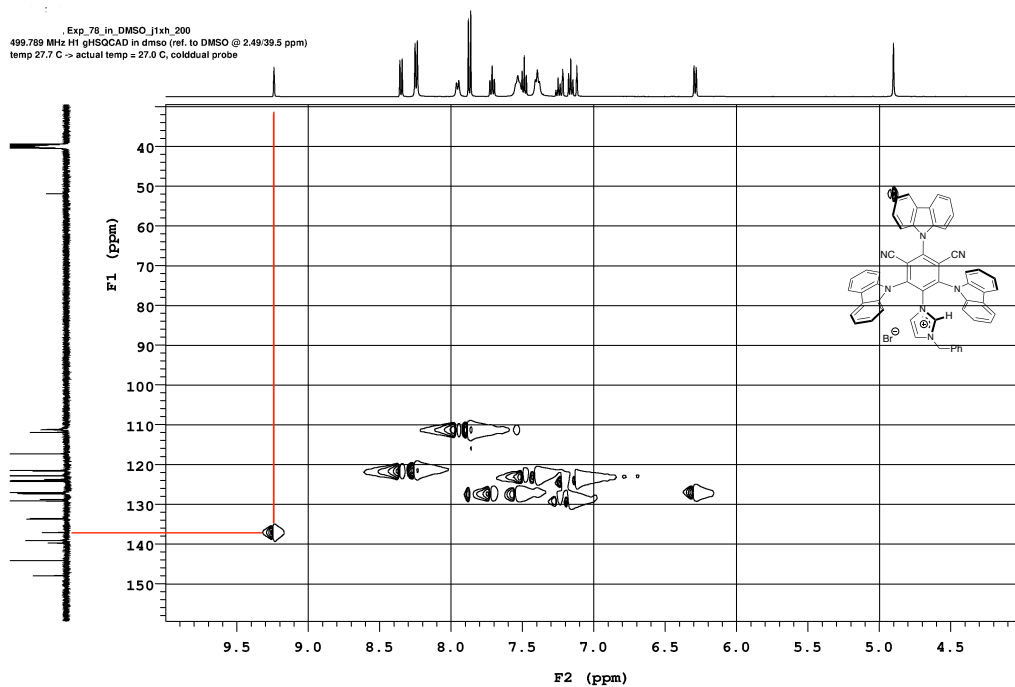
Figure 3.11. H1 gHSQCAD correlations for 1-(2,4,6-tri(9H-carbazol-9-yl)benzene-1,3-dicarbonitrile)-3-benzyl-Imidazolium bromide (4) in DMSO-*d6* with the C2-H correlation highlighted.

Synthesis of 1-(2,4,6-tri(9*H*-carbazol-9-yl)benzene-1,3-dicarbonitrile)-3-benzyl-imidazolium Tetrafluoroborates (5)
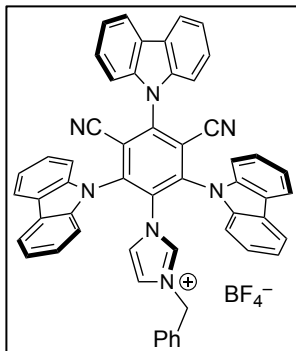
The imidazolium bromide salt (**4**, 400 mg, 0.46 mmol) was weighed into a 30 mL side-arm flask and evacuated and refilled with argon three times. Using a gas-tight syringe 10 mL of freshly distilled acetonitrile were transferred into the flask to disperse the dye (poorly soluble). The AgBF$_4$ (108.5 mg, 0.55 mmol) was weighed inside the glovebox in a Schlenk flask, and then connected to a Schlenk line. The silver salt was dissolved in 3 mL of acetonitrile and cannula transferred to the imidazolium salt, and extra 2 mL of solvent were used for quantitative transfer. The reaction mixture was stirred at room temperature for 1 h, an aliquot (NMR) showed that the reaction was complete. The yellow solution was filtered through a celite plug and concentrated under reduced pressure. The yellow solid was washed with diethyl ether (2 x 25 mL) to give the imidazolium tetrafluoroborate in 98% yield. **^{1}H NMR** (498.120 MHz, CD$_3$CN, 26.9 ºC): δ 4.65 (2H, s), 6.45 (2H, d, *J* = 7.5 Hz), 6.67 (1H, t, *J* = 1.9 Hz), 6.74 (1H, t, *J* = 1.9 Hz), 7.24 (2H, t, *J* = 7.5 Hz), 7.34 (1H, t, *J* = 7.5 Hz), 7.46–7.53 (4H, m), 7.54–7.58 (10H, m), 7.56 (2H, t, *J* = 7 Hz), 7.77 (2H, d, *J* = 1.0 Hz), 8.12 (1H, s), 8.20 (4H, d, *J* = 7.5 Hz), 8.31 (2H, d, *J* =7 .9 Hz). **^{13}C {^{1}H} NMR** (125.686 MHz, CD$_3$CN, 27.0 ºC): δ 51.9, 111.3, 111.9, 117.3, 121.5, 121.7, 122.9, 123.8, 124.1, 124.2, 124.3, 127.1, 127.4, 128.8, 129.2, 133.6, 133.8, 137.1, 139.2, 139.8, 144.2, 148.0. **HRMS (ESI)** m/z Calcd. for C$_{54}$H$_{34}$N$_7$ (M)$^+$: 780.2870. Found: 780.2870. Figure 3.12 (a) and (b) show the ^{1}H and ^{13}C NMR spectra of (**5**).
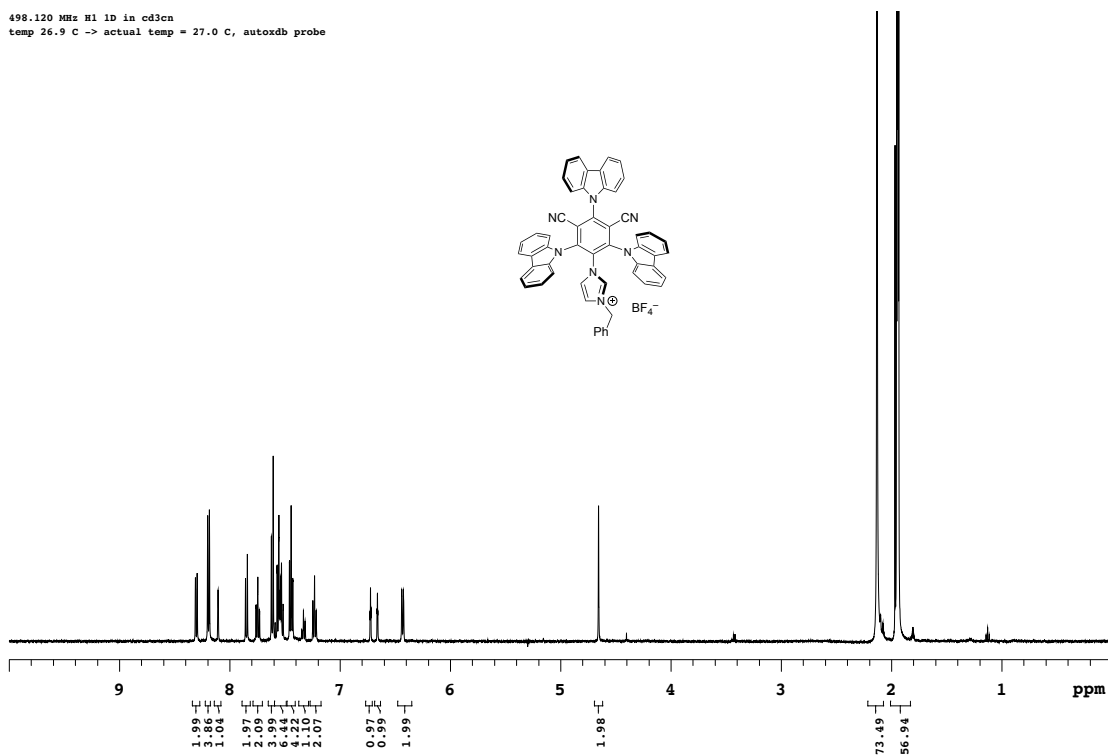
Figure 3.12. ¹H NMR (a) of 1-(2,4,6-tri(9*H*-carbazol-9-yl)benzene-1,3-dicarbonitrile)-3-benzyl-imidazolium tetrafluoroborate (**5**) in CH₃CN-*d*3.
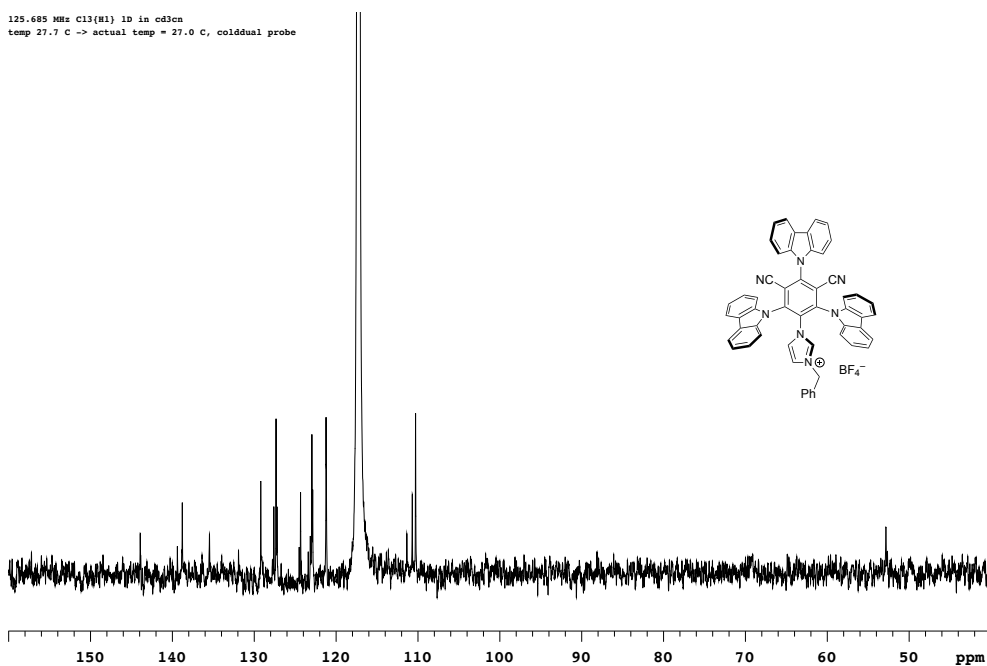
Figure 3.12. ¹³C NMR (b) of 1-(2,4,6-tri(9*H*-carbazol-9-yl)benzene-1,3-dicarbonitrile)-3-benzyl-imidazolium tetrafluoroborate (**5**) in CH₃CN-*d*3.

134
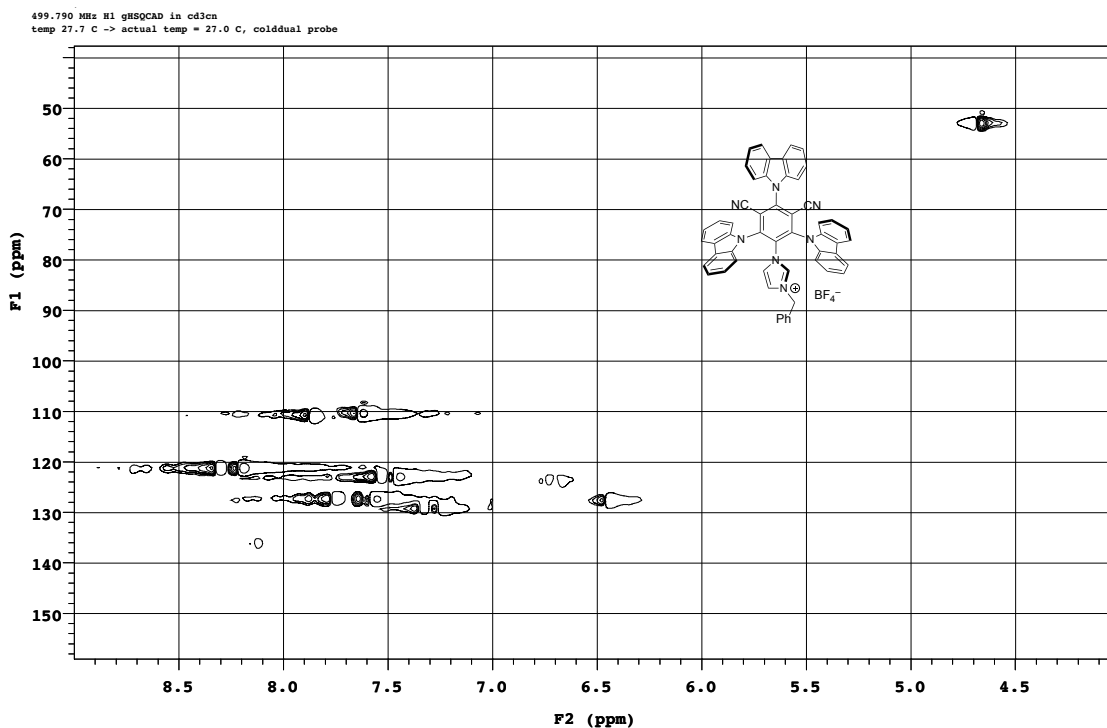
Figure 3.12. H1 *g*HSQCAD correlations (c) for 1-(2,4,6-tri(9*H*-carbazol-9-yl)benzene-1,3-dicarbonitrile)-3-benzyl-imidazolium tetrafluoroborate (**5**) in CH₃CN-*d*3.

Low T NMR-scale Deprotonation of the Imidazolium 3 by KN(SiMe₃)₂ or KO^t^Bu to Form 1-(2,4,6-tri(9*H*-carbazol-9-yl)benzene-1,3-dicarbonitrile)-3-benzyl-1,3-dihydro-2H-imidazol-2-ylidene (6)
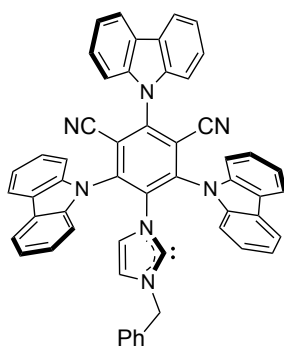
The imidazolium **4** (15 mg, 0.0174 mmol) and base (0.0174 mmol, 1 equiv.) were weighed into separate NMR tubes and sealed with septa inside a glove box. Freshly distilled, dry THF-*d*₈ (0.4 mL) was added into each NMR tube under argon atmosphere. The imidazolium **4** did not dissolve. After immersing the NMR tubes in a –80 °C (dry ice/acetone) cold bath, the solution of base was transferred to the NMR tube containing **4** through double ended needle under argon pressure. The reaction was monitored by NMR from –80 °C to 0 °C, which showed that deprotonation to form the NHC **6** was complete at –30 °C, which is roughly the temperature at which **4** partially dissolved. The THF solutions of the NHC were stable at temperatures below 0 °C. Figure 3.13 shows the ¹H and ¹³C NMR spectra of NHC **6** at –30 °C.
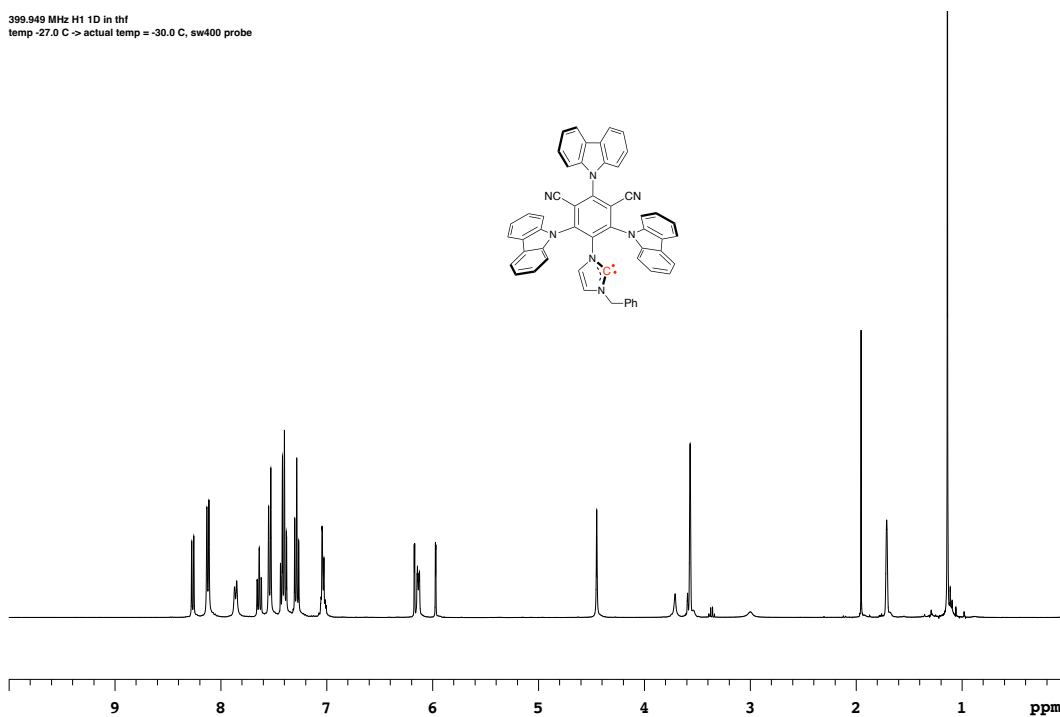
Figure 3.13. ^{1}H NMR (a) of the free NHC 6 formed by the reaction between 3CzIPN-Imidazolium[Br] **4** and KO*t*Bu in THF-*d₈*.
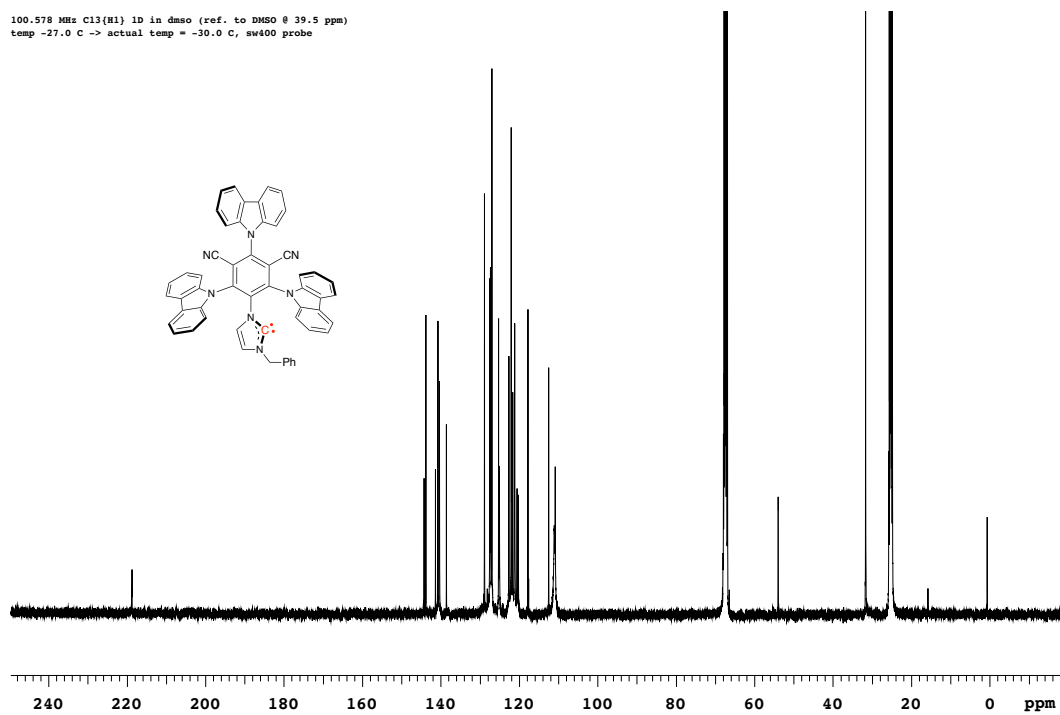
Figure 3.13. ^{13}C NMR (b) of the free NHC **6** formed by the reaction between 3CzIPN-Imidazolium[Br] **4** and KO*t*Bu in THF-*d₈*.

Deprotonation of 3CzIPN-Imidazolium[BF₄] with KH to form 1-(2,4,6-tri(9H-carbazol-9-yl)benzene-1,3-dicarbonitrile)-3-benzyl-1,3-dihydro-2H-imidazol-2-ylidene (6)

The 3CzIPN-Imidazolium[BF₄] **5** (30 mg, 0.035 mmol) and KH (13.9 mg, 0.035 mmol, 10 equiv.) were weighed into a 30 mL Schlenk flask and sealed with septa inside a glove box. Then, the Schlenk flask was moved to a Schlenk line and placed into an ice-water bath. Freshly distilled, dry, at 0 °C, THF (10 mL) was added into the Schlenk flask under argon atmosphere. The imidazolium **6** did not dissolve completely. The suspension was stirred for 3 h at 0 °C, under Argon bubbler pressure. The original yellow suspension became red, an aliquot taken showed (NMR) that the carbene was the only product present. 99% yield by ¹H NMR. **¹H NMR** (399.949 MHz, THF-d_8, 0 °C): δ 4.42 (2H, s), 5.93 (1H, s), 6.13–6.19 (3H, m), 6.99–7.05 (3H, m), 7.23–7.31 (4H, m), 7.34–7.42 (6H, m), 7.48 (4H, d, J = 8.1 Hz), 7.60 (2H, t, J = 7.8 Hz), 7.78 (2H, d, J = 8.2 Hz), 8.09 (4H, d, J = 7.7 Hz), 8.23 (2H, d, J = 7.8 Hz). **¹³C{¹H} NMR** (100.576 MHz, THF-d_8, 0.0 °C): δ 53.2, 103.8.4, 110.1, 111.3, 117.1, 119.2, 119.5, 119.7, 120.0, 120.1, 120.7, 121.1, 121.7, 124.2, 124.4, 126.0, 126.5, 126.6, 127.9, 137.6 139.6, 139.9, 140.9, 142.9, 143.4, 219.1. Figure 3.14. show the H1 gHSQCAD correlations at 0 °C.
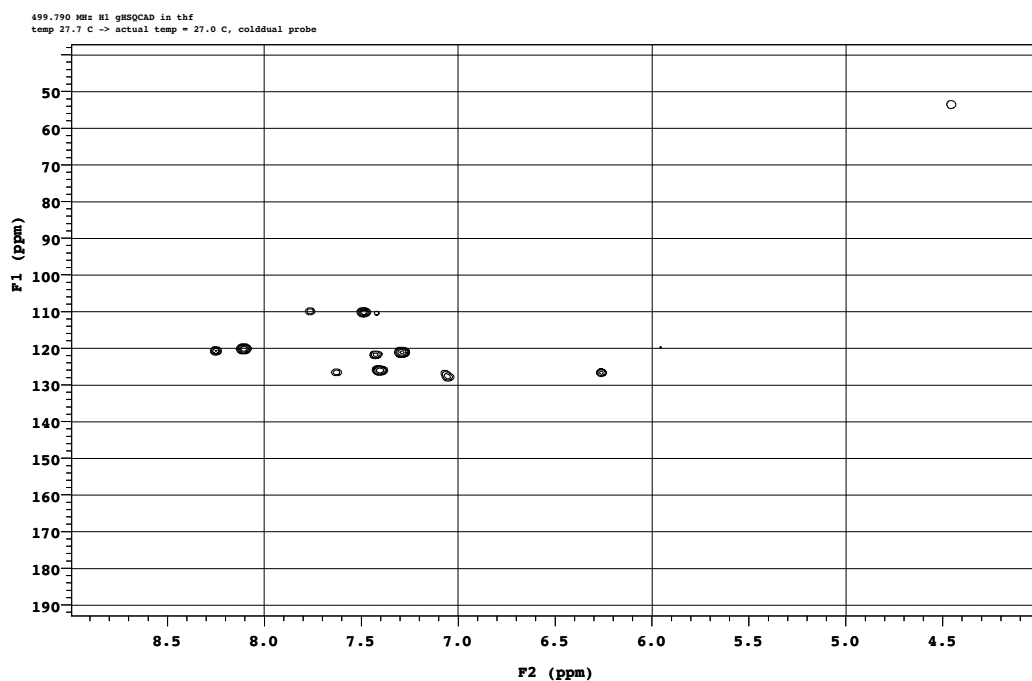
Figure 3.14. H1 gHSQCAD correlations for 1-(2,4,6-tri(9H-carbazol-9-yl)benzene-1,3-dicarbonitrile)-3-benzyl-1,3-dihydro-2H-imidazol-2-ylidene (**6**) in THF-d8.

Immobilization of the Chromophores onto TiO₂

The imidazolium tetraborate **5** (31.2 mg, 0.0359 mmol) and 14.6 mg of KH (0.36 mmol, 10 equiv.) were weighed into a 30 mL side arm flask inside a glovebox. The flask was sealed with a rubber septum, transferred to a Schlenk line, and cooled to 0 °C in an ice bath. 16 mL of freshly distilled, N₂-sparged THF cooled to 0 °C was then slowly cannula transferred into the flask charged with **5** and the KH. The resulting suspension was stirred at 0 °C for 3 h under N₂ -bubbler pressure to form an intense-red solution of the NHC **6**. In the meantime, in a separate 30 ml Schlenk tube, TiO₂ electrodes were immersed in the ice-water bath. The homogeneous solution of the NHC **6** was transferred through a cannula into the flask containing the TiO₂ electrodes and the resulting suspension was stirred at 0 °C for 1 h. After an hour, the solution containing the excess NHC **6** was cannula-removed and the TiO₂-**6** electrodes were washed with 60 mL of THF (3 x 20 mL). The resulting TiO₂-**6** electrodes were then dried under vacuum for 1 h and stored under N₂. Figure 3.15 shows the FT-IR ATR spectrum of the TiO₂-**6** electrode and **5**. Figure 3.16 shows the high-resolution XPS spectra of the TiO₂ and TiO₂-**6** electrodes.
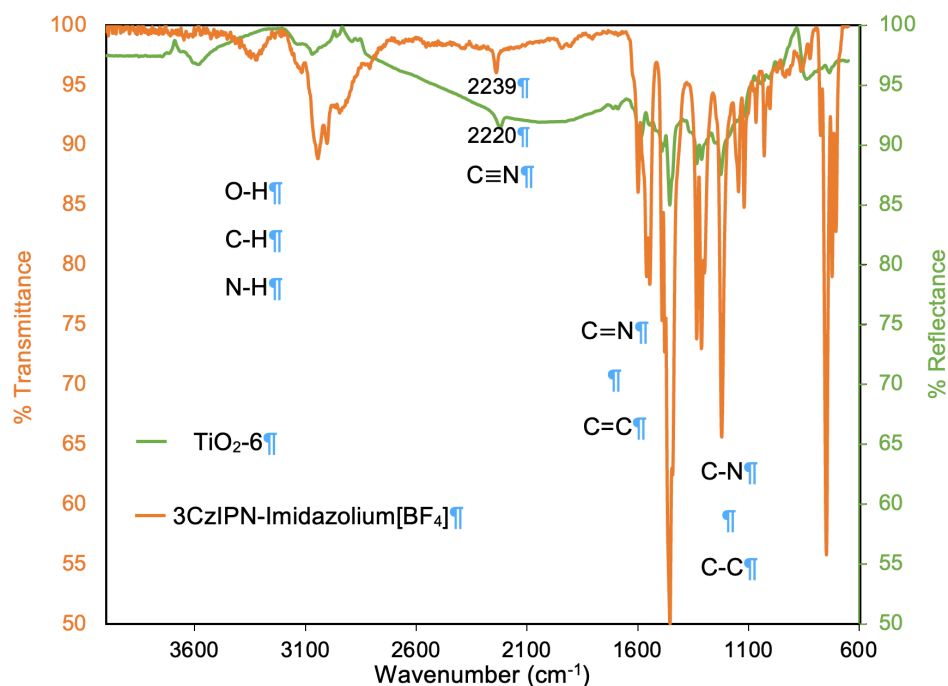
Figure 3.15. IR reflectance and transmittance of TiO₂-6 electrode and 3CzIPN-Imidazolium[BF₄].
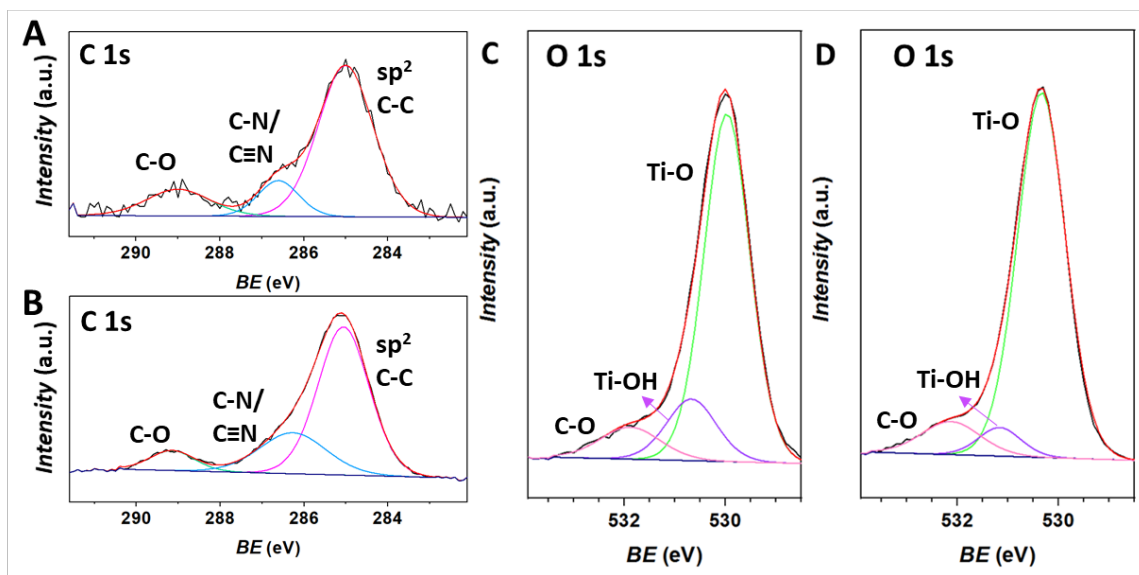
Figure 3.16. The high-resolution XPS spectra in C1s (A, B) and O1s (C, D) region for bare (A, C) TiO$_2$ and TiO$_2$-**6** (B, D) electrode.

Photoelectrochemistry

For photoelectrochemical studies, 0.1 M NaClO$_4$ solution (50 mL) containing either 0.02 M hydroquinone (pH = 7.0) or 0.5 M Et$_3$N (pH = 12.6) was used. The reference and counter electrodes were saturated calomel electrode (SCE) and platinum gauze, respectively. The reaction flask was a 100 mL four-neck quartz round bottom container with a flat window on the side. Before photoelectrochemical measurement, the solution was bubbled with argon for 30 min. An argon blanket was maintained on top of the solution during the studies. The electrolyte was stirred at 500 rpm throughout the measurements using a magnetic bar. The light source was a Newport QEPVSI-b system equipped with a 300 W Xe lamp and Cornerstone M 260 monochromator. The incident light intensity was measured with a Thorlab S121C light meter after the measurements and incident photon to current conversion efficiency (IPCE) at any specific wavelength was calculated using eq 3.1:

$$\text{IPCE (\%)} = ((1240 \times I) / (P \times \lambda)) \times 100 \qquad (3.1)$$

where I is the obtained photocurrent density (mA cm^{-2}), λ is the specific wavelength (nm), and P is light power density (mW cm^{-2}).

139

The XRD patterns for the TiO$_2$ nanoparticles (Figure 3.17) were the same before and after the deposition of the NHC surface layer. This is an expected result because the formation of an NHC monolayer (or near monolayer) on the surface of TiO$_2$ would not appreciably impact the bulk structure of the nanoparticles and thereby the diffraction pattern would not change.
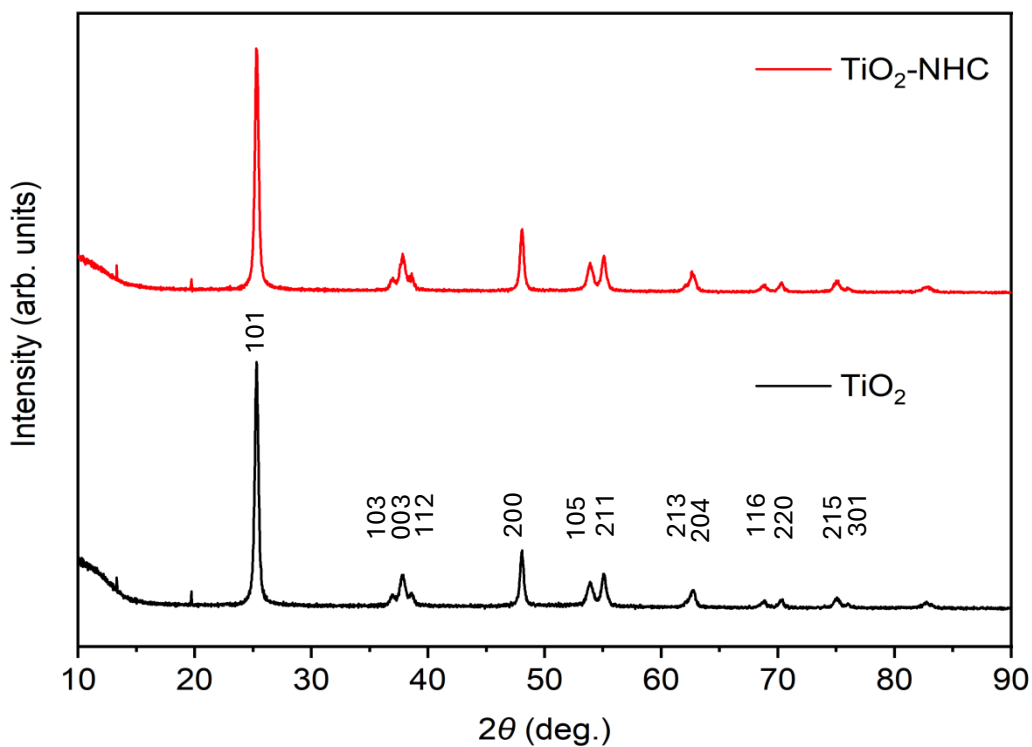
Figure 3.17. XRD pattern of TiO$_2$ and TiO$_2$-NHC electrodes (NPs in anatase form).

SEM images showed no change in the morphology or topography of the TiO$_2$ nanoparticles before and after the formation of the NHC surface layer. As expected, the surface layer of the NHC on TiO$_2$ did not affect the interior structure, morphology, or topography of the nanoparticles.
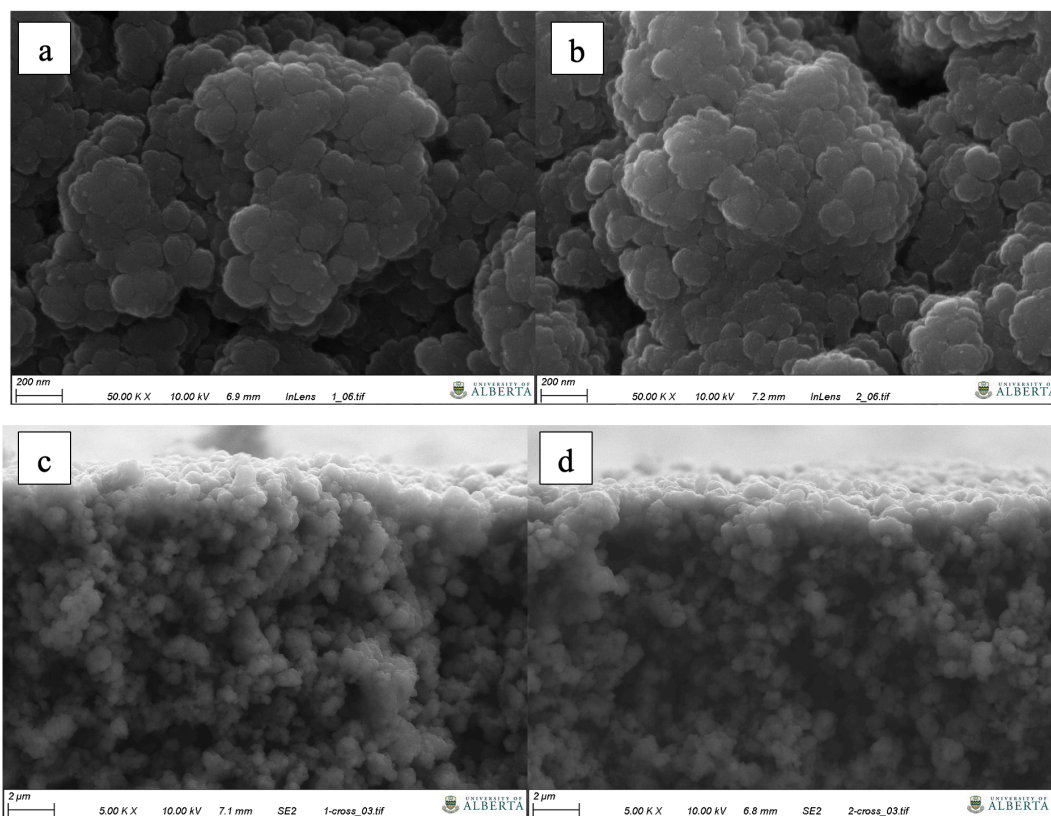
Figure 3.18. SEM images TiO$_2$ electrode a) Top view and c) sectional view. TiO$_2$-NHC b) Top view and d) sectional view.

3.5 References

(1) Zhang, B.; Sun, L. Artificial Photosynthesis: Opportunities and Challenges of Molecular Catalysts. *Chem. Soc. Rev.* **2019**, *48* (7), 2216–2264. https://doi.org/10.1039/C8CS00897C.

(2) Lewis, N. S. Research Opportunities to Advance Solar Energy Utilization. *Science* **2016**, *351* (6271), aad1920. https://doi.org/10.1126/science.aad1920.

(3) Kärkäs, M. D.; Verho, O.; Johnston, E. V.; Åkermark, B. Artificial Photosynthesis: Molecular Systems for Catalytic Water Oxidation. *Chem. Rev.* **2014**, *114* (24), 11863–12001. https://doi.org/10.1021/cr400572f.

(4) Lewis, N. S.; Nocera, D. G. Powering the Planet: Chemical Challenges in Solar Energy Utilization. *Proc. Natl. Acad. Sci. U.S.A.* **2006**, *103* (43), 15729–15735. https://doi.org/10.1073/pnas.0603395103.

(5) Xu, P.; McCool, N. S.; Mallouk, T. E. Water Splitting Dye-Sensitized Solar Cells. *Nano Today* **2017**, *14*, 42–58. https://doi.org/10.1016/j.nantod.2017.04.009.

(6) Wang, D.; Hu, J.; Sherman, B. D.; Sheridan, M. V.; Yan, L.; Dares, C. J.; Zhu, Y.; Li, F.; Huang, Q.; You, W.; Meyer, T. J. A Molecular Tandem Cell for Efficient Solar Water Splitting. *Proc. Natl. Acad. Sci. U.S.A.* **2020**, *117* (24), 13256–13260. https://doi.org/10.1073/pnas.2001753117.

(7) Roger, I.; Shipman, M. A.; Symes, M. D. Earth-Abundant Catalysts for Electrochemical and Photoelectrochemical Water Splitting. *Nat Rev Chem* **2017**, *1* (1), 0003. https://doi.org/10.1038/s41570-016-0003.

(8) Tang, S.; Qiu, W.; Xiao, S.; Tong, Y.; Yang, S. Harnessing Hierarchical Architectures to Trap Light for Efficient Photoelectrochemical Cells. *Energy Environ. Sci.* **2020**, *13* (3), 660–684. https://doi.org/10.1039/C9EE02986A.

(9) Castro, S.; Albo, J.; Irabien, A. Photoelectrochemical Reactors for CO_2 Utilization. *ACS Sustainable Chem. Eng.* **2018**, *6* (12), 15877–15894. https://doi.org/10.1021/acssuschemeng.8b03706.

(10) Brennaman, M. K.; Dillon, R. J.; Alibabaei, L.; Gish, M. K.; Dares, C. J.; Ashford, D. L.; House, R. L.; Meyer, G. J.; Papanikolas, J. M.; Meyer, T. J. Finding the Way to Solar Fuels with Dye-Sensitized Photoelectrosynthesis Cells. *J. Am. Chem. Soc.* **2016**, *138* (40), 13085–13102. https://doi.org/10.1021/jacs.6b06466.

(11) Kumar, B.; Llorente, M.; Froehlich, J.; Dang, T.; Sathrum, A.; Kubiak, C. P. Photochemical and Photoelectrochemical Reduction of CO_2. *Annu. Rev. Phys. Chem.* **2012**, *63* (1), 541–569. https://doi.org/10.1146/annurev-physchem-032511-143759.

(12) Ashford, D. L.; Gish, M. K.; Vannucci, A. K.; Brennaman, M. K.; Templeton, J. L.; Papanikolas, J. M.; Meyer, T. J. Molecular Chromophore–Catalyst Assemblies for Solar Fuel Applications. *Chem. Rev.* **2015**, *115* (23), 13006–13049. https://doi.org/10.1021/acs.chemrev.5b00229.

(13) Reece, S. Y.; Hamel, J. A.; Sung, K.; Jarvi, T. D.; Esswein, A. J.; Pijpers, J. J. H.; Nocera, D. G. Wireless Solar Water Splitting Using Silicon-Based Semiconductors and Earth-Abundant Catalysts. *Science* **2011**, *334* (6056), 645–648. https://doi.org/10.1126/science.1209816.

(14) Dongare, P.; Myron, B. D. B.; Wang, L.; Thompson, D. W.; Meyer, T. J. [Ru(Bpy)3]2+∗ Revisited. Is It Localized or Delocalized? How Does It Decay? *Coordination Chemistry Reviews* **2017**, *345*, 86–107. https://doi.org/10.1016/j.ccr.2017.03.009.

(15) Yuan, Y.-J.; Yu, Z.-T.; Chen, D.-Q.; Zou, Z.-G. Metal-Complex Chromophores for Solar Hydrogen Generation. *Chem. Soc. Rev.* **2017**, *46* (3), 603–631. https://doi.org/10.1039/C6CS00436A.

(16) Thompson, D. W.; Ito, A.; Meyer, T. J. [Ru(Bpy)3]2+* and Other Remarkable Metal-to-Ligand Charge Transfer (MLCT) Excited States. *Pure and Applied Chemistry* **2013**, *85* (7), 1257–1305. https://doi.org/10.1351/PAC-CON-13-03-04.

(17) Wang, Y.; Liu, T.; Chen, L.; Chao, D. Water-Assisted Highly Efficient Photocatalytic Reduction of CO_2 to CO with Noble Metal-Free Bis(Terpyridine)Iron(II) Complexes and an Organic Photosensitizer. *Inorg. Chem.* **2021**, *60* (8), 5590–5597. https://doi.org/10.1021/acs.inorgchem.0c03503.

(18) Farré, Y.; Maschietto, F.; Föhlinger, J.; Wykes, M.; Planchat, A.; Pellegrin, Y.; Blart, E.; Ciofini, I.; Hammarström, L.; Odobel, F. A Comparative Investigation of the Role of the Anchoring

Group on Perylene Monoimide Dyes in NiO-Based Dye-Sensitized Solar Cells. *ChemSusChem* **2020**, *13* (7), 1844–1855. https://doi.org/10.1002/cssc.201903182.

(19) Brennan, B. J.; Llansola Portolés, M. J.; Liddell, P. A.; Moore, T. A.; Moore, A. L.; Gust, D. Comparison of Silatrane, Phosphonic Acid, and Carboxylic Acid Functional Groups for Attachment of Porphyrin Sensitizers to TiO2 in Photoelectrochemical Cells. *Phys. Chem. Chem. Phys.* **2013**, *15* (39), 16605. https://doi.org/10.1039/c3cp52156g.

(20) Sullivan, I.; Goryachev, A.; Digdaya, I. A.; Li, X.; Atwater, H. A.; Vermaas, D. A.; Xiang, C. Coupling Electrochemical CO2 Conversion with CO2 Capture. *Nat Catal* **2021**, *4* (11), 952–958. https://doi.org/10.1038/s41929-021-00699-7.

(21) Bangle, R.; Sampaio, R. N.; Troian-Gautier, L.; Meyer, G. J. Surface Grafting of Ru(II) Diazonium-Based Sensitizers on Metal Oxides Enhances Alkaline Stability for Solar Energy Conversion. *ACS Appl. Mater. Interfaces* **2018**, *10* (3), 3121–3132. https://doi.org/10.1021/acsami.7b16641.

(22) Surendranath, Y.; Kanan, M. W.; Nocera, D. G. Mechanistic Studies of the Oxygen Evolution Reaction by a Cobalt-Phosphate Catalyst at Neutral pH. *J. Am. Chem. Soc.* **2010**, *132* (46), 16501–16509. https://doi.org/10.1021/ja106102b.

(23) Jamesh, M.-I.; Sun, X. Recent Progress on Earth Abundant Electrocatalysts for Oxygen Evolution Reaction (OER) in Alkaline Medium to Achieve Efficient Water Splitting – A Review. *Journal of Power Sources* **2018**, *400*, 31–68. https://doi.org/10.1016/j.jpowsour.2018.07.125.

(24) Rotundo, L.; Filippi, J.; Gobetto, R.; Miller, H. A.; Rocca, R.; Nervi, C.; Vizza, F. Electrochemical CO$_2$ Reduction in Water at Carbon Cloth Electrodes Functionalized with a *Fac* -Mn(Apbpy)(CO)$_3$ Br Complex. *Chem. Commun.* **2019**, *55* (6), 775–777. https://doi.org/10.1039/C8CC08385A.

(25) Shul, G.; Weissmann, M.; Bélanger, D. Electrochemical Characterization of Glassy Carbon Electrode Modified with 1,10-Phenanthroline Groups by Two Pathways: Reduction of the Corresponding Diazonium Ions and Reduction of Phenanthroline. *Electrochimica Acta* **2015**, *162*, 146–155. https://doi.org/10.1016/j.electacta.2014.12.116.

(26) Wang, C.; Amiri, M.; Endean, R. T.; Martinez Perez, O.; Varley, S.; Rennie, B.; Rasu, L.; Bergens, S. H. Modular Construction of Photoanodes with Covalently Bonded Ru- and Ir-Polypyridyl Visible Light Chromophores. *ACS Appl. Mater. Interfaces* **2018**, *10* (29), 24533–24542. https://doi.org/10.1021/acsami.8b06605.

(27) Amiri, M.; Martinez Perez, O.; Endean, R. T.; Rasu, L.; Nepal, P.; Xu, S.; Bergens, S. H. Solid-Phase Synthesis and Photoactivity of Ru-Polypyridyl Visible Light Chromophores Bonded through Carbon to Semiconductor Surfaces. *Dalton Trans.* **2020**, *49* (29), 10173–10184. https://doi.org/10.1039/D0DT01776K.

(28) Shang, T.-Y.; Lu, L.-H.; Cao, Z.; Liu, Y.; He, W.-M.; Yu, B. Recent Advances of 1,2,3,5-Tetrakis(Carbazol-9-Yl)-4,6-Dicyanobenzene (4CzIPN) in Photocatalytic Transformations. *Chem. Commun.* **2019**, *55* (38), 5408–5419. https://doi.org/10.1039/C9CC01047E.

(29) Dalle, K. E.; Warnan, J.; Leung, J. J.; Reuillard, B.; Karmel, I. S.; Reisner, E. Electro- and Solar-Driven Fuel Synthesis with First Row Transition Metal Complexes. *Chem. Rev.* **2019**, *119* (4), 2752–2875. https://doi.org/10.1021/acs.chemrev.8b00392.

(30) Nazeeruddin, M. K.; Kay, A.; Rodicio, I.; Humphry-Baker, R.; Mueller, E.; Liska, P.; Vlachopoulos, N.; Graetzel, M. Conversion of Light to Electricity by Cis-X2bis(2,2'-Bipyridyl-4,4'-Dicarboxylate)Ruthenium(II) Charge-Transfer Sensitizers (X = Cl-, Br-, I-, CN-, and SCN-) on Nanocrystalline Titanium Dioxide Electrodes. *J. Am. Chem. Soc.* **1993**, *115* (14), 6382–6390. https://doi.org/10.1021/ja00067a063.

(31) Ishimatsu, R.; Matsunami, S.; Kasahara, T.; Mizuno, J.; Edura, T.; Adachi, C.; Nakano, K.; Imato, T. Electrogenerated Chemiluminescence of Donor–Acceptor Molecules with Thermally Activated Delayed Fluorescence. *Angew Chem Int Ed* **2014**, *53* (27), 6993–6996. https://doi.org/10.1002/anie.201402615.

(32) Zigler, D. F.; Morseth, Z. A.; Wang, L.; Ashford, D. L.; Brennaman, M. K.; Grumstrup, E. M.; Brigham, E. C.; Gish, M. K.; Dillon, R. J.; Alibabaei, L.; Meyer, G. J.; Meyer, T. J.; Papanikolas, J. M. Disentangling the Physical Processes Responsible for the Kinetic Complexity in Interfacial Electron Transfer of Excited Ru(II) Polypyridyl Dyes on TiO $_2$. *J. Am. Chem. Soc.* **2016**, *138* (13), 4426–4438. https://doi.org/10.1021/jacs.5b12996.

(33) Purnama, I.; Salmahaminati, S.; Abe, M.; Hada, M.; Kubo, Y.; Mulyana, J. Y. Factors Influencing the Photoelectrochemical Device Performance Sensitized by Ruthenium Polypyridyl Dyes. *Dalton Trans.* **2019**, *48* (2), 688–695. https://doi.org/10.1039/C8DT03502D.

(34) Dares, C. J.; Lapides, A. M.; Mincher, B. J.; Meyer, T. J. Electrochemical Oxidation of [243] Am(III) in Nitric Acid by a Terpyridyl-Derivatized Electrode. *Science* **2015**, *350* (6261), 652–655. https://doi.org/10.1126/science.aac9217.

(35) Rasu, L.; Amiri, M.; Bergens, S. H. Carbazole–Cyanobenzene Dyes Electrografted to Carbon or Indium-Doped Tin Oxide Supports for Visible Light-Driven Photoanodes and Olefin Isomerizations. *ACS Appl. Mater. Interfaces* **2021**, *13* (15), 17745–17752. https://doi.org/10.1021/acsami.1c05064.

(36) Corpas, J.; Mauleón, P.; Gómez Arrayás, R.; Carretero, J. C. *E/Z* Photoisomerization of Olefins as an Emergent Strategy for the Control of Stereodivergence in Catalysis. *Adv Synth Catal* **2022**, *364* (8), 1348–1370. https://doi.org/10.1002/adsc.202200199.

(37) Peris, E. Smart N-Heterocyclic Carbene Ligands in Catalysis. *Chem. Rev.* **2018**, *118* (19), 9988–10031. https://doi.org/10.1021/acs.chemrev.6b00695.

(38) Samojłowicz, C.; Bieniek, M.; Grela, K. Ruthenium-Based Olefin Metathesis Catalysts Bearing *N* -Heterocyclic Carbene Ligands. *Chem. Rev.* **2009**, *109* (8), 3708–3742. https://doi.org/10.1021/cr800524f.

(39) Vougioukalakis, G. C.; Grubbs, R. H. Ruthenium-Based Heterocyclic Carbene-Coordinated Olefin Metathesis Catalysts. *Chem. Rev.* **2010**, *110* (3), 1746–1787. https://doi.org/10.1021/cr9002424.

(40) Bellotti, P.; Koy, M.; Hopkinson, M. N.; Glorius, F. Recent Advances in the Chemistry and Applications of N-Heterocyclic Carbenes. *Nat Rev Chem* **2021**, *5* (10), 711–725. https://doi.org/10.1038/s41570-021-00321-1.

(41) Smith, C. A.; Narouz, M. R.; Lummis, P. A.; Singh, I.; Nazemi, A.; Li, C.-H.; Crudden, C. M. *N*-Heterocyclic Carbenes in Materials Chemistry. *Chem. Rev.* **2019**, *119* (8), 4986–5056. https://doi.org/10.1021/acs.chemrev.8b00514.

(42) Zhukhovitskiy, A. V.; MacLeod, M. J.; Johnson, J. A. Carbene Ligands in Surface Chemistry: From Stabilization of Discrete Elemental Allotropes to Modification of Nanoscale and Bulk Substrates. *Chem. Rev.* **2015**, *115* (20), 11503–11532. https://doi.org/10.1021/acs.chemrev.5b00220.

(43) Crudden, C. M.; Horton, J. H.; Narouz, M. R.; Li, Z.; Smith, C. A.; Munro, K.; Baddeley, C. J.; Larrea, C. R.; Drevniok, B.; Thanabalasingam, B.; McLean, A. B.; Zenkina, O. V.; Ebralidze, I. I.; She, Z.; Kraatz, H.-B.; Mosey, N. J.; Saunders, L. N.; Yagi, A. Simple Direct Formation of Self-Assembled N-Heterocyclic Carbene Monolayers on Gold and Their Application in Biosensing. *Nat Commun* **2016**, *7* (1), 12654. https://doi.org/10.1038/ncomms12654.

(44) Crudden, C. M.; Horton, J. H.; Ebralidze, I. I.; Zenkina, O. V.; McLean, A. B.; Drevniok, B.; She, Z.; Kraatz, H.-B.; Mosey, N. J.; Seki, T.; Keske, E. C.; Leake, J. D.; Rousina-Webb, A.; Wu, G. Ultra Stable Self-Assembled Monolayers of N-Heterocyclic Carbenes on Gold. *Nature Chem* **2014**, *6* (5), 409–414. https://doi.org/10.1038/nchem.1891.

(45) Lara, P.; Rivada-Wheelaghan, O.; Conejero, S.; Poteau, R.; Philippot, K.; Chaudret, B. Ruthenium Nanoparticles Stabilized by N-Heterocyclic Carbenes: Ligand Location and Influence on Reactivity. *Angew Chem Int Ed* **2011**, *50* (50), 12080–12084. https://doi.org/10.1002/anie.201106348.

(46) Baquero, E. A.; Tricard, S.; Flores, J. C.; de Jesús, E.; Chaudret, B. Highly Stable Water-Soluble Platinum Nanoparticles Stabilized by Hydrophilic N-Heterocyclic Carbenes. *Angewandte Chemie* **2014**, *126* (48), 13436–13440. https://doi.org/10.1002/ange.201407758.

(47) Ernst, J. B.; Muratsugu, S.; Wang, F.; Tada, M.; Glorius, F. Tunable Heterogeneous Catalysis: N-Heterocyclic Carbenes as Ligands for Supported Heterogeneous Ru/K-Al $_2$ O $_3$ Catalysts To Tune Reactivity and Selectivity. *J. Am. Chem. Soc.* **2016**, *138* (34), 10718–10721. https://doi.org/10.1021/jacs.6b03821.

(48) Ernst, J. B.; Schwermann, C.; Yokota, G.; Tada, M.; Muratsugu, S.; Doltsinis, N. L.; Glorius, F. Molecular Adsorbates Switch on Heterogeneous Catalysis: Induction of Reactivity by N-Heterocyclic Carbenes. *J. Am. Chem. Soc.* **2017**, *139* (27), 9144–9147. https://doi.org/10.1021/jacs.7b05112.

(49) MacLeod, M. J.; Goodman, A. J.; Ye, H.-Z.; Nguyen, H. V.-T.; Van Voorhis, T.; Johnson, J. A. Robust Gold Nanorods Stabilized by Bidentate N-Heterocyclic-Carbene–Thiolate Ligands. *Nature Chem* **2019**, *11* (1), 57–63. https://doi.org/10.1038/s41557-018-0159-8.

(50) Narouz, M. R.; Takano, S.; Lummis, P. A.; Levchenko, T. I.; Nazemi, A.; Kaappa, S.; Malola, S.; Yousefalizadeh, G.; Calhoun, L. A.; Stamplecoskie, K. G.; Häkkinen, H.; Tsukuda, T.; Crudden, C. M. Robust, Highly Luminescent Au 13 Superatoms Protected by N-Heterocyclic Carbenes. *J. Am. Chem. Soc.* **2019**, *141* (38), 14997–15002. https://doi.org/10.1021/jacs.9b07854.

(51) Cao, Z.; Derrick, J. S.; Xu, J.; Gao, R.; Gong, M.; Nichols, E. M.; Smith, P. T.; Liu, X.; Wen, X.; Copéret, C.; Chang, C. J. Chelating N-Heterocyclic Carbene Ligands Enable Tuning of Electrocatalytic CO 2 Reduction to Formate and Carbon Monoxide: Surface Organometallic Chemistry. *Angew Chem Int Ed* **2018**, *57* (18), 4981–4985. https://doi.org/10.1002/anie.201800367.

(52) Cao, Z.; Kim, D.; Hong, D.; Yu, Y.; Xu, J.; Lin, S.; Wen, X.; Nichols, E. M.; Jeong, K.; Reimer, J. A.; Yang, P.; Chang, C. J. A Molecular Surface Functionalization Approach to Tuning Nanoparticle Electrocatalysts for Carbon Dioxide Reduction. *J. Am. Chem. Soc.* **2016**, *138* (26), 8120–8125. https://doi.org/10.1021/jacs.6b02878.

(53) Feroci, M.; Chiarotto, I.; D'Anna, F.; Gala, F.; Noto, R.; Ornano, L.; Zollo, G.; Inesi, A. N-Heterocyclic Carbenes and Parent Cations: Acidity, Nucleophilicity, Stability, and Hydrogen Bonding—Electrochemical Study and Ab Initio Calculations. *ChemElectroChem* **2016**, *3* (7), 1133–1141. https://doi.org/10.1002/celc.201600187.

(54) Hollóczki, O. Unveiling the Peculiar Hydrogen Bonding Behavior of Solvated N-Heterocyclic Carbenes. *Phys. Chem. Chem. Phys.* **2016**, *18* (1), 126–140. https://doi.org/10.1039/C5CP05369B.

(55) Gorodetsky, B.; Ramnial, T.; Branda, N. R.; Clyburne, J. A. C. Electrochemical Reduction of an Imidazolium Cation: A Convenient Preparation of Imidazol-2-Ylidenes and Their Observation in an Ionic Liquid. *Chem. Commun.* **2004**, No. 17, 1972. https://doi.org/10.1039/b407386j.

(56) Hahn, F. E.; Jahnke, M. C. Heterocyclic Carbenes: Synthesis and Coordination Chemistry. *Angew Chem Int Ed* **2008**, *47* (17), 3122–3172. https://doi.org/10.1002/anie.200703883.

(57) Kundu, S.; Xia, W.; Busser, W.; Becker, M.; Schmidt, D. A.; Havenith, M.; Muhler, M. The Formation of Nitrogen-Containing Functional Groups on Carbon Nanotube Surfaces: A Quantitative XPS and TPD Study. *Phys. Chem. Chem. Phys.* **2010**, *12* (17), 4351. https://doi.org/10.1039/b923651a.

(58) Iqbal, M. A.; Ali, S. I.; Amin, F.; Tariq, A.; Iqbal, M. Z.; Rizwan, S. La- and Mn-Codoped Bismuth Ferrite/Ti 3 C 2 MXene Composites for Efficient Photocatalytic Degradation of Congo Red Dye. *ACS Omega* **2019**, *4* (5), 8661–8668. https://doi.org/10.1021/acsomega.9b00493.

(59) Huynh, H. V.; Han, Y.; Jothibasu, R.; Yang, J. A. 13 C NMR Spectroscopic Determination of Ligand Donor Strengths Using N-Heterocyclic Carbene Complexes of Palladium(II). *Organometallics* **2009**, *28* (18), 5395–5404. https://doi.org/10.1021/om900667d.

(60) Agnès, C.; Arnault, J.-C.; Omnès, F.; Jousselme, B.; Billon, M.; Bidan, G.; Mailley, P. XPS Study of Ruthenium Tris-Bipyridine Electrografted from Diazonium Salt Derivative on

Microcrystalline Boron Doped Diamond. *Phys. Chem. Chem. Phys.* **2009**, *11* (48), 11647. https://doi.org/10.1039/b912468c.

(61) Singh, J.; Gusain, A.; Saxena, V.; Chauhan, A. K.; Veerender, P.; Koiry, S. P.; Jha, P.; Jain, A.; Aswal, D. K.; Gupta, S. K. XPS, UV–Vis, FTIR, and EXAFS Studies to Investigate the Binding Mechanism of N719 Dye onto Oxalic Acid Treated TiO_2 and Its Implication on Photovoltaic Properties. *J. Phys. Chem. C* **2013**, *117* (41), 21096–21104. https://doi.org/10.1021/jp4062994.

(62) Tang, H.; Li, Y.; Chen, Q.; Chen, B.; Qiao, Q.; Yang, W.; Wu, H.; Cao, Y. Efficient Yellow–Green Light-Emitting Cationic Iridium Complexes Based on 1,10-Phenanthroline Derivatives Containing Oxadiazole-Triphenylamine Unit. *Dyes and Pigments* **2014**, *100*, 79–86. https://doi.org/10.1016/j.dyepig.2013.07.029.

(63) Raber, M. M.; Brady, M. D.; Troian-Gautier, L.; Dickenson, J. C.; Marquard, S. L.; Hyde, J. T.; Lopez, S. J.; Meyer, G. J.; Meyer, T. J.; Harrison, D. P. Fundamental Factors Impacting the Stability of Phosphonate-Derivatized Ruthenium Polypyridyl Sensitizers Adsorbed on Metal Oxide Surfaces. *ACS Appl. Mater. Interfaces* **2018**, *10* (26), 22821–22833. https://doi.org/10.1021/acsami.8b04587.

(64) Brennaman, M. K.; Patrocinio, A. O. T.; Song, W.; Jurss, J. W.; Concepcion, J. J.; Hoertz, P. G.; Traub, M. C.; Murakami Iha, N. Y.; Meyer, T. J. Interfacial Electron Transfer Dynamics Following Laser Flash Photolysis of $[Ru(Bpy)_2((4,4'\text{-}PO_3H_2)_2Bpy)]^{2+}$ in TiO_2 Nanoparticle Films in Aqueous Environments. *ChemSusChem* **2011**, *4* (2), 216–227. https://doi.org/10.1002/cssc.201000356.

(65) Chen, Z.; Concepcion, J. J.; Jurss, J. W.; Meyer, T. J. Single-Site, Catalytic Water Oxidation on Oxide Surfaces. *J. Am. Chem. Soc.* **2009**, *131* (43), 15580–15581. https://doi.org/10.1021/ja906391w.

(66) Beranek, R. (Photo)Electrochemical Methods for the Determination of the Band Edge Positions of TiO_2-Based Nanomaterials. *Advances in Physical Chemistry* **2011**, *2011*, 1–20. https://doi.org/10.1155/2011/786759.

(67) Uoyama, H.; Goushi, K.; Shizu, K.; Nomura, H.; Adachi, C. Highly Efficient Organic Light-Emitting Diodes from Delayed Fluorescence. *Nature* **2012**, *492* (7428), 234–238. https://doi.org/10.1038/nature11687.

(68) Kinney, Z. J.; Rheingold, A. L.; Protasiewicz, J. D. Preferential N–H···:C◻ Hydrogen Bonding Involving Ditopic *NH*-Containing Systems and *N*-Heterocyclic Carbenes. *RSC Adv.* **2020**, *10* (69), 42164–42171. https://doi.org/10.1039/D0RA08490E.

(69) Gehrke, S.; Hollóczki, O. Hydrogen Bonding of N-Heterocyclic Carbenes in Solution: Mechanisms of Solvent Reorganization. *Chemistry A European J* **2018**, *24* (45), 11594–11604. https://doi.org/10.1002/chem.201802286.

(70) Martra, G. Lewis Acid and Base Sites at the Surface of Microcrystalline TiO2 Anatase: Relationships between Surface Morphology and Chemical Behaviour. *Applied Catalysis A: General* **2000**, *200* (1–2), 275–285. https://doi.org/10.1016/S0926-860X(00)00641-4.

Chapter 4

Visible-Light Driven CO$_2$ Photocatalysis with A Manganese-Imidazole-3CzIPN Complex.

4.1 Introduction

Anthropogenic carbon dioxide emissions are a primary driver of global climate change. Atmospheric CO$_2$ levels increased from 315 to 420 ppm over the last 60 years,[1] and in 2021, anthropogenic activities emitted more than 37124 megatons of carbon dioxide (MtCO$_2$) into the atmosphere.[2] Tragically, the annual global emissions of anthropogenic CO$_2$ continue to increase rather than level out or decline, reaching a global increment of 1.25 ºC.[3] The development of renewable energy technologies is a promising method to reduce greenhouse emissions.

Solar energy is widely accessible and inexhaustible.[4,5] Solar energy is, however, diffuse, and intermittent and must be stored for long-term, high-power applications. An approach to achieving sustainable and perdurable solar energy utilization is through artificial photosynthesis, which mimics the natural process of photosynthesis to convert solar into chemical energy. This approach offers several advantages, such as mild operating conditions and the potential to convert atmospheric or trapped CO$_2$ into hydrocarbon fuels, including CO, CH$_4$, and CH$_3$OH. The utilization of these solar fuels in applications, including long-range transportation or air travel would, in principle, provide large amounts of energy over long periods with zero net gains of atmospheric CO$_2$.

Several types of photocatalytic and photoelectrochemical systems that produce solar fuels are being studied.[6–9] As discussed in Chapter 1, systems that consist of molecular catalysts and chromophores offer direct insight into the fundamental processes that occur during solar fuel production by utilizing well-defined components that can be tailored individually and studied as they operate either on their own, or as part of the system. For example, the catalyst must facilitate the multielectron-proton transfer reduction of CO$_2$ and prevent parasitic reactions, like hydrogen evolution.[10–12] As discussed earlier in Sections 1.2.4, 1.4 and 1.6, the thermodynamic redox potentials

and kinetics from the photosensitizer and catalyst must align to promote effective electron transfer between them.[13]

Re(bpy)(CO)$_3$Br (bpy is 2,2'-bipyridine) and related complexes are well-studied electrocatalysts for the electroreduction of CO_2 to CO, as previously discussed in Section 1.8.2. They catalyze the reaction with high selectivity ($\Gamma > 99\%$) and with turnover numbers (TONs) reaching 3000.[14–17] As well, [Ru(bpy)$_2$(CO)$_2$](PF$_6$)$_2$ complexes are active for the reduction of CO_2 to CO and HCOOH production.[18,19] Recently, Co- and Ni-phthalocyanines compounds [20–24] as well as Co- and Fe-porphyrins[25–27] have proven active electrocatalysts towards the reduction of CO_2 to CO. Mn(bpy)(CO)$_3$Br and related complexes have been investigated to complement the studies of Re compounds.[28–30] A crucial factor to consider is the abundance (Re is 0.0007 ppm in the continental crust, in contrast to Mn at 1060 ppm),[31] hence affordability, particularly given the need for large-scale deployment. Unlike rhenium (Re), a noble transition metal, Mn is inexpensive (1635 US$/kg for Re vs 2 US$/kg for Mn).[32] Mn complexes of this type will be utilized as CO_2 electroreduction catalysts because of their relatively low cost, and because the mechanisms and activities of these complexes have been studied well, allowing for detailed benchmarking of the catalysts developed herein. For a detailed discussion, refer to Section 1.8.2 in the introduction, where Mn complexes are extensively analyzed.

The chromophore must absorb light, preferably over a wide range of wavelengths in the visible range, to form a charge-separated excited state with high efficiency and slow charge recombination.[19] Published molecular photocatalytic CO_2 reduction systems often utilize Ru- and Ir-polypyridyl complexes as chromophores. These chromophores operate by intermolecular electron transfer reactions between the lowest energy triplet excited state of the chromophore (T$_1$) and the catalyst or a sacrificial electron donor for the reduction (typically an amine). The Ru- and Ir-polypyridyl chromophores are favored for these types of studies because they undergo metal-to-ligand charge transfer excitations with relatively high molar extinction coefficients to form singlet excited states that undergo rapid intersystem crossing to form relatively long-lived T$_1$ excited states. The redox potentials of the T$_1$ state can be tuned by varying the structure of the chromophore, and intermolecular electron transfer

is rapid with these systems.[33] Similarly, these characteristics and properties related to the Ru chromophores are discussed previously in Section 1.6.1 of the introduction.

Carbazolyl dicyanobenzenes (CDCBs) are a relatively new family of organic molecules that have gained attention for their efficient properties in organic light-emitting diodes.[34–37] While 4CzIPN (tetracarbazole isophthalonitrile) is an inexpensive organic molecule, it shares several photophysical characteristics with well-established [Ru(Mebpy)$_3$](PF$_6$)$_2$ and Ir[dF(CF$_3$)ppy]$_2$-(dtbbpy)](PF$_6$) photocatalysts (Figure 4.1), such as a long-excited state lifetime (μ= 5.1 $\mu\mu$s for 4CzIPN vs τ = 2.3 μs, and 1.1 μs, for Ir- and Ru-complexes, respectively), wide redox window, and high fluorescence quantum yield.[33,34] Notably, 4CzIPN displays redox potentials similar [E$_{1/2}$(P*/P$^-$): +1.35 V vs SCE] to the widely used Ru- and Ir-photocatalysts [E$_{1/2}$(P*/P$^-$), +1.21 and 0.77 V vs SCE, respectively] rendering it an encouraging photosensitizer for artificial photosynthesis.[35] Additionally, the redox properties of 4CzIPN are readily tunable via strategic modifications of the electron donor (carbazole) and acceptor (dicyanobenzene) moieties.[35] These findings underscore the potential of 4CzIPN as a highly desirable photosensitizer and suggest a valuable addition to the artillery of molecular photocatalysts for synthetic transformations.
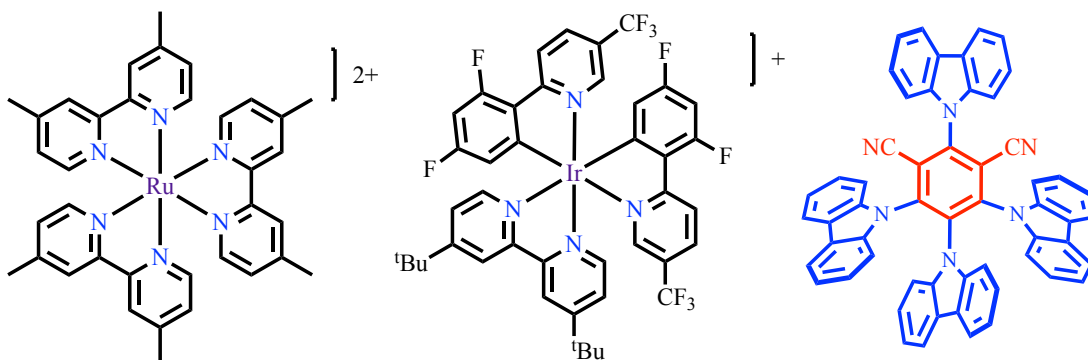
Figure 4.1. Structures of common [Ru(Mebpy)$_3$](PF$_6$)$_2$, Ir[dF(CF$_3$)ppy]$_2$-(dtbbpy)](PF$_6$), and 4CzIPN photosensitizers.

Despite significant progress in the field, current photocatalytic systems still need to improve their efficiency, selectivity, and quantitative electron transfer upon visible light irradiation and overall sustainable use.[8,38–42]

The advantages to coupling the catalyst and the photosensitizer include, in principle, inhibiting or reducing the back-recombination of photogenerated electron-hole pairs and providing a direct-close pathway for electron transfer.[19,43,44] 4CzIPN is a thermally-activated delayed fluorescence (TADF) photosensitizer.[36] DFT and ultrafast spectroscopy studies[45,46] show that this class of organic photosensitizer absorbs light in the visible range to undergo an intramolecular charge-transfer excitation from the HOMO, which is based largely within the carbazole π-orbital manifold, to the LUMO, largely based within the dicyanobenzene π^* manifold. The dihedral angles between the carbazole and dicyanobenzene rings are large (~60°) due to sterics, minimizing direct orbital overlap between their π systems, and thereby spatially separating the LUMO and HOMO orbitals. Further, the calculated energy difference (ΔE_{ST}) between the lowest energy singlet (S_1) and triplet (T_1) excited states is small (<100 meV). This small ΔE_{ST} is believed to promote intersystem crossing (ISC) between the S_1 and T_1 states. The T_1 excited state is long-lived (~5 µs,) for an organic chromophore, and these chromophores undergo thermally-activated reverse ISC (RISC) from the T_1 to S_1 excited states, allowing for TDAF (Figure 4.2).[34] TDAF from 4CzIPN photosensitizers is being explored as a strategy to overcome the 3:1 ratio of T_1 to S_1 states formed by charge recombination in organic light-emitting diode displays (OLEDs).[34]
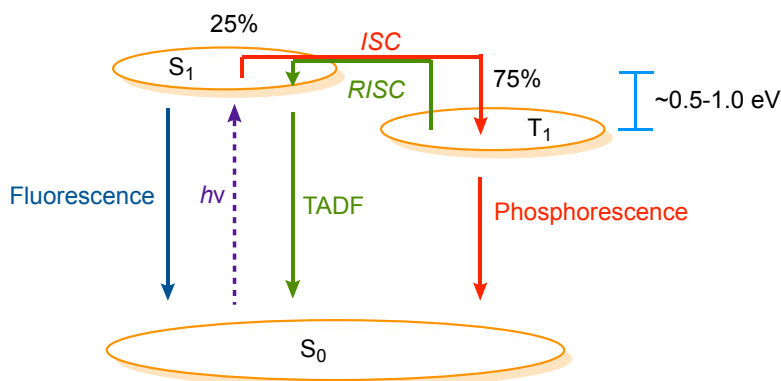
Figure 4.2. Simplified energy diagram illustrating energy transfer (ET) processes upon light excitation of a photosensitizer like 4CzIPN.

This lab recently published the preparation, analysis, and electropolymerization of the imidazole-substituted 4-CzIPN derivative, 1-(2,4,6-tri(9*H*-carbazol-9-

yl)benzene-1,3-dicarbonitrile)imidazole (3CzIPN-imidazole).[47] 3CzIPN-imidazole is prepared from commercially tetrafluoro-isophthalonitrile, carbazole, and imidazole in three high-yielding steps (Scheme 4.1).
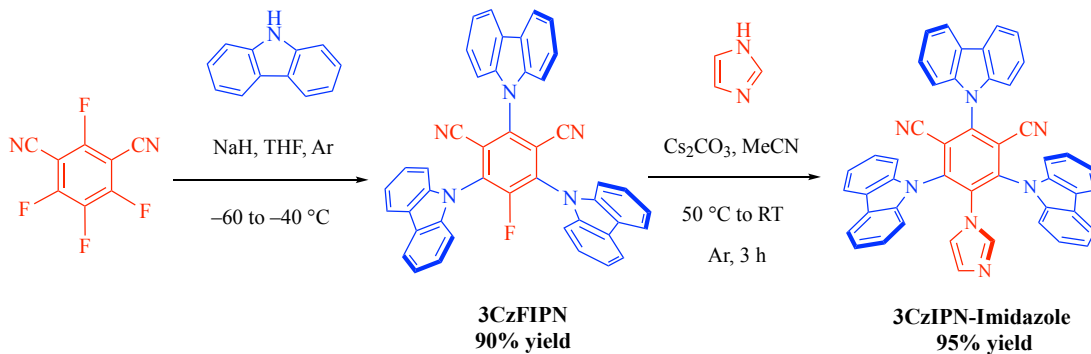
Scheme 4.1. Preparation of 3CzIPN-Imidazole (**2).**

The photoredox polymer resulting from the electropolymerization of **2** is a heterogeneous photocatalyst for olefin photoisomerization via Dexter Energy transfer, a photoanode for visible-light-driven electro-oxidations, and its photoemissions vary in the presence of lithium cations.[48] As well, studies in this group indicated that **2** shared many of the properties of the parent molecule, 4-CzIPN. For example, the steric hindrance between the carbazolyl and dicyanobenzene moieties results in large dihedral angles (~60º) between the planes of the carbazolyl and the dicyanobenzene groups. In consequence, the HOMO and LUMO were spatially separated. Preliminary time-dependent density functional theory (DFT) calculations suggested that ΔE_{ST} was small, and the photochemical behaviour of **2** was similar to 4CzIPN.[48] This study will investigate whether the imidazole group in **2** will coordinate to the well-studied, earth-abundant CO_2 electroreduction catalyst *fac*-[Mn(bpy)(CO)$_3$X] (extensively discussed in Section 1.8.2 in the introduction), where X is a halide or other donor ligand (Figure 4.3, 3CzIPN-Mn (**3**)). The resulting complex (**3**) will be investigated as a photocatalyst for visible-light-driven CO_2 reductions. [38,39]
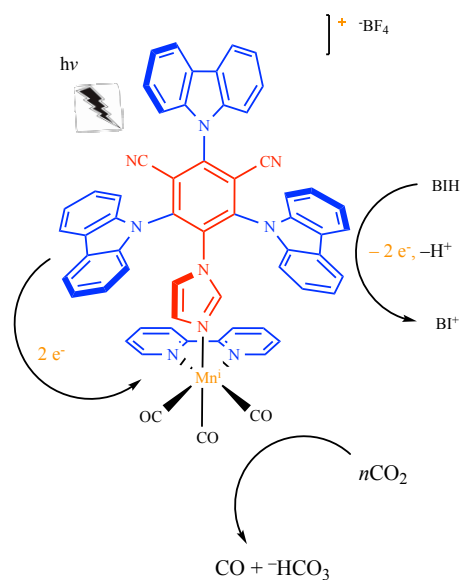
Figure 4.3. Schematic representation of the photocatalytic reduction of CO_2 with 3CzIPN-Mn (**3**) and BIH under visible light.

4.2 Results and Discussion

The reaction between *fac*-Mn(bpy)(CO)$_3$(Br) and AgBF$_4$ formed AgBr and the acetone complex [*fac*-Mn(bpy)(CO)$_3$((CH$_3$)$_2$CO)]$^+$ BF$_4$ (**1**) within 5 min at room temperature in the dark (Scheme 4.2).

(**1**)
96% yield
by ^{1}H NMR
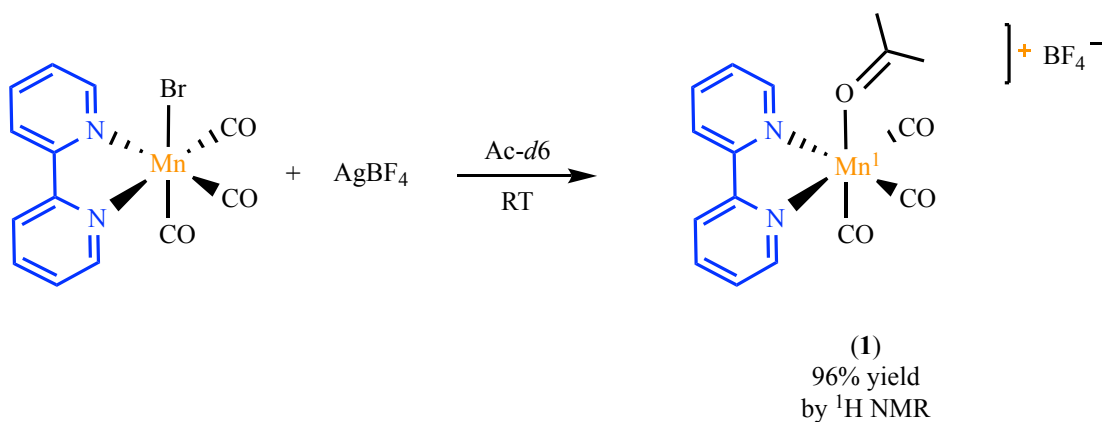
Scheme 4.2. Synthesis of *fac*-[Mn(bpy)(CO)$_3$(CH$_3$)$_2$CO]$^+$ BF$_4$(**1**).

Attempts were not made to isolate the labile compound **1**, but it was identified by ^{1}H- and ^{13}C-NMR studies, IR spectroscopy, and mass spectrometry.[49] The IR spectrum confirmed that the carbonyls were in the fac-geometry (2020 cm^{-1},

1920 cm^{-1}). The dark reaction between **1** and the imidazole-dye **2** was also complete within 5 min at room temperature, forming a mixture containing two major compounds, and several minor with similar ^{1}H NMR spectra (Figure 4.4). The mixture transformed, likely by isomerization, into predominantly one compound after ~18 h at room temperature in the dark, in 90% yield (Scheme 4.3).
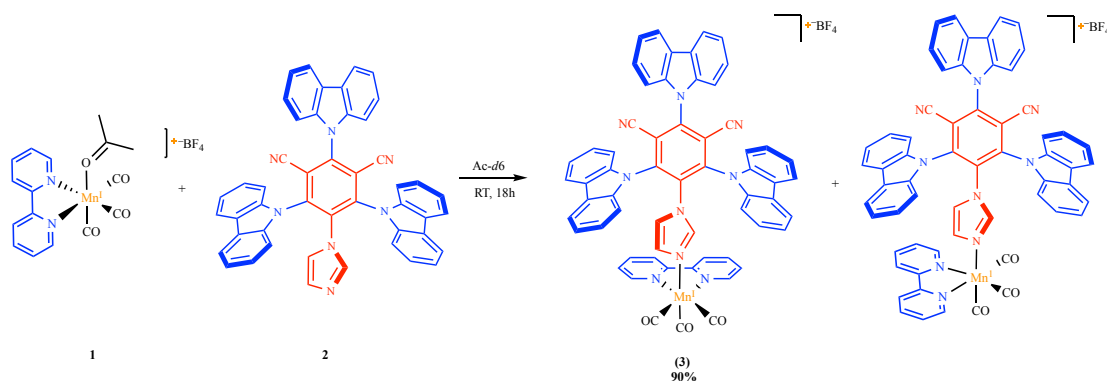
Scheme 4.3. Synthesis of 3CzIPN-Imidazole-Mn(bpy)(CO)$_3$BF$_4$ **(3).**
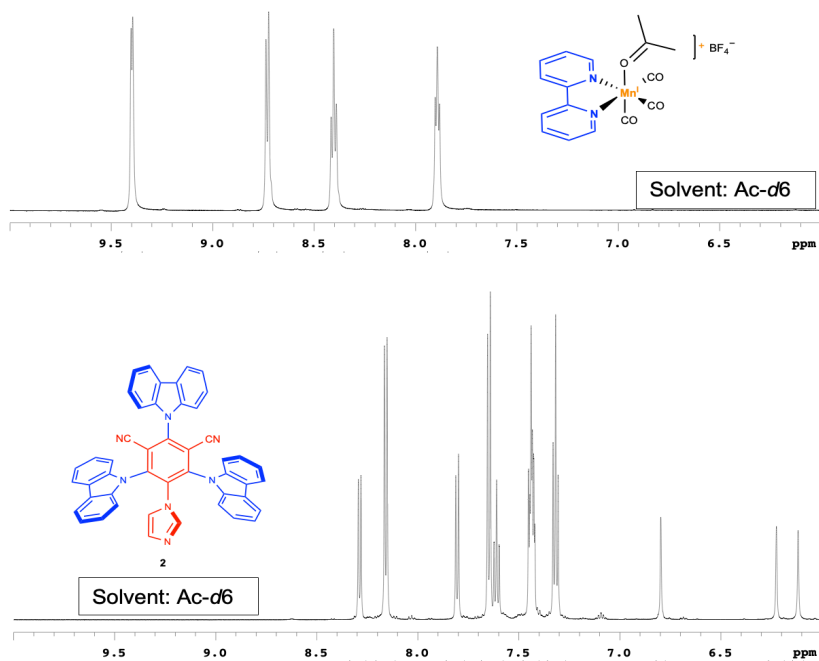
Figure 4.4. (a) ^{1}NMR spectra of **1**, **2** in Ac-*d*6.
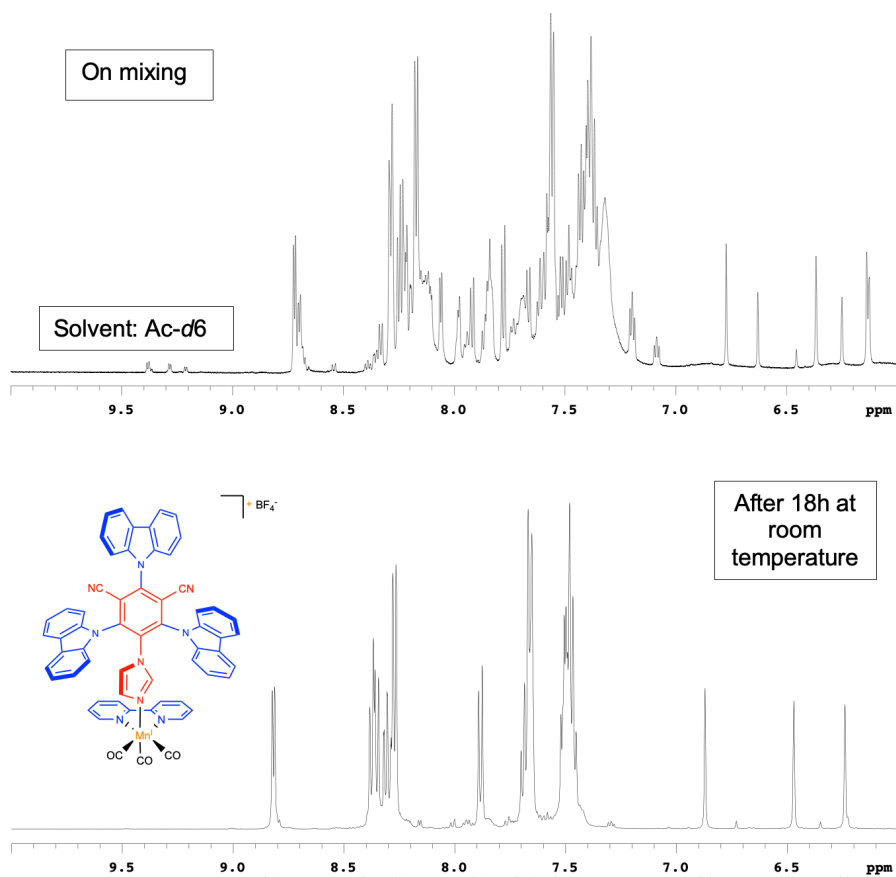
Figure 4.4.(b) [1]NMR spectra of **3** initial (on mixing) and final formation (after 18 h) in Ac-*d*6.

Inspection of molecular models shows that there is strong steric crowding within **3**. Indeed, it is well-known that the steric crowding within 4CzIPN and related compounds results in large dihedral angles between the carbazole and dicyanobenzene rings. The aromaticity engenders a substantive degree of conformational rigidity on their structures as well.[50,51] Figure 4.5 shows the solid-state structure of **2**, reproduced with permission from this group's prior publication. Indeed, the dihedral angles between the carbazole or imidazole rings and the core dicyanobenzene (isophthalonitrile) ring are all between 59.4º and 70.9º. It is, therefore, quite likely that steric crowding limits rotation about these bonds in the Mn complex **3**. Molecular models also show that rotation also is restricted about the N-imidazole-Mn bond (Figure 4.5). It is, therefore, reasonable that a kinetic mixture of rotamers results from the reaction between **1** and **2,** which then interconverts by slow rotation about these bonds into the major rotamer **3**. Figure 4.4 shows the aromatic regions of the ^{1}H NMR spectra of **1** and **2** and the initial- and final spectra for the reaction forming **3**.

156
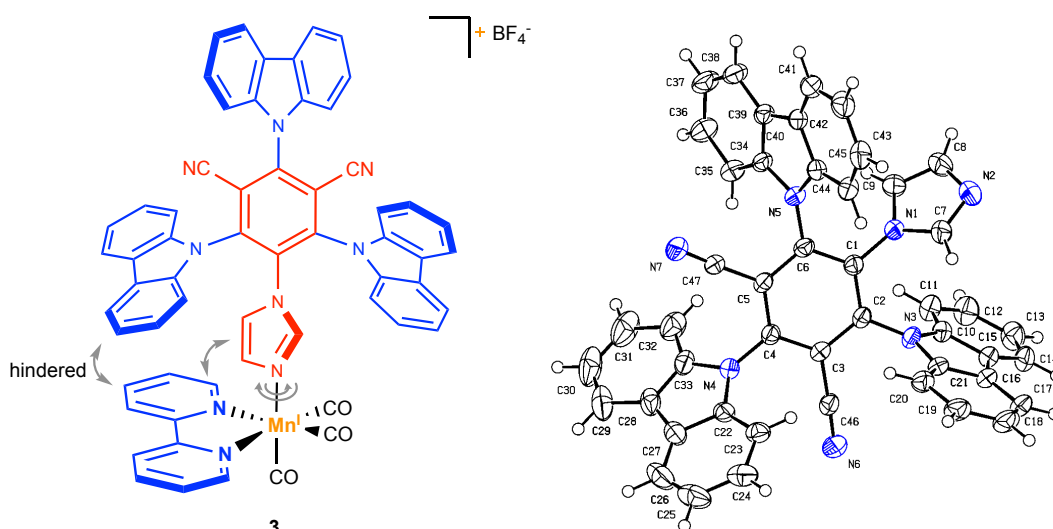
Figure 4.5. Hindered rotation in 3CzIPN-Imidazole-Mn (**3**) (left), X-Ray Structure of 3CzIPN-Imidazole (**2**, right) reproduced with permission from Liu et al.[48] Torsional dihedral angles: 70.9º, 62.6º, 59.4º.

The major rotamer of **3** (referred to as **3** from hereon) was isolated as an orange solid in 90% yield. Compound **3** was characterized by ^{1}H and ^{13}C NMR studies, elemental analysis, and high-resolution mass spectrometry. The IR spectrum confirmed that the carbonyl groups were in a fac-arrangement bonded to Mn.

Photochemistry

Figure 4.6 shows the UV-vis spectra of the free photosensitizer **2**, the Mn-photosensitizer complex **3** in CH_2Cl_2. The spectra of the photosensitizer **2** contain a broad absorbance at λ_{max} ~390 nm, with evidence for smaller peaks at λ ~ 410 and ~ 450 nm. Preliminary TD-DFT calculations suggest that this broad absorbance consists of charge-transfer excitation from S_0 to S_n, n = 1, 2, 3...[48] The longest wavelength absorption (λ ~ 448 nm) likely corresponds to S_0 to S_1, a charge-transfer excitation from the HOMO, with character centred on the carbazole rings, to the LUMO, with character largely centred on the π^* orbitals of the dicyanobenzene ring. Consequently, the lowest energy singly occupied molecular orbital (SOMO) of S_1 is centered on the carbazole rings, and the highest energy SOMO is largely centred on the π^* orbitals of the dicyanobenzene ring. The S_0 to S_n (n = 2,3,4…) excitations in the UV-vis spectrum of **1** are followed by rapid non-radiative relaxation to S_1. A variety of

polycarbazole-dicyanobenzene compounds are reported in the literature.[35] These processes are like those reported for the parent chromophore 4-CzIPN (Figure 4.6), with $\lambda_{max} \sim 382$ nm, and the apparent S_0 to S_1 absorption at $\lambda \sim 451$ nm.[34,35]
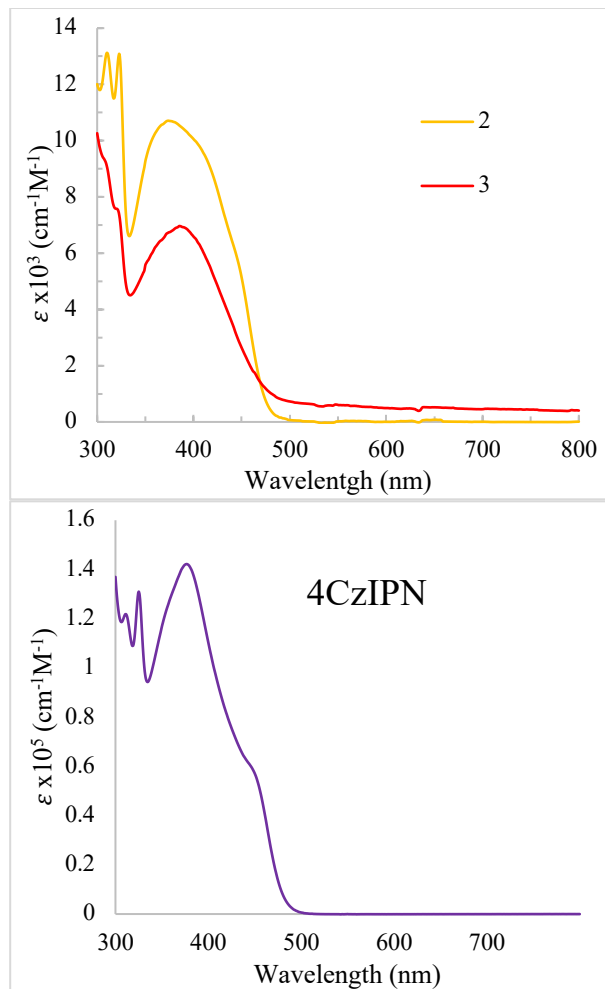
Figure 4.6. Molar extinction coefficient of **2** and **3** in CH_2Cl_2. Bottom: 4CzIPN in CH_2Cl_2.

The Mn-photosensitizer complex **3** contains a similar broad absorbance with $\lambda_{max} \sim 397$ nm, suggesting that the photochemistry of **2** is not dramatically altered upon coordination to Mn. This result indicates that any sigma effects on the dicyanobenzene moiety arising from the coordination of **2** to Mn via the imidazole group are small. The similarities in the UV-vis spectra of **2** and **3** also indicate that the large dihedral angle between the imidazole and dicyanobenzene rings prevents significant interactions between their π-systems.

Figure 4.7a shows the photoluminescence spectra of **2** and **3** in CHCl$_3$ (relative polarity = 0.259)[52] and MeCN (relative polarity = 0.460)[52] solutions (Figure 4.7b).
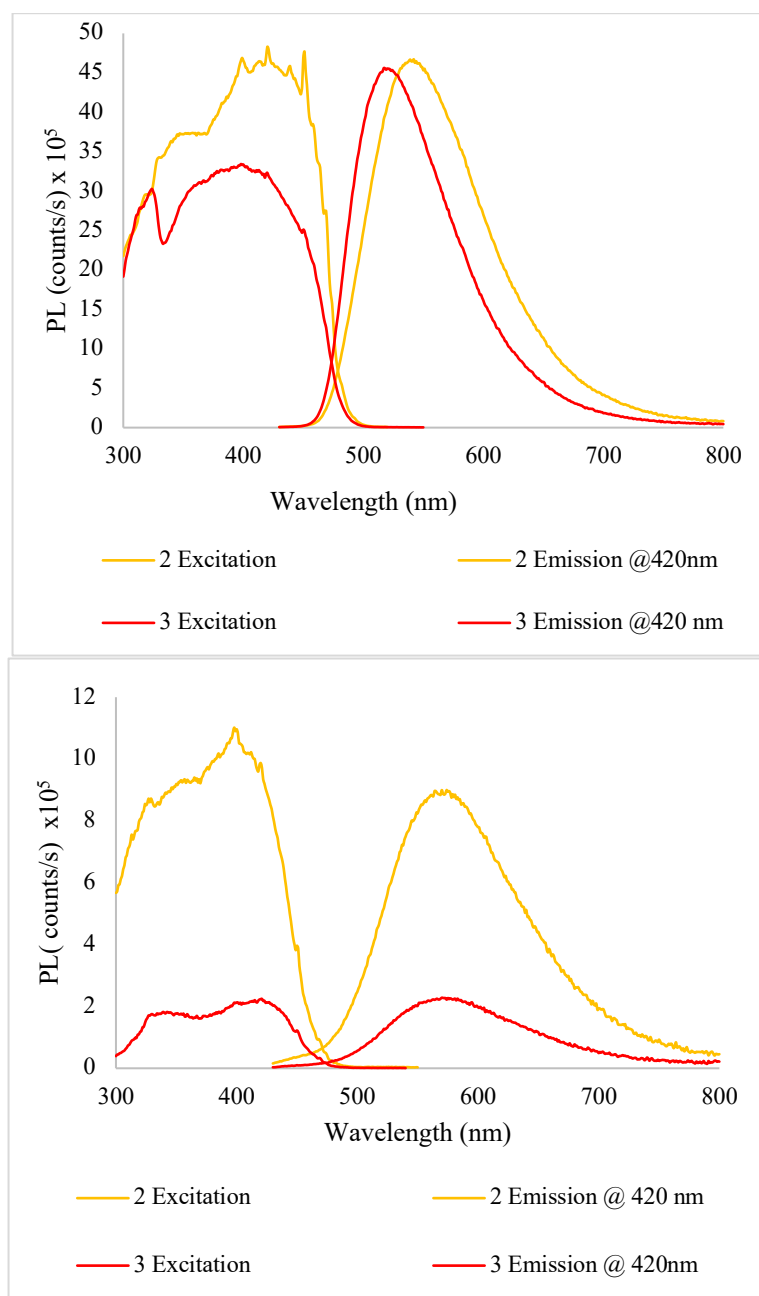
Figure 4.7. Photoluminescence spectra of **2** and **3** in CHCl$_3$ (top) (a) and MeCN (bottom) (b).

As expected, the spectrum of the control compound (Me-Imidazole-Mn(bpy)(CO)$_3$BF$_4$) **4** contains no photoluminescence peaks (Figure 4.23). There is a broad excitation peak with λ_{max} ~420 nm in CHCl$_3$, and λ_{max} ~ 400 nm in MeCN in the

photoluminescence spectrum of the free photosensitizer **2**, with the corresponding strong emission peaks at $\lambda_{max} \sim 545$ nm (CHCl$_3$) and $\lambda_{max} \sim 580$ nm (CH$_3$CN). Equivalent emissions have been published for polycarbazole-dicyanobenzene compounds, and they arise from prompt fluorescence from S$_1$ to S$_0$, along with thermally activated RISC from T$_1$ to S$_1$ and the prompt fluorescence. As stated above, ISC between S$_1$ and T$_1$ is relatively facile for **2** and related photosensitizers. The Stokes shift for **2** in CHCl$_3$ (124 nm) is relatively small for an organic chromophore, suggesting that significant conformation changes do not occur in the S$_1$ and T$_1$ states.[53] This observation is common among this class of photosensitizers. The Stokes shift is larger in the more polar solvent MeCN (171 nm), as is expected for an intramolecular charge-transfer excitation leading to a charge-separated excited state.

The photoluminescence spectrum of the Mn-photosensitizer complex **3** in CHCl$_3$ is similar to that of the free photosensitizer **2**. There is a shift towards shorter wavelengths in both the excitation and emission peaks in the spectrum of **3**, but the shapes are quite similar, suggesting that the photoactive electronic structure of **2** is not changed significantly upon coordination to Mn. The excitations and emissions of **3** in are reduced significantly in MeCN. These reductions may result from some form of intramolecular quenching (e.g., oxidative quenching through electron transfer from T$_1$ to Mn), or perhaps there is some interaction between **3** and the solvent that is reducing the probability of excitation or the lifetime of the excited state.[54,55] As **3** is a salt, it is expected that the interactions with the more polar and donating solvent MeCN would be stronger than those with CHCl$_3$. The Stokes shift in the emission spectrum of **3** in MeCN is larger than in CHCl$_3$, again consistent with an excited state resulting from a charge-transfer excitation. Detailed DFT and ultra-fast spectroscopy studies are required to investigate the light absorption by these complexes.

Figure 4.8 shows the photoluminescence spectra of **3** in MeCN with different concentrations of 1,3-dimethyl-2-phenyl-2,3-dihydro-1Hbenzo[d]imidazole (BIH). BIH is an effective 2-electron/1 proton sacrificial donor in photocatalytic reactions.[56] Scheme 4.4 shows the redox reactions BIH undergoes as it acts as a net 2 electron donor to generate BI$^+$ and H$^+$.
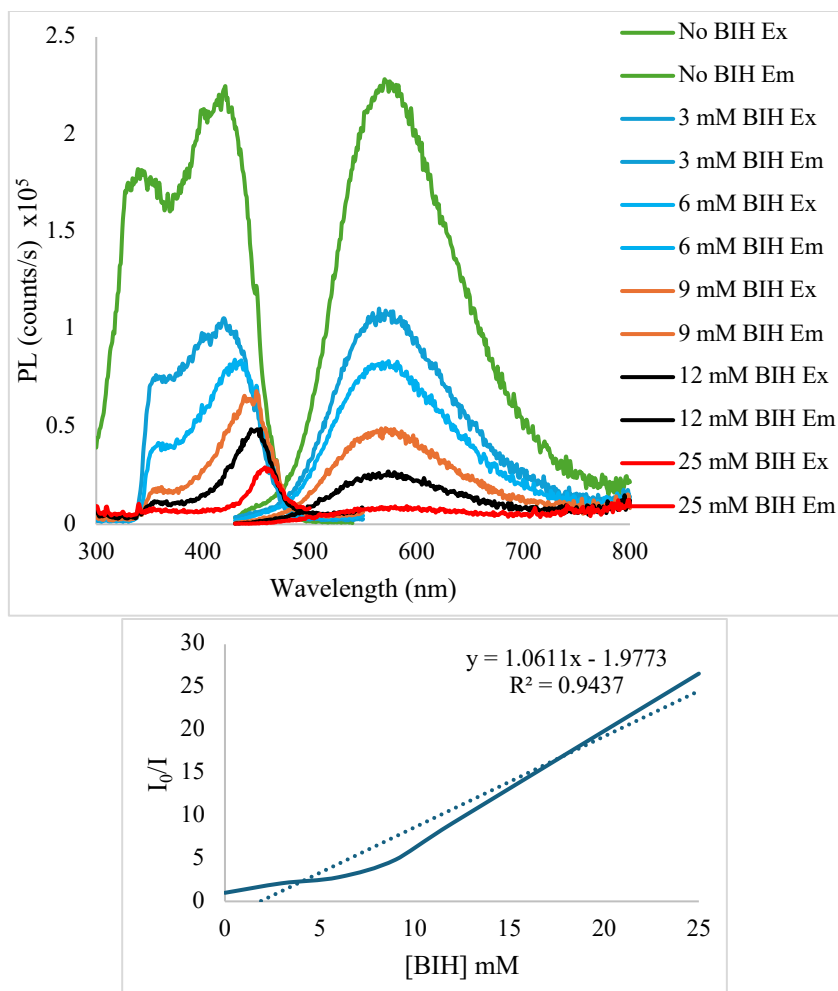
Figure 4.8. (a) Photoluminescence spectra of 3CzIPN-Imidazole-Mn (**3**) in MeCN with varying concentrations of BIH, top. (b) Stern-Volmer Plot for 3CzIPN-Imidazole-Mn (**3**) in MeCN, bottom.
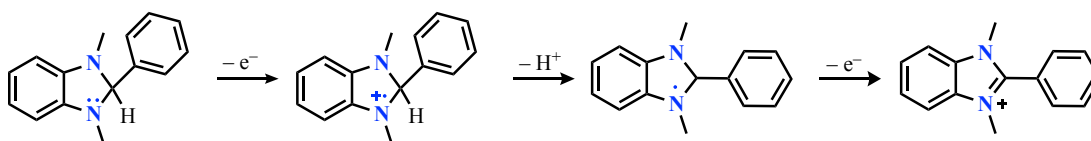
Scheme 4.4. Mechanism of BIH degradation upon monoelectronic oxidation.

For example, BIH reductively quenches Ru-polypyridine complexes by reducing Ru(III) to Ru(II) in the T_1 excited state.[56] Figure 4.24 shows that the control photoluminescence spectra of BIH in MeCN and $CHCl_3$ contain sharp excitation peaks at $\lambda_{max} \sim 380$nm, broad emissions at $\lambda \sim 480$nm, and sharp, strong emissions at $\lambda \sim 760$ nm. These peaks do not overlap with those in the photoluminescence spectrum of **3**. As shown in Figure 4.8a, BIH is an effective quenching agent for **3**. The absorptions and

emissions of **3** both diminish and shift as the [BIH] increases. Figure 4.8b also shows the Stern Volmer plot, depending upon the [BIH]. There are two regions, from [BIH] = 0 to ~10 mM, and from ~10 to 25 mM (the upper limit for this experiment). Upward inflections of Stern-Volmer plots typically are interpreted as the presence of two forms of quenching, dynamic and static. Dynamic quenching involves a collisional reaction between the excited state and the quenching agent. Static quenching involves the formation of some sort of complex (covalent or Van der Waals) between the ground state and the quenching agent that does not emit light at the excitation wavelength. The mechanism of dynamic quenching between **3** and BIH is almost certainly the donation of an electron from BIH to the lowest energy SOMO of the excited state of the photosensitizer ligand in **3**. The excited state that reacts with BIH can be either S_1 or T_1. Scheme 4.5 illustrates the processes discussed in this section. A detailed mechanistic study attended by TD-DFT calculations and ultrafast spectroscopy would be required to fully understand these processes fully.
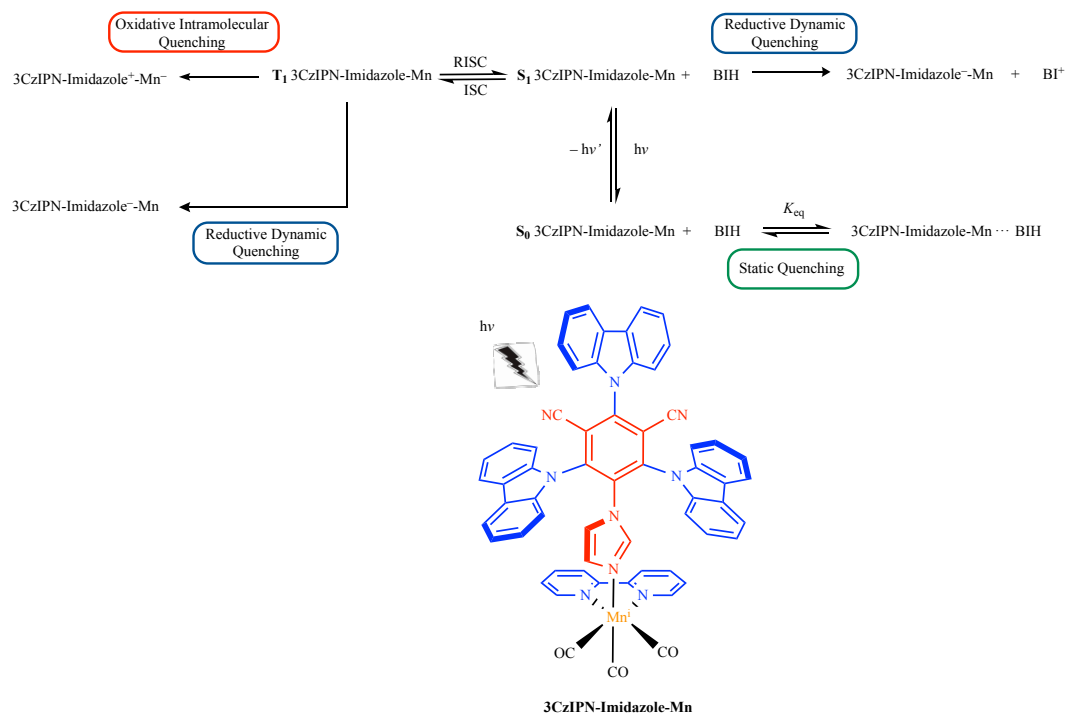
Scheme 4.5. Schematic representation of the different processes involved upon light excitation and quenching of 3CzIPN-Imidazole-Mn (**3**) with BIH.

Figure 4.9 shows the time-resolved photoluminescence (fast decay) of **2**, **3**, and 4-CzIPN as an internal control in MeCN solution, recorded after an instrument-determined excitation pulse at 405 nm, and Table 4.1 has the fitting parameters for the time-resolved photoluminescence decay.
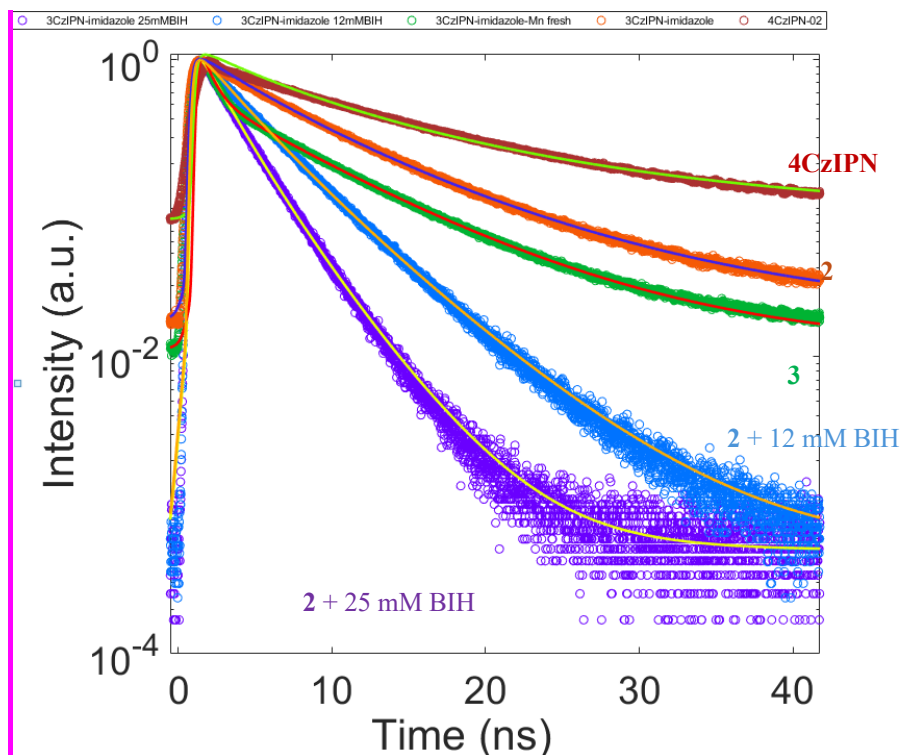
Figure 4.9. Time-resolved photoluminescence (Fast Decay) of **2**, **3**, (**2** + 12mM BIH), (**2**+ 25mM BIH), and 4CzIPN in MeCN. Emission spectra were recorded at 405 nm excitation.

The emission occurred at λ_{max} ~574 nm, consistent with the steady-state photoluminescence spectrum (Figures 4.7a, 4.7b), and results from the prompt relaxation from S_1 to S_0. The prompt fluorescence lifetime of the free photosensitizer **2** is 7.6 ns under these conditions. The prompt lifetime decreased in the presence of BIH (3.9 ns at 12 mM BIH and 2.4 ns at 25 mM), showing that BIH quenches the excited state. The prompt lifetime when coordinated to Mn in complex **3** is 3.4 ns. It is noted that there appear to be two temporal regions in the fast decay curve of the Mn complex **3**, an initial period of rapid decay (over the first few nanoseconds), followed by a region where the decay is slower. The initial, fast component was modelled with an additional single exponential function, therefore, this sample has a single exponential plus a lognormal distribution considered in the lifetime. The shortened prompt lifetime of **3**

vs **2** is consistent with the proposal that coordination of **2** to Mn does not cause extensive change to the π-structure of the dicyanobenzene ring and that there is some quenching of the excited state by Mn. Determining the exact nature of the electronic interactions between the Mn centre and **2** would require extensive theoretical and experimental study that is beyond the scope of this thesis. The prompt lifetime of 4-CzIPN measured under these conditions was 10.9 ns.

Table 4.1. Fitting parameters for the Time-Resolved Photoluminescence (Fast Decay)

Sample	Exponential		Lognormal		Lifetime (ns)
	t	B	s	m	
3CzIPN-Imidazole **(2)** + 25 mM BIH			0.305	0.8243	2.389
3CzIPN-Imidazole **(2)** + 12 mM BIH			0.3018	1.309	3.875
3CzIPN-Imidazole-Mn **(3)**	0.6776	0.6079	0.2976	1.986	3.398
3CzIPN-Imidazole **(2)**			0.4536	1.928	7.621
4CzIPN			0.5796	2.217	10.8587

Figure 4.10 shows the slow decay time-resolved photoluminescence of **2**, **2** + BIH, **3**, and 4-CzIPN in MeCN recorded after excitation at 354 nm. Based upon the excitation spectra in the steady-state photoluminescence spectrum of **2** (Figure 4.6 and 4.7) and preliminary TD-DFT calculations,[48] excitation of **2** at this wavelength likely resulted in a S_0 to S_N excitation ($N > 1$), followed by rapid nonradiative decay to the vibrational ground state of S_1. The quantum efficiency of this process is unknown. S_I then undergoes prompt fluorescence to S_0, or ISC to T_1.
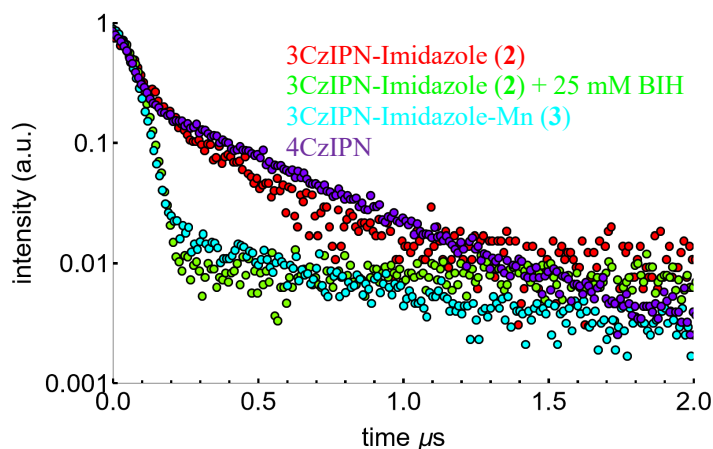
Figure 4.10. Time-resolved photoluminescence (Slow Decay) of **2**, **3**, (**2**+ 25mM BIH), and 4CzIPN in MeCN. Emission spectra were recorded at 354 nm excitation.

Table 4.4.2 lists the lifetimes for the slow decay. The delayed fluorescence lifetime of **2** was 0.24 μs in the absence of BIH. The delayed fluorescence in **2** arises from thermal spin upconversion from T_1 to S_1, followed by prompt emission from S_1 to S_0.[48,57] There was no delayed component left in the presence of BIH (25 mM), consistent with reductive quenching of the T_1 state in **2** by BIH. Similarly, there was a small delayed component in the time-resolved photoluminescence of **3**, and the lifetime was 0.45 μs. The delayed lifetime of 4CzIPN was 0.38 μs under these conditions.[57]

Table 4.2. Fitting Parameters for the Time-Resolved Photoluminescence (Slow Decay)

Sample	Lifetime (μs)
3CzIPN-Imidazole-Mn **(3)**	0.45
3CzIPN-Imidazole **(2)** + 25 mM BIH	NO delayed component left
3CzIPN-Imidazole **(2)**	0.24
4CzIPN	0.38

Again, a detailed study involving computations and experimental measurements is required to determine the exact nature of the photophysical properties of these compounds. Taken together, the results are consistent with **2** and compound **3** both being TADF systems that resemble the parent compound 4CzIPN. The coordination to Mn apparently does not alter significantly the electronic structure of **2**, but there is communication between them that alters the photophysics as described above.

Cyclic voltammetry.

Figure 4.11a shows the cyclic voltammogram of the free imidazole-dye **2** (0.1 mM) in CH_2Cl_2 (0.1 M n-Bu$_4$NPF$_6$) swept to negative potentials under an inert atmosphere (–0.3 to –2.4 V vs Fc/Fc$^+$ (Fc = ferrocene), sweep rate = 100 mV s^{-1}). A reversible, well-defined redox wave at –1.5 V (all potentials are quoted vs Fc/Fc$^+$, unless stated otherwise) corresponds to a one-electron reduction of the dicyanobenzene ring, presumably by the addition of an electron to the lowest energy unoccupied molecular orbital, more specifically the lowest energy π* orbital. This redox potential corresponds

to an orbital energy is –3.08 eV, as compared to the –2.71 eV for 4CzIPN.[48,51] Sweeping to high potentials results in the oxidation of the carbazole groups with an onset potential of ~0.3 V and a redox potential of ~1.2 V (Figure 4.11c), which is consistent with the reported value for the electrooxidation potential for the carbazole ring in 4CzIPN.[58]
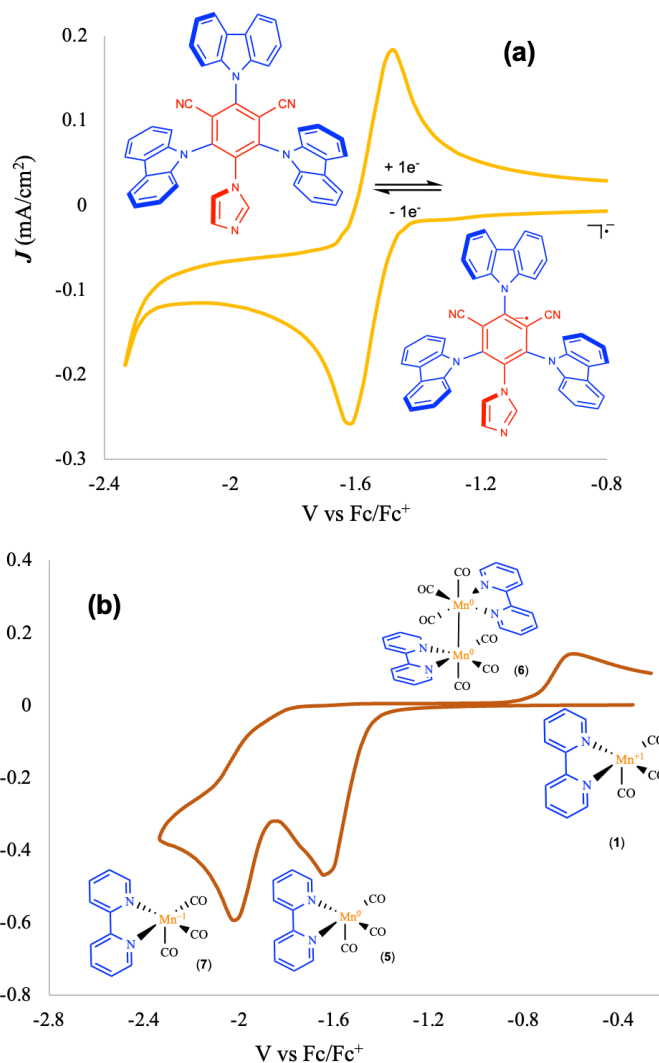
Figure 4.11. CV of (a) 3CzIPN-Imidazole (**2**), (b) [Mn(bpy)((CH$_3$)$_2$CO)(CO)$_3$]$^+$ BF$_4^{-1}$ (**1**).

Figures 4.11 (b) show the CVs of [Mn(bpy)((CH$_3$)$_2$CO)(CO)$_3$]$^+$ (**1**) in MeCN (0.1 mM, 0.1 M nBu$_4$NPF$_6$, 100 mV s^{-1}, sweep ranges as shown in the figure). The CV of **1** has been studied extensively in the literature. The first cathodic wave in the negative-going sweep at –1.62 V, corresponds to the one-electron reduction of Mn$^+$ to

166

Mn^0 to give, after the loss of MeCN, the 17 e⁻ complex $(bpy)Mn(CO)_3$ (**5**).[10,30] There is discussion in the literature on the fate of the unstable 17 e⁻ Mn^0 complex **5**. One school of thought is that **5** rapidly dimerizes via the formation of a Mn^0–Mn^0 bond to give one equivalent (1/2 molar stoichiometry) of the 18 e⁻ dimer $(bpy)(CO)_3Mn$–$Mn(CO)_3(bpy)$ (**6**) (Scheme 4.6).
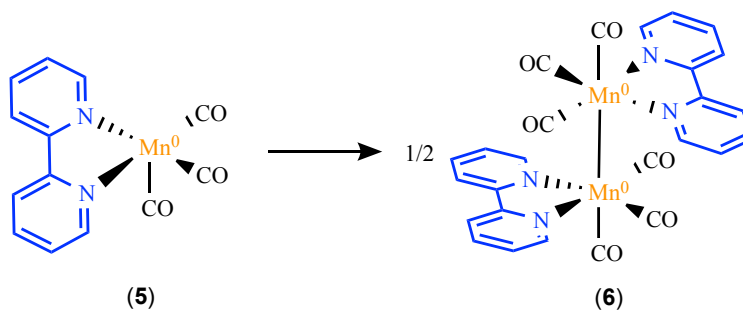
Scheme 4.6. Dimerization of $Mn^0(bpy)(CO)_3$ (**5**).

Another pathway discussed in the literature is that reduction of the 17 e⁻ monomer **5** is rapid and occurs at the same potential to generate the 18 e⁻ anionic monomer $[(bpy)Mn^{-1}(CO)_3]^-$ (**7**).[59] The identity of **7** has been confirmed by independent synthesis, X-ray crystal structure determination, and calculations.[10,60,61] It is believed that the $(bpy)Mn^{-1}$ complex **7** is short-lived, and undergoes a parent-child redox reaction with excess **4** in solution to (eventually) form the Mn^0–Mn^0 dimer **6** (Scheme 4.7).
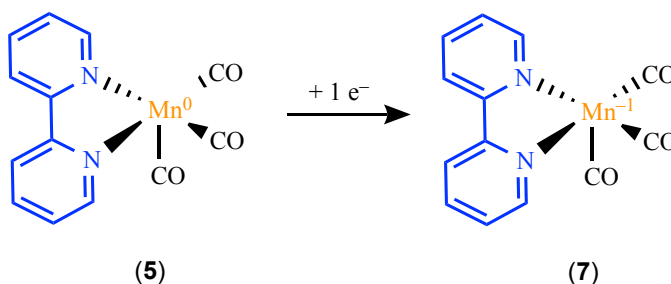
Scheme 4.7. Subsequent electron reduction of $Mn^0(bpy)(CO)_3$.

The literature is in agreement that the second cathodic wave at –2 V corresponds to a 2 e⁻ reduction of the dimer **6** to generate the anionic monomer $[(bpy)Mn^{-1}(CO)_3]^-$

(**7**). Again, it is proposed that complex **7** is short-lived, and undergoes a parent-child redox reaction with excess **1** in solution to form the Mn^0–Mn^0 dimer **6** (Scheme 4.8).
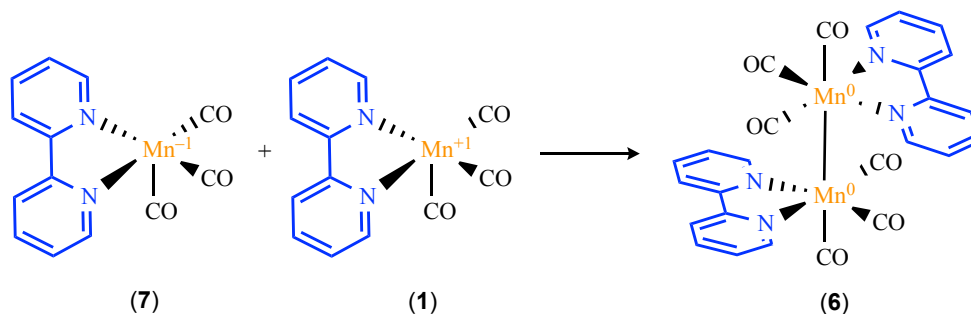
Scheme 4.8. Rapid dimer formation with **1** and **7**.

The anodic wave at –0.65 V in the positive-going sweep corresponds to the two e^- oxidation of **6** to regenerate the 17 e^- monomer **1**. In contrast with the assertion in the literature that **5** is reduced to **7** at –1.6 V, there is a small anodic wave at –1.9 V in the positive-going sweep that may correspond to oxidation of **7** to **5** (Figure 4.11b).

Figure 4.12 shows the CV of the Mn-dye complex (**3**) in MeCN (0.1 mM, 0.1 M nBu$_4$NPF$_6$, 100 mV s^{-1}). The CV of the 3CzIPN-Imidazole-Mn complex **3** (–2 $\leftrightarrow$ 1.2 V) contains a large, 2 e- cathodic peak in the negative going sweep at –1.45 V. Based upon similarities in potentials, this wave very likely arises from the 1 e^- reduction of the dicyanobenzene ring in the coordinated dye **2**, overlapping with the 1e$^-$ reduction of Mn$^+$ to Mn^0, forming [Mn^0(bpy)(CO)$_3$(**2**$^-$)]$^-$ (**8**) (Scheme 4.9). The similar reduction peaks around –1.5 V for the dicyanobenzene unit in both the free photosensitizer **2** and the Mn compound **3** suggest that the π^* cloud in the dicyanobenzene ring is not significantly influenced by the coordination of **2** to Mn. The charge under this peak is 3.628 x 10^{-5} C or 3.76 x 10^{-10} moles, assigned to a 2 e$^-$ reduction. The peak in the positive-going sweep at –1.4 V corresponds to the 1 e$^-$ oxidation of coordinated **2**$^{-1}$ (1.815 x 10^{-5} C or 1.88 x 10^{-10} moles), showing that the **2**/**2**$^-$ redox couple in the coordinated dye is reversible.
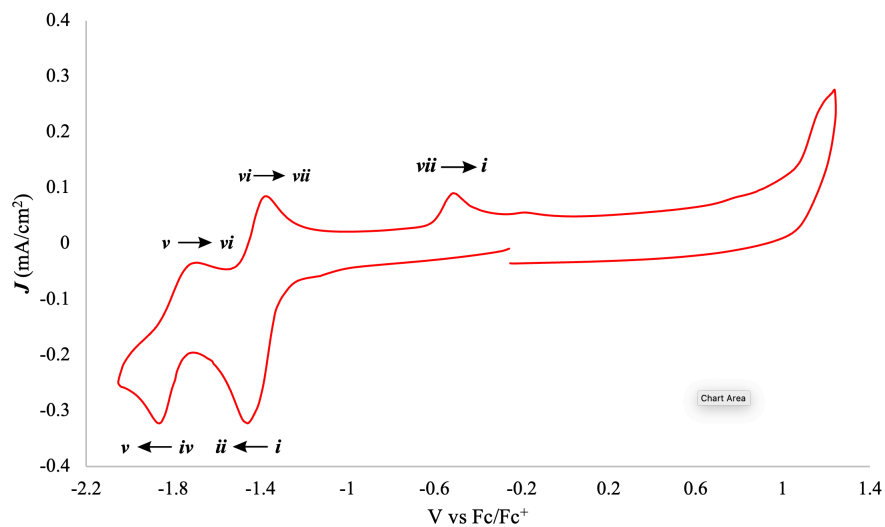
Figure 4.12. CV of 3CzIPN-Imidazole-Mn (**3**). The electrochemical processes in this figure, are schematically represented in Scheme 4.10.
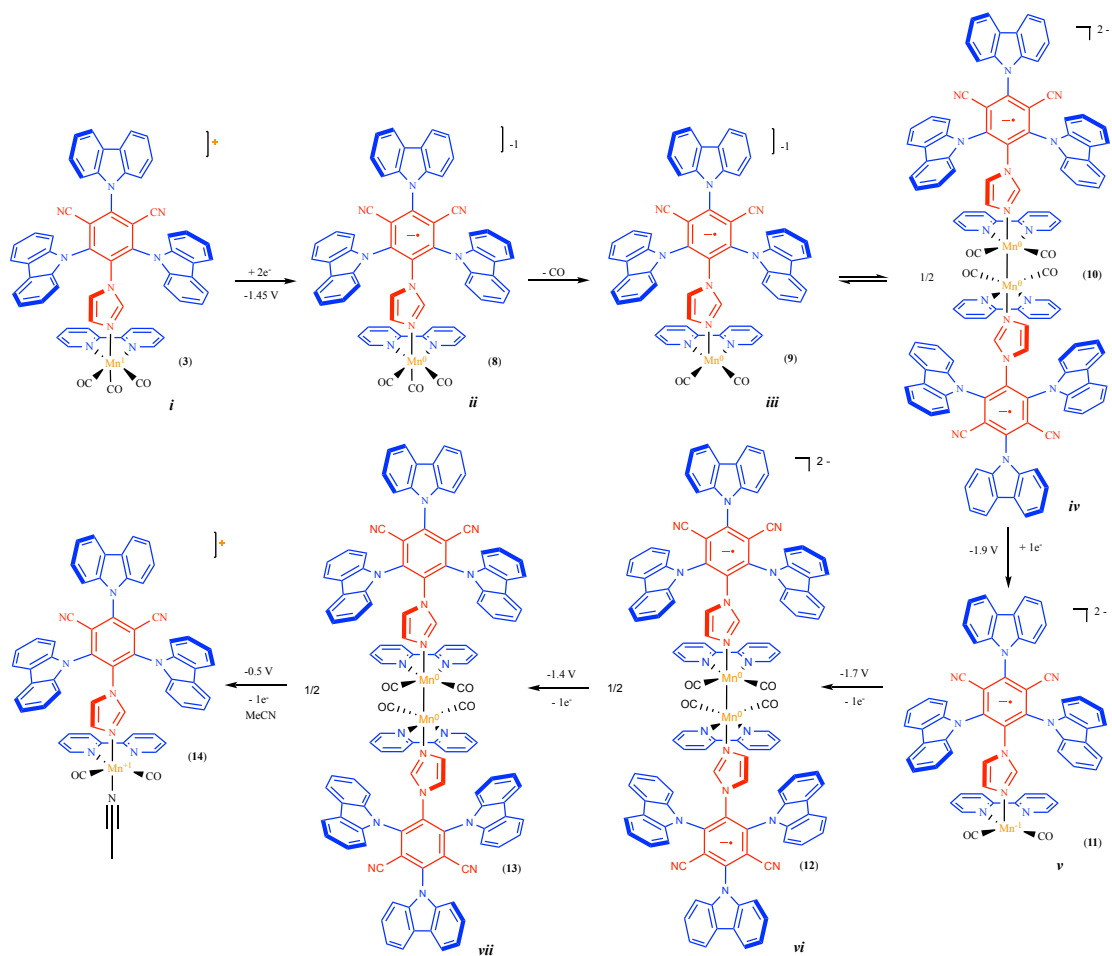
Scheme 4.9. Proposed reactions for the electrochemical processes occurring in the CV of 3CzIPN-Imidazole-Mn (**3**).

The immediate product of the 2 e$^-$ reduction of **3** would be the 19 e$^-$, anionic complex **8**. We propose that the 19 e$^-$ configuration of the Mn centre in **8**, which results in partial occupation of the e_{2g} σ* antibonding orbitals, combined with the trans-labilizing effect of the imidazole ligand results in rapid dissociation of the axial CO ligand in **8** ([Mn^0(bpy)(CO)$_3$(**2**$^-$)]$^-$) to form the 17 e$^-$ complex **9** ([Mn^0(bpy)(CO)$_2$(**2**$^-$)]$^-$) that then undergoes rapid dimerization to form the dianonic dimer **10** (Scheme 4.9).

The rapid dissociation of CO from 19 e$^-$ complexes like **8** has a good deal of precedent: a similar dissociation from the 19 e$^-$ catalytic intermediate (bpy)Mn(CO)$_4$ is proposed universally to be the last step in the electrocatalytic reduction of CO$_2$ by (bpy)Mn(CO)$_3$-type complexes.[10,60] Note there are broad cathodic waves in the positive going sweep at about –0.5 and –0.2 V that integrate to ~1 e$^-$ in charge. These waves occur after the reversible 1 e$^-$oxidation of coordinated **2**$^-$ at –1.4 V. Further, the potentials and shapes of these waves are highly typical for the oxidation of Mn^0–Mn^0 dimers to generate the corresponding Mn^1 monomers.[49] The broad cationic waves at about –0.5 and –0.2 V, therefore, likely correspond to oxidation of isomers of the neutral dimer **13** to form [**trans**-Mn^1(bpy)(CO)$_2$(**2**)(MeCN)]$^+$ (**14**) or related species.

Note that another possibility to CO loss from **8** ([Mn^0(bipy)(CO)$_3$(**2**$^-$)]$^-$) would be loss of **2**$^-$ forming [Mn^0(bipy)(CO)$_3$]. The 1 e$^-$ cathodic wave at –1.4 V, corresponding to oxidation of coordinated **2**$^-$, and the large anionic waves starting at ~1.1 V that correspond to oxidation of the carbazole rings,[62] show that **2** does not dissociate from Mn during these processes. As well, another researcher in the group has shown that **2** does not dissociate from Mn during the electrocatalytic reduction of CO$_2$ with **3** as electrocatalyst.

Extending the sweep limits to –2.2 and 1.4 V reveals a new net one e$^-$ reductive peak at –1.9 V in the negative-going direction that likely arises reduction of Mn^0 to Mn^{-1} in [(bpy)(CO)$_2$(**2**$^-$)Mn^0–Mn^0(**2**$^-$)(CO)$_2$(bpy)]$^{2-}$ (**10**) to form the 18 e$^-$ monomer [Mn^{-1}(bpy)(CO)$_2$(**2**$^-$)]$^{2-}$ (**11**) (1.52 x 10^{-5} C or 1.57 x1 0^{-10} moles). The reduction is reversible, with the corresponding net one e$^-$ oxidation occurring at –1.7 V in the positive going sweep (**12**) (1.44 x 10^{-5} C, 1.49 x 10^{-10} moles). For the model compound (**4**), as expected for this range, we only observed an irreversible one e$^-$ reduction at –1.48 V, corresponding to the Mn (I) to Mn (0) reduction reaction. (Figure 4.26).

Scheme 4.9 illustrates the proposed reactions to account for these electrochemical observations with **3**. Again, the reversible 1 e⁻ wave at –1.45 V for reduction of the dicyanobenzene ring and the large anodic currents for oxidation of the carbazole groups commencing at ~1.1 V are solid evidence that the imidazole-dye **2** remains coordinated to Mn during these experiments. The net results of these CV studies are: 1) that the redox behaviour of **2** is retained upon coordination to Mn; 2) that 2^- has sufficient potential to reduce Mn^1 to Mn^0 in these compounds; 3) that **2** does not readily dissociate during these processes; and **4)** that 2^- as the potential and capacity to act as a 1 e⁻ reservoir for net 2 e⁻ reductions of CO_2 to CO.

Photocatalytic Reduction of CO_2

The photocatalytic reduction of CO_2 by **3** was investigated in MeCN with BIH as the sacrificial electron donor at room temperature under 1 atm CO_2. DMF or MeCN is a typical solvent utilized for these reactions in the literature.[95] MeCN was utilized for this study to avoid contact with DMF. Many reported photocatalytic CO_2 reductions utilize comparable conditions. More specifically, the majority of systems in the literature utilize an AM 1.5 G light source (calibrated to 100 mW/cm²), with some studies utilizing blue LEDs.[116–118] The reported optimum catalyst/PS concentrations are typically around 0.1 mM and [BIH] is kept around 0.1 M.[116–118] In addition to MeCN and BIH, triethanolamine (TEOA) is a common additive that can act as an electron donor and proton source.[116–119] Summarizing, the photocatalytic CO_2 reductions reported in this dissertation were carried out in a 10:1 (v/v) mixed solution of acetonitrile (MeCN) and TEOA, which contained varying concentrations of 3CzIPN-Imidazole–Mn (**3**) and 0.1 M dimethylphenylbenzimidazoline (BIH) as the sacrificial electron donor. AM 1.5 G was used as a light source with infrared and ultraviolet cut-off filters (Scheme 4.10). Some reactions were carried out with AM 1.5 G with infrared and ultraviolet cut-off filters that were also passed through a 1% in water $K_2Cr_2O_7$ solution (>485 nm) as an additional filter to ensure that no higher energy blue visible light reached the reaction. The gas- and liquid-phase reaction products were analyzed by GC-TCD and ¹H NMR, respectively. The catalytic conditions employed for this experiment as well as any other additives are commonly employed in the CO_2 reduction

photocatalysis arena, these were discussed previously in the introduction for this dissertation, Sections 1.4 and 1.6.
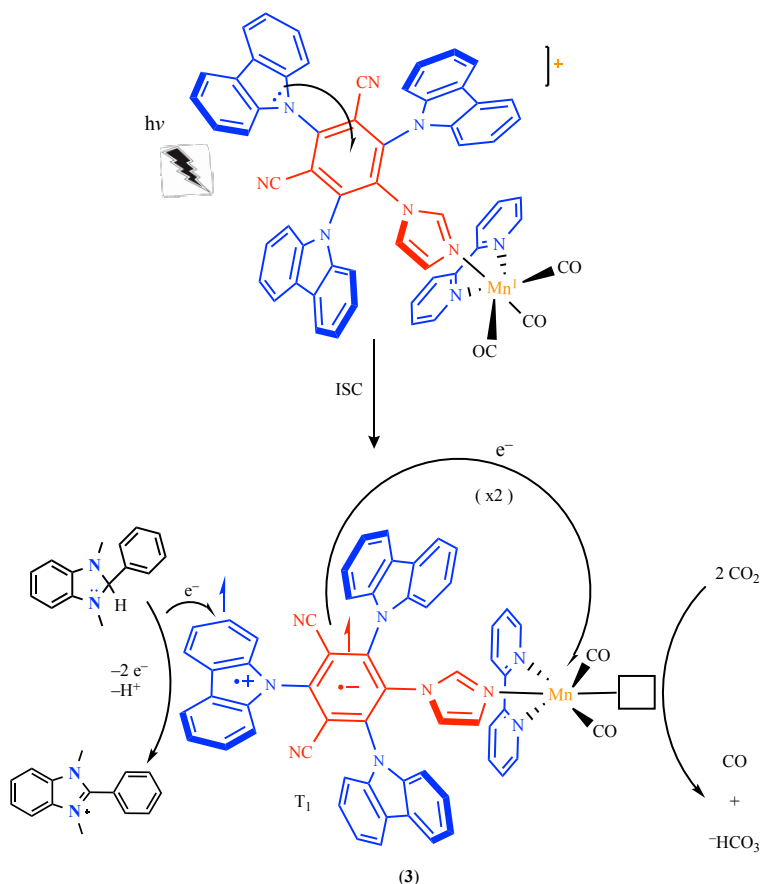
Scheme 4.10. Schematic representation of the CO_2 photocatalytic reduction with **3**.

Table 4.3 summarizes the results of the visible-light-driven photocatalytic CO_2 reduction to CO over time, in TON values, with different concentrations of the photocatalyst. The 3CzIPN-Imidazole-Mn photosystem **3** (0.5 mM) produced 61 TON of CO after 48 h at 0.5 mM under AM 1.5G light. Figure 4.13 plots TON_{CO} vs time for this reaction measured by calibrated GC-TCD aliquots taken over the course of the reaction. There is an initial burst over the first 3 hours of reaction with $TON_{CO} = 40$. The slope was linear at the onset, indicating there was little initiation time, and the slowdown after 3 h resulted from some sort of catalyst inhibition. There was a white solid at the end of the burst that scattered the incident light. NMR analysis showed that the solid was $BI^+HCO_3^-$. Specifically, the reaction mixture of solid and solution was

pumped down with a rotavap, and the entire contents were dissolved in DMSO-d_6. The ^{1}H NMR spectra of the reaction mixture contained peaks assigned to BIH (before and after the reaction) and $BI^+HCO_3^-$.[56,63] The amounts of BIH and $BI^+HCO_3^-$ at the end of the reaction were determined using the internal standard 1,3,5-trimethoxybenzene (TMB). Based on peak integrals, the quantity of BIH remaining at the end of the reaction was ~2.0 x 10^{-4} moles. The starting amount of BIH was 3.0 x 10^{-4} moles, corresponding to 1 x 10^{-4} moles of BIH consumed. The amount of $BI^+HCO_3^-$ formed by the reaction was 1 x 10^{-4} moles, consistent with the amount of BIH consumed, and with the number of moles of CO produced (1.002 x 10^{-4} moles), indicating BIH is the main source of electrons in this reaction.

Table 4.3. CO_2 Photocatalytic Reactions with 3CzIPN-Imidazole-Mn (3) and Controls

Entry	Concentration (mM)	Photocatalyst	Irradiation time (h)^a	TON CO	H$_2$
1	0.5	3CzIPN-Imidazole-Mn	48	61 ± 2^b	0.1
2	0.1	3CzIPN-Imidazole-Mn	48	14	0.2
3	0.01	3CzIPN-Imidazole-Mn	48	4	0.1
4	0.5	3CzIPN-Imdiazole-Mn + 10% MeOH	48	3	0.1
5	0.5	Me-Imidazole-Mn	48	5.8	0.2
6	0.5	Mn(bpy)(CO)$_3$(C$_3$H$_6$O)BF$_4$	48	5.4	0.2
7	0.5 + 0.5	Mn(bpy)(CO)$_3$(C$_3$H$_6$O)BF$_4$ + 4CzIPN	48	6.3	2.2
8	0.5	3CzIPN-Imidazole-Mn ($^{13}CO_2$)	48	60	0.1

Conducted on an acetonitrile solution containing BIH (0.1 M) and 10% v/v TEOA under a CO_2 atmosphere. ^{a}Irradiation with a sunlight simulator A.M. 1.5 G (100 mW/cm^2). ^{b}TON average of 3 measurements.
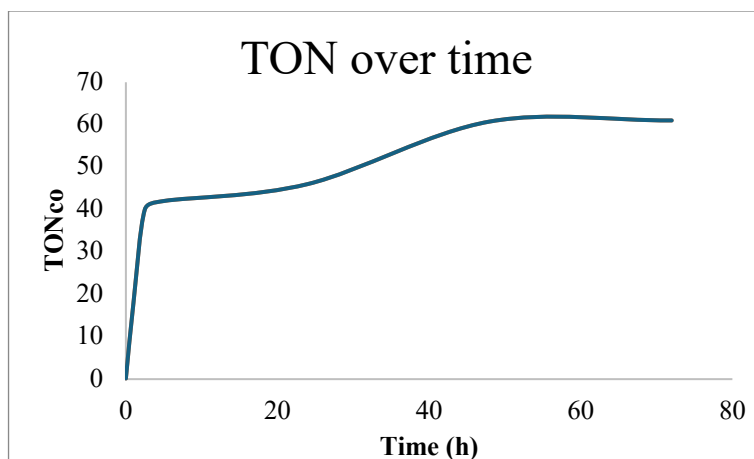
Figure 4.13. TON_{CO} vs Time (h) for the photocatalytic reduction of CO_2 with (**3**).

The control experiments with Me-Imidazole-Mn (**4**) or $[Mn(bpy)(CO)_3(MeCN)]^+(BF_4)^-$ produced 6 and 5.8 equivalents CO under these conditions after 48 h, respectively, demonstrating that the Mn catalyst itself does not drive the reaction under these conditions significantly. In another control, the AM 1.5G light was filtered through a 1% in water $K_2Cr_2O_7$ solution (>485 nm) in addition to the UV and IR cut-off filters. This reaction generated 40 equivalents of CO ($TON_{CO} = 40$) in 3 h, demonstrating that not even blue sunlight (>485 nm) is required for this photochemical CO_2 reduction.

The reaction between the acetonitrile complex $[Mn(bpy)(CO)_3(MeCN)]^+(BF_4)^-$ and the imidazole-photosensitizer **2** is slow in the MeCN solution at room temperature. No product was identified after 2 h at room temperature. A control photochemical CO_2 reduction using BIH, TEOA, and a 1:1 mixture of **2** and $[Mn(bpy)(CO)_3(MeCN)](BF_4)$ in MeCN solution under 1.5 AM G light failed to produce significant amounts of CO (TON = 6.3) after 48 h, showing that the intramolecular complex **3** is more active than its separate, intermolecular components.

4.3 Conclusions

The synthesis and photocatalytic activity for the Mn (I) $[Mn(CO)_3(bpy)]$ catalyst coupled to an organic photosensitizer unit derived from 4CzIPN, 3-CzIPN-imidazole was described in this chapter. The synthesis of this photocatalytic system is the first reported derivatization of their type, showing relatively long-lived excited states and

efficient charge transfer from the triplet state (T_1) on the dye to the catalytic center on Mn. The complexes are highly selective for the photoreduction of CO_2 to CO in CO_2-saturated acetonitrile (MeCN) solution under AM 1.5 G light, employing BIH (1,3-dimethyl-2-phenyl-2,3-dihydro-1H-benzo[d]imidazole) as a sacrificial electron donor. Achieving up to 60 TON_{CO}, the facile, robust, and low-cost preparation, in addition to strong absorption in the visible light range, promotes this photocatalyst as a potent candidate for further family expansion and development into electro and photoelectrocatalysis. Again, the reversible reduction of the dicyanobenzene ring and the large anodic currents for oxidation of the carbazole groups are solid evidence that the imidazole-dye **2** remains coordinated to Mn during these experiments. The net results of these CV studies are:1) that the redox behaviour of **2** is retained upon coordination to Mn; 2) that **2**$^-$ has sufficient potential to reduce Mn^1 to Mn^0 in these compounds; 3) that (**2**) does not readily dissociate during these processes; and 4) that (**2**$^-$) as the potential and capacity to act as a 1 e$^-$ reservoir for net 2 e$^-$ reductions of CO_2 to CO. The other possibility is that CV shows that the reduced dye has enough potential to reduce Mn^+ to Mn^0, perhaps photosynthesis is operating within this redox range, utilizing coordinated (**2**) as a photo source of electrons with BIH, and also as an electron reservoir for a 2 e- reduction of CO_2 to CO (**2**$^-$). Therefore, the dimer might be shutting down the catalyst, and the dye does not have enough reducing power to open the dimer. Kinetics, isolation of electrochemistry intermediates, and calculations are required to investigate these theories.

4.4 Experimental

Materials

Chemicals were used without any further treatment, unless mentioned otherwise. Following chemicals were obtained from Sigma Aldrich: Carbazole ($\geq$95%), NaH, NaCl, NaClO$_4$ (ACS reagent, $\geq$98.0%), Calcium hydride (reagent grade, 95%), triethanolamine (TEOA), distilled (EtOH)$_3$N $\geq$ 99.0%), tetrabutylammonium hexafluorophosphate (NBu$_4$PF$_6$; for electrochemical analysis, $\geq$99.0%), acetonitrile, distilled (MeCN for HPLC, gradient grade, $\geq$99.9%), dichloromethane, distilled (DCM; ACS reagent, $\geq$99.5%), tetrahydrofuran, distilled (THF; ACS reagent, $\geq$99.0%),

potassium tert-butoxide (95%), potassium hydride (from 60% oil suspension, THF washed, dried). Tetrafluoroisophthalonitrile (>98.0%) was purchased from TCI Chemicals. Triple distilled water was used to prepare aqueous solutions. The solvents DCM (CaH$_2$), acetonitrile (CaH$_2$), and tetrahydrofuran-d_8/tetrahydrofuran (Na/benzophenone) were distilled from the appropriate drying agent under N$_2$. Argon or N$_2$ gas was bubbled through solvents for a minimum of 30 min before use unless noted otherwise.

Instrumentation

Electrochemical studies were carried out using a Solartron SI 1287 Electrochemical Interface. UV-vis spectra were collected using a Cary 5000 UV-Vis spectrometer for chromophores dissolved in various solvents. ^{1}H NMR spectra were acquired using 500 MHz and 600 MHz Varian Inova NMR spectrometers. ^{13}C NMR spectra were acquired using a Varian VNMRS 500 MHz NMR spectrometer. The chemical shifts are reported in parts per million relative to TMS with the solvent as the internal standard. Abbreviations used in reporting NMR data are s (singlet), d (doublet), t (triplet), q (quartet), dd (doublet of doublet), dq (doublet of quartet), and m (multiplet). Photoluminescence spectra were collected using a Horiba-PTI QM-8075-11 Fluorescence System. FT-IR was measured by Thermo Nicolet 8700 FTIR Spectrometer and Continuum FTIR Microscope on ATR. HRMS spectra were acquired using electrospray ionization in an Agilent 6220 ao TOF mass spectrometer. Gas chromatography evaluation was acquired with an HP 6890 series GC system equipped with a thermal conductivity detector (TCD), and a Restek micropacked shincarbon column (st, 2mx1mm, 1/16' OD, 100/120 mesh, RK19808)

Electrochemistry

For electrochemical studies, 0.1 M TBAPF$_6$ solution in acetonitrile was used. The pseudo-reference and the counter electrodes were silver wire and platinum gauze, respectively (ferrocene was added at the end of every measurement to determine the reference voltage), GC as WE. The reaction flask was a 50 mL four-neck flask. Before the electrochemical measurement, the solution was sparged with N$_2$ for 20 min. The

flask was under N_2 dynamic pressure at two bubbles per second during the measurements.

Photocatalysis

For photochemical studies, various concentrations of catalyst solution (3 mL) were used, containing 0.1 M BIH (1,3-dimethyl-2-phenyl-2,3-dihydro-1*H*-benzo[*d*]imidazole) and 0.3 mL TEOA (Triethanolamine, 10%) was used. The CO2RR reaction was carried out in a 10 mL test tube capped with a rubber septum. Before photochemical CO_2 reduction, the solution was bubbled with CO_2 or $^{13}CO_2$ for 10 min. A CO_2 blanket was maintained on top of the solution during the reaction time. The reaction mixture was stirred at 500 rpm throughout the measurements using a magnetic bar. The light source was a Sunlight simulator system with a 300 W Xe lamp and an AM 1.5G optical filter. The incident light intensity was measured with a Thorlab S121C light meter before and after each experiment; it was maintained at 100 ± 2 mW/cm^2. Cut-off filters were employed at 400 and 800 nm to prevent UV or IR light interference. 20 μL of methane gas was used as an internal standard for each experiment. The corresponding calibration curve for CH_4/CO was measured to calculate the amount of CO produced. To measure the CO produced by CO_2 reduction, 100 μL from the gas phase of the reaction mixture was collected and manually injected into the GC instrument.

Preparation of the 3CzIPN-Imidazole-Mn and Me-Imidazole-Mn

Synthesis of Mn(bpy)(CO)$_3$BF$_4$ (**1**).
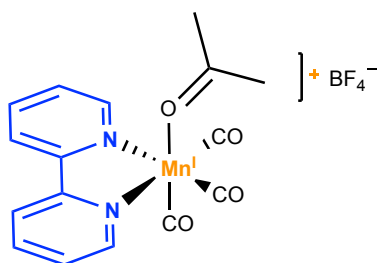
Mn(bpy)(CO)$_3$Br (0.149 g, 0.40 mmol) and AgBF$_4$ (0.079g, 0.40 mmol) were placed in a 25 mL Schlenk flask inside the glovebox. The Schlenk flask was transferred to a Schlenk line, and the substrates were dissolved in 10 mL of freshly distilled, N_2-sparged acetone. Upon stirring, the orange solution quickly becomes yellow, and a white solid precipitated at the bottom of the flask, after only 5 min at room temperature. The flask was covered from the light

with aluminum foil throughout the process. The mixture was filtered through a dry, N_2-flushed celite column. According to ^{1}H NMR, the reaction was complete. Product (**1**) was obtained as a yellow solution and used as is. **^{1}H NMR** (599.929 MHz, Ac-*d*6, 26.9 °C): δ 7.89 (2H, t, *J* = 6.0 Hz), 8.40 (2H, t, *J* = 7.2 Hz), 8.73 (2H, d, *J* = 8.4 Hz), 9.34(2H, d, *J* = 4.8Hz). **^{13}C{^{1}H} NMR** (125.686 MHz, Ac-*d*6, 27.0 °C): δ 124.80, 128.76, 141.94, 155.56, 157.43. **HRMS (ESI)** m/z Calcd. for $C_{16}H_{14}MnN_2O_4$ (M*+): 353.0329. Found: 353.0326. Figure 4.14 shows the ^{1}H, and Figure 4.15 the ^{13}C NMR spectra of (**1**).

599.929 MHz H1 1D in acetone (ref. to acetone @ 2.04 ppm)
temp 26.2 C -> actual temp = 27.0 C, autoxid probe
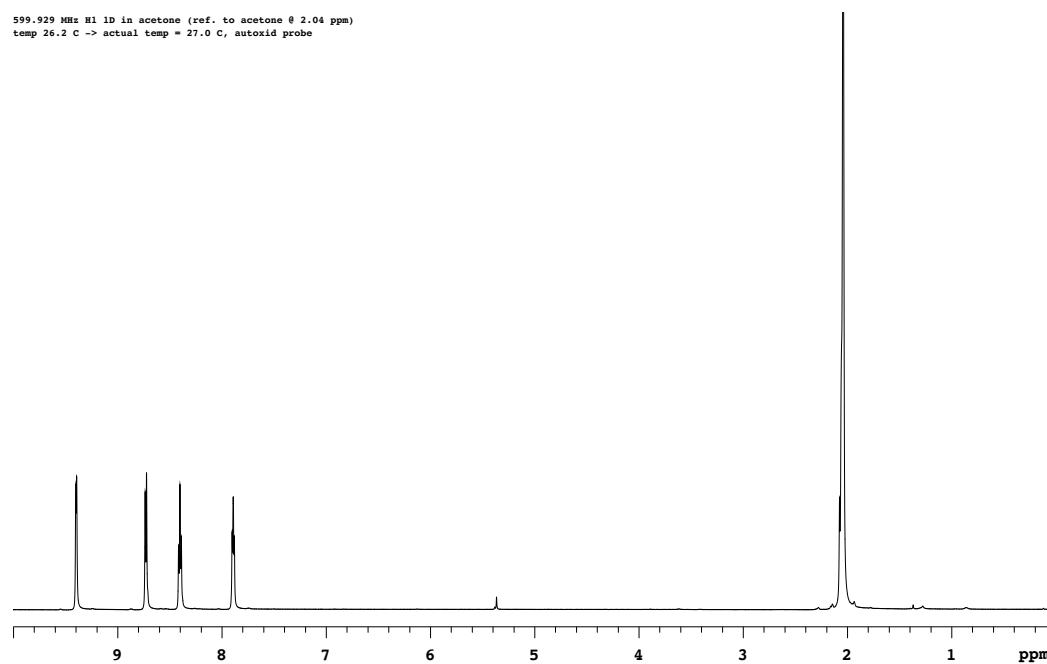
Figure 4.14. ^{1}H NMR spectrum of Mn(bpy)(CO)$_3$BF$_4$ **(1.)**
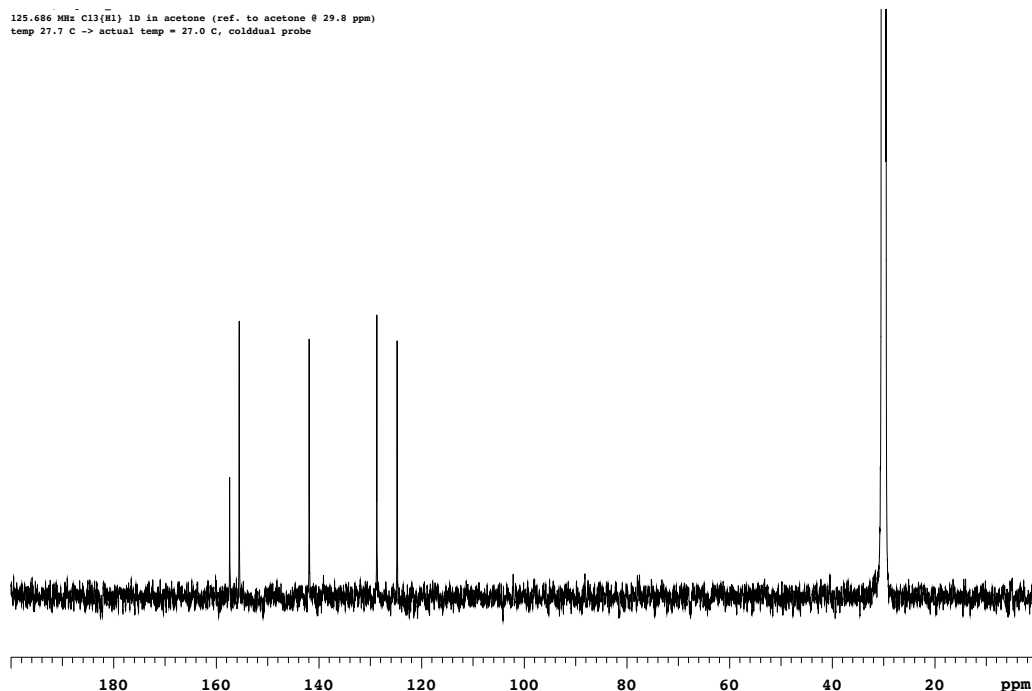
Figure 4.15. ^{13}C NMR spectrum of Mn(bpy)(CO)$_3$BF$_4$ **(1).**

Synthesis of 3CzIPN-Imidazole-Mn(bpy)(CO)$_3$BF$_4$ (3)
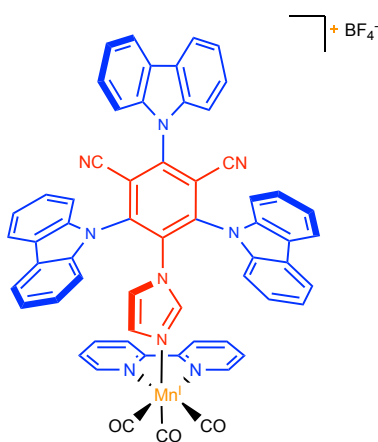
3CzIPN-Imidazole (**2**, 0.262g, 0.39 mmol) was placed in a 25 mL Schlenk flask, degassed, and filled with N$_2$. The Mn complex (**1,** 0.40 mmol), dissolved in 10 mL of acetone, was cannula transferred into the flask with the dye. At room temperature, covered with aluminum foil, after 5 min of stirring the compound, the mixture changed from yellow to orange colour. The mixture was stirred at room temperature for 18 hours, after this time the acetone volume was reduced to half under high vacuum, and a yellow solid precipitated upon addition of diethyl ether. The product (**3**) was washed with diethyl ether (3 x 10 mL) and dried to obtain a yellow solid in 90% yield. **^{1}H NMR** (599.929 MHz, Ac-*d*6, 26.9 °C): δ 6.24 (1H, s), 6.47 (1H, s), 6.87 (1H, s), 7.40-7.45 (14H, m), 7.48(2H, t, *J* = 7.2), 7.89 (2H, t, *J* = 6.0 Hz), 8.40 (2H, t, *J* = 7.2 Hz), 8.73 (2H, d, *J* = 8.4 Hz), 9.34(2H, d, *J* = 4.8Hz). **^{13}C{^{1}H} NMR** (125.686 MHz, Ac-*d*6, 27.0

179

°C): δ 124.80, 128.76, 141.94, 155.56, 157.43. **HRMS (ESI)** m/z Calcd. for $C_{60}H_{35}MnN_9O_3$ (M*+): 984.2243. Found: 984.2242. Figure 4.16 shows the ^{1}H, Figure 4.17 the ^{13}C NMR, Figure 4.18 gHSQC, and Figure 4.19 FTIR spectra of (**3**).
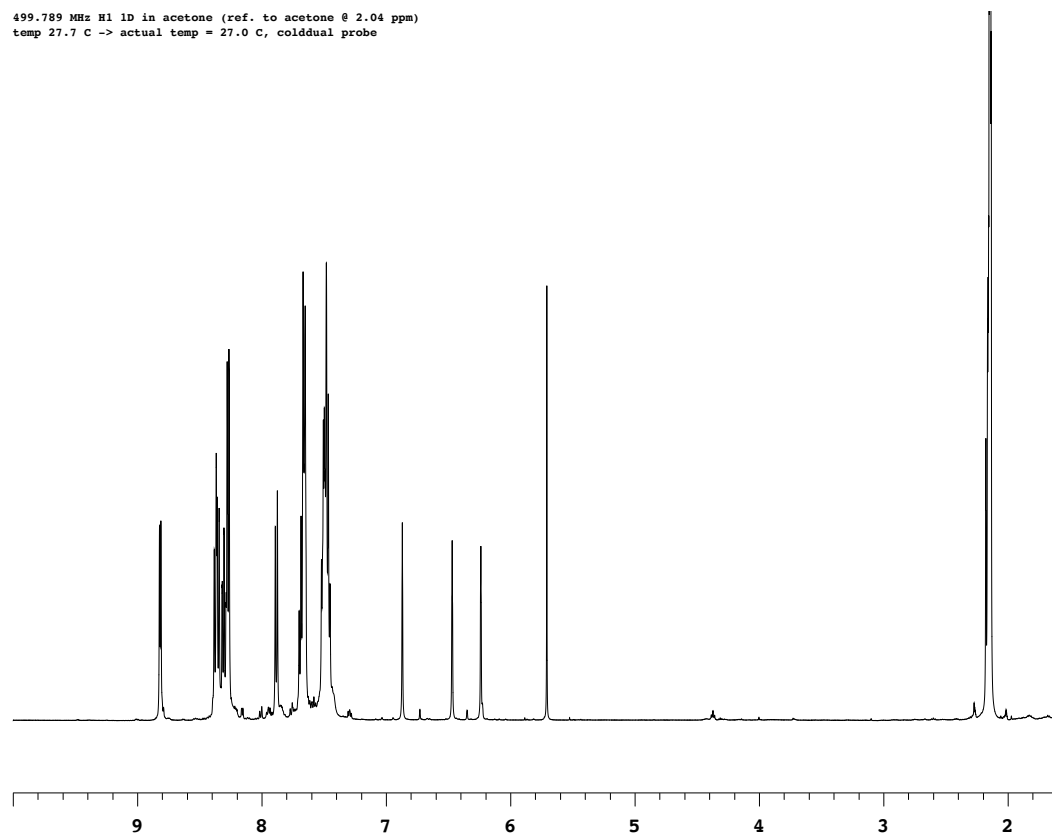
Figure 4.16. ^{1}H NMR spectrum of 3CzIPN-Imidazole-Mn(bpy)(CO)₃BF₄ **(3).**

Figure 4.17. ^{13}C NMR spectrum of 3CzIPN-Imidazole-Mn(bpy)(CO)$_3$BF$_4$ **(3).**

Figure 4.18. 2D gHSQC NMR spectrum of 3CzIPN-Imidazole-Mn(bpy)(CO)$_3$BF$_4$ **(3).**

181
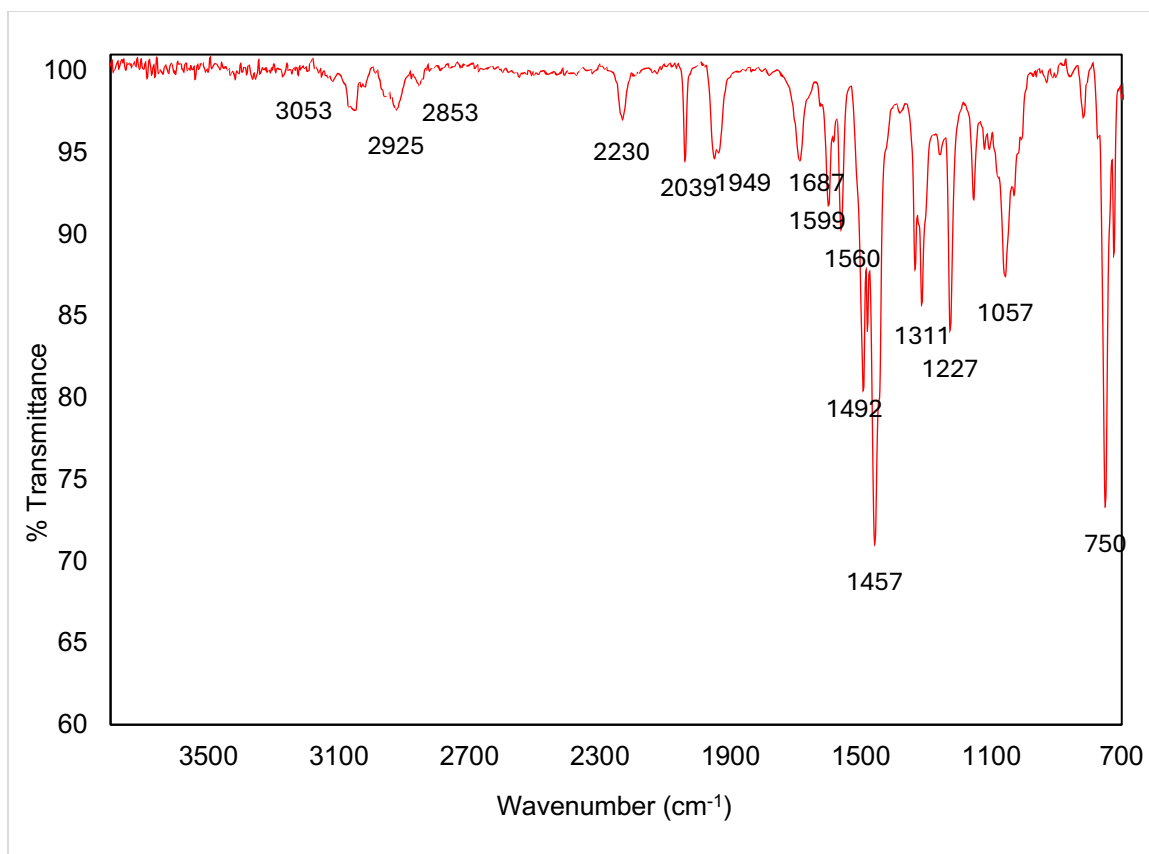
Figure 4.19. FTIR spectrum of 3CzIPN-Imidazole-Mn(bpy)(CO)$_3$BF$_4$ **(3).**

Synthesis of Me-Imidazole-Mn(bpy)(CO)$_3$BF$_4$ (4).
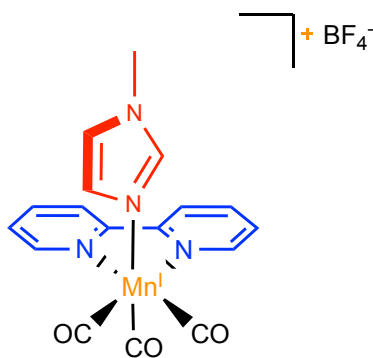
1-Methylimidazole (0.0328 g, 0.39 mmol) was placed in a 25 mL Schlenk flask and purged with N$_2$ for 20 min. The Mn complex (**1,** 0.40 mmol), dissolved in 10 mL of acetone, was cannula-transferred into the flask. At room temperature, covered with aluminum foil, and after 5 min of stirring the compound, the mixture changed from yellow to orange-brown colour. The mixture was stirred at room temperature for 18 h. After this time the acetone volume was reduced to half under high vacuum, and a brown solid precipitated upon the addition of diethyl ether. The product (**4**) was washed with diethyl ether (3 x 10 mL) and dried to obtain a yellow solid in % yield. **^{1}H NMR** (599.929 MHz, CD$_3$CN, 27.7 °C): δ 3.42 (3H, s),

6.42 (1H, s), 6.88 (1H, s), 7.20 (1H, s), 7.72 (2H, t, $J = 6.6$ Hz), 8.19 (2H, t, $J = 7.2$ Hz), 8.33 (2H, d, $J = 8.4$), 8.25 (2H, d, $J = 4.8$). **$^{13}C\{^1H\}$ NMR** (125.686 MHz, CD$_3$CN, 27.0 °C): δ 35.0, 123.7, 124.6, 128.7, 129.8, 141.1, 155.0, 156.5. **HRMS (ESI)** m/z Calcd. for C$_{17}$H$_{14}$MnN$_4$O$_3$ (M*+): 377.0446 Found: 377.0444.

Figure 4.20 shows the ^{1}H and Figure 4.21 ^{13}C NMR spectra of (**4**), and Figure 4.22 shows the H1 gHSQCAD correlations. Figure 4.23 shows the photoluminescence spectrum in MeCN.
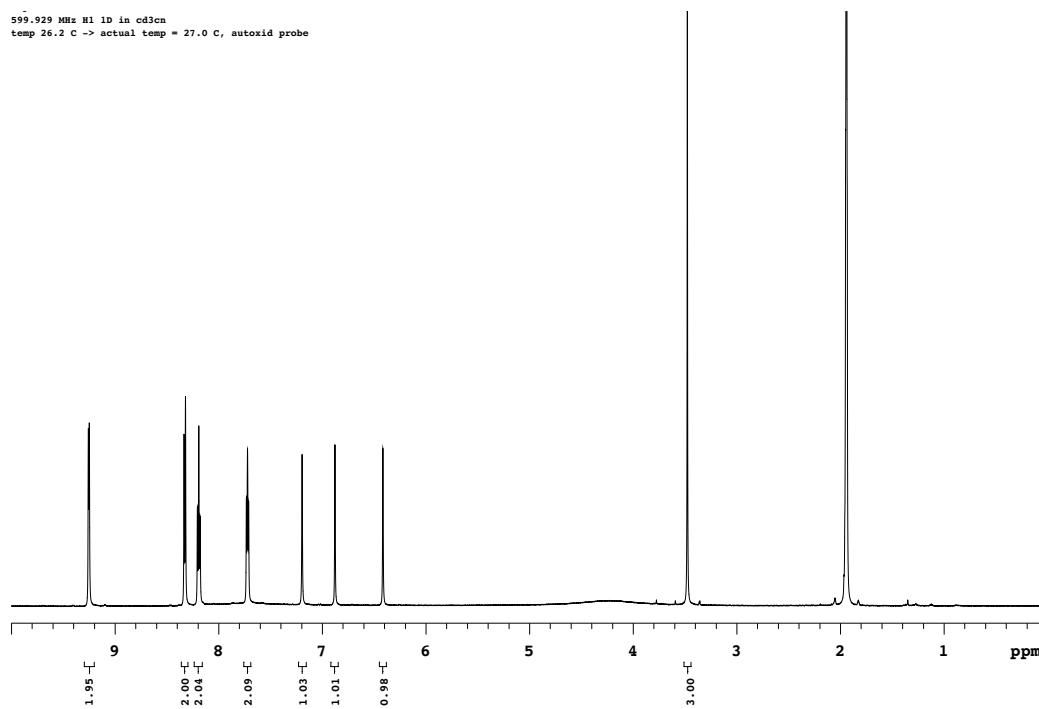
Figure 4.20. ^{1}H NMR spectrum of Me-Imidazole-Mn(bpy)(CO)$_3$BF$_4$ (**4**).
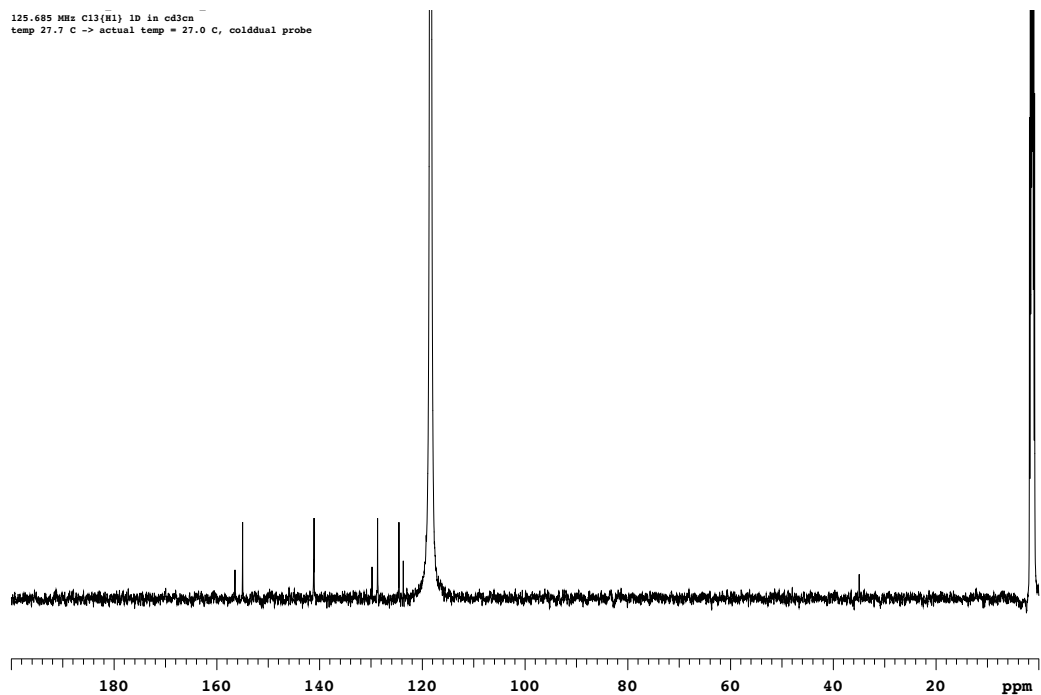
Figure 4.21. ^{13}C NMR spectrum of Me-Imidazole-Mn(bpy)(CO)$_3$BF$_4$ **(4).**
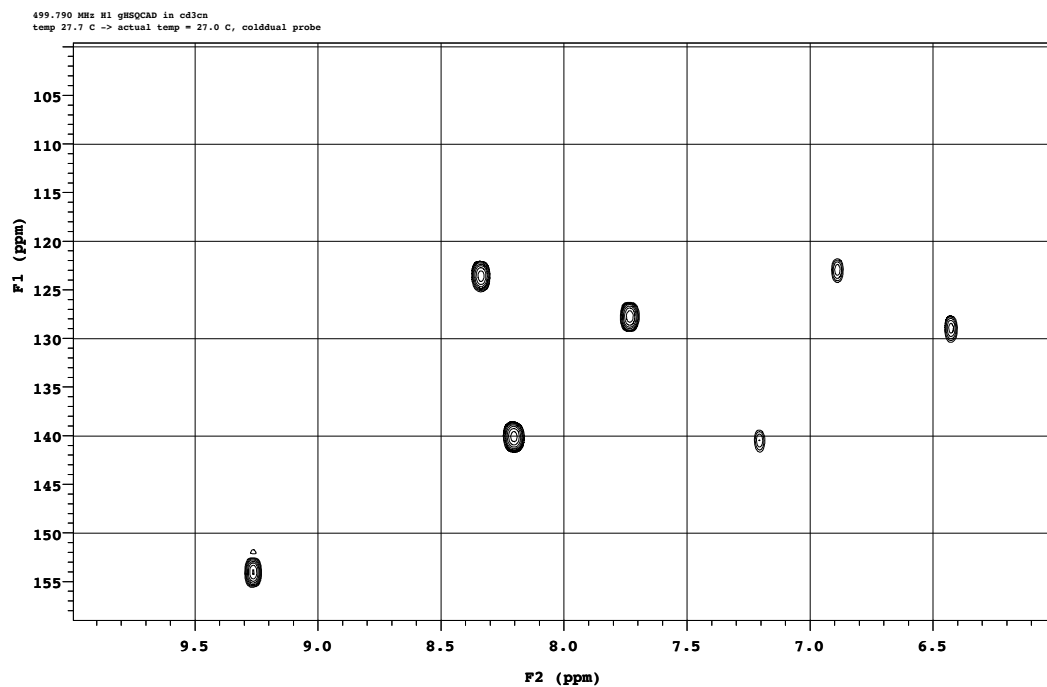
Figure 4.22. 2D gHSQC NMR spectrum of Me-Imidazole-Mn(bpy)(CO)$_3$BF$_4$ **(4).**

184
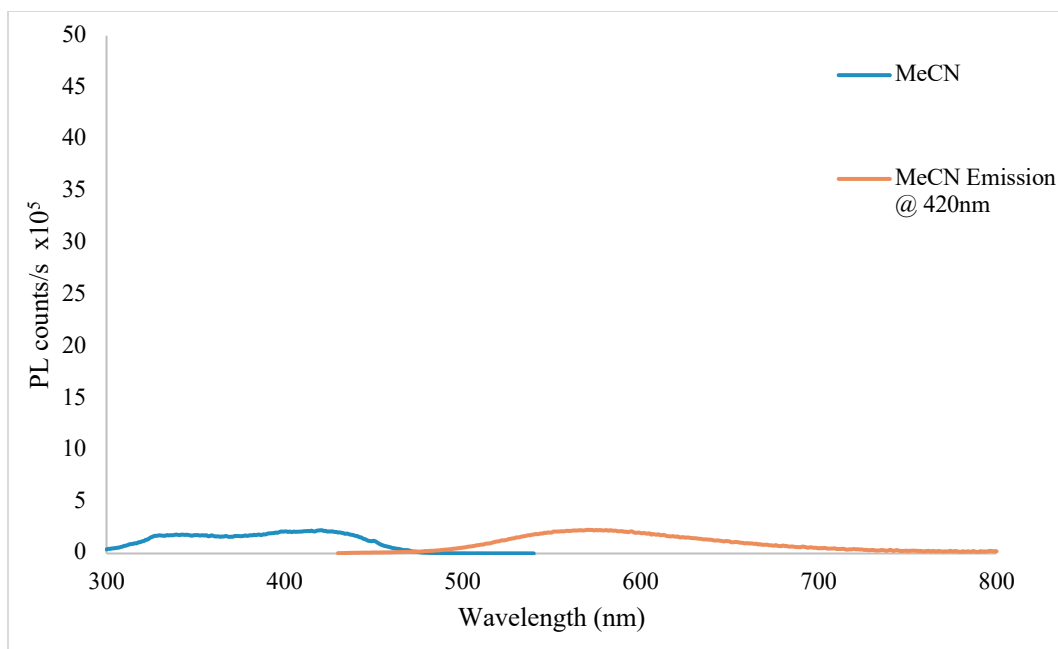
Figure 4.23. Photoluminescence spectrum of Me-Imidazole-Mn(bpy)(CO)$_3$BF$_4$ **(4).**

The photoluminescence spectra of the BIH in different solvents (MeCN and CHCl$_3$) are included to confirm the absence of any absorption or emission interfering with the emission of (**2**) (Figure 4.24).
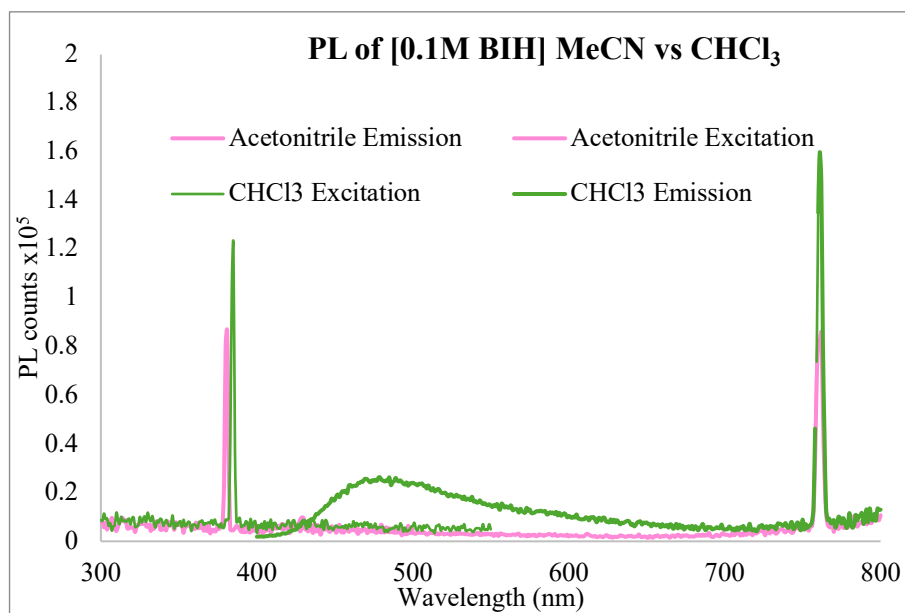
Figure 4.24. Photoluminescence spectra of 0.1M BIH in MeCN and CHCl$_3$. Emission spectra were recorded at 380 nm excitation.

As a comparison, the full CV of the compound 3CzIPN-Imidazole (**2**) (Figure 4.25) and cathodic CV Me-Imidazole-Mn (**4**) (Figure 4.26) are included as part of the electrochemical analysis for these compounds.
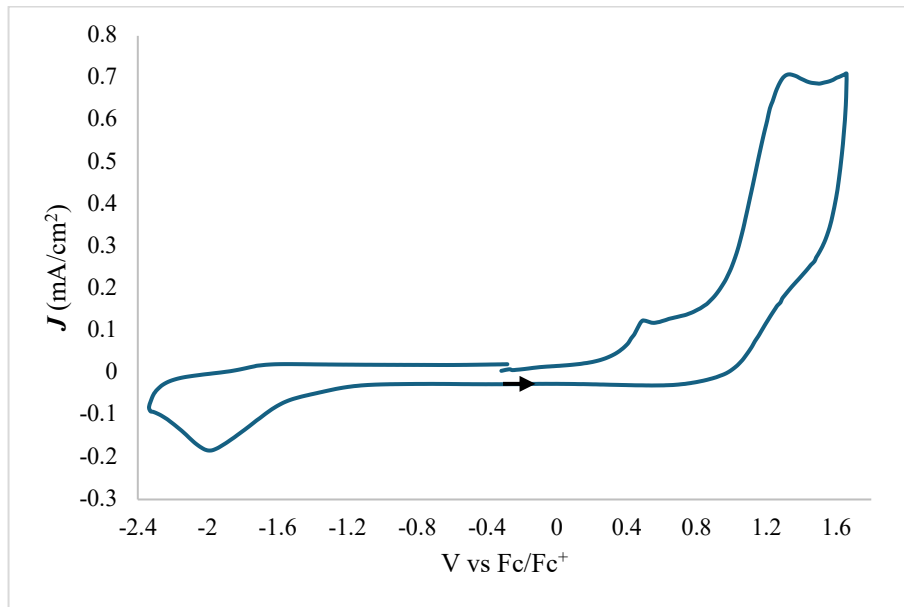
Figure 4.25. CV of 3CzIPN-Imidazole (**2**) (0.1 mM, MeCN, 0.1 M nBu$_4$NPF$_6$, 100 mV s^{-1} GC as WE).
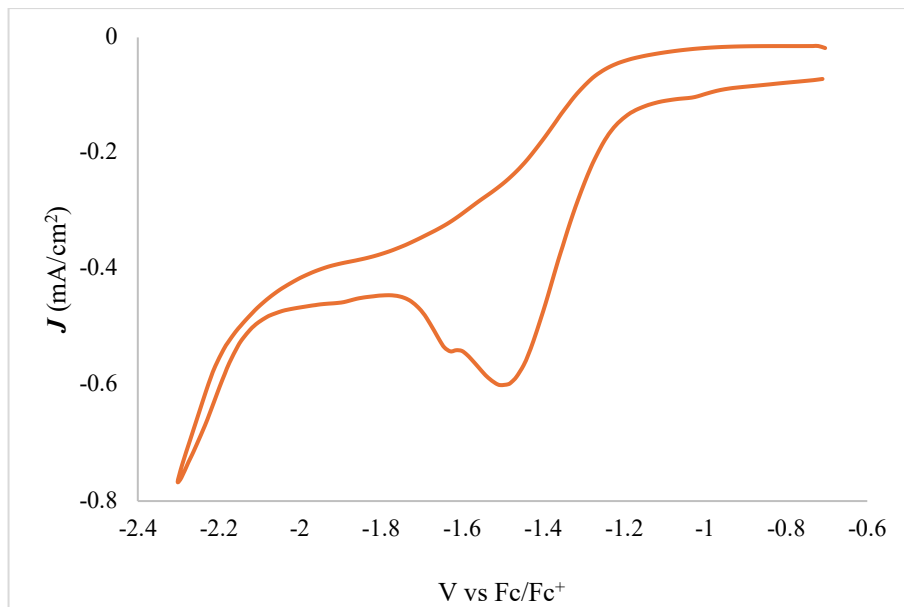
Figure 4.26. CV of Me-Imidazole (**4**) (0.1 mM, MeCN, 0.1 M nBu$_4$NPF$_6$, 100 mV s^{-1} GC as WE).

4.5 References

(1) US Department of Commerce, N. *Global Monitoring Laboratory - Carbon Cycle Greenhouse Gases*. https://gml.noaa.gov/ccgg/trends/global.html (accessed 2023-04-28).

(2) *Met Office Hadley Centre observations datasets*. https://www.metoffice.gov.uk/hadobs/hadcrut5/#:~:text=HadCRUT5%20is%20a%20gridded%20dataset,and%20regional%20average%20time%20series. (accessed 2023-05-11).

(3) *CO2 Emissions | Global Carbon Atlas*. http://www.globalcarbonatlas.org/en/CO2-emissions (accessed 2023-04-28).

(4) Lewis, N. S. Research Opportunities to Advance Solar Energy Utilization. *Science* **2016**, *351* (6271), aad1920. https://doi.org/10.1126/science.aad1920.

(5) Aneke, M.; Wang, M. Energy Storage Technologies and Real Life Applications – A State of the Art Review. *Applied Energy* **2016**, *179*, 350–377. https://doi.org/10.1016/j.apenergy.2016.06.097.

(6) Lv, J.; Xie, J.; Mohamed, A. G. A.; Zhang, X.; Feng, Y.; Jiao, L.; Zhou, E.; Yuan, D.; Wang, Y. Solar Utilization beyond Photosynthesis. *Nat Rev Chem* **2022**, *7* (2), 91–105. https://doi.org/10.1038/s41570-022-00448-9.

(7) Crabtree, R. H. Alternate Strategies for Solar Fuels from Carbon Dioxide. *ACS Energy Lett.* **2020**, *5* (8), 2505–2507. https://doi.org/10.1021/acsenergylett.0c01359.

(8) Dalle, K. E.; Warnan, J.; Leung, J. J.; Reuillard, B.; Karmel, I. S.; Reisner, E. Electro- and Solar-Driven Fuel Synthesis with First Row Transition Metal Complexes. *Chem. Rev.* **2019**, *119* (4), 2752–2875. https://doi.org/10.1021/acs.chemrev.8b00392.

(9) Tu, W.; Zhou, Y.; Zou, Z. Photocatalytic Conversion of CO_2 into Renewable Hydrocarbon Fuels: State-of-the-Art Accomplishment, Challenges, and Prospects. *Adv. Mater.* **2014**, *26* (27), 4607–4626. https://doi.org/10.1002/adma.201400087.

(10) Grills, D. C.; Ertem, M. Z.; McKinnon, M.; Ngo, K. T.; Rochford, J. Mechanistic Aspects of CO2 Reduction Catalysis with Manganese-Based Molecular Catalysts. *Coordination Chemistry Reviews* **2018**, *374*, 173–217. https://doi.org/10.1016/j.ccr.2018.05.022.

(11) Agarwal, J.; Fujita, E.; Schaefer, H. F.; Muckerman, J. T. Mechanisms for CO Production from CO_2 Using Reduced Rhenium Tricarbonyl Catalysts. *J. Am. Chem. Soc.* **2012**, *134* (11), 5180–5186. https://doi.org/10.1021/ja2105834.

(12) Schneider, T. W.; Ertem, M. Z.; Muckerman, J. T.; Angeles-Boza, A. M. Mechanism of Photocatalytic Reduction of CO_2 by Re(Bpy)(CO)$_3$Cl from Differences in Carbon Isotope Discrimination. *ACS Catal.* **2016**, *6* (8), 5473–5481. https://doi.org/10.1021/acscatal.6b01208.

(13) Kuramochi, Y.; Ishitani, O.; Ishida, H. Reaction Mechanisms of Catalytic Photochemical CO2 Reduction Using Re(I) and Ru(II) Complexes. *Coordination Chemistry Reviews* **2018**, *373*, 333–356. https://doi.org/10.1016/j.ccr.2017.11.023.

(14) Cancelliere, A. M.; Puntoriero, F.; Serroni, S.; Campagna, S.; Tamaki, Y.; Saito, D.; Ishitani, O. Efficient Trinuclear Ru(II)–Re(I) Supramolecular Photocatalysts for CO_2 Reduction Based on

a New Tris-Chelating Bridging Ligand Built around a Central Aromatic Ring. *Chem. Sci.* **2020**, *11* (6), 1556–1563. https://doi.org/10.1039/C9SC04532E.

(15) Tamaki, Y.; Koike, K.; Morimoto, T.; Ishitani, O. Substantial Improvement in the Efficiency and Durability of a Photocatalyst for Carbon Dioxide Reduction Using a Benzoimidazole Derivative as an Electron Donor. *Journal of Catalysis* **2013**, *304*, 22–28. https://doi.org/10.1016/j.jcat.2013.04.002.

(16) Sahara, G.; Ishitani, O. Efficient Photocatalysts for CO_2 Reduction. *Inorg. Chem.* **2015**, *54* (11), 5096–5104. https://doi.org/10.1021/ic502675a.

(17) Tamaki, Y.; Ishitani, O. Supramolecular Photocatalysts for the Reduction of CO_2. *ACS Catal.* **2017**, *7* (5), 3394–3409. https://doi.org/10.1021/acscatal.7b00440.

(18) Kuramochi, Y.; Kamiya, M.; Ishida, H. Photocatalytic CO_2 Reduction in *N , N* -Dimethylacetamide/Water as an Alternative Solvent System. *Inorg. Chem.* **2014**, *53* (7), 3326–3332. https://doi.org/10.1021/ic500050q.

(19) Ashford, D. L.; Song, W.; Concepcion, J. J.; Glasson, C. R. K.; Brennaman, M. K.; Norris, M. R.; Fang, Z.; Templeton, J. L.; Meyer, T. J. Photoinduced Electron Transfer in a Chromophore–Catalyst Assembly Anchored to TiO_2. *J. Am. Chem. Soc.* **2012**, *134* (46), 19189–19198. https://doi.org/10.1021/ja3084362.

(20) Wang, F. Artificial Photosynthetic Systems for CO_2 Reduction: Progress on Higher Efficiency with Cobalt Complexes as Catalysts. *ChemSusChem* **2017**, *10* (22), 4393–4402. https://doi.org/10.1002/cssc.201701385.

(21) Wang, M.; Torbensen, K.; Salvatore, D.; Ren, S.; Joulié, D.; Dumoulin, F.; Mendoza, D.; Lassalle-Kaiser, B.; Işci, U.; Berlinguette, C. P.; Robert, M. CO2 Electrochemical Catalytic Reduction with a Highly Active Cobalt Phthalocyanine. *Nat Commun* **2019**, *10* (1), 3602. https://doi.org/10.1038/s41467-019-11542-w.

(22) Hu, X.-M.; Rønne, M. H.; Pedersen, S. U.; Skrydstrup, T.; Daasbjerg, K. Enhanced Catalytic Activity of Cobalt Porphyrin in CO_2 Electroreduction upon Immobilization on Carbon Materials. *Angew. Chem. Int. Ed.* **2017**, *56* (23), 6468–6472. https://doi.org/10.1002/anie.201701104.

(23) Zhang, X.; Wu, Z.; Zhang, X.; Li, L.; Li, Y.; Xu, H.; Li, X.; Yu, X.; Zhang, Z.; Liang, Y.; Wang, H. Highly Selective and Active CO2 Reduction Electrocatalysts Based on Cobalt Phthalocyanine/Carbon Nanotube Hybrid Structures. *Nat Commun* **2017**, *8* (1), 14675. https://doi.org/10.1038/ncomms14675.

(24) Ren, S.; Joulié, D.; Salvatore, D.; Torbensen, K.; Wang, M.; Robert, M.; Berlinguette, C. P. Molecular Electrocatalysts Can Mediate Fast, Selective CO_2 Reduction in a Flow Cell. *Science* **2019**, *365* (6451), 367–369. https://doi.org/10.1126/science.aax4608.

(25) Yuan, H.; Du, J.; Ming, M.; Chen, Y.; Jiang, L.; Han, Z. Combination of Organic Dye and Iron for CO_2 Reduction with Pentanuclear Fe_2Na_3 Purpurin Photocatalysts. *J. Am. Chem. Soc.* **2022**, *144* (10), 4305–4309. https://doi.org/10.1021/jacs.1c13081.

(26) Derrick, J. S.; Loipersberger, M.; Nistanaki, S. K.; Rothweiler, A. V.; Head-Gordon, M.; Nichols, E. M.; Chang, C. J. Templating Bicarbonate in the Second Coordination Sphere Enhances Electrochemical CO_2 Reduction Catalyzed by Iron Porphyrins. *J. Am. Chem. Soc.* **2022**, *144* (26), 11656–11663. https://doi.org/10.1021/jacs.2c02972.

(27) Azcarate, I.; Costentin, C.; Robert, M.; Savéant, J.-M. Through-Space Charge Interaction Substituent Effects in Molecular Catalysis Leading to the Design of the Most Efficient Catalyst of CO_2-to-CO Electrochemical Conversion. *J. Am. Chem. Soc.* **2016**, *138* (51), 16639–16644. https://doi.org/10.1021/jacs.6b07014.

(28) Smieja, J. M.; Sampson, M. D.; Grice, K. A.; Benson, E. E.; Froehlich, J. D.; Kubiak, C. P. Manganese as a Substitute for Rhenium in CO_2 Reduction Catalysts: The Importance of Acids. *Inorg. Chem.* **2013**, *52* (5), 2484–2491. https://doi.org/10.1021/ic302391u.

(29) Sampson, M. D.; Nguyen, A. D.; Grice, K. A.; Moore, C. E.; Rheingold, A. L.; Kubiak, C. P. Manganese Catalysts with Bulky Bipyridine Ligands for the Electrocatalytic Reduction of Carbon Dioxide: Eliminating Dimerization and Altering Catalysis. *J. Am. Chem. Soc.* **2014**, *136* (14), 5460–5471. https://doi.org/10.1021/ja501252f.

(30) Grice, K. A.; Kubiak, C. P. Recent Studies of Rhenium and Manganese Bipyridine Carbonyl Catalysts for the Electrochemical Reduction of CO2. In *Advances in Inorganic Chemistry*; Elsevier, 2014; Vol. 66, pp 163–188. https://doi.org/10.1016/B978-0-12-420221-4.00005-6.

(31) Manganese, Technetium and Rhenium. In *Chemistry of the Elements*; Elsevier, 1997; pp 1040–1069. https://doi.org/10.1016/B978-0-7506-3365-9.50030-4.

(32) Becker, L. *Chemical elements by market price*. http://www.leonland.de/elements_by_price/en/ (accessed 2023-05-02).

(33) Thompson, D. W.; Ito, A.; Meyer, T. J. [Ru(Bpy)3]2+* and Other Remarkable Metal-to-Ligand Charge Transfer (MLCT) Excited States. *Pure and Applied Chemistry* **2013**, *85* (7), 1257–1305. https://doi.org/10.1351/PAC-CON-13-03-04.

(34) Uoyama, H.; Goushi, K.; Shizu, K.; Nomura, H.; Adachi, C. Highly Efficient Organic Light-Emitting Diodes from Delayed Fluorescence. *Nature* **2012**, *492* (7428), 234–238. https://doi.org/10.1038/nature11687.

(35) Shang, T.-Y.; Lu, L.-H.; Cao, Z.; Liu, Y.; He, W.-M.; Yu, B. Recent Advances of 1,2,3,5-Tetrakis(Carbazol-9-Yl)-4,6-Dicyanobenzene (4CzIPN) in Photocatalytic Transformations. *Chem. Commun.* **2019**, *55* (38), 5408–5419. https://doi.org/10.1039/C9CC01047E.

(36) Bryden, M. A.; Zysman-Colman, E. Organic Thermally Activated Delayed Fluorescence (TADF) Compounds Used in Photocatalysis. *Chem. Soc. Rev.* **2021**, *50* (13), 7587–7680. https://doi.org/10.1039/D1CS00198A.

(37) Yu, Z.-J.; Lou, W.-Y.; Junge, H.; Päpcke, A.; Chen, H.; Xia, L.-M.; Xu, B.; Wang, M.-M.; Wang, X.-J.; Wu, Q.-A.; Lou, B.-Y.; Lochbrunner, S.; Beller, M.; Luo, S.-P. Thermally Activated Delayed Fluorescence (TADF) Dyes as Efficient Organic Photosensitizers for Photocatalytic Water Reduction. *Catalysis Communications* **2019**, *119*, 11–15. https://doi.org/10.1016/j.catcom.2018.09.018.

(38) Ma, F.; Luo, Z.-M.; Wang, J.-W.; Aramburu-Trošelj, B. M.; Ouyang, G. Earth-Abundant-Metal Complexes as Photosensitizers in Molecular Systems for Light-Driven CO2 Reduction. *Coordination Chemistry Reviews* **2024**, *500*, 215529. https://doi.org/10.1016/j.ccr.2023.215529.

(39) Wang, L. Recent Advances in Metal-Based Molecular Photosensitizers for Artificial Photosynthesis. *Catalysts* **2022**, *12* (8), 919. https://doi.org/10.3390/catal12080919.

(40) Du, Y.; Pearson, R. M.; Lim, C.; Sartor, S. M.; Ryan, M. D.; Yang, H.; Damrauer, N. H.; Miyake, G. M. Strongly Reducing, Visible-Light Organic Photoredox Catalysts as Sustainable Alternatives to Precious Metals. *Chemistry A European J* **2017**, *23* (46), 10962–10968. https://doi.org/10.1002/chem.201702926.

(41) Leung, C.-F.; Lau, T.-C. Organic Photosensitizers for Catalytic Solar Fuel Generation. *Energy Fuels* **2021**, *35* (23), 18888–18899. https://doi.org/10.1021/acs.energyfuels.1c02675.

(42) Takeda, H.; Cometto, C.; Ishitani, O.; Robert, M. Electrons, Photons, Protons and Earth-Abundant Metal Complexes for Molecular Catalysis of CO$_2$ Reduction. *ACS Catal.* **2017**, *7* (1), 70–88. https://doi.org/10.1021/acscatal.6b02181.

(43) Bullock, R. M.; Das, A. K.; Appel, A. M. Surface Immobilization of Molecular Electrocatalysts for Energy Conversion. *Chem. Eur. J.* **2017**, *23* (32), 7626–7641. https://doi.org/10.1002/chem.201605066.

(44) Whang, D. R. Immobilization of Molecular Catalysts for Artificial Photosynthesis. *Nano Convergence* **2020**, *7* (1), 37. https://doi.org/10.1186/s40580-020-00248-1.

(45) Kobayashi, T.; Kawate, D.; Niwa, A.; Nagase, T.; Goushi, K.; Adachi, C.; Naito, H. Intersystem Crossing Rate in Thermally Activated Delayed Fluorescence Emitters. *Phys. Status Solidi A* **2020**, *217* (3), 1900616. https://doi.org/10.1002/pssa.201900616.

(46) Cho, E.; Hong, M.; Coropceanu, V.; Brédas, J. The Role of Intermolecular Interactions on the Performance of Organic Thermally Activated Delayed Fluorescence (TADF) Materials. *Advanced Optical Materials* **2021**, *9* (14), 2002135. https://doi.org/10.1002/adom.202002135.

(47) Martinez-Perez, O.; Amiri, M.; Rasu, L.; Bergens, S. H. N-Heterocyclic Carbene Organic Dyes Derived from 2,4,5,6-Tetra(9H-Carbazol-9-Yl)Isophthalonitrile (4CzIPN) Bonded to TiO$_2$ Surfaces. *ECS J. Solid State Sci. Technol.* **2023**, *12* (10), 105006. https://doi.org/10.1149/2162-8777/acfff4.

(48) Liu, J.; Perez, O. M.; Lavergne, D.; Rasu, L.; Murphy, E.; Galvez-Rodriguez, A.; Bergens, S. H. One-Step Electropolymerization of a Dicyanobenzene-Carbazole-Imidazole Dye to Prepare

Photoactive Redox Polymer Films. *Polymers* **2023**, *15* (16), 3340. https://doi.org/10.3390/polym15163340.

(49) Bourrez, M.; Molton, F.; Chardon-Noblat, S.; Deronzier, A. [Mn(Bipyridyl)(CO)3Br]: An Abundant Metal Carbonyl Complex as Efficient Electrocatalyst for CO2 Reduction. *Angew. Chem. Int. Ed.* **2011**, *50* (42), 9903–9906. https://doi.org/10.1002/anie.201103616.

(50) Evans, E. W.; Olivier, Y.; Puttisong, Y.; Myers, W. K.; Hele, T. J. H.; Menke, S. M.; Thomas, T. H.; Credgington, D.; Beljonne, D.; Friend, R. H.; Greenham, N. C. Vibrationally Assisted Intersystem Crossing in Benchmark Thermally Activated Delayed Fluorescence Molecules. *J. Phys. Chem. Lett.* **2018**, *9* (14), 4053–4058. https://doi.org/10.1021/acs.jpclett.8b01556.

(51) Hundemer, F.; Graf Von Reventlow, L.; Leonhardt, C.; Polamo, M.; Nieger, M.; Seifermann, S. M.; Colsmann, A.; Bräse, S. Acceptor Derivatization of the 4CzIPN TADF System: Color Tuning and Introduction of Functional Groups. *ChemistryOpen* **2019**, *8* (12), 1413–1420. https://doi.org/10.1002/open.201900141.

(52) *Reagents & Solvents*. https://www.chem.rochester.edu/notvoodoo/pages/reagents.php?page=solvent_polarity (accessed 2023-12-05).

(53) Mertz, E. L.; Tikhomirov, V. A.; Krishtalik, L. I. Stokes Shift as a Tool for Probing the Solvent Reorganization Energy. *J. Phys. Chem. A* **1997**, *101* (19), 3433–3442. https://doi.org/10.1021/jp963042b.

(54) Lakowicz, J. R. Effects of Solvents on Fluorescence Emission Spectra. In *Principles of Fluorescence Spectroscopy*; Springer US: Boston, MA, 1983; pp 187–215. https://doi.org/10.1007/978-1-4615-7658-7_7.

(55) Ishimatsu, R.; Matsunami, S.; Shizu, K.; Adachi, C.; Nakano, K.; Imato, T. Solvent Effect on Thermally Activated Delayed Fluorescence by 1,2,3,5-Tetrakis(Carbazol-9-Yl)-4,6-Dicyanobenzene. *J. Phys. Chem. A* **2013**, *117* (27), 5607–5612. https://doi.org/10.1021/jp404120s.

(56) Pellegrin, Y.; Odobel, F. Sacrificial Electron Donor Reagents for Solar Fuel Production. *Comptes Rendus Chimie* **2017**, *20* (3), 283–295. https://doi.org/10.1016/j.crci.2015.11.026.

(57) Ishimatsu, R.; Edura, T.; Adachi, C.; Nakano, K.; Imato, T. Photophysical Properties and Efficient, Stable, Electrogenerated Chemiluminescence of Donor–Acceptor Molecules Exhibiting Thermal Spin Upconversion. *Chemistry A European J* **2016**, *22* (14), 4889–4898. https://doi.org/10.1002/chem.201600077.

(58) Lundberg, P.; Tsuchiya, Y.; Lindh, E. M.; Tang, S.; Adachi, C.; Edman, L. Thermally Activated Delayed Fluorescence with 7% External Quantum Efficiency from a Light-Emitting Electrochemical Cell. *Nat Commun* **2019**, *10* (1), 5307. https://doi.org/10.1038/s41467-019-13289-w.

(59) Rønne, M. H.; Madsen, M. R.; Skrydstrup, T.; Pedersen, S. U.; Daasbjerg, K. Mechanistic Elucidation of Dimer Formation and Strategies for Its Suppression in Electrochemical Reduction of *Fac* -Mn(Bpy)(CO) $_3$ Br. *ChemElectroChem* **2021**, *8* (11), 2108–2114. https://doi.org/10.1002/celc.202100279.

(60) Siritanaratkul, B.; Eagle, C.; Cowan, A. J. Manganese Carbonyl Complexes as Selective Electrocatalysts for CO $_2$ Reduction in Water and Organic Solvents. *Acc. Chem. Res.* **2022**, *55* (7), 955–965. https://doi.org/10.1021/acs.accounts.1c00692.

(61) Grills, D. C.; Farrington, J. A.; Layne, B. H.; Lymar, S. V.; Mello, B. A.; Preses, J. M.; Wishart, J. F. Mechanism of the Formation of a Mn-Based CO $_2$ Reduction Catalyst Revealed by Pulse Radiolysis with Time-Resolved Infrared Detection. *J. Am. Chem. Soc.* **2014**, *136* (15), 5563–5566. https://doi.org/10.1021/ja501051s.

(62) Liu, J.; Bergens, S. H. Electronically Conductive, Multifunctional Polymer Binder for Highly Active, Stable, and Abundant Composite Electrodes for Oxygen Evolution. *ACS Appl. Mater. Interfaces* **2023**, *15* (21), 25624–25632. https://doi.org/10.1021/acsami.3c04573.

(63) Tamaki, Y.; Koike, K.; Ishitani, O. Highly Efficient, Selective, and Durable Photocatalytic System for CO $_2$ Reduction to Formic Acid. *Chem. Sci.* **2015**, *6* (12), 7213–7221. https://doi.org/10.1039/C5SC02018B.

Chapter 5

Conclusions and Future Work

The projects presented in this Ph.D. dissertation have been focused on the development of CO_2 reduction photocatalysts and their integration on various semiconductors aided by the functionalization of the material surface. The surface of the semiconductor has been modified such that it allows the modular assembly of the photosensitizer-catalyst via solid-state synthesis. The molecular photosensitizer, originally based on the well-studied Ru polypyridyl complexes, was designed to react with bipyridyl-modified Mn- or Re- carbonyl complexes. Additionally, the 4CzIPN derivatives were developed to replace the noble metal Ru photosensitizers and to attach to the semiconductor surface (as the NHC-3CzIPN compound directly or to form a supramolecular catalyst bonded to Mn catalyst (3CzIPN-Imidazole-Mn).

The catalysts and surfaces were characterized fully via NMR (^{1}H, ^{13}C, ^{19}F), UV-vis, FTIR, photoluminescence (PL), time-resolved photoluminescence (TRPL), CV, SEM, XPS, ICP–MS, and XRD. Moreover, the solid-phase synthesis can be used to prepare high molecular weight photosensitizers with multiple, mixed metal centers in a controlled, stepwise manner, while avoiding difficulties arising from insolubility. The newly developed systems have been studied for the electro- and photochemical activities of the CO_2-to-CO conversion, their potential application for water oxidation, and photophysical properties for a better understanding of the electron transfer processes during CO_2 reduction. The mechanisms for different catalysts towards electrochemical catalytic reactions were investigated, and attempts to correlate the electrocatalytic activity with the structure of the catalyst were made. Lastly, their catalytic activities were compared with recently reported catalytic systems in the literature.

Chapter 2 describes a reproducible method to fabricate photoelectrodes by covalent grafting of 1,10-phenanthroline (phen) at C5 to ITO and TiO_2 surfaces via diazonium electroreduction and subsequent coordination to Ru polypyridyl precursors to form the corresponding SC-Photosensitizers. Surface characterization confirmed

that the photosensitizers SC-Ru-polypyridyl formed in near quantitative yields by these reactions. In collaboration with other research members of our group, it was discovered that the resulting photoanodes were active towards the oxidation of triethylamine in basic conditions and of hydroquinone in neutral conditions. Photocurrent stability was investigated with calculated IPCE. Under neutral conditions, better photocurrent stability was observed using the photoanodes with C5–O covalently bond chromophores compared to those with phosphonic acid anchors. Under strong alkaline conditions, the photoanodes with C5–O covalently-bonded photosensitizers exhibited better IPCE and good photocurrent stability, while the phosphonic acid anchors hydrolyzed. This novel deposition method opens the possibility of fabricating a stable chromophore-SC assembly under strong alkaline conditions, expanding the application of the DSPECs to the alkaline environment. An interesting future direction would be to vary the structure of the ligands within the dimer systematically and investigate the effect on hole transfer between the Ru centres and the overall photoactivity of the bonded photosensitizer. Future research involves detailed photophysical studies to determine the origins of the differences in photoactivity between these systems.

Chapter 3 describes a high-yield route to N-heterocyclic carbene (NHC) derivatives of 2,4,5,6-tetra(9H-carbazol-9-yl)benzene-1,3-dicarbonitrile (4CzIPN) chromophore (NHC-3CzIPN). Additionally, it describes the bonding of an NHC group in the NHC-3CzIPN complex to the surface of TiO_2, which is the first observation for this NHC-semiconductor bonding. Studies of steady-state photoluminescence show that the light absorption properties of the ligand are maintained upon coordination to TiO_2. The preliminary studies demonstrated that the TiO_2-NHC-3CzIPN surface functions as a visible-light-driven photoanode for the oxidation of sacrificial electron donors under neutral and alkaline conditions, showing that this new system has applications in the fundamental study of solar fuel processes. Future work includes the studies of time-resolved photoluminescence spectroscopy (TRPL) to understand the photophysical properties involved in the process of electron transfer as well as the DFT calculations and kinetics of the photooxidation processes. To expand further the application of this TiO_2-NHC bonding, it is suggested the integration of these

photoelectrodes to the Ni_3Fe_1 catalysts, capable of performing water oxidation reaction (OER) under basic conditions.

Chapter 4 describes the synthesis and photocatalytic activity of the derivative of 4CzIPN, 3CzIPN-Imidazole coupled to a Mn (I) [Mn(CO)$_3$(bpy)] catalyst, the complex 3CzIPN-Imidazole-Mn. This complex is highly selective for the photoreduction of CO_2 to CO and achieves 60 TON (CO) under visible light. It was synthesized through a facile, robust, and low-cost preparation method. According to the electrochemistry studies performed on this complex, it was discovered that the redox behaviour of the photosensitizing unit is maintained upon coordination with the Mn center. Also, during the photosynthesis processes, the catalytic and light-absorbing units do not dissociate, indicating good stability and that the complex acts as an electron reservoir for the two-electron reduction of CO_2.

The time-resolved photoluminescence indicates that the excited state survives long enough to promote efficient electron charge transfer from the triplet excited state (T$_1$) in the photosensitizer (3CzIPN-Imidazole) to the catalytic center on Mn. One theory developed here suggested that upon excitation and following catalytic processes, the 3CzIPN-Imidazole-Mn dimerizes. The dimer, unable to coordinate and reduce CO_2, might be stopping the catalytic activity, and the photosensitizing unit does not have enough reducing power to break the dimer. Therefore, future work includes the study of kinetics, isolation of electrochemistry intermediates, and calculations that are required to investigate this theory.

Another approach to overcome and avoid dimerization is to polymerize the photocatalyst (3CzIPN-Imidazole-Mn) on the electrode. The polymerization of 3CzIPN-Imidazole has been proved, suggesting the polymerization of this complex using a similar methodology, as discussed in Chapter 4. Another potential solution for preventing dimerization is to synthesize a Mn(R-bpy)(CO$_3$)Br compound with a bulky bpy ligand such as ^{t}BuBpy or MesBpy, a method previously discussed in the introduction (Section 1.8). Overall, this photocatalyst is a potent candidate for further family expansion and development into electro and photoelectrocatalysis.

In pursuit of expanding on these photocatalytic systems, it is highly attractive to study the integration of the ligand NHC-3CzIPN (studied in Chapter 3), to

Mn(R-bpy)(CO$_3$)Br catalyst derivatives, as demonstrated in a parallel study carried out in our lab, where Re(bpy)(CO$_3$)Cl was successfully coordinated to the NHC ligand. The 3CzIPN-NHC-Mn complex might present a strong trans effect and influence from the NHC ligand that will weaken or prevent any Mn–Mn bond formation in the corresponding dimer, thus promoting an increased rate and prolonged CO$_2$ reduction in the transposition on Mn.

In summary, this thesis describes the development of various photocatalysts, photoelectrodes, and a modular solid-state and in-solution synthesis methodology that can be applied to the fabrication of energy conversion devices, such as dye-sensitized photoelectrochemical cells. Through the implementation of these approaches into the development of artificial photosynthesis devices, it is possible to move one step closer to a renewable and sustainable energy system.

Bibliography

Chapter 1

(1) Statistical Review of World Energy 2022. **2022**.

(2) Brennaman, M. K.; Dillon, R. J.; Alibabaei, L.; Gish, M. K.; Dares, C. J.; Ashford, D. L.; House, R. L.; Meyer, G. J.; Papanikolas, J. M.; Meyer, T. J. Finding the Way to Solar Fuels with Dye-Sensitized Photoelectrosynthesis Cells. *J. Am. Chem. Soc.* **2016**, *138* (40), 13085–13102. https://doi.org/10.1021/jacs.6b06466.

(3) Blankenship, R. E.; Tiede, D. M.; Barber, J.; Brudvig, G. W.; Fleming, G.; Ghirardi, M.; Gunner, M. R.; Junge, W.; Kramer, D. M.; Melis, A.; Moore, T. A.; Moser, C. C.; Nocera, D. G.; Nozik, A. J.; Ort, D. R.; Parson, W. W.; Prince, R. C.; Sayre, R. T. Comparing Photosynthetic and Photovoltaic Efficiencies and Recognizing the Potential for Improvement. *Science* **2011**, *332* (6031), 805–809. https://doi.org/10.1126/science.1200165.

(4) Haegel, N. M.; Verlinden, P.; Victoria, M.; Altermatt, P.; Atwater, H.; Barnes, T.; Breyer, C.; Case, C.; De Wolf, S.; Deline, C.; Dharmrin, M.; Dimmler, B.; Gloeckler, M.; Goldschmidt, J. C.; Hallam, B.; Haussener, S.; Holder, B.; Jaeger, U.; Jaeger-Waldau, A.; Kaizuka, I.; Kikusato, H.; Kroposki, B.; Kurtz, S.; Matsubara, K.; Nowak, S.; Ogimoto, K.; Peter, C.; Peters, I. M.; Philipps, S.; Powalla, M.; Rau, U.; Reindl, T.; Roumpani, M.; Sakurai, K.; Schorn, C.; Schossig, P.; Schlatmann, R.; Sinton, R.; Slaoui, A.; Smith, B. L.; Schneidewind, P.; Stanbery, B.; Topic, M.; Tumas, W.; Vasi, J.; Vetter, M.; Weber, E.; Weeber, A. W.; Weidlich, A.; Weiss, D.; Bett, A. W. Photovoltaics at Multi-Terawatt Scale: Waiting Is Not an Option. *Science* **2023**, *380* (6640), 39–42. https://doi.org/10.1126/science.adf6957.

(5) Geisz, J. F.; France, R. M.; Schulte, K. L.; Steiner, M. A.; Norman, A. G.; Guthrey, H. L.; Young, M. R.; Song, T.; Moriarty, T. Six-Junction III–V Solar Cells with 47.1% Conversion Efficiency under 143 Suns Concentration. *Nat Energy* **2020**, *5* (4), 326–335. https://doi.org/10.1038/s41560-020-0598-5.

(6) *Best Research-Cell Efficiency Chart*. https://www.nrel.gov/pv/cell-efficiency.html (accessed 2023-05-30).

(7) Polman, A.; Knight, M.; Garnett, E. C.; Ehrler, B.; Sinke, W. C. Photovoltaic Materials: Present Efficiencies and Future Challenges. *Science* **2016**, *352* (6283), aad4424. https://doi.org/10.1126/science.aad4424.

(8) O'Regan, B.; Gratzelt, M. A Low-Cost, High-Efficiency Solar Cell Based on Dye-Sensitized Colloidal Ti02 Films. **1991**, *353*.

(9) Mathew, S.; Yella, A.; Gao, P.; Humphry-Baker, R.; Curchod, B. F. E.; Ashari-Astani, N.; Tavernelli, I.; Rothlisberger, U.; Nazeeruddin, Md. K.; Grätzel, M. Dye-Sensitized Solar Cells with 13% Efficiency Achieved through the Molecular Engineering of Porphyrin Sensitizers. *Nature Chem* **2014**, *6* (3), 242–247. https://doi.org/10.1038/nchem.1861.

(10) *Photovoltaics Report - Fraunhofer ISE*. Fraunhofer Institute for Solar Energy Systems ISE. https://www.ise.fraunhofer.de/en/publications/studies/photovoltaics-report.html (accessed 2023-05-31).

(11) Lewis, N. S. Research Opportunities to Advance Solar Energy Utilization. *Science* **2016**, *351* (6271), aad1920. https://doi.org/10.1126/science.aad1920.

(12) Park, N.-G. Perovskite Solar Cells: An Emerging Photovoltaic Technology. *Materials Today* **2015**, *18* (2), 65–72. https://doi.org/10.1016/j.mattod.2014.07.007.

(13) Cui, Y.; Yao, H.; Zhang, J.; Zhang, T.; Wang, Y.; Hong, L.; Xian, K.; Xu, B.; Zhang, S.; Peng, J.; Wei, Z.; Gao, F.; Hou, J. Over 16% Efficiency Organic Photovoltaic Cells Enabled by a Chlorinated Acceptor with Increased Open-Circuit Voltages. *Nat Commun* **2019**, *10* (1), 2515. https://doi.org/10.1038/s41467-019-10351-5.

(14) Meng, L.; Zhang, Y.; Wan, X.; Li, C.; Zhang, X.; Wang, Y.; Ke, X.; Xiao, Z.; Ding, L.; Xia, R.; Yip, H.-L.; Cao, Y.; Chen, Y. Organic and Solution-Processed Tandem Solar Cells with 17.3% Efficiency. *Science* **2018**, *361* (6407), 1094–1098. https://doi.org/10.1126/science.aat2612.

(15) Zhang, G.; Zhao, J.; Chow, P. C. Y.; Jiang, K.; Zhang, J.; Zhu, Z.; Zhang, J.; Huang, F.; Yan, H. Nonfullerene Acceptor Molecules for Bulk Heterojunction Organic Solar Cells. *Chem. Rev.* **2018**, *118* (7), 3447–3507. https://doi.org/10.1021/acs.chemrev.7b00535.

(16) Lu, L.; Zheng, T.; Wu, Q.; Schneider, A. M.; Zhao, D.; Yu, L. Recent Advances in Bulk Heterojunction Polymer Solar Cells. *Chem. Rev.* **2015**, *115* (23), 12666–12731. https://doi.org/10.1021/acs.chemrev.5b00098.

(17) Lee, C.; Lee, S.; Kim, G.-U.; Lee, W.; Kim, B. J. Recent Advances, Design Guidelines, and Prospects of All-Polymer Solar Cells. *Chem. Rev.* **2019**, *119* (13), 8028–8086. https://doi.org/10.1021/acs.chemrev.9b00044.

(18) Chen, L. X. Organic Solar Cells: Recent Progress and Challenges. *ACS Energy Lett.* **2019**, *4* (10), 2537–2539. https://doi.org/10.1021/acsenergylett.9b02071.

(19) Yao, H.; Bai, F.; Hu, H.; Arunagiri, L.; Zhang, J.; Chen, Y.; Yu, H.; Chen, S.; Liu, T.; Lai, J. Y. L.; Zou, Y.; Ade, H.; Yan, H. Efficient All-Polymer Solar Cells Based on a New Polymer Acceptor Achieving 10.3% Power Conversion Efficiency. *ACS Energy Lett.* **2019**, *4* (2), 417–422. https://doi.org/10.1021/acsenergylett.8b02114.

(20) Gibson, T. L.; Kelly, N. A. Solar Photovoltaic Charging of Lithium-Ion Batteries. *Journal of Power Sources* **2010**, *195* (12), 3928–3932. https://doi.org/10.1016/j.jpowsour.2009.12.082.

(21) Tian, Z.; Sun, Z.; Shao, Y.; Gao, L.; Huang, R.; Shao, Y.; Kaner, R. B.; Sun, J. Ultrafast Rechargeable Zn Micro-Batteries Endowing a Wearable Solar Charging System with High Overall Efficiency. *Energy Environ. Sci.* **2021**, *14* (3), 1602–1611. https://doi.org/10.1039/D0EE03623D.

(22) Lv, J.; Abbas, S. C.; Huang, Y.; Liu, Q.; Wu, M.; Wang, Y.; Dai, L. A Photo-Responsive Bifunctional Electrocatalyst for Oxygen Reduction and Evolution Reactions. *Nano Energy* **2018**, *43*, 130–137. https://doi.org/10.1016/j.nanoen.2017.11.020.

(23) *Solar thermal power plants - U.S. Energy Information Administration (EIA)*. https://www.eia.gov/energyexplained/solar/solar-thermal-power-plants.php (accessed 2023-07-10).

(24) *HTST: High-Temperature Solar Thermal*. Solar Power Authority. https://www.solarpowerauthority.com/high-temperature-solar-thermal/ (accessed 2023-06-05).

(25) *Renewable heat consumption, 2007-2024 – Charts – Data & Statistics*. IEA. https://www.iea.org/data-and-statistics/charts/renewable-heat-consumption-2007-2024 (accessed 2023-06-05).

(26) Wang, Q.; Domen, K. Particulate Photocatalysts for Light-Driven Water Splitting: Mechanisms, Challenges, and Design Strategies. *Chem. Rev.* **2020**, *120* (2), 919–985. https://doi.org/10.1021/acs.chemrev.9b00201.

(27) Francke, R.; Schille, B.; Roemelt, M. Homogeneously Catalyzed Electroreduction of Carbon Dioxide—Methods, Mechanisms, and Catalysts. *Chem. Rev.* **2018**, *118* (9), 4631–4701. https://doi.org/10.1021/acs.chemrev.7b00459.

(28) Nishioka, S.; Osterloh, F. E.; Wang, X.; Mallouk, T. E.; Maeda, K. Photocatalytic Water Splitting. *Nat Rev Methods Primers* **2023**, *3* (1), 42. https://doi.org/10.1038/s43586-023-00226-x.

(29) Dalle, K. E.; Warnan, J.; Leung, J. J.; Reuillard, B.; Karmel, I. S.; Reisner, E. Electro- and Solar-Driven Fuel Synthesis with First Row Transition Metal Complexes. *Chem. Rev.* **2019**, *119* (4), 2752–2875. https://doi.org/10.1021/acs.chemrev.8b00392.

(30) Matheu, R.; Ertem, M. Z.; Gimbert-Suriñach, C.; Sala, X.; Llobet, A. Seven Coordinated Molecular Ruthenium–Water Oxidation Catalysts: A Coordination Chemistry Journey: Focus Review. *Chem. Rev.* **2019**, *119* (6), 3453–3471. https://doi.org/10.1021/acs.chemrev.8b00537.

(31) Wang, Y.; Suzuki, H.; Xie, J.; Tomita, O.; Martin, D. J.; Higashi, M.; Kong, D.; Abe, R.; Tang, J. Mimicking Natural Photosynthesis: Solar to Renewable H$_2$ Fuel Synthesis by Z-Scheme Water Splitting Systems. *Chem. Rev.* **2018**, *118* (10), 5201–5241. https://doi.org/10.1021/acs.chemrev.7b00286.

(32) Brereton, K. R.; Bonn, A. G.; Miller, A. J. M. Molecular Photoelectrocatalysts for Light-Driven Hydrogen Production. *ACS Energy Lett.* **2018**, *3* (5), 1128–1136. https://doi.org/10.1021/acsenergylett.8b00255.

(33) Blakemore, J. D.; Crabtree, R. H.; Brudvig, G. W. Molecular Catalysts for Water Oxidation. *Chem. Rev.* **2015**, *115* (23), 12974–13005. https://doi.org/10.1021/acs.chemrev.5b00122.

(34) Kärkäs, M. D.; Verho, O.; Johnston, E. V.; Åkermark, B. Artificial Photosynthesis: Molecular Systems for Catalytic Water Oxidation. *Chem. Rev.* **2014**, *114* (24), 11863–12001. https://doi.org/10.1021/cr400572f.

(35) Sala, X.; Romero, I.; Rodríguez, M.; Escriche, L.; Llobet, A. Molecular Catalysts That Oxidize Water to Dioxygen. *Angewandte Chemie International Edition* **2009**, *48* (16), 2842–2852. https://doi.org/10.1002/anie.200802659.

(36) Gersten, S. W.; Samuels, G. J.; Meyer, T. J. Catalytic Oxidation of Water by an Oxo-Bridged Ruthenium Dimer. *J. Am. Chem. Soc.* **1982**, *104* (14), 4029–4030. https://doi.org/10.1021/ja00378a053.

(37) Kumar, M.; Meena, B.; Subramanyam, P.; Suryakala, D.; Subrahmanyam, C. Recent Trends in Photoelectrochemical Water Splitting: The Role of Cocatalysts. *NPG Asia Mater* **2022**, *14* (1), 88. https://doi.org/10.1038/s41427-022-00436-x.

(38) Marwat, M. A.; Humayun, M.; Afridi, M. W.; Zhang, H.; Abdul Karim, M. R.; Ashtar, M.; Usman, M.; Waqar, S.; Ullah, H.; Wang, C.; Luo, W. Advanced Catalysts for Photoelectrochemical Water Splitting. *ACS Appl. Energy Mater.* **2021**, *4* (11), 12007–12031. https://doi.org/10.1021/acsaem.1c02548.

(39) Kang, D.; Kim, T. W.; Kubota, S. R.; Cardiel, A. C.; Cha, H. G.; Choi, K.-S. Electrochemical Synthesis of Photoelectrodes and Catalysts for Use in Solar Water Splitting. *Chem. Rev.* **2015**, *115* (23), 12839–12887. https://doi.org/10.1021/acs.chemrev.5b00498.

(40) Walter, M. G.; Warren, E. L.; McKone, J. R.; Boettcher, S. W.; Mi, Q.; Santori, E. A.; Lewis, N. S. Solar Water Splitting Cells. *Chem. Rev.* **2010**, *110* (11), 6446–6473. https://doi.org/10.1021/cr1002326.

(41) Concepcion, J. J.; Zhong, D. K.; Szalda, D. J.; Muckerman, J. T.; Fujita, E. Mechanism of Water Oxidation by [Ru(Bda)(L)$_2$]: The Return of the "Blue Dimer." *Chem. Commun.* **2015**, *51* (19), 4105–4108. https://doi.org/10.1039/C4CC07968J.

(42) Yi, J.; Zhan, S.; Chen, L.; Tian, Q.; Wang, N.; Li, J.; Xu, W.; Zhang, B.; Ahlquist, M. S. G. Electrostatic Interactions Accelerating Water Oxidation Catalysis via Intercatalyst O–O Coupling. *J. Am. Chem. Soc.* **2021**, *143* (6), 2484–2490. https://doi.org/10.1021/jacs.0c07103.

(43) Okamura, M.; Kondo, M.; Kuga, R.; Kurashige, Y.; Yanai, T.; Hayami, S.; Praneeth, V. K. K.; Yoshida, M.; Yoneda, K.; Kawata, S.; Masaoka, S. A Pentanuclear Iron Catalyst Designed for Water Oxidation. *Nature* **2016**, *530* (7591), 465–468. https://doi.org/10.1038/nature16529.

(44) Takanabe, K. Photocatalytic Water Splitting: Quantitative Approaches toward Photocatalyst by Design. *ACS Catal.* **2017**, *7* (11), 8006–8022. https://doi.org/10.1021/acscatal.7b02662.

(45) Liu, J.; Liu, Y.; Liu, N.; Han, Y.; Zhang, X.; Huang, H.; Lifshitz, Y.; Lee, S.-T.; Zhong, J.; Kang, Z. Metal-Free Efficient Photocatalyst for Stable Visible Water Splitting via a Two-Electron Pathway. *Science* **2015**, *347* (6225), 970–974. https://doi.org/10.1126/science.aaa3145.

(46) Balzani, V.; Credi, A.; Venturi, M. Photochemical Conversion of Solar Energy. *ChemSusChem* **2008**, *1* (1–2), 26–58. https://doi.org/10.1002/cssc.200700087.

(47) Kumagai, H.; Tamaki, Y.; Ishitani, O. Photocatalytic Systems for CO_2 Reduction: Metal-Complex Photocatalysts and Their Hybrids with Photofunctional Solid Materials. *Acc. Chem. Res.* **2022**, *55* (7), 978–990. https://doi.org/10.1021/acs.accounts.1c00705.

(48) Tamaki, Y.; Ishitani, O. Supramolecular Photocatalysts for the Reduction of CO_2. *ACS Catal.* **2017**, *7* (5), 3394–3409. https://doi.org/10.1021/acscatal.7b00440.

(49) Kuramochi, Y.; Ishitani, O.; Ishida, H. Reaction Mechanisms of Catalytic Photochemical CO2 Reduction Using Re(I) and Ru(II) Complexes. *Coordination Chemistry Reviews* **2018**, *373*, 333–356. https://doi.org/10.1016/j.ccr.2017.11.023.

(50) Yamazaki, Y.; Takeda, H.; Ishitani, O. Photocatalytic Reduction of CO2 Using Metal Complexes. *Journal of Photochemistry and Photobiology C: Photochemistry Reviews* **2015**, *25*, 106–137. https://doi.org/10.1016/j.jphotochemrev.2015.09.001.

(51) Gholamkhass, B.; Mametsuka, H.; Koike, K.; Tanabe, T.; Furue, M.; Ishitani, O. Architecture of Supramolecular Metal Complexes for Photocatalytic CO_2 Reduction: Ruthenium−Rhenium Bi- and Tetranuclear Complexes. *Inorg. Chem.* **2005**, *44* (7), 2326–2336. https://doi.org/10.1021/ic048779r.

(52) Koike, K.; Naito, S.; Sato, S.; Tamaki, Y.; Ishitani, O. Architecture of Supramolecular Metal Complexes for Photocatalytic CO2 Reduction. *Journal of Photochemistry and Photobiology A: Chemistry* **2009**, *207* (1), 109–114. https://doi.org/10.1016/j.jphotochem.2008.12.014.

(53) Fabry, D. C.; Koizumi, H.; Ghosh, D.; Yamazaki, Y.; Takeda, H.; Tamaki, Y.; Ishitani, O. A Ru(II)–Mn(I) Supramolecular Photocatalyst for CO_2 Reduction. *Organometallics* **2020**, *39* (9), 1511–1518. https://doi.org/10.1021/acs.organomet.9b00755.

(54) Roger, I.; Shipman, M. A.; Symes, M. D. Earth-Abundant Catalysts for Electrochemical and Photoelectrochemical Water Splitting. *Nat Rev Chem* **2017**, *1* (1), 0003. https://doi.org/10.1038/s41570-016-0003.

(55) Takeda, H.; Kamiyama, H.; Okamoto, K.; Irimajiri, M.; Mizutani, T.; Koike, K.; Sekine, A.; Ishitani, O. Highly Efficient and Robust Photocatalytic Systems for CO_2 Reduction Consisting of a Cu(I) Photosensitizer and Mn(I) Catalysts. *J. Am. Chem. Soc.* **2018**, *140* (49), 17241–17254. https://doi.org/10.1021/jacs.8b10619.

(56) Fujishima, A.; Honda, K. Electrochemical Photolysis of Water at a Semiconductor Electrode. *Nature* **1972**, *238* (5358), 37–38. https://doi.org/10.1038/238037a0.

(57) Nandal, N.; Jain, S. L. A Review on Progress and Perspective of Molecular Catalysis in Photoelectrochemical Reduction of CO2. *Coordination Chemistry Reviews* **2022**, *451*, 214271. https://doi.org/10.1016/j.ccr.2021.214271.

(58) Tang, B.; Xiao, F.-X. An Overview of Solar-Driven Photoelectrochemical CO_2 Conversion to Chemical Fuels. *ACS Catal.* **2022**, *12* (15), 9023–9057. https://doi.org/10.1021/acscatal.2c01667.

(59) Castro, S.; Albo, J.; Irabien, A. Photoelectrochemical Reactors for CO$_2$ Utilization. *ACS Sustainable Chem. Eng.* **2018**, *6* (12), 15877–15894. https://doi.org/10.1021/acssuschemeng.8b03706.

(60) Sahara, G.; Abe, R.; Higashi, M.; Morikawa, T.; Maeda, K.; Ueda, Y.; Ishitani, O. Photoelectrochemical CO$_2$ Reduction Using a Ru(II)–Re(I) Multinuclear Metal Complex on a p-Type Semiconducting NiO Electrode. *Chem. Commun.* **2015**, *51* (53), 10722–10725. https://doi.org/10.1039/C5CC02403J.

(61) Li, T.-T.; Shan, B.; Meyer, T. J. Stable Molecular Photocathode for Solar-Driven CO$_2$ Reduction in Aqueous Solutions. *ACS Energy Lett.* **2019**, *4* (3), 629–636. https://doi.org/10.1021/acsenergylett.8b02512.

(62) Chen, Z.; Chen, C.; Weinberg, D. R.; Kang, P.; Concepcion, J. J.; Harrison, D. P.; Brookhart, M. S.; Meyer, T. J. Electrocatalytic Reduction of CO2 to CO by Polypyridyl Ruthenium Complexes. *Chem. Commun.* **2011**, *47* (47), 12607. https://doi.org/10.1039/c1cc15071e.

(63) Kuramochi, Y.; Ishitani, O. Iridium(III) 1-Phenylisoquinoline Complexes as a Photosensitizer for Photocatalytic CO$_2$ Reduction: A Mixed System with a Re(I) Catalyst and a Supramolecular Photocatalyst. *Inorg. Chem.* **2016**, *55* (11), 5702–5709. https://doi.org/10.1021/acs.inorgchem.6b00777.

(64) Kuramochi, Y.; Kamiya, M.; Ishida, H. Photocatalytic CO$_2$ Reduction in N , N - Dimethylacetamide/Water as an Alternative Solvent System. *Inorg. Chem.* **2014**, *53* (7), 3326–3332. https://doi.org/10.1021/ic500050q.

(65) Tamaki, Y.; Morimoto, T.; Koike, K.; Ishitani, O. Photocatalytic CO$_2$ Reduction with High Turnover Frequency and Selectivity of Formic Acid Formation Using Ru(II) Multinuclear Complexes. *Proc. Natl. Acad. Sci. U.S.A.* **2012**, *109* (39), 15673–15678. https://doi.org/10.1073/pnas.1118336109.

(66) Ashford, D. L.; Song, W.; Concepcion, J. J.; Glasson, C. R. K.; Brennaman, M. K.; Norris, M. R.; Fang, Z.; Templeton, J. L.; Meyer, T. J. Photoinduced Electron Transfer in a Chromophore–Catalyst Assembly Anchored to TiO$_2$. *J. Am. Chem. Soc.* **2012**, *134* (46), 19189–19198. https://doi.org/10.1021/ja3084362.

(67) Yoshitomi, F.; Sekizawa, K.; Maeda, K.; Ishitani, O. Selective Formic Acid Production via CO$_2$ Reduction with Visible Light Using a Hybrid of a Perovskite Tantalum Oxynitride and a Binuclear Ruthenium(II) Complex. *ACS Appl. Mater. Interfaces* **2015**, *7* (23), 13092–13097. https://doi.org/10.1021/acsami.5b03509.

(68) Juris, A.; Balzani, V.; Barigelletti, F.; Campagna, S.; Belser, P.; Zelewsky, A. V. COMPLEXES: PHOTOPI3YSICS, ELECl?ROCHEMISTRY, SCENCE.

(69) Lemercier, G.; Bonne, A.; Four, M.; Lawson-Daku, L. M. 3MLCT Excited States in Ru(II) Complexes: Reactivity and Related Two-Photon Absorption Applications in the near-Infrared

Spectral Range. *Comptes Rendus Chimie* **2008**, *11* (6–7), 709–715. https://doi.org/10.1016/j.crci.2007.11.012.

(70) Thompson, D. W.; Ito, A.; Meyer, T. J. [Ru(Bpy)3]2+* and Other Remarkable Metal-to-Ligand Charge Transfer (MLCT) Excited States. *Pure and Applied Chemistry* **2013**, *85* (7), 1257–1305. https://doi.org/10.1351/PAC-CON-13-03-04.

(71) Lumpkin, R. S.; Kober, E. M.; Worl, L. A.; Murtaza, Zakir.; Meyer, T. J. Metal-to-Ligand Charge-Transfer (MLCT) Photochemistry: Experimental Evidence for the Participation of a Higher Lying MLCT State in Polypyridyl Complexes of Ruthenium(II) and Osmium(II). *J. Phys. Chem.* **1990**, *94* (1), 239–243. https://doi.org/10.1021/j100364a039.

(72) Leung, C.-F.; Lau, T.-C. Organic Photosensitizers for Catalytic Solar Fuel Generation. *Energy Fuels* **2021**, *35* (23), 18888–18899. https://doi.org/10.1021/acs.energyfuels.1c02675.

(73) Du, Y.; Pearson, R. M.; Lim, C.; Sartor, S. M.; Ryan, M. D.; Yang, H.; Damrauer, N. H.; Miyake, G. M. Strongly Reducing, Visible-Light Organic Photoredox Catalysts as Sustainable Alternatives to Precious Metals. *Chemistry A European J* **2017**, *23* (46), 10962–10968. https://doi.org/10.1002/chem.201702926.

(74) Rybicka-Jasińska, K.; Shan, W.; Zawada, K.; Kadish, K. M.; Gryko, D. Porphyrins as Photoredox Catalysts: Experimental and Theoretical Studies. *J. Am. Chem. Soc.* **2016**, *138* (47), 15451–15458. https://doi.org/10.1021/jacs.6b09036.

(75) Shang, T.-Y.; Lu, L.-H.; Cao, Z.; Liu, Y.; He, W.-M.; Yu, B. Recent Advances of 1,2,3,5-Tetrakis(Carbazol-9-Yl)-4,6-Dicyanobenzene (4CzIPN) in Photocatalytic Transformations. *Chem. Commun.* **2019**, *55* (38), 5408–5419. https://doi.org/10.1039/C9CC01047E.

(76) Poelma, S. O.; Burnett, G. L.; Discekici, E. H.; Mattson, K. M.; Treat, N. J.; Luo, Y.; Hudson, Z. M.; Shankel, S. L.; Clark, P. G.; Kramer, J. W.; Hawker, C. J.; Read De Alaniz, J. Chemoselective Radical Dehalogenation and C–C Bond Formation on Aryl Halide Substrates Using Organic Photoredox Catalysts. *J. Org. Chem.* **2016**, *81* (16), 7155–7160. https://doi.org/10.1021/acs.joc.6b01034.

(77) Luo, J.; Zhang, J. Donor–Acceptor Fluorophores for Visible-Light-Promoted Organic Synthesis: Photoredox/Ni Dual Catalytic C(Sp^3)–C(Sp^2) Cross-Coupling. *ACS Catal.* **2016**, *6* (2), 873–877. https://doi.org/10.1021/acscatal.5b02204.

(78) Uoyama, H.; Goushi, K.; Shizu, K.; Nomura, H.; Adachi, C. Highly Efficient Organic Light-Emitting Diodes from Delayed Fluorescence. *Nature* **2012**, *492* (7428), 234–238. https://doi.org/10.1038/nature11687.

(79) Speckmeier, E.; Fischer, T. G.; Zeitler, K. A Toolbox Approach To Construct Broadly Applicable Metal-Free Catalysts for Photoredox Chemistry: Deliberate Tuning of Redox Potentials and Importance of Halogens in Donor–Acceptor Cyanoarenes. *J. Am. Chem. Soc.* **2018**, *140* (45), 15353–15365. https://doi.org/10.1021/jacs.8b08933.

(80) Karakaya, I.; Primer, D. N.; Molander, G. A. Photoredox Cross-Coupling: Ir/Ni Dual Catalysis for the Synthesis of Benzylic Ethers. *Org. Lett.* **2015**, *17* (13), 3294–3297. https://doi.org/10.1021/acs.orglett.5b01463.

(81) Meng, Q.-Y.; Wang, S.; Huff, G. S.; König, B. Ligand-Controlled Regioselective Hydrocarboxylation of Styrenes with CO_2 by Combining Visible Light and Nickel Catalysis. *J. Am. Chem. Soc.* **2018**, *140* (9), 3198–3201. https://doi.org/10.1021/jacs.7b13448.

(82) Choi, J.; Martín-Gago, P.; Fu, G. C. Stereoconvergent Arylations and Alkenylations of Unactivated Alkyl Electrophiles: Catalytic Enantioselective Synthesis of Secondary Sulfonamides and Sulfones. *J. Am. Chem. Soc.* **2014**, *136* (34), 12161–12165. https://doi.org/10.1021/ja506885s.

(83) Seo, H.; Liu, A.; Jamison, T. F. Direct β-Selective Hydrocarboxylation of Styrenes with CO_2 Enabled by Continuous Flow Photoredox Catalysis. *J. Am. Chem. Soc.* **2017**, *139* (40), 13969–13972. https://doi.org/10.1021/jacs.7b05942.

(84) Wang, Y.; Gao, X.-W.; Li, J.; Chao, D. Merging an Organic TADF Photosensitizer and a Simple Terpyridine–Fe(III) Complex for Photocatalytic CO_2 Reduction. *Chem. Commun.* **2020**, *56* (81), 12170–12173. https://doi.org/10.1039/D0CC05047D.

(85) Ponnada, S.; Kiai, M. S.; Gorle, D. B.; Nowduri, A.; Sharma, R. K. Insight into the Role and Strategies of Metal–Organic Frameworks in Direct Methanol Fuel Cells: A Review. *Energy Fuels* **2021**, *35* (19), 15265–15284. https://doi.org/10.1021/acs.energyfuels.1c02010.

(86) Grice, K. A.; Kubiak, C. P. Recent Studies of Rhenium and Manganese Bipyridine Carbonyl Catalysts for the Electrochemical Reduction of CO2. In *Advances in Inorganic Chemistry*; Elsevier, 2014; Vol. 66, pp 163–188. https://doi.org/10.1016/B978-0-12-420221-4.00005-6.

(87) Moura De Salles Pupo, M.; Kortlever, R. Electrolyte Effects on the Electrochemical Reduction of CO_2. *ChemPhysChem* **2019**, *20* (22), 2926–2935. https://doi.org/10.1002/cphc.201900680.

(88) Lucile, F.; Cézac, P.; Contamine, F.; Serin, J.-P.; Houssin, D.; Arpentinier, P. Solubility of Carbon Dioxide in Water and Aqueous Solution Containing Sodium Hydroxide at Temperatures from (293.15 to 393.15) K and Pressure up to 5 MPa: Experimental Measurements. *J. Chem. Eng. Data* **2012**, *57* (3), 784–789. https://doi.org/10.1021/je200991x.

(89) König, M.; Vaes, J.; Klemm, E.; Pant, D. Solvents and Supporting Electrolytes in the Electrocatalytic Reduction of CO2. *iScience* **2019**, *19*, 135–160. https://doi.org/10.1016/j.isci.2019.07.014.

(90) Costentin, C.; Drouet, S.; Passard, G.; Robert, M.; Savéant, J.-M. Proton-Coupled Electron Transfer Cleavage of Heavy-Atom Bonds in Electrocatalytic Processes. Cleavage of a C–O Bond in the Catalyzed Electrochemical Reduction of CO_2. *J. Am. Chem. Soc.* **2013**, *135* (24), 9023–9031. https://doi.org/10.1021/ja4030148.

(91) Costentin, C.; Savéant, J. Multielectron, Multistep Molecular Catalysis of Electrochemical Reactions: Benchmarking of Homogeneous Catalysts. *ChemElectroChem* **2014**, *1* (7), 1226–1236. https://doi.org/10.1002/celc.201300263.

(92) Mukherjee, J.; Siewert, I. Manganese and Rhenium Tricarbonyl Complexes Equipped with Proton Relays in the Electrochemical CO_2 Reduction Reaction. *Eur. J. Inorg. Chem.* **2020**, *2020* (46), 4319–4333. https://doi.org/10.1002/ejic.202000738.

(93) Hawecker, J.; Lehn, J.-M.; Ziessel, R. Electrocatalytic Reduction of Carbon Dioxide Mediated by Re(Bipy)(CO)&I (Bipy = 2,2'-Bipyridine).

(94) Guyot, M.; Lalloz, M.-N.; Aguirre-Araque, J. S.; Rogez, G.; Costentin, C.; Chardon-Noblat, S. Rhenium Carbonyl Molecular Catalysts for CO_2 Electroreduction: Effects on Catalysis of Bipyridine Substituents Mimicking Anchorage Functions to Modify Electrodes. *Inorg. Chem.* **2022**, *61* (40), 16072–16080. https://doi.org/10.1021/acs.inorgchem.2c02473.

(95) Clark, M. L.; Cheung, P. L.; Lessio, M.; Carter, E. A.; Kubiak, C. P. Kinetic and Mechanistic Effects of Bipyridine (Bpy) Substituent, Labile Ligand, and Brønsted Acid on Electrocatalytic CO_2 Reduction by Re(Bpy) Complexes. *ACS Catal.* **2018**, *8* (3), 2021–2029. https://doi.org/10.1021/acscatal.7b03971.

(96) Talukdar, K.; Sinha Roy, S.; Amatya, E.; Sleeper, E. A.; Le Magueres, P.; Jurss, J. W. Enhanced Electrochemical CO_2 Reduction by a Series of Molecular Rhenium Catalysts Decorated with Second-Sphere Hydrogen-Bond Donors. *Inorg. Chem.* **2020**, *59* (9), 6087–6099. https://doi.org/10.1021/acs.inorgchem.0c00154.

(97) Riplinger, C.; Sampson, M. D.; Ritzmann, A. M.; Kubiak, C. P.; Carter, E. A. Mechanistic Contrasts between Manganese and Rhenium Bipyridine Electrocatalysts for the Reduction of Carbon Dioxide. *J. Am. Chem. Soc.* **2014**, *136* (46), 16285–16298. https://doi.org/10.1021/ja508192y.

(98) Vakula, N. I.; Kuramshina, G. M.; Makhmutova, S. F.; Pentin, Yu. A. DFT Theoretical Studies of Anions of Aniline and Its Several Derivatives. *Struct Chem* **2011**, *22* (2), 345–356. https://doi.org/10.1007/s11224-010-9724-5.

(99) Portenkirchner, E.; Oppelt, K.; Ulbricht, C.; Egbe, D. A. M.; Neugebauer, H.; Knör, G.; Sariciftci, N. S. Electrocatalytic and Photocatalytic Reduction of Carbon Dioxide to Carbon Monoxide Using the Alkynyl-Substituted Rhenium(I) Complex (5,5′-Bisphenylethynyl-2,2′-Bipyridyl)Re(CO)3Cl. *Journal of Organometallic Chemistry* **2012**, *716*, 19–25. https://doi.org/10.1016/j.jorganchem.2012.05.021.

(100) Portenkirchner, E.; Gasiorowski, J.; Oppelt, K.; Schlager, S.; Schwarzinger, C.; Neugebauer, H.; Knör, G.; Sariciftci, N. S. Electrocatalytic Reduction of Carbon Dioxide to Carbon Monoxide by a Polymerized Film of an Alkynyl-Substituted Rhenium(I) Complex. *ChemCatChem* **2013**, *5* (7), 1790–1796. https://doi.org/10.1002/cctc.201200904.

(101) Liang, Y.; Nguyen, M. T.; Holliday, B. J.; Jones, R. A. Electrocatalytic Reduction of CO2 Using Rhenium Complexes with Dipyrido[3,2-a:2′,3′-c]Phenazine Ligands. *Inorganic Chemistry Communications* **2017**, *84*, 113–117. https://doi.org/10.1016/j.inoche.2017.08.002.

(102) Takeda, H.; Cometto, C.; Ishitani, O.; Robert, M. Electrons, Photons, Protons and Earth-Abundant Metal Complexes for Molecular Catalysis of CO_2 Reduction. *ACS Catal.* **2017**, *7* (1), 70–88. https://doi.org/10.1021/acscatal.6b02181.

(103) Bizzarri, C. Homogeneous Systems Containing Earth-Abundant Metal Complexes for Photoactivated CO_2 Reduction: Recent Advances. *European J Organic Chem* **2022**, *2022* (24). https://doi.org/10.1002/ejoc.202200185.

(104) Bourrez, M.; Molton, F.; Chardon-Noblat, S.; Deronzier, A. [Mn(Bipyridyl)(CO)3Br]: An Abundant Metal Carbonyl Complex as Efficient Electrocatalyst for CO2 Reduction. *Angew. Chem. Int. Ed.* **2011**, *50* (42), 9903–9906. https://doi.org/10.1002/anie.201103616.

(105) Smieja, J. M.; Sampson, M. D.; Grice, K. A.; Benson, E. E.; Froehlich, J. D.; Kubiak, C. P. Manganese as a Substitute for Rhenium in CO_2 Reduction Catalysts: The Importance of Acids. *Inorg. Chem.* **2013**, *52* (5), 2484–2491. https://doi.org/10.1021/ic302391u.

(106) Agarwal, J.; Shaw, T. W.; Schaefer, H. F.; Bocarsly, A. B. Design of a Catalytic Active Site for Electrochemical CO_2 Reduction with Mn(I)-Tricarbonyl Species. *Inorg. Chem.* **2015**, *54* (11), 5285–5294. https://doi.org/10.1021/acs.inorgchem.5b00233.

(107) Sampson, M. D.; Nguyen, A. D.; Grice, K. A.; Moore, C. E.; Rheingold, A. L.; Kubiak, C. P. Manganese Catalysts with Bulky Bipyridine Ligands for the Electrocatalytic Reduction of Carbon Dioxide: Eliminating Dimerization and Altering Catalysis. *J. Am. Chem. Soc.* **2014**, *136* (14), 5460–5471. https://doi.org/10.1021/ja501252f.

(108) Sampson, M. D.; Kubiak, C. P. Manganese Electrocatalysts with Bulky Bipyridine Ligands: Utilizing Lewis Acids To Promote Carbon Dioxide Reduction at Low Overpotentials. *J. Am. Chem. Soc.* **2016**, *138* (4), 1386–1393. https://doi.org/10.1021/jacs.5b12215.

(109) Rønne, M. H.; Cho, D.; Madsen, M. R.; Jakobsen, J. B.; Eom, S.; Escoudé, É.; Hammershøj, H. C. D.; Nielsen, D. U.; Pedersen, S. U.; Baik, M.-H.; Skrydstrup, T.; Daasbjerg, K. Ligand-Controlled Product Selectivity in Electrochemical Carbon Dioxide Reduction Using Manganese Bipyridine Catalysts. *J. Am. Chem. Soc.* **2020**, *142* (9), 4265–4275. https://doi.org/10.1021/jacs.9b11806.

(110) Grills, D. C.; Ertem, M. Z.; McKinnon, M.; Ngo, K. T.; Rochford, J. Mechanistic Aspects of CO2 Reduction Catalysis with Manganese-Based Molecular Catalysts. *Coordination Chemistry Reviews* **2018**, *374*, 173–217. https://doi.org/10.1016/j.ccr.2018.05.022.

(111) Agarwal, J.; Fujita, E.; Schaefer, H. F.; Muckerman, J. T. Mechanisms for CO Production from CO_2 Using Reduced Rhenium Tricarbonyl Catalysts. *J. Am. Chem. Soc.* **2012**, *134* (11), 5180–5186. https://doi.org/10.1021/ja2105834.

(112) Agarwal, J.; Johnson, R. P.; Li, G. Reduction of CO_2 on a Tricarbonyl Rhenium(I) Complex: Modeling a Catalytic Cycle. *J. Phys. Chem. A* **2011**, *115* (13), 2877–2881. https://doi.org/10.1021/jp111342r.

(113) Grills, D. C.; Farrington, J. A.; Layne, B. H.; Lymar, S. V.; Mello, B. A.; Preses, J. M.; Wishart, J. F. Mechanism of the Formation of a Mn-Based CO_2 Reduction Catalyst Revealed by Pulse Radiolysis with Time-Resolved Infrared Detection. *J. Am. Chem. Soc.* **2014**, *136* (15), 5563–5566. https://doi.org/10.1021/ja501051s.

(114) Zhou, X.; Micheroni, D.; Lin, Z.; Poon, C.; Li, Z.; Lin, W. Graphene-Immobilized *Fac* - Re(Bipy)(CO)₃ Cl for Syngas Generation from Carbon Dioxide. *ACS Appl. Mater. Interfaces* **2016**, *8* (6), 4192–4198. https://doi.org/10.1021/acsami.5b11958.

(115) Bullock, R. M.; Das, A. K.; Appel, A. M. Surface Immobilization of Molecular Electrocatalysts for Energy Conversion. *Chem. Eur. J.* **2017**, *23* (32), 7626–7641. https://doi.org/10.1002/chem.201605066.

(116) Orchanian, N. M.; Hong, L. E.; Skrainka, J. A.; Esterhuizen, J. A.; Popov, D. A.; Marinescu, S. C. Surface-Immobilized Conjugated Polymers Incorporating Rhenium Bipyridine Motifs for Electrocatalytic and Photocatalytic CO_2 Reduction. *ACS Appl. Energy Mater.* **2019**, *2* (1), 110–123. https://doi.org/10.1021/acsaem.8b01745.

(117) Oh, S.; Gallagher, J. R.; Miller, J. T.; Surendranath, Y. Graphite-Conjugated Rhenium Catalysts for Carbon Dioxide Reduction. *J. Am. Chem. Soc.* **2016**, *138* (6), 1820–1823. https://doi.org/10.1021/jacs.5b13080.

(118) Walsh, J. J.; Neri, G.; Smith, C. L.; Cowan, A. J. Electrocatalytic CO_2 Reduction with a Membrane Supported Manganese Catalyst in Aqueous Solution. *Chem. Commun.* **2014**, *50* (84), 12698–12701. https://doi.org/10.1039/C4CC06404F.

(119) Reuillard, B.; Ly, K. H.; Rosser, T. E.; Kuehnel, M. F.; Zebger, I.; Reisner, E. Tuning Product Selectivity for Aqueous CO_2 Reduction with a Mn(Bipyridine)-Pyrene Catalyst Immobilized on a Carbon Nanotube Electrode. *J. Am. Chem. Soc.* **2017**, *139* (41), 14425–14435. https://doi.org/10.1021/jacs.7b06269.

(120)   Atoguchi, T.; Aramata, A.; Kazusaka, A.; Enyo, M. Electrocatalytic Activity of Co II TPP-Pyridine Complex Modified Carbon Electrode for CO2 Reduction. *1991 318*, 309–320.

Chapter 2

(1) Tilley, S. D. Recent Advances and Emerging Trends in Photo-Electrochemical Solar Energy Conversion. *Advanced Energy Materials* **2019**, *9* (2), 1802877. https://doi.org/10.1002/aenm.201802877.

(2) Chu, S.; Cui, Y.; Liu, N. The Path towards Sustainable Energy. *Nature Mater* **2017**, *16* (1), 16–22. https://doi.org/10.1038/nmat4834.

(3) Lewis, N. S. Research Opportunities to Advance Solar Energy Utilization. *Science* **2016**, *351* (6271), aad1920. https://doi.org/10.1126/science.aad1920.

(4) Zhu, X.-G.; Long, S. P.; Ort, D. R. What Is the Maximum Efficiency with Which Photosynthesis Can Convert Solar Energy into Biomass? *Current Opinion in Biotechnology* **2008**, *19* (2), 153–159. https://doi.org/10.1016/j.copbio.2008.02.004.

(5)   Zhang, B.; Sun, L. Artificial Photosynthesis: Opportunities and Challenges of Molecular Catalysts. *Chem. Soc. Rev.* **2019**, *48* (7), 2216–2264. https://doi.org/10.1039/C8CS00897C.

(6)   Niu, F.; Wang, D.; Li, F.; Liu, Y.; Shen, S.; Meyer, T. J. Hybrid Photoelectrochemical Water Splitting Systems: From Interface Design to System Assembly. *Advanced Energy Materials* **2020**, *10* (11), 1900399. https://doi.org/10.1002/aenm.201900399.

(7)   Yan, Z.; Hitt, J. L.; Turner, J. A.; Mallouk, T. E. Renewable Electricity Storage Using Electrolysis. *Proc. Natl. Acad. Sci. U.S.A.* **2020**, *117* (23), 12558–12563. https://doi.org/10.1073/pnas.1821686116.

(8)   Lewis, N. S. A Prospective on Energy and Environmental Science. *Energy Environ. Sci.* **2019**, *12* (1), 16–18. https://doi.org/10.1039/C8EE90070A.

(9)   Concepcion, J. J.; House, R. L.; Papanikolas, J. M.; Meyer, T. J. Chemical Approaches to Artificial Photosynthesis. *Proc. Natl. Acad. Sci. U.S.A.* **2012**, *109* (39), 15560–15564. https://doi.org/10.1073/pnas.1212254109.

(10) Davis, S. J.; Caldeira, K.; Matthews, H. D. Future CO_2 Emissions and Climate Change from Existing Energy Infrastructure. *Science* **2010**, *329* (5997), 1330–1333. https://doi.org/10.1126/science.1188566.

(11) Zhang, J. Z.; Reisner, E. Advancing Photosystem II Photoelectrochemistry for Semi-Artificial Photosynthesis. *Nat Rev Chem* **2019**, *4* (1), 6–21. https://doi.org/10.1038/s41570-019-0149-4.

(12) Low, J.; Jiang, C.; Cheng, B.; Wageh, S.; Al-Ghamdi, A. A.; Yu, J. A Review of Direct Z-Scheme Photocatalysts. *Small Methods* **2017**, *1* (5), 1700080. https://doi.org/10.1002/smtd.201700080.

(13) Fujishima, A.; Honda, K. Electrochemical Photolysis of Water at a Semiconductor Electrode. *Nature* **1972**, *238* (5358), 37–38. https://doi.org/10.1038/238037a0.

(14) Chen, S.; Hossain, M. N.; Chen, A. Significant Enhancement of the Photoelectrochemical Activity of $CuWO_4$ by Using a Cobalt Phosphate Nanoscale Thin Film. *ChemElectroChem* **2018**, *5* (3), 523–530. https://doi.org/10.1002/celc.201700991.

(15) Wang, Z.; Inoue, Y.; Hisatomi, T.; Ishikawa, R.; Wang, Q.; Takata, T.; Chen, S.; Shibata, N.; Ikuhara, Y.; Domen, K. Overall Water Splitting by Ta3N5 Nanorod Single Crystals Grown on the Edges of KTaO3 Particles. *Nat Catal* **2018**, *1* (10), 756–763. https://doi.org/10.1038/s41929-018-0134-1.

(16) Agbe, H.; Nyankson, E.; Raza, N.; Dodoo-Arhin, D.; Chauhan, A.; Osei, G.; Kumar, V.; Kim, K.-H. Recent Advances in Photoinduced Catalysis for Water Splitting and Environmental Applications. *Journal of Industrial and Engineering Chemistry* **2019**, *72*, 31–49. https://doi.org/10.1016/j.jiec.2019.01.004.

(17) Wu, L.; Eberhart, M.; Shan, B.; Nayak, A.; Brennaman, M. K.; Miller, A. J. M.; Shao, J.; Meyer, T. J. Stable Molecular Surface Modification of Nanostructured, Mesoporous Metal Oxide Photoanodes by Silane and Click Chemistry. *ACS Appl. Mater. Interfaces* **2019**, *11* (4), 4560–4567. https://doi.org/10.1021/acsami.8b17824.

(18) Xu, P.; McCool, N. S.; Mallouk, T. E. Water Splitting Dye-Sensitized Solar Cells. *Nano Today* **2017**, *14*, 42–58. https://doi.org/10.1016/j.nantod.2017.04.009.

(19) Brennaman, M. K.; Dillon, R. J.; Alibabaei, L.; Gish, M. K.; Dares, C. J.; Ashford, D. L.; House, R. L.; Meyer, G. J.; Papanikolas, J. M.; Meyer, T. J. Finding the Way to Solar Fuels with Dye-Sensitized Photoelectrosynthesis Cells. *J. Am. Chem. Soc.* **2016**, *138* (40), 13085–13102. https://doi.org/10.1021/jacs.6b06466.

(20) Orbelli Biroli, A.; Tessore, F.; Di Carlo, G.; Pizzotti, M.; Benazzi, E.; Gentile, F.; Berardi, S.; Bignozzi, C. A.; Argazzi, R.; Natali, M.; Sartorel, A.; Caramori, S. Fluorinated Zn ^{II} Porphyrins for Dye-Sensitized Aqueous Photoelectrosynthetic Cells. *ACS Appl. Mater. Interfaces* **2019**, *11* (36), 32895–32908. https://doi.org/10.1021/acsami.9b08042.

(21) Shaw, G. B.; Styers-Barnett, D. J.; Gannon, E. Z.; Granger, J. C.; Papanikolas, J. M. Interligand Electron Transfer Dynamics in [Os(Bpy) $_3$] $^{2+}$: Exploring the Excited State Potential Surfaces with Femtosecond Spectroscopy. *J. Phys. Chem. A* **2004**, *108* (23), 4998–5006. https://doi.org/10.1021/jp0363850.

(22) Lanoë, P.-H.; Chan, J.; Groué, A.; Gontard, G.; Jutand, A.; Rager, M.-N.; Armaroli, N.; Monti, F.; Barbieri, A.; Amouri, H. Cyclometalated N-Heterocyclic Carbene Iridium($_{III}$) Complexes with Naphthalimide Chromophores: A Novel Class of Phosphorescent Heteroleptic Compounds. *Dalton Trans.* **2018**, *47* (10), 3440–3451. https://doi.org/10.1039/C7DT04369D.

(23) Shan, B.; Nayak, A.; Brennaman, M. K.; Liu, M.; Marquard, S. L.; Eberhart, M. S.; Meyer, T. J. Controlling Vertical and Lateral Electron Migration Using a Bifunctional Chromophore Assembly in Dye-Sensitized Photoelectrosynthesis Cells. *J. Am. Chem. Soc.* **2018**, *140* (20), 6493–6500. https://doi.org/10.1021/jacs.8b03453.

(24) Zigler, D. F.; Morseth, Z. A.; Wang, L.; Ashford, D. L.; Brennaman, M. K.; Grumstrup, E. M.; Brigham, E. C.; Gish, M. K.; Dillon, R. J.; Alibabaei, L.; Meyer, G. J.; Meyer, T. J.; Papanikolas, J. M. Disentangling the Physical Processes Responsible for the Kinetic Complexity in Interfacial Electron Transfer of Excited Ru(II) Polypyridyl Dyes on TiO $_2$. *J. Am. Chem. Soc.* **2016**, *138* (13), 4426–4438. https://doi.org/10.1021/jacs.5b12996.

(25) Amthor, S.; Braun, H.; Gröne, J.; Nauroozi, D.; Jacob, T.; Rau, S. Tailored Protective Groups for Surface Immobilization of Ruthenium Dyes. *Dalton Trans.* **2020**, *49* (12), 3735–3742. https://doi.org/10.1039/C9DT03591E.

(26) Troian-Gautier, L.; Marcélis, L.; De Winter, J.; Gerbaux, P.; Moucheron, C. Two Ruthenium Complexes Capable of Storing Multiple Electrons on a Single Ligand – Photophysical, Photochemical and Electrochemical Properties of [Ru(Phen) $_2$ (TAPHAT)] $^{2+}$ and [Ru(Phen) $_2$ (TAPHAT)Ru(Phen) $_2$] $^{4+}$. *Dalton Trans.* **2017**, *46* (44), 15287–15300. https://doi.org/10.1039/C7DT03232C.

(27) Bangle, R.; Sampaio, R. N.; Troian-Gautier, L.; Meyer, G. J. Surface Grafting of Ru(II) Diazonium-Based Sensitizers on Metal Oxides Enhances Alkaline Stability for Solar Energy Conversion. *ACS Appl. Mater. Interfaces* **2018**, *10* (3), 3121–3132. https://doi.org/10.1021/acsami.7b16641.

(28) Evans, R. C.; Douglas, P.; Winscom, C. J. Coordination Complexes Exhibiting Room-Temperature Phosphorescence: Evaluation of Their Suitability as Triplet Emitters in Organic Light Emitting Diodes. *Coordination Chemistry Reviews* **2006**, *250* (15–16), 2093–2126. https://doi.org/10.1016/j.ccr.2006.02.007.

(29) Yuan, Y.-J.; Yu, Z.-T.; Chen, D.-Q.; Zou, Z.-G. Metal-Complex Chromophores for Solar Hydrogen Generation. *Chem. Soc. Rev.* **2017**, *46* (3), 603–631. https://doi.org/10.1039/C6CS00436A.

(30) Purnama, I.; Salmahaminati, S.; Abe, M.; Hada, M.; Kubo, Y.; Mulyana, J. Y. Factors Influencing the Photoelectrochemical Device Performance Sensitized by Ruthenium Polypyridyl Dyes. *Dalton Trans.* **2019**, *48* (2), 688–695. https://doi.org/10.1039/C8DT03502D.

(31) Raber, M. M.; Brady, M. D.; Troian-Gautier, L.; Dickenson, J. C.; Marquard, S. L.; Hyde, J. T.; Lopez, S. J.; Meyer, G. J.; Meyer, T. J.; Harrison, D. P. Fundamental Factors Impacting the Stability of Phosphonate-Derivatized Ruthenium Polypyridyl Sensitizers Adsorbed on Metal Oxide Surfaces. *ACS Appl. Mater. Interfaces* **2018**, *10* (26), 22821–22833. https://doi.org/10.1021/acsami.8b04587.

(32) Materna, K. L.; Crabtree, R. H.; Brudvig, G. W. Anchoring Groups for Photocatalytic Water Oxidation on Metal Oxide Surfaces. *Chem. Soc. Rev.* **2017**, *46* (20), 6099–6110. https://doi.org/10.1039/C7CS00314E.

(33) Surendranath, Y.; Kanan, M. W.; Nocera, D. G. Mechanistic Studies of the Oxygen Evolution Reaction by a Cobalt-Phosphate Catalyst at Neutral pH. *J. Am. Chem. Soc.* **2010**, *132* (46), 16501–16509. https://doi.org/10.1021/ja106102b.

(34) Watanabe, M.; Motoo, S. Electrocatalysis by Ad-Atoms. *Journal of Electroanalytical Chemistry and Interfacial Electrochemistry* **1975**, *60* (3), 275–283. https://doi.org/10.1016/S0022-0728(75)80262-2.

(35) Alibabaei, L.; Dillon, R. J.; Reilly, C. E.; Brennaman, M. K.; Wee, K.-R.; Marquard, S. L.; Papanikolas, J. M.; Meyer, T. J. Chromophore-Catalyst Assembly for Water Oxidation Prepared by Atomic Layer Deposition. *ACS Appl. Mater. Interfaces* **2017**, *9* (44), 39018–39026. https://doi.org/10.1021/acsami.7b11905.

(36) Combellas, C.; Kanoufi, F.; Pinson, J.; Podvorica, F. I. Sterically Hindered Diazonium Salts for the Grafting of a Monolayer on Metals. *J. Am. Chem. Soc.* **2008**, *130* (27), 8576–8577. https://doi.org/10.1021/ja8018912.

(37) Cao, C.; Zhang, Y.; Jiang, C.; Qi, M.; Liu, G. Advances on Aryldiazonium Salt Chemistry Based Interfacial Fabrication for Sensing Applications. *ACS Appl. Mater. Interfaces* **2017**, *9* (6), 5031–5049. https://doi.org/10.1021/acsami.6b16108.

(38) Volatron, F.; Noël, J.-M.; Rinfray, C.; Decorse, P.; Combellas, C.; Kanoufi, F.; Proust, A. Electron Transfer Properties of a Monolayer of Hybrid Polyoxometalates on Silicon. *J. Mater. Chem. C* **2015**, *3* (24), 6266–6275. https://doi.org/10.1039/C5TC00074B.

(39) Leroux, Y. R.; Fei, H.; Noël, J.-M.; Roux, C.; Hapiot, P. Efficient Covalent Modification of a Carbon Surface: Use of a Silyl Protecting Group To Form an Active Monolayer. *J. Am. Chem. Soc.* **2010**, *132* (40), 14039–14041. https://doi.org/10.1021/ja106971x.

(40) Malmos, K.; Dong, M.; Pillai, S.; Kingshott, P.; Besenbacher, F.; Pedersen, S. U.; Daasbjerg, K. Using a Hydrazone-Protected Benzenediazonium Salt to Introduce a Near-Monolayer of Benzaldehyde on Glassy Carbon Surfaces. *J. Am. Chem. Soc.* **2009**, *131* (13), 4928–4936. https://doi.org/10.1021/ja809816x.

(41) Menanteau, T.; Levillain, E.; Downard, A. J.; Breton, T. Evidence of Monolayer Formation via Diazonium Grafting with a Radical Scavenger: Electrochemical, AFM and XPS Monitoring. *Phys. Chem. Chem. Phys.* **2015**, *17* (19), 13137–13142. https://doi.org/10.1039/C5CP01401H.

(42) Cao, L.; Fang, G.; Wang, Y. Electroreduction of Viologen Phenyl Diazonium Salts as a Strategy To Control Viologen Coverage on Electrodes. *Langmuir* **2017**, *33* (4), 980–987. https://doi.org/10.1021/acs.langmuir.6b04317.

(43) Tran, QuangT.; Pellon, P.; Jeannin, O.; Geneste, F.; Lagrost, C. Multi-Modal Surface Grafting of [Trans-Bis(Aminodiphenylphosphine) Terpyridine-Ru(II)Cl]+Cl− Complex onto Glassy Carbon Electrode. *Electrochimica Acta* **2018**, *259*, 151–160. https://doi.org/10.1016/j.electacta.2017.10.142.

(44) Nguyen, V. Q.; Sun, X.; Lafolet, F.; Audibert, J.-F.; Miomandre, F.; Lemercier, G.; Loiseau, F.; Lacroix, J.-C. Unprecedented Self-Organized Monolayer of a Ru(II) Complex by Diazonium Electroreduction. *J. Am. Chem. Soc.* **2016**, *138* (30), 9381–9384. https://doi.org/10.1021/jacs.6b04827.

(45) Kim, Y.; Fournier, S.; Lau-Truong, S.; Decorse, P.; Devillers, C. H.; Lucas, D.; Harris, K. D.; Limoges, B.; Balland, V. Introducing Molecular Functionalities within High Surface Area Nanostructured ITO Electrodes through Diazonium Electrografting. *ChemElectroChem* **2018**, *5* (13), 1625–1630. https://doi.org/10.1002/celc.201800418.

(46) Wang, C.; Amiri, M.; Endean, R. T.; Martinez Perez, O.; Varley, S.; Rennie, B.; Rasu, L.; Bergens, S. H. Modular Construction of Photoanodes with Covalently Bonded Ru- and Ir-Polypyridyl Visible Light Chromophores. *ACS Appl. Mater. Interfaces* **2018**, *10* (29), 24533–24542. https://doi.org/10.1021/acsami.8b06605.

(47) Konduri, R.; Ye, H.; MacDonnell, F. M.; Serroni, S.; Campagna, S.; Rajeshwar, K. Ruthenium Photocatalysts Capable of Reversibly Storing up to Four Electrons in a Single Acceptor Ligand: A Step Closer to Artificial Photosynthesis. *Angew. Chem.* **2002**, *114* (17), 3317–3319. https://doi.org/10.1002/1521-3757(20020902)114:17<3317::AID-ANGE3317>3.0.CO;2-R.

(48) Aslan, J. M.; Yousufuddin, M.; Boston, D. J.; MacDonnell, F. M. Quadruple Electron Storage Using Visible Light with Nitrogen-Heterocycles under Metal-Free Conditions. *Inorganica Chimica Acta* **2017**, *454*, 216–221. https://doi.org/10.1016/j.ica.2016.06.025.

(49) Hayes, D.; Kohler, L.; Hadt, R. G.; Zhang, X.; Liu, C.; Mulfort, K. L.; Chen, L. X. Excited State Electron and Energy Relays in Supramolecular Dinuclear Complexes Revealed by Ultrafast Optical and X-Ray Transient Absorption Spectroscopy. *Chem. Sci.* **2018**, *9* (4), 860–875. https://doi.org/10.1039/C7SC04055E.

(50) Tsuji, Y.; Yamamoto, K.; Yamauchi, K.; Sakai, K. Near-Infrared Light-Driven Hydrogen Evolution from Water Using a Polypyridyl Triruthenium Photosensitizer. *Angew Chem Int Ed* **2018**, *57* (1), 208–212. https://doi.org/10.1002/anie.201708996.

(51) Zhang, L.-J.; Wang, Y.-H.; Liu, J.; Xu, M.-C.; Zhang, X.-M. Efficient and Environmentally Friendly Glaser Coupling of Terminal Alkynes Catalyzed by Multinuclear Copper Complexes under Base-Free Conditions. *RSC Adv.* **2016**, *6* (34), 28653–28657. https://doi.org/10.1039/C6RA01262K.

(52) Rathnayaka, S. C.; Lindeman, S. V.; Mankad, N. P. Multinuclear Cu(I) Clusters Featuring a New Triply Bridging Coordination Mode of Phosphaamidinate Ligands. *Inorg. Chem.* **2018**, *57* (15), 9439–9445. https://doi.org/10.1021/acs.inorgchem.8b01422.

(53) Palomo, J. M. Solid-Phase Peptide Synthesis: An Overview Focused on the Preparation of Biologically Relevant Peptides. *RSC Adv.* **2014**, *4* (62), 32658–32672. https://doi.org/10.1039/C4RA02458C.

(54) Wang, J. C.; Hill, S. P.; Dilbeck, T.; Ogunsolu, O. O.; Banerjee, T.; Hanson, K. Multimolecular Assemblies on High Surface Area Metal Oxides and Their Role in Interfacial Energy and Electron Transfer. *Chem. Soc. Rev.* **2018**, *47* (1), 104–148. https://doi.org/10.1039/C7CS00565B.

(55) Shul, G.; Weissmann, M.; Bélanger, D. Electrochemical Formation of an Ultrathin Electroactive Film from 1,10-Phenanthroline on a Glassy Carbon Electrode in Acidic Electrolyte. *Langmuir* **2014**, *30* (22), 6612–6621. https://doi.org/10.1021/la500349t.

(56) Gunasekar, G. H.; Park, K.; Ganesan, V.; Lee, K.; Kim, N.-K.; Jung, K.-D.; Yoon, S. A Covalent Triazine Framework, Functionalized with Ir/N-Heterocyclic Carbene Sites, for the Efficient Hydrogenation of CO_2 to Formate. *Chem. Mater.* **2017**, *29* (16), 6740–6748. https://doi.org/10.1021/acs.chemmater.7b01539.

(57) Shul, G.; Weissmann, M.; Bélanger, D. Electrochemical Characterization of Glassy Carbon Electrode Modified with 1,10-Phenanthroline Groups by Two Pathways: Reduction of the Corresponding Diazonium Ions and Reduction of Phenanthroline. *Electrochimica Acta* **2015**, *162*, 146–155. https://doi.org/10.1016/j.electacta.2014.12.116.

(58) Pinczewska, A.; Sosna, M.; Bloodworth, S.; Kilburn, J. D.; Bartlett, P. N. High-Throughput Synthesis and Electrochemical Screening of a Library of Modified Electrodes for NADH Oxidation. *J. Am. Chem. Soc.* **2012**, *134* (43), 18022–18033. https://doi.org/10.1021/ja307390x.

(59) Buzzeo, M. C.; Hardacre, C.; Compton, R. G. Extended Electrochemical Windows Made Accessible by Room Temperature Ionic Liquid/Organic Solvent Electrolyte Systems. *ChemPhysChem* **2006**, *7* (1), 176–180. https://doi.org/10.1002/cphc.200500361.

(60) Murphy, D. M.; McNamara, K.; Richardson, P.; Sanchez-Romaguera, V.; Winpenny, R. E. P.; Yellowlees, L. J. Electrochemical and Spectroelectrochemical Studies of Complexes of 1,10-Phenanthroline-5,6-Dione. *Inorganica Chimica Acta* **2011**, *374* (1), 435–441. https://doi.org/10.1016/j.ica.2011.02.050.

(61) Liang, Y.; Nguyen, M. T.; Holliday, B. J.; Jones, R. A. Electrocatalytic Reduction of CO2 Using Rhenium Complexes with Dipyrido[3,2-a:2′,3′-c]Phenazine Ligands. *Inorganic Chemistry Communications* **2017**, *84*, 113–117. https://doi.org/10.1016/j.inoche.2017.08.002.

(62) Agnès, C.; Arnault, J.-C.; Omnès, F.; Jousselme, B.; Billon, M.; Bidan, G.; Mailley, P. XPS Study of Ruthenium Tris-Bipyridine Electrografted from Diazonium Salt Derivative on Microcrystalline Boron Doped Diamond. *Phys. Chem. Chem. Phys.* **2009**, *11* (48), 11647. https://doi.org/10.1039/b912468c.

(63) Singh, J.; Gusain, A.; Saxena, V.; Chauhan, A. K.; Veerender, P.; Koiry, S. P.; Jha, P.; Jain, A.; Aswal, D. K.; Gupta, S. K. XPS, UV–Vis, FTIR, and EXAFS Studies to Investigate the Binding Mechanism of N719 Dye onto Oxalic Acid Treated TiO $_2$ and Its Implication on Photovoltaic Properties. *J. Phys. Chem. C* **2013**, *117* (41), 21096–21104. https://doi.org/10.1021/jp4062994.

(64) Lund, T.; Nguyen, P. T.; Ruhland, T. Electrochemical Grafting of TiO2-Based Photo-Anodes and Its Effect in Dye-Sensitized Solar Cells. *Journal of Electroanalytical Chemistry* **2015**, *758*, 85–92. https://doi.org/10.1016/j.jelechem.2015.10.021.

(65) Jama, C.; Al Khawwam, A.; Loir, A.; Goudmand, P.; Dessaux, O.; Gengembre, L.; Grimblot, J. X-ray Photoelectron Spectroscopy Study of Carbon Nitride Coatings Deposited by IR Laser Ablation in a Remote Nitrogen Plasma Atmosphere. *Surface & Interface Analysis* **2001**, *31* (9), 815–824. https://doi.org/10.1002/sia.1110.

(66) Tang, H.; Li, Y.; Chen, Q.; Chen, B.; Qiao, Q.; Yang, W.; Wu, H.; Cao, Y. Efficient Yellow–Green Light-Emitting Cationic Iridium Complexes Based on 1,10-Phenanthroline Derivatives Containing Oxadiazole-Triphenylamine Unit. *Dyes and Pigments* **2014**, *100*, 79–86. https://doi.org/10.1016/j.dyepig.2013.07.029.

(67) Goss, C. A.; Abruna, H. D. Spectral, Electrochemical and Electrocatalytic Properties of 1,10-Phenanthroline-5,6-Dione Complexes of Transition Metals. *Inorg. Chem.* **1985**, *24* (25), 4263–4267. https://doi.org/10.1021/ic00219a012.

(68) Brennaman, M. K.; Patrocinio, A. O. T.; Song, W.; Jurss, J. W.; Concepcion, J. J.; Hoertz, P. G.; Traub, M. C.; Murakami Iha, N. Y.; Meyer, T. J. Interfacial Electron Transfer Dynamics

Following Laser Flash Photolysis of [Ru(Bpy)$_2$((4,4′-PO$_3$H$_2$)$_2$Bpy)]$^{2+}$ in TiO$_2$ Nanoparticle Films in Aqueous Environments. *ChemSusChem* **2011**, *4* (2), 216–227. https://doi.org/10.1002/cssc.201000356.

(69) Saito, D.; Yamazaki, Y.; Tamaki, Y.; Ishitani, O. Photocatalysis of a Dinuclear Ru(II)–Re(I) Complex for CO$_2$ Reduction on a Solid Surface. *J. Am. Chem. Soc.* **2020**, *142* (45), 19249–19258. https://doi.org/10.1021/jacs.0c09170.

(70) Kamata, R.; Kumagai, H.; Yamazaki, Y.; Sahara, G.; Ishitani, O. Photoelectrochemical CO$_2$ Reduction Using a Ru(II)–Re(I) Supramolecular Photocatalyst Connected to a Vinyl Polymer on a NiO Electrode. *ACS Appl. Mater. Interfaces* **2019**, *11* (6), 5632–5641. https://doi.org/10.1021/acsami.8b05495.

(71) Sahara, G.; Abe, R.; Higashi, M.; Morikawa, T.; Maeda, K.; Ueda, Y.; Ishitani, O. Photoelectrochemical CO$_2$ Reduction Using a Ru(Ⅱ)–Re(Ⅰ) Multinuclear Metal Complex on a p-Type Semiconducting NiO Electrode. *Chem. Commun.* **2015**, *51* (53), 10722–10725. https://doi.org/10.1039/C5CC02403J.

(72) Li, T.-T.; Shan, B.; Meyer, T. J. Stable Molecular Photocathode for Solar-Driven CO$_2$ Reduction in Aqueous Solutions. *ACS Energy Lett.* **2019**, *4* (3), 629–636. https://doi.org/10.1021/acsenergylett.8b02512.

(73) Koike, K.; Naito, S.; Sato, S.; Tamaki, Y.; Ishitani, O. Architecture of Supramolecular Metal Complexes for Photocatalytic CO2 Reduction. *Journal of Photochemistry and Photobiology A: Chemistry* **2009**, *207* (1), 109–114. https://doi.org/10.1016/j.jphotochem.2008.12.014.

(74) Gholamkhass, B.; Mametsuka, H.; Koike, K.; Tanabe, T.; Furue, M.; Ishitani, O. Architecture of Supramolecular Metal Complexes for Photocatalytic CO$_2$ Reduction: Ruthenium−Rhenium Bi- and Tetranuclear Complexes. *Inorg. Chem.* **2005**, *44* (7), 2326–2336. https://doi.org/10.1021/ic048779r.

(75) Tamaki, Y.; Ishitani, O. Supramolecular Photocatalysts for the Reduction of CO$_2$. *ACS Catal.* **2017**, *7* (5), 3394–3409. https://doi.org/10.1021/acscatal.7b00440.

(76) Tamaki, Y.; Koike, K.; Morimoto, T.; Ishitani, O. Substantial Improvement in the Efficiency and Durability of a Photocatalyst for Carbon Dioxide Reduction Using a Benzoimidazole Derivative as an Electron Donor. *Journal of Catalysis* **2013**, *304*, 22–28. https://doi.org/10.1016/j.jcat.2013.04.002.

(77) Tamaki, Y.; Watanabe, K.; Koike, K.; Inoue, H.; Morimoto, T.; Ishitani, O. Development of Highly Efficient Supramolecular CO$_2$ Reduction Photocatalysts with High Turnover Frequency and Durability. *Faraday Discuss.* **2012**, *155*, 115–127. https://doi.org/10.1039/C1FD00091H.

(78) Yeşildağ, A.; Ekinci, D. Covalent Attachment of Pyridine-Type Molecules to Glassy Carbon Surfaces by Electrochemical Reduction of in Situ Generated Diazonium Salts. Formation of Ruthenium Complexes on Ligand-Modified Surfaces. *Electrochimica Acta* **2010**, *55* (23), 7000–7009. https://doi.org/10.1016/j.electacta.2010.06.020.

(79) Mack, J. B. C.; Walker, K. L.; Robinson, S. G.; Zare, R. N.; Sigman, M. S.; Waymouth, R. M.; Du Bois, J. Mechanistic Study of Ruthenium-Catalyzed C–H Hydroxylation Reveals an Unexpected Pathway for Catalyst Arrest. *J. Am. Chem. Soc.* **2019**, *141* (2), 972–980. https://doi.org/10.1021/jacs.8b10950.

(80) Viala, C.; Coudret, C. An Expeditious Route to Cis-Ru(Bpy)2C12 (Bpy=2,2′-Bipyridine) Using Carbohydrates as Reducers. *Inorganica Chimica Acta* **2006**, *359* (3), 984–989. https://doi.org/10.1016/j.ica.2005.07.019.

(81) O'Regan, B.; Gratzelt, M. A Low-Cost, High-Efficiency Solar Cell Based on Dye-Sensitized Colloidal Ti02 Films. **1991**, *353*.

(82) Sabuzi, F.; Tiravia, M.; Vecchi, A.; Gatto, E.; Venanzi, M.; Floris, B.; Conte, V.; Galloni, P. Deposition of Tetraferrocenylporphyrins on ITO Surfaces for Photo-Catalytic O_2 Activation. *Dalton Trans.* **2016**, *45* (37), 14745–14753. https://doi.org/10.1039/C6DT01821A.

Chapter 3

(1) Zhang, B.; Sun, L. Artificial Photosynthesis: Opportunities and Challenges of Molecular Catalysts. *Chem. Soc. Rev.* **2019**, *48* (7), 2216–2264. https://doi.org/10.1039/C8CS00897C.

(2) Lewis, N. S. Research Opportunities to Advance Solar Energy Utilization. *Science* **2016**, *351* (6271), aad1920. https://doi.org/10.1126/science.aad1920.

(3) Kärkäs, M. D.; Verho, O.; Johnston, E. V.; Åkermark, B. Artificial Photosynthesis: Molecular Systems for Catalytic Water Oxidation. *Chem. Rev.* **2014**, *114* (24), 11863–12001. https://doi.org/10.1021/cr400572f.

(4) Lewis, N. S.; Nocera, D. G. Powering the Planet: Chemical Challenges in Solar Energy Utilization. *Proc. Natl. Acad. Sci. U.S.A.* **2006**, *103* (43), 15729–15735. https://doi.org/10.1073/pnas.0603395103.

(5) Xu, P.; McCool, N. S.; Mallouk, T. E. Water Splitting Dye-Sensitized Solar Cells. *Nano Today* **2017**, *14*, 42–58. https://doi.org/10.1016/j.nantod.2017.04.009.

(6) Wang, D.; Hu, J.; Sherman, B. D.; Sheridan, M. V.; Yan, L.; Dares, C. J.; Zhu, Y.; Li, F.; Huang, Q.; You, W.; Meyer, T. J. A Molecular Tandem Cell for Efficient Solar Water Splitting. *Proc. Natl. Acad. Sci. U.S.A.* **2020**, *117* (24), 13256–13260. https://doi.org/10.1073/pnas.2001753117.

(7) Roger, I.; Shipman, M. A.; Symes, M. D. Earth-Abundant Catalysts for Electrochemical and Photoelectrochemical Water Splitting. *Nat Rev Chem* **2017**, *1* (1), 0003. https://doi.org/10.1038/s41570-016-0003.

(8) Tang, S.; Qiu, W.; Xiao, S.; Tong, Y.; Yang, S. Harnessing Hierarchical Architectures to Trap Light for Efficient Photoelectrochemical Cells. *Energy Environ. Sci.* **2020**, *13* (3), 660–684. https://doi.org/10.1039/C9EE02986A.

(9) Castro, S.; Albo, J.; Irabien, A. Photoelectrochemical Reactors for CO$_2$ Utilization. *ACS Sustainable Chem. Eng.* **2018**, *6* (12), 15877–15894. https://doi.org/10.1021/acssuschemeng.8b03706.

(10) Brennaman, M. K.; Dillon, R. J.; Alibabaei, L.; Gish, M. K.; Dares, C. J.; Ashford, D. L.; House, R. L.; Meyer, G. J.; Papanikolas, J. M.; Meyer, T. J. Finding the Way to Solar Fuels with Dye-Sensitized Photoelectrosynthesis Cells. *J. Am. Chem. Soc.* **2016**, *138* (40), 13085–13102. https://doi.org/10.1021/jacs.6b06466.

(11) Kumar, B.; Llorente, M.; Froehlich, J.; Dang, T.; Sathrum, A.; Kubiak, C. P. Photochemical and Photoelectrochemical Reduction of CO$_2$. *Annu. Rev. Phys. Chem.* **2012**, *63* (1), 541–569. https://doi.org/10.1146/annurev-physchem-032511-143759.

(12) Ashford, D. L.; Gish, M. K.; Vannucci, A. K.; Brennaman, M. K.; Templeton, J. L.; Papanikolas, J. M.; Meyer, T. J. Molecular Chromophore–Catalyst Assemblies for Solar Fuel Applications. *Chem. Rev.* **2015**, *115* (23), 13006–13049. https://doi.org/10.1021/acs.chemrev.5b00229.

(13) Reece, S. Y.; Hamel, J. A.; Sung, K.; Jarvi, T. D.; Esswein, A. J.; Pijpers, J. J. H.; Nocera, D. G. Wireless Solar Water Splitting Using Silicon-Based Semiconductors and Earth-Abundant Catalysts. *Science* **2011**, *334* (6056), 645–648. https://doi.org/10.1126/science.1209816.

(14) Dongare, P.; Myron, B. D. B.; Wang, L.; Thompson, D. W.; Meyer, T. J. [Ru(Bpy)3]2+∗ Revisited. Is It Localized or Delocalized? How Does It Decay? *Coordination Chemistry Reviews* **2017**, *345*, 86–107. https://doi.org/10.1016/j.ccr.2017.03.009.

(15) Yuan, Y.-J.; Yu, Z.-T.; Chen, D.-Q.; Zou, Z.-G. Metal-Complex Chromophores for Solar Hydrogen Generation. *Chem. Soc. Rev.* **2017**, *46* (3), 603–631. https://doi.org/10.1039/C6CS00436A.

(16) Thompson, D. W.; Ito, A.; Meyer, T. J. [Ru(Bpy)3]2+* and Other Remarkable Metal-to-Ligand Charge Transfer (MLCT) Excited States. *Pure and Applied Chemistry* **2013**, *85* (7), 1257–1305. https://doi.org/10.1351/PAC-CON-13-03-04.

(17) Wang, Y.; Liu, T.; Chen, L.; Chao, D. Water-Assisted Highly Efficient Photocatalytic Reduction of CO$_2$ to CO with Noble Metal-Free Bis(Terpyridine)Iron(II) Complexes and an Organic Photosensitizer. *Inorg. Chem.* **2021**, *60* (8), 5590–5597. https://doi.org/10.1021/acs.inorgchem.0c03503.

(18) Farré, Y.; Maschietto, F.; Föhlinger, J.; Wykes, M.; Planchat, A.; Pellegrin, Y.; Blart, E.; Ciofini, I.; Hammarström, L.; Odobel, F. A Comparative Investigation of the Role of the Anchoring Group on Perylene Monoimide Dyes in NiO-Based Dye-Sensitized Solar Cells. *ChemSusChem* **2020**, *13* (7), 1844–1855. https://doi.org/10.1002/cssc.201903182.

(19) Brennan, B. J.; Llansola Portolés, M. J.; Liddell, P. A.; Moore, T. A.; Moore, A. L.; Gust, D. Comparison of Silatrane, Phosphonic Acid, and Carboxylic Acid Functional Groups for Attachment of Porphyrin Sensitizers to TiO2 in Photoelectrochemical Cells. *Phys. Chem. Chem. Phys.* **2013**, *15* (39), 16605. https://doi.org/10.1039/c3cp52156g.

(20) Sullivan, I.; Goryachev, A.; Digdaya, I. A.; Li, X.; Atwater, H. A.; Vermaas, D. A.; Xiang, C. Coupling Electrochemical CO2 Conversion with CO2 Capture. *Nat Catal* **2021**, *4* (11), 952–958. https://doi.org/10.1038/s41929-021-00699-7.

(21) Bangle, R.; Sampaio, R. N.; Troian-Gautier, L.; Meyer, G. J. Surface Grafting of Ru(II) Diazonium-Based Sensitizers on Metal Oxides Enhances Alkaline Stability for Solar Energy Conversion. *ACS Appl. Mater. Interfaces* **2018**, *10* (3), 3121–3132. https://doi.org/10.1021/acsami.7b16641.

(22) Surendranath, Y.; Kanan, M. W.; Nocera, D. G. Mechanistic Studies of the Oxygen Evolution Reaction by a Cobalt-Phosphate Catalyst at Neutral pH. *J. Am. Chem. Soc.* **2010**, *132* (46), 16501–16509. https://doi.org/10.1021/ja106102b.

(23) Jamesh, M.-I.; Sun, X. Recent Progress on Earth Abundant Electrocatalysts for Oxygen Evolution Reaction (OER) in Alkaline Medium to Achieve Efficient Water Splitting – A Review. *Journal of Power Sources* **2018**, *400*, 31–68. https://doi.org/10.1016/j.jpowsour.2018.07.125.

(24) Rotundo, L.; Filippi, J.; Gobetto, R.; Miller, H. A.; Rocca, R.; Nervi, C.; Vizza, F. Electrochemical CO $_2$ Reduction in Water at Carbon Cloth Electrodes Functionalized with a *Fac* - Mn(Apbpy)(CO) $_3$ Br Complex. *Chem. Commun.* **2019**, *55* (6), 775–777. https://doi.org/10.1039/C8CC08385A.

(25) Shul, G.; Weissmann, M.; Bélanger, D. Electrochemical Characterization of Glassy Carbon Electrode Modified with 1,10-Phenanthroline Groups by Two Pathways: Reduction of the Corresponding Diazonium Ions and Reduction of Phenanthroline. *Electrochimica Acta* **2015**, *162*, 146–155. https://doi.org/10.1016/j.electacta.2014.12.116.

(26) Wang, C.; Amiri, M.; Endean, R. T.; Martinez Perez, O.; Varley, S.; Rennie, B.; Rasu, L.; Bergens, S. H. Modular Construction of Photoanodes with Covalently Bonded Ru- and Ir-Polypyridyl Visible Light Chromophores. *ACS Appl. Mater. Interfaces* **2018**, *10* (29), 24533–24542. https://doi.org/10.1021/acsami.8b06605.

(27) Amiri, M.; Martinez Perez, O.; Endean, R. T.; Rasu, L.; Nepal, P.; Xu, S.; Bergens, S. H. Solid-Phase Synthesis and Photoactivity of Ru-Polypyridyl Visible Light Chromophores Bonded through Carbon to Semiconductor Surfaces. *Dalton Trans.* **2020**, *49* (29), 10173–10184. https://doi.org/10.1039/D0DT01776K.

(28) Shang, T.-Y.; Lu, L.-H.; Cao, Z.; Liu, Y.; He, W.-M.; Yu, B. Recent Advances of 1,2,3,5-Tetrakis(Carbazol-9-Yl)-4,6-Dicyanobenzene (4CzIPN) in Photocatalytic Transformations. *Chem. Commun.* **2019**, *55* (38), 5408–5419. https://doi.org/10.1039/C9CC01047E.

(29) Dalle, K. E.; Warnan, J.; Leung, J. J.; Reuillard, B.; Karmel, I. S.; Reisner, E. Electro- and Solar-Driven Fuel Synthesis with First Row Transition Metal Complexes. *Chem. Rev.* **2019**, *119* (4), 2752–2875. https://doi.org/10.1021/acs.chemrev.8b00392.

(30) Nazeeruddin, M. K.; Kay, A.; Rodicio, I.; Humphry-Baker, R.; Mueller, E.; Liska, P.; Vlachopoulos, N.; Graetzel, M. Conversion of Light to Electricity by Cis-X2bis(2,2'-Bipyridyl-4,4'-Dicarboxylate)Ruthenium(II) Charge-Transfer Sensitizers (X = Cl-, Br-, I-, CN-, and SCN-

) on Nanocrystalline Titanium Dioxide Electrodes. *J. Am. Chem. Soc.* **1993**, *115* (14), 6382–6390. https://doi.org/10.1021/ja00067a063.

(31) Ishimatsu, R.; Matsunami, S.; Kasahara, T.; Mizuno, J.; Edura, T.; Adachi, C.; Nakano, K.; Imato, T. Electrogenerated Chemiluminescence of Donor–Acceptor Molecules with Thermally Activated Delayed Fluorescence. *Angew Chem Int Ed* **2014**, *53* (27), 6993–6996. https://doi.org/10.1002/anie.201402615.

(32) Zigler, D. F.; Morseth, Z. A.; Wang, L.; Ashford, D. L.; Brennaman, M. K.; Grumstrup, E. M.; Brigham, E. C.; Gish, M. K.; Dillon, R. J.; Alibabaei, L.; Meyer, G. J.; Meyer, T. J.; Papanikolas, J. M. Disentangling the Physical Processes Responsible for the Kinetic Complexity in Interfacial Electron Transfer of Excited Ru(II) Polypyridyl Dyes on TiO 2. *J. Am. Chem. Soc.* **2016**, *138* (13), 4426–4438. https://doi.org/10.1021/jacs.5b12996.

(33) Purnama, I.; Salmahaminati, S.; Abe, M.; Hada, M.; Kubo, Y.; Mulyana, J. Y. Factors Influencing the Photoelectrochemical Device Performance Sensitized by Ruthenium Polypyridyl Dyes. *Dalton Trans.* **2019**, *48* (2), 688–695. https://doi.org/10.1039/C8DT03502D.

(34) Dares, C. J.; Lapides, A. M.; Mincher, B. J.; Meyer, T. J. Electrochemical Oxidation of [243] Am(III) in Nitric Acid by a Terpyridyl-Derivatized Electrode. *Science* **2015**, *350* (6261), 652–655. https://doi.org/10.1126/science.aac9217.

(35) Rasu, L.; Amiri, M.; Bergens, S. H. Carbazole–Cyanobenzene Dyes Electrografted to Carbon or Indium-Doped Tin Oxide Supports for Visible Light-Driven Photoanodes and Olefin Isomerizations. *ACS Appl. Mater. Interfaces* **2021**, *13* (15), 17745–17752. https://doi.org/10.1021/acsami.1c05064.

(36) Corpas, J.; Mauleón, P.; Gómez Arrayás, R.; Carretero, J. C. *E/Z* Photoisomerization of Olefins as an Emergent Strategy for the Control of Stereodivergence in Catalysis. *Adv Synth Catal* **2022**, *364* (8), 1348–1370. https://doi.org/10.1002/adsc.202200199.

(37) Peris, E. Smart N-Heterocyclic Carbene Ligands in Catalysis. *Chem. Rev.* **2018**, *118* (19), 9988–10031. https://doi.org/10.1021/acs.chemrev.6b00695.

(38) Samojłowicz, C.; Bieniek, M.; Grela, K. Ruthenium-Based Olefin Metathesis Catalysts Bearing *N*-Heterocyclic Carbene Ligands. *Chem. Rev.* **2009**, *109* (8), 3708–3742. https://doi.org/10.1021/cr800524f.

(39) Vougioukalakis, G. C.; Grubbs, R. H. Ruthenium-Based Heterocyclic Carbene-Coordinated Olefin Metathesis Catalysts. *Chem. Rev.* **2010**, *110* (3), 1746–1787. https://doi.org/10.1021/cr9002424.

(40) Bellotti, P.; Koy, M.; Hopkinson, M. N.; Glorius, F. Recent Advances in the Chemistry and Applications of N-Heterocyclic Carbenes. *Nat Rev Chem* **2021**, *5* (10), 711–725. https://doi.org/10.1038/s41570-021-00321-1.

(41) Smith, C. A.; Narouz, M. R.; Lummis, P. A.; Singh, I.; Nazemi, A.; Li, C.-H.; Crudden, C. M. *N*-Heterocyclic Carbenes in Materials Chemistry. *Chem. Rev.* **2019**, *119* (8), 4986–5056. https://doi.org/10.1021/acs.chemrev.8b00514.

(42) Zhukhovitskiy, A. V.; MacLeod, M. J.; Johnson, J. A. Carbene Ligands in Surface Chemistry: From Stabilization of Discrete Elemental Allotropes to Modification of Nanoscale and Bulk Substrates. *Chem. Rev.* **2015**, *115* (20), 11503–11532. https://doi.org/10.1021/acs.chemrev.5b00220.

(43) Crudden, C. M.; Horton, J. H.; Narouz, M. R.; Li, Z.; Smith, C. A.; Munro, K.; Baddeley, C. J.; Larrea, C. R.; Drevniok, B.; Thanabalasingam, B.; McLean, A. B.; Zenkina, O. V.; Ebralidze, I. I.; She, Z.; Kraatz, H.-B.; Mosey, N. J.; Saunders, L. N.; Yagi, A. Simple Direct Formation of Self-Assembled N-Heterocyclic Carbene Monolayers on Gold and Their Application in Biosensing. *Nat Commun* **2016**, *7* (1), 12654. https://doi.org/10.1038/ncomms12654.

(44) Crudden, C. M.; Horton, J. H.; Ebralidze, I. I.; Zenkina, O. V.; McLean, A. B.; Drevniok, B.; She, Z.; Kraatz, H.-B.; Mosey, N. J.; Seki, T.; Keske, E. C.; Leake, J. D.; Rousina-Webb, A.; Wu, G. Ultra Stable Self-Assembled Monolayers of N-Heterocyclic Carbenes on Gold. *Nature Chem* **2014**, *6* (5), 409–414. https://doi.org/10.1038/nchem.1891.

(45) Lara, P.; Rivada-Wheelaghan, O.; Conejero, S.; Poteau, R.; Philippot, K.; Chaudret, B. Ruthenium Nanoparticles Stabilized by N-Heterocyclic Carbenes: Ligand Location and Influence on Reactivity. *Angew Chem Int Ed* **2011**, *50* (50), 12080–12084. https://doi.org/10.1002/anie.201106348.

(46) Baquero, E. A.; Tricard, S.; Flores, J. C.; de Jesús, E.; Chaudret, B. Highly Stable Water-Soluble Platinum Nanoparticles Stabilized by Hydrophilic N-Heterocyclic Carbenes. *Angewandte Chemie* **2014**, *126* (48), 13436–13440. https://doi.org/10.1002/ange.201407758.

(47) Ernst, J. B.; Muratsugu, S.; Wang, F.; Tada, M.; Glorius, F. Tunable Heterogeneous Catalysis: N-Heterocyclic Carbenes as Ligands for Supported Heterogeneous Ru/K-Al $_2$ O $_3$ Catalysts To Tune Reactivity and Selectivity. *J. Am. Chem. Soc.* **2016**, *138* (34), 10718–10721. https://doi.org/10.1021/jacs.6b03821.

(48) Ernst, J. B.; Schwermann, C.; Yokota, G.; Tada, M.; Muratsugu, S.; Doltsinis, N. L.; Glorius, F. Molecular Adsorbates Switch on Heterogeneous Catalysis: Induction of Reactivity by N-Heterocyclic Carbenes. *J. Am. Chem. Soc.* **2017**, *139* (27), 9144–9147. https://doi.org/10.1021/jacs.7b05112.

(49) MacLeod, M. J.; Goodman, A. J.; Ye, H.-Z.; Nguyen, H. V.-T.; Van Voorhis, T.; Johnson, J. A. Robust Gold Nanorods Stabilized by Bidentate N-Heterocyclic-Carbene–Thiolate Ligands. *Nature Chem* **2019**, *11* (1), 57–63. https://doi.org/10.1038/s41557-018-0159-8.

(50) Narouz, M. R.; Takano, S.; Lummis, P. A.; Levchenko, T. I.; Nazemi, A.; Kaappa, S.; Malola, S.; Yousefalizadeh, G.; Calhoun, L. A.; Stamplecoskie, K. G.; Häkkinen, H.; Tsukuda, T.; Crudden, C. M. Robust, Highly Luminescent Au $_{13}$ Superatoms Protected by N-Heterocyclic Carbenes. *J. Am. Chem. Soc.* **2019**, *141* (38), 14997–15002. https://doi.org/10.1021/jacs.9b07854.

(51) Cao, Z.; Derrick, J. S.; Xu, J.; Gao, R.; Gong, M.; Nichols, E. M.; Smith, P. T.; Liu, X.; Wen, X.; Copéret, C.; Chang, C. J. Chelating N-Heterocyclic Carbene Ligands Enable Tuning of

Electrocatalytic CO$_2$ Reduction to Formate and Carbon Monoxide: Surface Organometallic Chemistry. *Angew Chem Int Ed* **2018**, *57* (18), 4981–4985. https://doi.org/10.1002/anie.201800367.

(52) Cao, Z.; Kim, D.; Hong, D.; Yu, Y.; Xu, J.; Lin, S.; Wen, X.; Nichols, E. M.; Jeong, K.; Reimer, J. A.; Yang, P.; Chang, C. J. A Molecular Surface Functionalization Approach to Tuning Nanoparticle Electrocatalysts for Carbon Dioxide Reduction. *J. Am. Chem. Soc.* **2016**, *138* (26), 8120–8125. https://doi.org/10.1021/jacs.6b02878.

(53) Feroci, M.; Chiarotto, I.; D'Anna, F.; Gala, F.; Noto, R.; Ornano, L.; Zollo, G.; Inesi, A. N-Heterocyclic Carbenes and Parent Cations: Acidity, Nucleophilicity, Stability, and Hydrogen Bonding—Electrochemical Study and Ab Initio Calculations. *ChemElectroChem* **2016**, *3* (7), 1133–1141. https://doi.org/10.1002/celc.201600187.

(54) Hollóczki, O. Unveiling the Peculiar Hydrogen Bonding Behavior of Solvated N-Heterocyclic Carbenes. *Phys. Chem. Chem. Phys.* **2016**, *18* (1), 126–140. https://doi.org/10.1039/C5CP05369B.

(55) Gorodetsky, B.; Ramnial, T.; Branda, N. R.; Clyburne, J. A. C. Electrochemical Reduction of an Imidazolium Cation: A Convenient Preparation of Imidazol-2-Ylidenes and Their Observation in an Ionic Liquid. *Chem. Commun.* **2004**, No. 17, 1972. https://doi.org/10.1039/b407386j.

(56) Hahn, F. E.; Jahnke, M. C. Heterocyclic Carbenes: Synthesis and Coordination Chemistry. *Angew Chem Int Ed* **2008**, *47* (17), 3122–3172. https://doi.org/10.1002/anie.200703883.

(57) Kundu, S.; Xia, W.; Busser, W.; Becker, M.; Schmidt, D. A.; Havenith, M.; Muhler, M. The Formation of Nitrogen-Containing Functional Groups on Carbon Nanotube Surfaces: A Quantitative XPS and TPD Study. *Phys. Chem. Chem. Phys.* **2010**, *12* (17), 4351. https://doi.org/10.1039/b923651a.

(58) Iqbal, M. A.; Ali, S. I.; Amin, F.; Tariq, A.; Iqbal, M. Z.; Rizwan, S. La- and Mn-Codoped Bismuth Ferrite/Ti$_3$C$_2$ MXene Composites for Efficient Photocatalytic Degradation of Congo Red Dye. *ACS Omega* **2019**, *4* (5), 8661–8668. https://doi.org/10.1021/acsomega.9b00493.

(59) Huynh, H. V.; Han, Y.; Jothibasu, R.; Yang, J. A. ^{13}C NMR Spectroscopic Determination of Ligand Donor Strengths Using N-Heterocyclic Carbene Complexes of Palladium(II). *Organometallics* **2009**, *28* (18), 5395–5404. https://doi.org/10.1021/om900667d.

(60) Agnès, C.; Arnault, J.-C.; Omnès, F.; Jousselme, B.; Billon, M.; Bidan, G.; Mailley, P. XPS Study of Ruthenium Tris-Bipyridine Electrografted from Diazonium Salt Derivative on Microcrystalline Boron Doped Diamond. *Phys. Chem. Chem. Phys.* **2009**, *11* (48), 11647. https://doi.org/10.1039/b912468c.

(61) Singh, J.; Gusain, A.; Saxena, V.; Chauhan, A. K.; Veerender, P.; Koiry, S. P.; Jha, P.; Jain, A.; Aswal, D. K.; Gupta, S. K. XPS, UV–Vis, FTIR, and EXAFS Studies to Investigate the Binding Mechanism of N719 Dye onto Oxalic Acid Treated TiO$_2$ and Its Implication on Photovoltaic Properties. *J. Phys. Chem. C* **2013**, *117* (41), 21096–21104. https://doi.org/10.1021/jp4062994.

(62) Tang, H.; Li, Y.; Chen, Q.; Chen, B.; Qiao, Q.; Yang, W.; Wu, H.; Cao, Y. Efficient Yellow–Green Light-Emitting Cationic Iridium Complexes Based on 1,10-Phenanthroline Derivatives Containing Oxadiazole-Triphenylamine Unit. *Dyes and Pigments* **2014**, *100*, 79–86. https://doi.org/10.1016/j.dyepig.2013.07.029.

(63) Raber, M. M.; Brady, M. D.; Troian-Gautier, L.; Dickenson, J. C.; Marquard, S. L.; Hyde, J. T.; Lopez, S. J.; Meyer, G. J.; Meyer, T. J.; Harrison, D. P. Fundamental Factors Impacting the Stability of Phosphonate-Derivatized Ruthenium Polypyridyl Sensitizers Adsorbed on Metal Oxide Surfaces. *ACS Appl. Mater. Interfaces* **2018**, *10* (26), 22821–22833. https://doi.org/10.1021/acsami.8b04587.

(64) Brennaman, M. K.; Patrocinio, A. O. T.; Song, W.; Jurss, J. W.; Concepcion, J. J.; Hoertz, P. G.; Traub, M. C.; Murakami Iha, N. Y.; Meyer, T. J. Interfacial Electron Transfer Dynamics Following Laser Flash Photolysis of $[Ru(Bpy)_2((4,4'\text{-}PO_3H_2)_2 Bpy)]^{2+}$ in TiO_2 Nanoparticle Films in Aqueous Environments. *ChemSusChem* **2011**, *4* (2), 216–227. https://doi.org/10.1002/cssc.201000356.

(65) Chen, Z.; Concepcion, J. J.; Jurss, J. W.; Meyer, T. J. Single-Site, Catalytic Water Oxidation on Oxide Surfaces. *J. Am. Chem. Soc.* **2009**, *131* (43), 15580–15581. https://doi.org/10.1021/ja906391w.

(66) Beranek, R. (Photo)Electrochemical Methods for the Determination of the Band Edge Positions of TiO_2-Based Nanomaterials. *Advances in Physical Chemistry* **2011**, *2011*, 1–20. https://doi.org/10.1155/2011/786759.

(67) Uoyama, H.; Goushi, K.; Shizu, K.; Nomura, H.; Adachi, C. Highly Efficient Organic Light-Emitting Diodes from Delayed Fluorescence. *Nature* **2012**, *492* (7428), 234–238. https://doi.org/10.1038/nature11687.

(68) Kinney, Z. J.; Rheingold, A. L.; Protasiewicz, J. D. Preferential N–H⋯:C⍰ Hydrogen Bonding Involving Ditopic *NH*-Containing Systems and *N*-Heterocyclic Carbenes. *RSC Adv.* **2020**, *10* (69), 42164–42171. https://doi.org/10.1039/D0RA08490E.

(69) Gehrke, S.; Hollóczki, O. Hydrogen Bonding of N-Heterocyclic Carbenes in Solution: Mechanisms of Solvent Reorganization. *Chemistry A European J* **2018**, *24* (45), 11594–11604. https://doi.org/10.1002/chem.201802286.

(70) Martra, G. Lewis Acid and Base Sites at the Surface of Microcrystalline TiO2 Anatase: Relationships between Surface Morphology and Chemical Behaviour. *Applied Catalysis A: General* **2000**, *200* (1–2), 275–285. https://doi.org/10.1016/S0926-860X(00)00641-4.

Chapter 4

(1) US Department of Commerce, N. *Global Monitoring Laboratory - Carbon Cycle Greenhouse Gases*. https://gml.noaa.gov/ccgg/trends/global.html (accessed 2023-04-28).

(2) *Met Office Hadley Centre observations datasets*. https://www.metoffice.gov.uk/hadobs/hadcrut5/#:~:text=HadCRUT5%20is%20a%20gridded%20dataset,and%20regional%20average%20time%20series. (accessed 2023-05-11).

(3) *CO2 Emissions | Global Carbon Atlas*. http://www.globalcarbonatlas.org/en/CO2-emissions (accessed 2023-04-28).

(4) Lewis, N. S. Research Opportunities to Advance Solar Energy Utilization. *Science* **2016**, *351* (6271), aad1920. https://doi.org/10.1126/science.aad1920.

(5) Aneke, M.; Wang, M. Energy Storage Technologies and Real Life Applications – A State of the Art Review. *Applied Energy* **2016**, *179*, 350–377. https://doi.org/10.1016/j.apenergy.2016.06.097.

(6) Lv, J.; Xie, J.; Mohamed, A. G. A.; Zhang, X.; Feng, Y.; Jiao, L.; Zhou, E.; Yuan, D.; Wang, Y. Solar Utilization beyond Photosynthesis. *Nat Rev Chem* **2022**, *7* (2), 91–105. https://doi.org/10.1038/s41570-022-00448-9.

(7) Crabtree, R. H. Alternate Strategies for Solar Fuels from Carbon Dioxide. *ACS Energy Lett.* **2020**, *5* (8), 2505–2507. https://doi.org/10.1021/acsenergylett.0c01359.

(8) Dalle, K. E.; Warnan, J.; Leung, J. J.; Reuillard, B.; Karmel, I. S.; Reisner, E. Electro- and Solar-Driven Fuel Synthesis with First Row Transition Metal Complexes. *Chem. Rev.* **2019**, *119* (4), 2752–2875. https://doi.org/10.1021/acs.chemrev.8b00392.

(9) Tu, W.; Zhou, Y.; Zou, Z. Photocatalytic Conversion of CO_2 into Renewable Hydrocarbon Fuels: State-of-the-Art Accomplishment, Challenges, and Prospects. *Adv. Mater.* **2014**, *26* (27), 4607–4626. https://doi.org/10.1002/adma.201400087.

(10) Grills, D. C.; Ertem, M. Z.; McKinnon, M.; Ngo, K. T.; Rochford, J. Mechanistic Aspects of CO2 Reduction Catalysis with Manganese-Based Molecular Catalysts. *Coordination Chemistry Reviews* **2018**, *374*, 173–217. https://doi.org/10.1016/j.ccr.2018.05.022.

(11) Agarwal, J.; Fujita, E.; Schaefer, H. F.; Muckerman, J. T. Mechanisms for CO Production from CO_2 Using Reduced Rhenium Tricarbonyl Catalysts. *J. Am. Chem. Soc.* **2012**, *134* (11), 5180–5186. https://doi.org/10.1021/ja2105834.

(12) Schneider, T. W.; Ertem, M. Z.; Muckerman, J. T.; Angeles-Boza, A. M. Mechanism of Photocatalytic Reduction of CO_2 by Re(Bpy)(CO)$_3$ Cl from Differences in Carbon Isotope Discrimination. *ACS Catal.* **2016**, *6* (8), 5473–5481. https://doi.org/10.1021/acscatal.6b01208.

(13) Kuramochi, Y.; Ishitani, O.; Ishida, H. Reaction Mechanisms of Catalytic Photochemical CO2 Reduction Using Re(I) and Ru(II) Complexes. *Coordination Chemistry Reviews* **2018**, *373*, 333–356. https://doi.org/10.1016/j.ccr.2017.11.023.

(14) Cancelliere, A. M.; Puntoriero, F.; Serroni, S.; Campagna, S.; Tamaki, Y.; Saito, D.; Ishitani, O. Efficient Trinuclear Ru(II)–Re(I) Supramolecular Photocatalysts for CO_2 Reduction Based on a New Tris-Chelating Bridging Ligand Built around a Central Aromatic Ring. *Chem. Sci.* **2020**, *11* (6), 1556–1563. https://doi.org/10.1039/C9SC04532E.

(15) Tamaki, Y.; Koike, K.; Morimoto, T.; Ishitani, O. Substantial Improvement in the Efficiency and Durability of a Photocatalyst for Carbon Dioxide Reduction Using a Benzoimidazole Derivative as an Electron Donor. *Journal of Catalysis* **2013**, *304*, 22–28. https://doi.org/10.1016/j.jcat.2013.04.002.

(16) Sahara, G.; Ishitani, O. Efficient Photocatalysts for CO_2 Reduction. *Inorg. Chem.* **2015**, *54* (11), 5096–5104. https://doi.org/10.1021/ic502675a.

(17) Tamaki, Y.; Ishitani, O. Supramolecular Photocatalysts for the Reduction of CO_2. *ACS Catal.* **2017**, *7* (5), 3394–3409. https://doi.org/10.1021/acscatal.7b00440.

(18) Kuramochi, Y.; Kamiya, M.; Ishida, H. Photocatalytic CO_2 Reduction in N , N - Dimethylacetamide/Water as an Alternative Solvent System. *Inorg. Chem.* **2014**, *53* (7), 3326–3332. https://doi.org/10.1021/ic500050q.

(19) Ashford, D. L.; Song, W.; Concepcion, J. J.; Glasson, C. R. K.; Brennaman, M. K.; Norris, M. R.; Fang, Z.; Templeton, J. L.; Meyer, T. J. Photoinduced Electron Transfer in a Chromophore–Catalyst Assembly Anchored to TiO_2. *J. Am. Chem. Soc.* **2012**, *134* (46), 19189–19198. https://doi.org/10.1021/ja3084362.

(20) Wang, F. Artificial Photosynthetic Systems for CO_2 Reduction: Progress on Higher Efficiency with Cobalt Complexes as Catalysts. *ChemSusChem* **2017**, *10* (22), 4393–4402. https://doi.org/10.1002/cssc.201701385.

(21) Wang, M.; Torbensen, K.; Salvatore, D.; Ren, S.; Joulié, D.; Dumoulin, F.; Mendoza, D.; Lassalle-Kaiser, B.; Işci, U.; Berlinguette, C. P.; Robert, M. CO2 Electrochemical Catalytic Reduction with a Highly Active Cobalt Phthalocyanine. *Nat Commun* **2019**, *10* (1), 3602. https://doi.org/10.1038/s41467-019-11542-w.

(22) Hu, X.-M.; Rønne, M. H.; Pedersen, S. U.; Skrydstrup, T.; Daasbjerg, K. Enhanced Catalytic Activity of Cobalt Porphyrin in CO_2 Electroreduction upon Immobilization on Carbon Materials. *Angew. Chem. Int. Ed.* **2017**, *56* (23), 6468–6472. https://doi.org/10.1002/anie.201701104.

(23) Zhang, X.; Wu, Z.; Zhang, X.; Li, L.; Li, Y.; Xu, H.; Li, X.; Yu, X.; Zhang, Z.; Liang, Y.; Wang, H. Highly Selective and Active CO2 Reduction Electrocatalysts Based on Cobalt Phthalocyanine/Carbon Nanotube Hybrid Structures. *Nat Commun* **2017**, *8* (1), 14675. https://doi.org/10.1038/ncomms14675.

(24) Ren, S.; Joulié, D.; Salvatore, D.; Torbensen, K.; Wang, M.; Robert, M.; Berlinguette, C. P. Molecular Electrocatalysts Can Mediate Fast, Selective CO_2 Reduction in a Flow Cell. *Science* **2019**, *365* (6451), 367–369. https://doi.org/10.1126/science.aax4608.

(25) Yuan, H.; Du, J.; Ming, M.; Chen, Y.; Jiang, L.; Han, Z. Combination of Organic Dye and Iron for CO_2 Reduction with Pentanuclear $Fe_2 Na_3$ Purpurin Photocatalysts. *J. Am. Chem. Soc.* **2022**, *144* (10), 4305–4309. https://doi.org/10.1021/jacs.1c13081.

(26) Derrick, J. S.; Loipersberger, M.; Nistanaki, S. K.; Rothweiler, A. V.; Head-Gordon, M.; Nichols, E. M.; Chang, C. J. Templating Bicarbonate in the Second Coordination Sphere Enhances Electrochemical CO_2 Reduction Catalyzed by Iron Porphyrins. *J. Am. Chem. Soc.* **2022**, *144* (26), 11656–11663. https://doi.org/10.1021/jacs.2c02972.

(27) Azcarate, I.; Costentin, C.; Robert, M.; Savéant, J.-M. Through-Space Charge Interaction Substituent Effects in Molecular Catalysis Leading to the Design of the Most Efficient Catalyst of CO_2-to-CO Electrochemical Conversion. *J. Am. Chem. Soc.* **2016**, *138* (51), 16639–16644. https://doi.org/10.1021/jacs.6b07014.

(28) Smieja, J. M.; Sampson, M. D.; Grice, K. A.; Benson, E. E.; Froehlich, J. D.; Kubiak, C. P. Manganese as a Substitute for Rhenium in CO_2 Reduction Catalysts: The Importance of Acids. *Inorg. Chem.* **2013**, *52* (5), 2484–2491. https://doi.org/10.1021/ic302391u.

(29) Sampson, M. D.; Nguyen, A. D.; Grice, K. A.; Moore, C. E.; Rheingold, A. L.; Kubiak, C. P. Manganese Catalysts with Bulky Bipyridine Ligands for the Electrocatalytic Reduction of Carbon Dioxide: Eliminating Dimerization and Altering Catalysis. *J. Am. Chem. Soc.* **2014**, *136* (14), 5460–5471. https://doi.org/10.1021/ja501252f.

(30) Grice, K. A.; Kubiak, C. P. Recent Studies of Rhenium and Manganese Bipyridine Carbonyl Catalysts for the Electrochemical Reduction of CO2. In *Advances in Inorganic Chemistry*; Elsevier, 2014; Vol. 66, pp 163–188. https://doi.org/10.1016/B978-0-12-420221-4.00005-6.

(31) Manganese, Technetium and Rhenium. In *Chemistry of the Elements*; Elsevier, 1997; pp 1040–1069. https://doi.org/10.1016/B978-0-7506-3365-9.50030-4.

(32) Becker, L. *Chemical elements by market price*. http://www.leonland.de/elements_by_price/en/ (accessed 2023-05-02).

(33) Thompson, D. W.; Ito, A.; Meyer, T. J. [Ru(Bpy)3]2+* and Other Remarkable Metal-to-Ligand Charge Transfer (MLCT) Excited States. *Pure and Applied Chemistry* **2013**, *85* (7), 1257–1305. https://doi.org/10.1351/PAC-CON-13-03-04.

(34) Uoyama, H.; Goushi, K.; Shizu, K.; Nomura, H.; Adachi, C. Highly Efficient Organic Light-Emitting Diodes from Delayed Fluorescence. *Nature* **2012**, *492* (7428), 234–238. https://doi.org/10.1038/nature11687.

(35) Shang, T.-Y.; Lu, L.-H.; Cao, Z.; Liu, Y.; He, W.-M.; Yu, B. Recent Advances of 1,2,3,5-Tetrakis(Carbazol-9-Yl)-4,6-Dicyanobenzene (4CzIPN) in Photocatalytic Transformations. *Chem. Commun.* **2019**, *55* (38), 5408–5419. https://doi.org/10.1039/C9CC01047E.

(36) Bryden, M. A.; Zysman-Colman, E. Organic Thermally Activated Delayed Fluorescence (TADF) Compounds Used in Photocatalysis. *Chem. Soc. Rev.* **2021**, *50* (13), 7587–7680. https://doi.org/10.1039/D1CS00198A.

(37) Yu, Z.-J.; Lou, W.-Y.; Junge, H.; Päpcke, A.; Chen, H.; Xia, L.-M.; Xu, B.; Wang, M.-M.; Wang, X.-J.; Wu, Q.-A.; Lou, B.-Y.; Lochbrunner, S.; Beller, M.; Luo, S.-P. Thermally Activated Delayed Fluorescence (TADF) Dyes as Efficient Organic Photosensitizers for Photocatalytic

Water Reduction. *Catalysis Communications* **2019**, *119*, 11–15. https://doi.org/10.1016/j.catcom.2018.09.018.

(38) Ma, F.; Luo, Z.-M.; Wang, J.-W.; Aramburu-Trošelj, B. M.; Ouyang, G. Earth-Abundant-Metal Complexes as Photosensitizers in Molecular Systems for Light-Driven CO2 Reduction. *Coordination Chemistry Reviews* **2024**, *500*, 215529. https://doi.org/10.1016/j.ccr.2023.215529.

(39) Wang, L. Recent Advances in Metal-Based Molecular Photosensitizers for Artificial Photosynthesis. *Catalysts* **2022**, *12* (8), 919. https://doi.org/10.3390/catal12080919.

(40) Du, Y.; Pearson, R. M.; Lim, C.; Sartor, S. M.; Ryan, M. D.; Yang, H.; Damrauer, N. H.; Miyake, G. M. Strongly Reducing, Visible-Light Organic Photoredox Catalysts as Sustainable Alternatives to Precious Metals. *Chemistry A European J* **2017**, *23* (46), 10962–10968. https://doi.org/10.1002/chem.201702926.

(41) Leung, C.-F.; Lau, T.-C. Organic Photosensitizers for Catalytic Solar Fuel Generation. *Energy Fuels* **2021**, *35* (23), 18888–18899. https://doi.org/10.1021/acs.energyfuels.1c02675.

(42) Takeda, H.; Cometto, C.; Ishitani, O.; Robert, M. Electrons, Photons, Protons and Earth-Abundant Metal Complexes for Molecular Catalysis of CO $_2$ Reduction. *ACS Catal.* **2017**, *7* (1), 70–88. https://doi.org/10.1021/acscatal.6b02181.

(43) Bullock, R. M.; Das, A. K.; Appel, A. M. Surface Immobilization of Molecular Electrocatalysts for Energy Conversion. *Chem. Eur. J.* **2017**, *23* (32), 7626–7641. https://doi.org/10.1002/chem.201605066.

(44) Whang, D. R. Immobilization of Molecular Catalysts for Artificial Photosynthesis. *Nano Convergence* **2020**, *7* (1), 37. https://doi.org/10.1186/s40580-020-00248-1.

(45) Kobayashi, T.; Kawate, D.; Niwa, A.; Nagase, T.; Goushi, K.; Adachi, C.; Naito, H. Intersystem Crossing Rate in Thermally Activated Delayed Fluorescence Emitters. *Phys. Status Solidi A* **2020**, *217* (3), 1900616. https://doi.org/10.1002/pssa.201900616.

(46) Cho, E.; Hong, M.; Coropceanu, V.; Brédas, J. The Role of Intermolecular Interactions on the Performance of Organic Thermally Activated Delayed Fluorescence (TADF) Materials. *Advanced Optical Materials* **2021**, *9* (14), 2002135. https://doi.org/10.1002/adom.202002135.

(47) Martinez-Perez, O.; Amiri, M.; Rasu, L.; Bergens, S. H. N-Heterocyclic Carbene Organic Dyes Derived from 2,4,5,6-Tetra(9H-Carbazol-9-Yl)Isophthalonitrile (4CzIPN) Bonded to TiO $_2$ Surfaces. *ECS J. Solid State Sci. Technol.* **2023**, *12* (10), 105006. https://doi.org/10.1149/2162-8777/acfff4.

(48) Liu, J.; Perez, O. M.; Lavergne, D.; Rasu, L.; Murphy, E.; Galvez-Rodriguez, A.; Bergens, S. H. One-Step Electropolymerization of a Dicyanobenzene-Carbazole-Imidazole Dye to Prepare Photoactive Redox Polymer Films. *Polymers* **2023**, *15* (16), 3340. https://doi.org/10.3390/polym15163340.

(49) Bourrez, M.; Molton, F.; Chardon-Noblat, S.; Deronzier, A. [Mn(Bipyridyl)(CO)3Br]: An Abundant Metal Carbonyl Complex as Efficient Electrocatalyst for CO2 Reduction. *Angew. Chem. Int. Ed.* **2011**, *50* (42), 9903–9906. https://doi.org/10.1002/anie.201103616.

(50) Evans, E. W.; Olivier, Y.; Puttisong, Y.; Myers, W. K.; Hele, T. J. H.; Menke, S. M.; Thomas, T. H.; Credgington, D.; Beljonne, D.; Friend, R. H.; Greenham, N. C. Vibrationally Assisted Intersystem Crossing in Benchmark Thermally Activated Delayed Fluorescence Molecules. *J. Phys. Chem. Lett.* **2018**, *9* (14), 4053–4058. https://doi.org/10.1021/acs.jpclett.8b01556.

(51) Hundemer, F.; Graf Von Reventlow, L.; Leonhardt, C.; Polamo, M.; Nieger, M.; Seifermann, S. M.; Colsmann, A.; Bräse, S. Acceptor Derivatization of the 4CzIPN TADF System: Color Tuning and Introduction of Functional Groups. *ChemistryOpen* **2019**, *8* (12), 1413–1420. https://doi.org/10.1002/open.201900141.

(52) *Reagents & Solvents*. https://www.chem.rochester.edu/notvoodoo/pages/reagents.php?page=solvent_polarity (accessed 2023-12-05).

(53) Mertz, E. L.; Tikhomirov, V. A.; Krishtalik, L. I. Stokes Shift as a Tool for Probing the Solvent Reorganization Energy. *J. Phys. Chem. A* **1997**, *101* (19), 3433–3442. https://doi.org/10.1021/jp963042b.

(54) Lakowicz, J. R. Effects of Solvents on Fluorescence Emission Spectra. In *Principles of Fluorescence Spectroscopy*; Springer US: Boston, MA, 1983; pp 187–215. https://doi.org/10.1007/978-1-4615-7658-7_7.

(55) Ishimatsu, R.; Matsunami, S.; Shizu, K.; Adachi, C.; Nakano, K.; Imato, T. Solvent Effect on Thermally Activated Delayed Fluorescence by 1,2,3,5-Tetrakis(Carbazol-9-Yl)-4,6-Dicyanobenzene. *J. Phys. Chem. A* **2013**, *117* (27), 5607–5612. https://doi.org/10.1021/jp404120s.

(56) Pellegrin, Y.; Odobel, F. Sacrificial Electron Donor Reagents for Solar Fuel Production. *Comptes Rendus Chimie* **2017**, *20* (3), 283–295. https://doi.org/10.1016/j.crci.2015.11.026.

(57) Ishimatsu, R.; Edura, T.; Adachi, C.; Nakano, K.; Imato, T. Photophysical Properties and Efficient, Stable, Electrogenerated Chemiluminescence of Donor–Acceptor Molecules Exhibiting Thermal Spin Upconversion. *Chemistry A European J* **2016**, *22* (14), 4889–4898. https://doi.org/10.1002/chem.201600077.

(58) Lundberg, P.; Tsuchiya, Y.; Lindh, E. M.; Tang, S.; Adachi, C.; Edman, L. Thermally Activated Delayed Fluorescence with 7% External Quantum Efficiency from a Light-Emitting Electrochemical Cell. *Nat Commun* **2019**, *10* (1), 5307. https://doi.org/10.1038/s41467-019-13289-w.

(59) Rønne, M. H.; Madsen, M. R.; Skrydstrup, T.; Pedersen, S. U.; Daasbjerg, K. Mechanistic Elucidation of Dimer Formation and Strategies for Its Suppression in Electrochemical Reduction

of *Fac* -Mn(Bpy)(CO) $_3$ Br. *ChemElectroChem* **2021**, *8* (11), 2108–2114. https://doi.org/10.1002/celc.202100279.

(60) Siritanaratkul, B.; Eagle, C.; Cowan, A. J. Manganese Carbonyl Complexes as Selective Electrocatalysts for CO_2 Reduction in Water and Organic Solvents. *Acc. Chem. Res.* **2022**, *55* (7), 955–965. https://doi.org/10.1021/acs.accounts.1c00692.

(61) Grills, D. C.; Farrington, J. A.; Layne, B. H.; Lymar, S. V.; Mello, B. A.; Preses, J. M.; Wishart, J. F. Mechanism of the Formation of a Mn-Based CO_2 Reduction Catalyst Revealed by Pulse Radiolysis with Time-Resolved Infrared Detection. *J. Am. Chem. Soc.* **2014**, *136* (15), 5563– 5566. https://doi.org/10.1021/ja501051s.

(62) Liu, J.; Bergens, S. H. Electronically Conductive, Multifunctional Polymer Binder for Highly Active, Stable, and Abundant Composite Electrodes for Oxygen Evolution. *ACS Appl. Mater. Interfaces* **2023**, *15* (21), 25624–25632. https://doi.org/10.1021/acsami.3c04573.

(63) Tamaki, Y.; Koike, K.; Ishitani, O. Highly Efficient, Selective, and Durable Photocatalytic System for CO_2 Reduction to Formic Acid. *Chem. Sci.* **2015**, *6* (12), 7213–7221. https://doi.org/10.1039/C5SC02018B.